Ballistocardiography and applications

Guillaume Cathelain

PSL
UNIVERSITÉ PARIS

THÈSE DE DOCTORAT
DE L'UNIVERSITÉ PSL

Préparée à l'École Pratique des Hautes Études

Ballistocardiographie et applications

Soutenue par
Guillaume Cathelain
Le 8 septembre 2020

École doctorale n° 472
École doctorale de l'École Pratique des Hautes Études

Spécialité
Informatique, mathématique et applications

Composition du jury :

Isis, TRUCK Professeur, Paris 8	*Président*
Catherine, ACHARD MCF, ISIR - UPMC	*Rapporteur*
Anne, HUMEAU-HEURTIER Professeur, LARIS - UA	*Rapporteur*
Jean, BERGOUNIOUX PU-PH, APHP	*Examinateur*
Bertrand, RIVET MCF, GIPSA	*Examinateur*
Joel, SWENDSEN Directeur d'études, EPHE	*Examinateur*
Sophie, ACHARD DR, GIPSA	*Co-directrice de thèse*
François, JOUEN Directeur d'études, EPHE	*Directeur de thèse*

École Pratique des Hautes Études | PSL

Contents

Contents 1

Abstract 5

English abstract 5

Résumé Français 7

List of Publications 9

Peer reviewed conference papers 9

Unpublished conference presentation 9

Journal paper under review 9

Patent application 10

List of abbreviations 11

Statement of original authorship 12

Preface 13

Acknowledgments 15

Chapter 1 17

1. General introduction 17

1.1. Clinical background 17

1.1.1. Global epidemiology 17

1.1.2. Physiological monitoring 18

1.1.3. Telehealth 21

1.2. Connected devices for physiological monitoring 24

1.2.1. Patient engagement in telehealth 24

1.2.2. The quantified self 25

1.2.3. Commercial connected devices 25

1.3. Ballistocardiography 26
1.3.1. Definition and mechanism 27
1.3.2. Brief history 29
1.3.3. Physiological waveforms 32
1.3.4. Potential for contactless monitoring and telehealth 33
1.3.5. Limitations 34
1.4. Research question and methodology 35
1.5. Outline 36
Chapter 2 37
2. Instrumentation in ballistocardiography 37
2.1. Benchmark of existing BCG instrumentations 37
2.1.1. Historical BCG instrumentations 37
2.1.2. Recent advances in BCG instrumentations 42
2.1.3. Commercial BCG modules with raw data access 46
2.1.4. Related physiological signals 49
2.2. Guidelines for designing a BCG accelerometer 51
2.2.1. Sensor 52
2.2.2. Conditioning circuit 54
2.2.3. Mechanical integration 64
2.3. The Baby Heartbeat Simulator 66
2.3.1. The experimental model 66
2.3.2. The cardiac force simulation 67
2.4. Signal amplification for smartphone BCG 68
2.4.1. Introduction 68
2.4.2. Bedding waveguide 71

2.4.3. Smartphone-based BCG 76
2.4.4. Conclusion 79
2.5. Signal multiplexing for BCG imaging 80
2.5.1. Introduction 80
2.5.2. Materials 81
2.5.3. Baseline wander removal 85
2.5.4. Noise frequency identification and filtering 90
2.5.5. Conclusion 92
Chapter 3 93
3. Digital signal processing in ballistocardiography 93
3.1. Recording and preprocessing of ballistocardiographic databases 94
3.1.1. CHArt 95
3.1.2. LSI 96
3.1.3. Ollie 97
3.1.4. R2P2 99
3.1.5. Preprocessing 100
3.1.6. Signal-to-noise ratio 100
3.1.7. ECG synchronization 101
3.2. Movement and occupancy segmentation 103
3.2.1. State of the art 103
3.2.2. Features 111
3.2.3. Classification 118
3.2.4. Benchmark of the literature and developed methods 125
3.3. Heart and respiratory rates measurement 126
3.3.1. State of the art 127

3.3.2. Dynamic Time Warping 139

3.3.3. Hidden Markov Models 146

3.3.4. U-Net Neural network 161

Chapter 4 167

4. General discussion and future perspectives 167

Consolidated list of references 168

Consolidated list of figures 201

Abstract

English abstract

Globally, healthcare systems have increasing costs and the number of hospitalizations grows. Telehealth brings hospital at home and provides health structures with new opportunities to improve the patient care pathway.

Physiological monitoring is a prerequisite in efficient telehealth systems and is performed by connected medical devices that are not fully automated. Patients need to use them actively on a day-to-day basis: these drawbacks lead either to patient disengagement or additional caregiver support.

Passive contactless vital signs' monitors, such as ballistocardiograms sleep trackers that measure motor, respiratory and cardiac activities, can solve the telehealth inefficiency. Moreover, they are more comfortable and safer for patients than traditional monitors, which is crucial for neonatal neurological development or in case of mental degeneration, though they are currently less accurate. How to improve physiological monitoring accuracy in ballistocardiography to increase telehealth efficiency?

In this thesis, materials are provided by a self-designed accelerometer-based instrumentation, a dedicated software, a heartbeat simulator, and measurement campaigns for raw ballistocardiograms' databases.

Novel analog amplification and digital filtering methods are investigated to improve ballistocardiography accuracy. The ballistocardiographic force, coming from the aortic arch deformation during the ventricular systole and measured on the bedside, is indeed modulated by respiratory and motor activities. It is also polluted by environmental mechanical artifacts. Furthermore, the ballistocardiography is unstandardized and ballistocardiograms have high inter- and intra-variabilities, depending on the beddings, the position in bed, the morphology, and the physiology of the patient.

Analog amplification is studied from two perspectives: the mechanical amplification of ballistocardiograms from the patient to the sensor, and the electronic amplification of the analog acceleration signal.

First, concerning the mechanical amplification, a novel waveguide bedding, a cotton tape encircling the mattress, was invented to concentrate the strain energy of the ballistocardiographic force in one direction, from the thorax straight to the attached sensor. Second, concerning the electronic amplification, a mixed-signal front-end was conceived to optimize the tradeoff between the electronic amplifier gain and the saturation time after a movement. The conditioning circuit measures the unamplified sensor output, passes it through a digital filter with a sharp transition frequency bandwidth and a proper initialization, and analogically amplifies the difference between this unwanted synthesized signal and the unamplified sensor output using a low noise instrumentation amplifier.

Digital filtering methods aim at separating signal sources, removing artifacts then detecting vital signs. Three original algorithms have been designed to efficiently recognize heartbeats in ballistocardiograms. The first algorithm is dynamic time warping template matching, where a heartbeat template is used to match heartbeats using a warping distance. The second algorithm models ballistocardiograms with periodic hidden Markov models. The third algorithm, the U-Net neural network, is supervised and segments heartbeats in ballistocardiograms.

Finally, ballistocardiograms are mechanically and electronically amplified by 12 dB and 21 dB respectively, without saturation time; and digital filtering algorithms reach a 97% precision and 96% recall for heartbeats detection.

Shortly, the designed ballistocardiograph will be clinically evaluated in a pediatric intensive care unit and telemedicine against other ballistocardiographs and the gold standard methods.

Résumé Français

À l'échelle mondiale, les systèmes de santé ont des coûts croissants et le nombre d'hospitalisations augmente. La télémédecine permet de ramener l'hôpital à la maison et offre aux structures de santé de nouvelles possibilités d'améliorer le parcours de soins des patients.

La surveillance physiologique est une condition préalable à l'efficacité des systèmes de télémédecine et est assurée par des dispositifs médicaux connectés qui ne sont pas entièrement automatisés. Les patients doivent les utiliser activement au quotidien : ces inconvénients entraînent soit un désengagement du patient, soit du personnel soignant supplémentaire.

Les moniteurs passifs et sans contact des signes vitaux, tels que les ballistocardiographes qui mesurent les activités motrices, respiratoires et cardiaques, peuvent résoudre l'inefficacité de la télémédecine. En outre, ils sont plus confortables et plus sûrs pour les patients que les moniteurs traditionnels, ce qui est crucial pour le développement neurologique néonatal ou dans les cas de dégénérescence mentale, bien qu'ils soient actuellement moins précis. Comment améliorer la précision de la surveillance physiologique en ballistocardiographie pour accroître l'efficacité de la télémédecine ?

Dans cette thèse, le matériel est fourni par une instrumentation propriétaire basée sur un accéléromètre, un logiciel dédié, un simulateur de battements cardiaques, et des campagnes de mesure pour les bases de données de ballistocardiogrammes bruts.

De nouvelles méthodes d'amplification analogique et de filtrage numérique sont étudiées pour améliorer la précision de la ballistocardiographie. La force ballistocardiographique, provenant de la déformation de la crosse aortique lors de la systole ventriculaire et mesurée sur le côté du lit, est en effet modulée par les activités respiratoires et motrices, et est polluée par les artefacts mécaniques de l'environnement. En outre, la ballistocardiographie n'est pas normalisée et les ballistocardiogrammes présentent des

variabilités inter et intra-individuelles élevées, en fonction de la literie, de la position au lit, de la morphologie et de la physiologie du patient.

L'amplification analogique est étudiée d'un point de vue mécanique et électronique.

Premièrement, en ce qui concerne l'amplification mécanique, un nouveau guide d'ondes, prenant la forme d'un ruban de coton qui encercle le matelas, a été inventé pour concentrer l'énergie de la force ballistocardiographique dans une direction, du thorax jusqu'au capteur. Deuxièmement, en ce qui concerne l'amplification électronique, un circuit de conditionnement hybride a été conçu pour optimiser le compromis entre le gain de l'amplificateur électronique et la durée de saturation après un mouvement.

Les méthodes de filtrage numérique visent à séparer les sources de signaux, à éliminer les artefacts puis à détecter les signes vitaux. Trois algorithmes originaux ont été conçus pour reconnaître efficacement les battements de cœur dans les ballistocardiogrammes. Le premier algorithme est la comparaison par déformation temporelle dynamique, où un modèle battement cardiaque est utilisé pour reconnaître les battements cardiaques en utilisant une distance non-linéaire. Le second algorithme modélise les ballistocardiogrammes avec des modèles de Markov cachés périodiques. Le troisième algorithme, le réseau neuronal U-Net, est supervisé et segmente les battements cardiaques en ballistocardiogrammes.

Finalement, les ballistocardiogrammes sont amplifiés mécaniquement et électroniquement de 12 dB et 21 dB respectivement, sans saturation après mouvement ; et les algorithmes de filtrage numérique atteignent une précision de 97 % et une sensibilité de 96 % pour la détection des battements cardiaques.

Prochainement, le ballistocardiographe conçu sera évalué cliniquement dans une unité de soins intensifs pédiatriques et en télémédecine par rapport à d'autres ballistocardiographes et aux méthodes de référence.

List of Publications

Peer reviewed conference papers

G. Cathelain, B. Rivet, S. Achard, J. Bergounioux and F. Jouen, “Dynamic Time Warping for Heartbeat Detection in Ballistocardiography”, *2019 Computing in Cardiology (CinC)*, Singapore, 2019, pp. 1- 4.

G. Cathelain, B. Rivet, S. Achard, J. Bergounioux and F. Jouen, “Smart ballistocardiography front-end”, *2020 IEEE International Instrumentation and Measurement Technology Conference (I2MTC)*, Croatia, 2020.

G. Cathelain, J. Bergounioux and F. Jouen, “Bedding waveguide for smartphone-based ballistocardiography”, *2020 IEEE International Symposium on Medical Measurements and Applications (MeMeA)*, Italy, 2020.

G. Cathelain, B. Rivet, S. Achard, J. Bergounioux and F. Jouen, “U-Net Neural Network for Heartbeat Detection in Ballistocardiography”, *2020 42nd Annual International Conference of the IEEE Engineering in Medicine and Biology Society (EMBC),* Canada, 2020.

Unpublished conference presentation

G. Cathelain, B. Rivet, S. Achard and F. Jouen, “Model Reduction of Ballistocardiogram Hidden Markov Model”. *Presented in the 10th congress of the European Union for Systemics (EUS2018), Brussels, 2018.*

Journal paper under review

G. Cathelain, A. Perrier, L. Folliot, C. Le Gloanec, M. Rarrbo, F. Jouen, E. Saudeau, G. Costa, R. Carlier and J. Bergounioux, “Bench testing of tracheostomy tubes conflicts using an instrumented mannequin”. *Under review for JAMA Otolaryngology-Head & Neck Surgery.*

Patent application

G. Cathelain, F. Jouen, R. Jaffrès, “Guide de contrainte pour ballistocardiographie”, FR1903297, WO32128.

G. Cathelain, “Imagerie ballistocardiographique”, FR2002547.

List of abbreviations

EPHE	Ecole Pratique Des Hautes Etudes
API	Application Programming Interface
APHP	Assistance Publique Des Hopitaux De Paris
UVSQ	Universite Versailles - Saint Quentin En Yvelines
PSL	Paris Sciences Lettres
RPM	Remote Patient Monitoring
BCG	Ballistocardiography, Ballistocardiogram, Ballistocardiograph
ECG	Electrocardiography, Electrocardiogram, Electrocardiograph
PPG	Photoplethysmography, Photoplethysmogram, Photoplethysmograph
HRV	Heart Rate Variability
MCC	Multiple Chronic Conditions
ICU	Intensive Care Unit
PICU	Pediatric Intensive Care Unit
NICU	Neonatal Intensive Care Unit
WHO	World Health Organization
SAMU	Service d'Aide Medicale D'urgence
IoT	Internet of Things
B2C	Business-To-Consumer
CPAP	Continuous Positive Airway Pressure
MEMS	Micro-Electromechanical Systems
PSG	Polysomnography

Statement of original authorship

The work contained in this thesis has not been previously submitted for a degree at any other higher education institution to the best of my knowledge and belief. This thesis contains no material previously published or submitted for publication by another person except where due reference has been made.

Signed: Date:

(Guillaume Cathelain)

Preface

"Anything that won't sell, I don't want to invent. Its sale is proof of utility, and utility is success" said Thomas Edison, a man of the 19th century who was both an entrepreneur and a scientist. He invented the phonograph, was a pioneer of direct current electricity and cinematography, filed more than a thousand patents, and funded the General Electric company.

This radical philosophy wants to bring the research out of the laboratory and technology to the masses. This inspired me a lot when I decided, in August 2016, to join an entrepreneurship master's degree after I passed my Electrical Engineering “Agrégation” during my Ecole Supérieure curriculum in Rennes, France. The first part of this degree consisted of a four-months long stay at the Berkeley campus of the University of California to learn how innovation works in Silicon Valley. In January 2017, I came back to the Ecole Polytechnique in Paris with a smart mattress project for predictive medicine. To develop the technology, I met several researchers, and finally, Professor François Jouen convinced me to start an internship then a Ph.D. thesis at the Cognitions Humaine et Artificielle laboratory of Ecole Pratique des Hautes Etudes in Paris. Meanwhile, I was allowed to found my startup Fealing as an entrepreneur student in the Paris Sciences Lettres University to sell devices and solutions to clinicians and individuals to gather the data needed for the research work. Some of these developed tools are presented in this thesis.

The initial focus of the project was neonatology and I landed in the pediatric intensive care unit of Dr. Jean Bergounioux in the Raymond Poincaré Hospital of the Assistance Publique des Hôpitaux de Paris. Reglementary issues with monitoring babies using new prototype hardware lead me first to monitor adults; other collaborations with industrials and

researchers finished broadening my clinical scope to neonatology, geriatrics, and the general population.

Even if this research work has a French focus, for example concerning the epidemiology or the healthcare system, the English language, more universal than French nowadays, was chosen in this document and will help to make its content available to a broader community.

Acknowledgments

The completion of this research work would not have been possible without the help of many people and institutions.

First, my main thesis supervisor, François Jouen, for answering my scientific questions, teaching me the research methodology, and reviewing my conference articles. You always have supported both of my research and entrepreneur work. A big thank you for all of that, François.

Thank you, Sophie Achard and Bertrand Rivet for your warm welcome in the GIPSA lab in Grenoble and your valuable insights.

Two physicians have also helped me to understand the basic human physiology knowledge underlying ballistocardiography: thank you Dr. Pierre-Emmanuel Cailleaux, and special thanks to you, Dr. Jean Bergounioux, for hosting my research team in your clinical unit.

Thank you, Bruno Rostand, and the whole technology transfer office of the Paris Sciences Lettres University, for supporting, funding, and protecting my work since the beginning. Thank you, Geoffrey Tissier, for having helped me design my first ballistocardiographs.

I would also like to acknowledge other members of this thesis jury, Joel Swendsen, Isis Truck, and especially Catherine Achard and Anne Humeau-Heurtier for reviewing my work.

I would like to thank my parents for having offered me the opportunity to undergo a lengthy education and taught me a sense of curiosity.

And last but not least, I dedicate this work to my first and beloved reader, Clemence Collon, whom I should have already married. I address her a special thanks for bearing me every day in my ups and downs since I began my research.

Chapter 1

1. General introduction

1.1. Clinical background

This thesis has a clinical context where the number and cost of hospital admissions are high. During these hospitalizations, physiological monitoring is necessary but sometimes inadequate.

1.1.1. Global epidemiology

1.1.1.1. Number of hospitalizations

In 2017, 12 million patients have been admitted to complete hospitalization and 16.8 million patients have been admitted for partial hospitalization in France according to the Direction de la Recherche, des Etudes, des Evaluations et des Statistiques [1]. Complete hospitalization days are slightly diminishing by -0.8% while partial hospitalization days are increasing by +2%. This trend is mainly due to population aging and the rise of multiple chronic conditions.

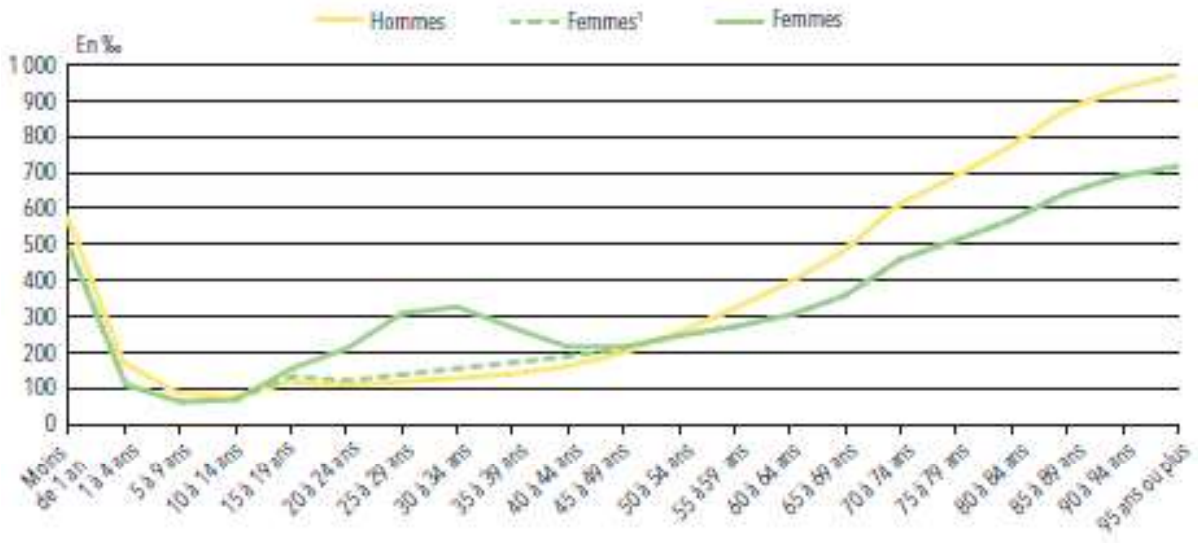

Figure 1: Hospitalization rate of short-term care units in France, 2017. The dashed green curve represents women excluding pregnancy, childbirth, and puerperium.

The hospitalized population is mainly segmented into three categories: babies, pregnant mothers, and seniors, defined as 65 years old and older. This age pattern is typical in

health, where the two extreme periods of life are weaker and need more care than the general population. Later in this section, a focus is made on pediatrics and geriatrics.

1.1.1.2. Chronic diseases

Chronic diseases are defined by the World Health Organization (WHO) as long-term diseases that generally evolve slowly [2]. They mainly comprise cardiovascular diseases, cancers, diabetes, and chronic lung diseases. Chronic diseases are responsible for 36 million deaths worldwide in 2008, which is 63% of the global number of deaths every year. Low and middle-income countries carry 80% of these deaths, and three-quarters of deaths are more than 60 years old.

This epidemy is accelerated by several risk factors: alcohol, tobacco, malnutrition, low physical activity, among others. Primary prevention, such as law regulation of sugar rate in sodas, can reduce these risk factors on a nation-wide scale. However, it is generally insufficient and needs to be combined with healthcare interventions.

For healthcare systems in developed countries, chronic patients typically go back and forth between home and hospital because their diseases can last several years and lead to comorbidities. In France, 35% of the general population suffers from chronic diseases and their care costs 84 billion euros to the CNAM (Caisse Nationale d'Assurance Maladie), which is the French public health insurance [3].

1.1.2. Physiological monitoring

1.1.2.1. Usual equipment

The physiological state and stability of a patient are reflected by her or his vital signs. They should be monitored, especially in acute stages of the hospitalization which require close attention and monitoring of caregivers, but also during home care or for secondary prevention.

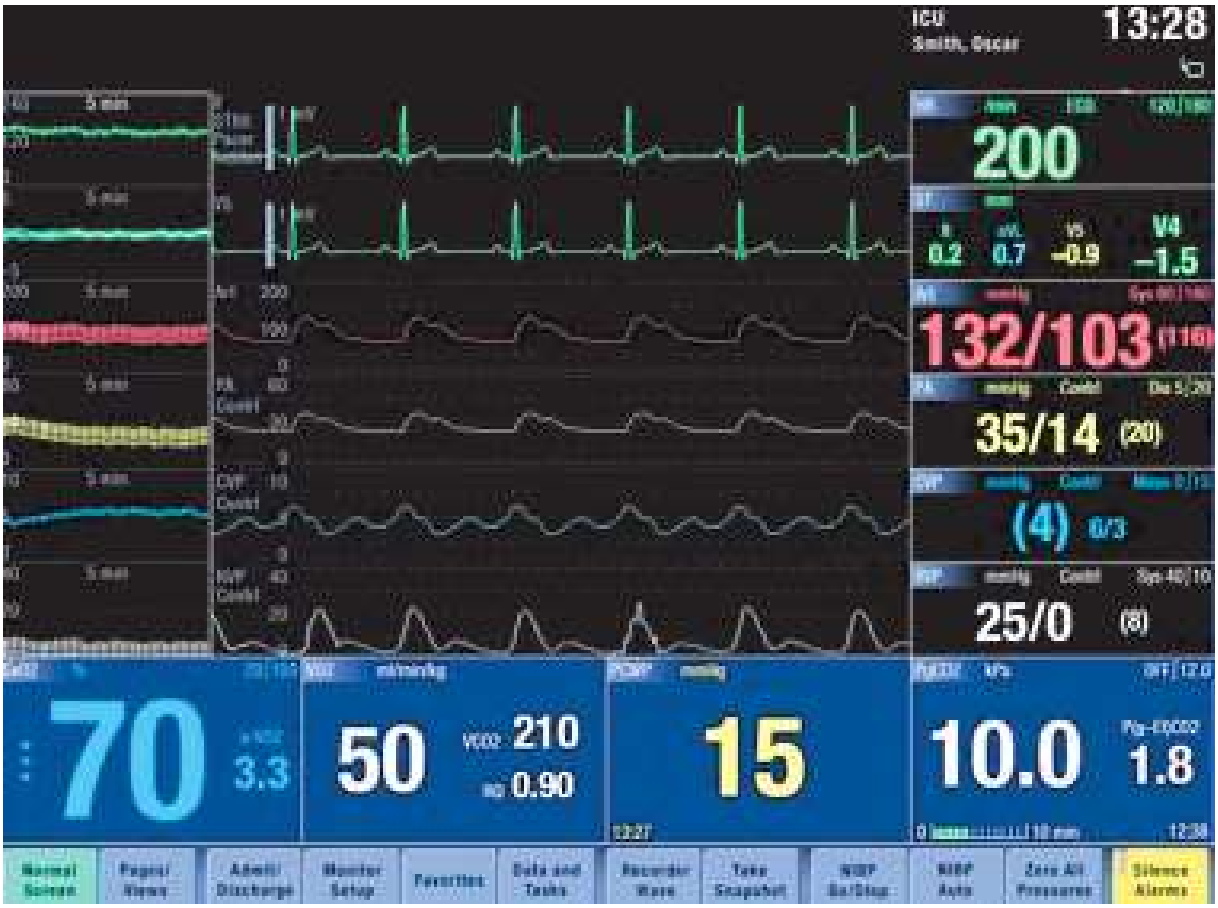

Figure 2: Multi-parameter patient monitor screen

Vital signs of patients are continuously monitored during hospitalization by a multi-parameter patient monitor: it is indeed part of any modern medical care unit, for example in surgery unit or intensive care unit. This versatile and increasingly sophisticated instrument displays, records, and transmits to the hospital computer system many vital signs or physiological parameters, for example, the heart rate, the blood pressure, the oxygen saturation, and the respiratory rate. Also, it notifies caregivers when one of those physiological parameters crosses its normal range without interruption in real-time. These normal ranges are usually defined by the medical staff depending on the age and the pathology of the patient, and aim at keeping him safe and comfortable. The multi-parameter patient monitor has portable equivalents for ambulatory or home care.

Instruments designed for rectifying a physiological failure also always provide vital signs monitoring. This is the case of pacemakers that monitor cardiac activities and

continuous positive airways pressures that monitor respiratory activities. Physicians may also prescribe single parameter monitors, for example, a tensiometer in case of heart failure.

In many cases such as those explicated above, the physiological monitoring equipment used for medical care is intrusive, i.e. they touch the patient, and need the involvement of either the patient, either the caregiver, or both.

1.1.2.2. Difficulties in pediatrics

A multi-parameter patient monitor usually comprises electrodes, stuck on the thorax and the limb extremities, for electrocardiography (ECG) and a pulse oximeter, closed in on a finger or a toe, for photoplethysmography (PPG). Monitoring children is difficult because of their high mobility that leads to repetitive artifacts and false alarms. Moreover, electrodes may peel off the epidermis, and pulse oximetry probes can regularly detach from the finger or toe. Several factors are involved: the child twitches and pulls the probes, the electrode adhesive is worn, or the nursing staff could not properly set up the electrodes. The extended application of pulse oximeter is likely to cause pressure ulcers, as it has been observed in pediatric intensive care units (PICU) [4].

Monitoring a child may thus lead to stress and possibly pain. However, children's pain affects neuro-motor and cognitive development, especially for preterm neonates. In a neonatal care unit, researchers indeed observed on very premature infants that pain exposure has a primary and early effect on subcortical structures with white matter changes [5].

Finally, this equipment is expensive to install and maintain; given the elements described above, probes must be changed or replaced several times during hospitalization.

1.1.2.3. Difficulties in geriatrics

Monitoring the elderly is also a challenge for other reasons. According to the WHO, 15% of the 60 years-old patients have mental illness worldwide. Those pathologies cause

aggressive behavior and oblivion: patients either refuse or forget their treatments. This lack of adherence prevents them from being efficiently monitored.

No pulse oximeter pressure ulcer case has been found in geriatrics literature; however geriatric patients are as children likely to be concerned because of their fragile epidermis.

1.1.3. Telehealth

1.1.3.1. Definition

Telehealth is defined as by the WHO as *"the use of telecommunication and virtual technology to deliver health care outside the traditional health-care facilities."*. Telehealth, or telemedicine, can be classified into several categories: remote patient monitoring, tele-expertise, teleconsultation, and teleassistance.

Remote patient monitoring (RPM), or telemonitoring, explicitly consists of monitoring the patient remotely. RPM tools are usually digital questionnaires on tablets or smartphones and connected devices for vital signs, e.g. glucometers for diabetes or heart rate and blood pressure monitors for heart failure.

Tele-expertise, also referred to as store-and-forward telemedicine or asynchronous telemedicine, is a remote way to share expertise between different medical specialties. It may be used by a primary care physician who needs specific expertise from a secondary care physician; or between several secondary care physicians in case of a pathology that involves several specialties.

Teleconsultation, or real-time telemedicine, is a face-to-face consultation using a videoconference software between a patient and a physician. Patients spare time with teleconsultation because they don't have to move to the physician's office. It also prevents ill patients from contaminating others, which is essential for example during the coronavirus confinement. However, it is sometimes difficult for the physician to diagnose trouble without

watching its patient in real life. Therefore, teleconsultation must not be systematic and only concern mild troubles.

Teleassistance allows the patient to call a medical assistant in case of an emergency. The medical assistant will often ask a few questions to understand the nature and severity of the emergency. He will then elaborate on a strategy to solve the emergency, for example calling an ambulance. In France, private teleassistance providers equip elderly homes with connected devices and wearables, that can automatically send an alarm to the computer system and establish a phone connection between the medical assistant and the patient, for example when the patient falls. Teleassistance is also part of the prehospital emergency medicine for the general population, where a regulating doctor tries to find the best care strategy with the available medical resources. In France, it is called the SAMU, for *Service d'Aide Médicale d'Urgence*, and can be called by dialing 15 on one's phone.

1.1.3.2. Care efficiency of remote patient monitoring

The two main promises of telehealth strategies are the quality of care delivery and the reduction of healthcare costs. Multiple clinical studies have been conducted for several decades and have shown a growing interest in telehealth, in times where digital telecommunications make it easier and easier to record and share behavioral and physiological data.

The Commonwealth Fund supported a study to learn lessons from early RPM programs in the US, including the Veterans Health Administration (VHA) that deployed a telehealth system since 2003. The VHA experiment was a scaled up with 70 000 patients involved in 2012. In the conclusion of the study, during the 2004-2007 period, patients significantly stayed 25% fewer days in hospital [6].

Telemonitoring of heart failure patients was also conducted using phone calls and weighing scales on 826 patients compared to a control group with usual care [7]. The median

age of the patients was 61 years. The results of this randomized controlled trial were that there are no significant differences between the two groups in terms of readmission or death for any reason within 180 days after enrollment, hospitalization for heart failure, number of days in the hospital, and number of hospitalizations. Weighing scales were chosen as RPM tools by Chaudhry after he demonstrated in 2007 that the weight gain, resulting from heart failure decompensation and fluid retention, was significantly different from HF patients and control patients up to 30 days before hospitalization [8].

A more recent experiment focused on 1 437 heart failure patients from 2011 to 2013 [9]. The cohort has been divided into two groups: a control group with the usual nurse care and an RPM group with different telemedicine tools such as phone calls but also connected devices. This study concludes RPM and usual care lead to similar hospital readmission and mortality rate within 30 or 180 days after discharge. Moreover, RPM patients experienced better quality of life after 180 days than usual cared patients.

Because of the diversity of pathologies that unstandardized RPM systems may monitor, the results of RPM clinical studies are never the same and difficult to compare. However, conclusions of these studies generally state that RPM experimentations produce as least as good morbidity and mortality rates as usual care.

1.1.3.3. Cost efficiency of remote patient monitoring

RPM patient programs cost must not be underestimated. It was evaluated in 2016 in $275 to $7 963 per patient per year range, which includes equipment purchase, servicing, and monitoring [10]. The upper bound of this range is quite impressive and does not include the cost of hospital readmissions that still happen. Cheaper technologies have the potential to make RPM programs cost- and care-efficient.

Looking at these promising consequences, many governments in developed countries have been encouraging telehealth, especially remote patient monitoring. For example, in

France, 199 200 hospitalizations have been moved at home using RPM in 2017, which is 5% more than in 2016 [1].

1.2. Connected devices for physiological monitoring

Connected devices might be used for telehealth, a solution to chronic care, as well as for contactless monitoring in ICU. However patient engagement to telehealth programs is an issue.

1.2.1. Patient engagement in telehealth

An engaged patient respects the prescriptions of the physician. In the medical context, engagement is also referred to as adherence or compliance. Engagement is a huge issue because a disengaged patient refuses care, therefore puts himself or herself in danger. This is particularly true at home when it is the patient's responsibility to respect the prescription of the physician.

Patient engagement is key to the success of RPM systems. A systematic review study was conducted in 2015 over 72 recent peer-reviewed scientific papers [11]. This review concluded that patient engagement could vary from 40 to 90 % in RPM experiments. Moreover, patient engagement can drop easily after the installation of RPM equipment. In an example of a hypertension monitoring study, blood pressure had to be self-measured three times in the morning, at lunch, and in the evening. After 10 months, the engagement of the involved patients fell from 89 down to 50 %.

One good practice to maintain or improve patient engagement is pedagogy, in terms of explaining the illness and of the use of medical devices. Another key factor is the automation of RPM devices, to implement when it is possible and relevant. For example, when it comes to transmitting physiological data, answering a questionnaire more fastidious than wearing a wearable, but only if the patient agrees with this wearable.

Nowadays, treatments such as continuous positive airway pressure (CPAP) machines and pacemakers already include physiological data transmitters in addition to their active functions. Engagement to RPM programs is eased for the patients following these kinds of treatments because they are not asked to be active in the monitoring process. However, it concerns few patients, for example, 63 000 to 69 000 French patients in 2009 for pacemakers, only about one-thousandth of the general population [12].

1.2.2. The quantified self

Connected health devices are multiple but share one common definition: they record and transmit behavioral or physiological data through the Internet. They are besides referred to as the Internet of Things (IoT) devices. The most common examples are standalone mobile application, smartwatches as well as sleep trackers.

The quantified self is a sociologic phenomenon that empowers people by giving them basic medical knowledge and helping them monitor their health without medical intervention.

The quantified self is limited because there is in people's minds a confusion between the medical data that is not always available on connected devices and wellness data. Moreover, the best medical equipment can only provide pre-diagnoses and it is a bit naïve to consider that everyone can become in a few days its doctor and diagnoses its troubles.

Nevertheless, user experience is particularly considered while developing quantified-self connected devices, like every other B2C product because the consumer must want to buy it. While developing a connected device for RPM, manufacturers should always put the user experience as a priority feature to get more engagement from the patients and employees that uses the system.

1.2.3. Commercial connected devices

Typical commercial connected devices for remote patient monitoring systems are listed in the following table. The retained key functionalities of connected devices for RPM are patient

intervention and patient contact, which may influence patient engagement. One can add the cost related to the measured vital signs and their relevance with the patient pathology.

The patient intervention is specified as active or passive. The patient intervention is active when the monitoring needs a short effort; it is passive when the monitoring is effortless. The device may be contactless, or on the contrary, may need to be in contact with the patient. Other features can influence patient engagement, though they generally do not depend on connected devices nature: the pedagogy, patient motivation, etc.

Table 1: Commercial connected devices for remote patient monitoring

Device	Vital signs	Engagement	Contact
Tensiometer	Heart rate, blood pressure	Yes	Yes
Smartwatch	Heart rate, oxygen saturation, falls	No	Yes
Glucometer	Glycemia	Yes	Yes
Oximeter	Heart rate, oxygen saturation	Yes	Yes
Scale	Weight	Yes	Yes
Thermometer	Body temperature	Yes	Yes
ECG	Heart rate	Yes	Yes
Fall detector	Falls	No	Yes
Bed exit detector	Falls	No	No
Smartphone	Heart rate	Yes	Yes

In the case of a standalone smartphone, the smartphone is self-sufficing, relies only on its internal sensors, and does not require any external sensor. For example, heart rate mobile applications use the smartphone flash and the camera to measure heart rate using the same principle as oximeters. Some of these applications are certified as medical devices.

Contactless connected devices seem to promote best patient monitoring since they do not require patient intervention and are better accepted. However, these devices can monitor very few vital signs and are not adapted for monitoring most pathologies.

1.3. Ballistocardiography

The ballistocardiographic monitoring technology has the potential to increase patient engagement to telehealth programs and to improve the safety and well-being of the patient in hospitals. However, this technology is not yet clinically mature.

1.3.1. Definition and mechanism

Ballistocardiography is a contactless monitoring method for cardiac activity. It relies on measuring ballistic forces: during ventricular systole, blood is ejected from the left ventricle through the aortic arch, generating a pulsed cardiac ballistic force.

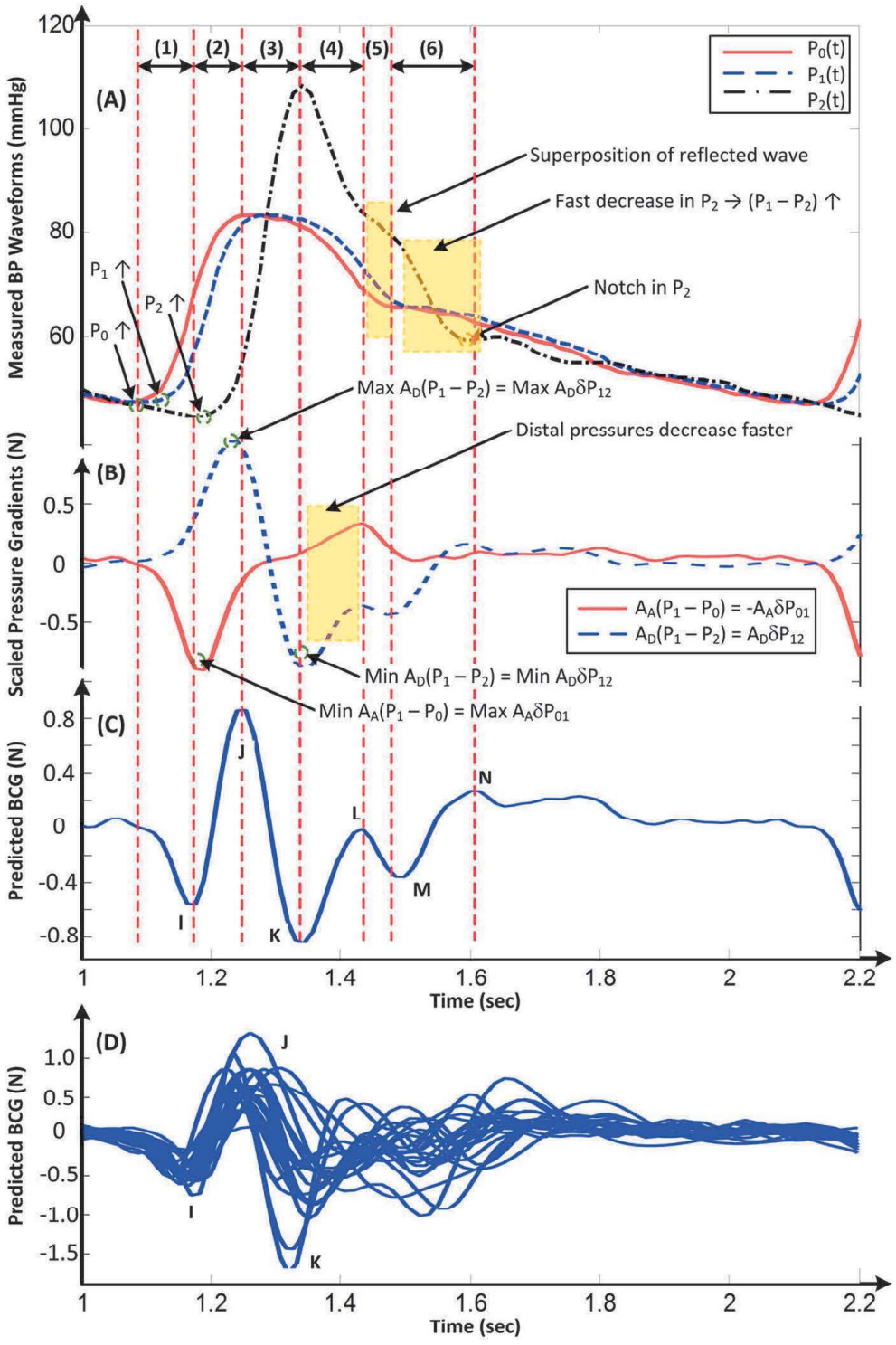

Figure 3 : Ballistocardiogram waveform construction

The ballistocardiographic force has been modeled [13] by mathematical equations as the hydraulic pressure loss occurring through the aortic arch. In this model, the ascending part of the aortic arteria between the aortic valve and the aortic arch after the aortic arch are denoted by subscripts A and D respectively. The aortic arch is not represented. These parts of the aortic arteria are cylinders with sections of nearly fixed areas A. P stands for blood pressure while Q stands for the volume flow rate, those quantities being dynamic. The inlet of the ascending aorta, the apex of the aortic arch and outlet of the descending aorta are thus respectively defined by the $(P_0(t), Q_0(t))$, $(P_1(t), Q_1(t))$ and $(P_2(t), Q_2(t))$ with A_A and A_D for the areas of the ascending and descending parts. The Newton's second law implies that the ascending aorta and the descending aorta are subject to the following forces, with ρ the blood volumic mass:

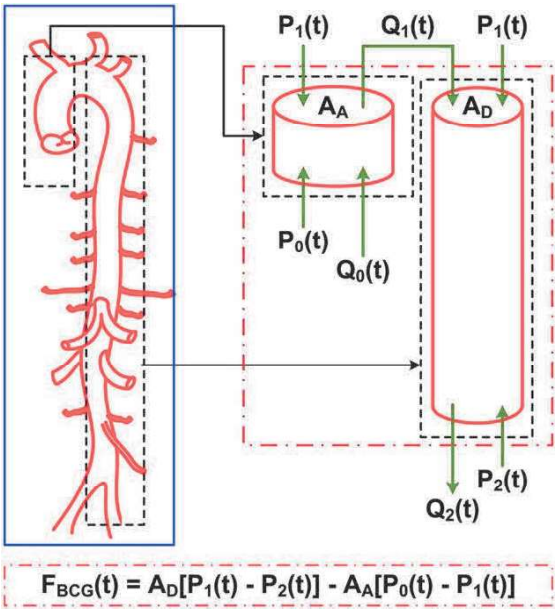

Figure 4 : Fluid mechanics model of ballistocardiography

$$\begin{cases} F_A(t) = \left[P_0(t)A_A + \dfrac{\rho Q_0^2(t)}{A_A}\right] - \left[P_1(t)A_A + \dfrac{\rho Q_1^2(t)}{A_A}\right] \\ F_D(t) = \left[P_2(t)A_D + \dfrac{\rho Q_2^2(t)}{A_D}\right] - \left[P_1(t)A_D + \dfrac{\rho Q_1^2(t)}{A_D}\right] \end{cases}$$

Finally and according to Newton's third law, the aortic arch is subject to a ballistocardiographic force :

$$\begin{aligned} F_{BCG}(t) &= -[F_A(t) + F_D(t)] \\ &= A_D\left[\left(P_1(t) + \rho\left[\frac{Q_1(t)}{A_D}\right]^2\right) - \left(P_2(t) + \rho\left[\frac{Q_2(t)}{A_D}\right]^2\right)\right] \\ &= -A_A\left[\left(P_0(t) + \rho\left[\frac{Q_0(t)}{A_A}\right]^2\right) - \left(P_1(t) + \rho\left[\frac{Q_1(t)}{A_A}\right]^2\right)\right] \\ &\approx A_D[P_1(t) - P_2(t)] - A_A[P_0(t) - P_1(t)] \end{aligned}$$

In this equation, the velocity contribution is negligible (1.6-1.9 mmHg) compared to the blood pressure contribution (100 mmHg). The ballistocardiographic waveform, called ballistocardiogram, is illustrated in Figure 3.

The ballistocardiographic force reverberates from the aortic arch to the whole body through organic tissues, then from the body to the patient support, for example, a bed. Consequently, the whole bed is subject to a short and tiny mechanical stress that can be measured as a displacement on free-stress surfaces, e.g. on the mattress surface using an accelerometer, or as stress on constrained surfaces, e.g. below the mattress using strain gauges.

1.3.2. Brief history

1.3.2.1. Origins

In 1877, Gordon measured body movement due to cardiovascular forces [14]. He observed, while a man was standing on an analogic weighing scale, that the needle vibrated synchronously with the heartbeats. Heartbeats could also be measured in a supine position on a suspended bed. From this experiment, many researchers had been working on different instrumentation including tables, weighing scales, and chairs to mechanically measure this cardiac output: Henderson [15] in 1905, Heald and Tucker [16] in 1922, Angenheister and Lau [17] in 1928, and Abramson [18] in 1933, among others.

In 1939, Starr theorized these observations and called them “ballistocardiogram”, from the contraction of the « ballein », « kardia » et « graphia » ancient Greek terms that respectively mean throw, heart, and description [19]. Starr designed a lying table and an

optomechanical system that was able to amplify 8 000 times the table movement. Despite improvements brought to Starr's table in the following years, ballistocardiography never reached clinical use. The contemporaneous electrography [20] was indeed preferred for cardiac activity monitoring, especially because it was much more reliable, standardized, interpretable, and portable at that time. Finally, two non-invasive cardiac and hemodynamics ultrasonic technique dug the grave of ballistocardiography: echocardiography [21] and magnetic resonance imaging [22] invented in 1953 and 1973 respectively. Ballistocardiography progressively lost this interest of clinicians and researchers until the

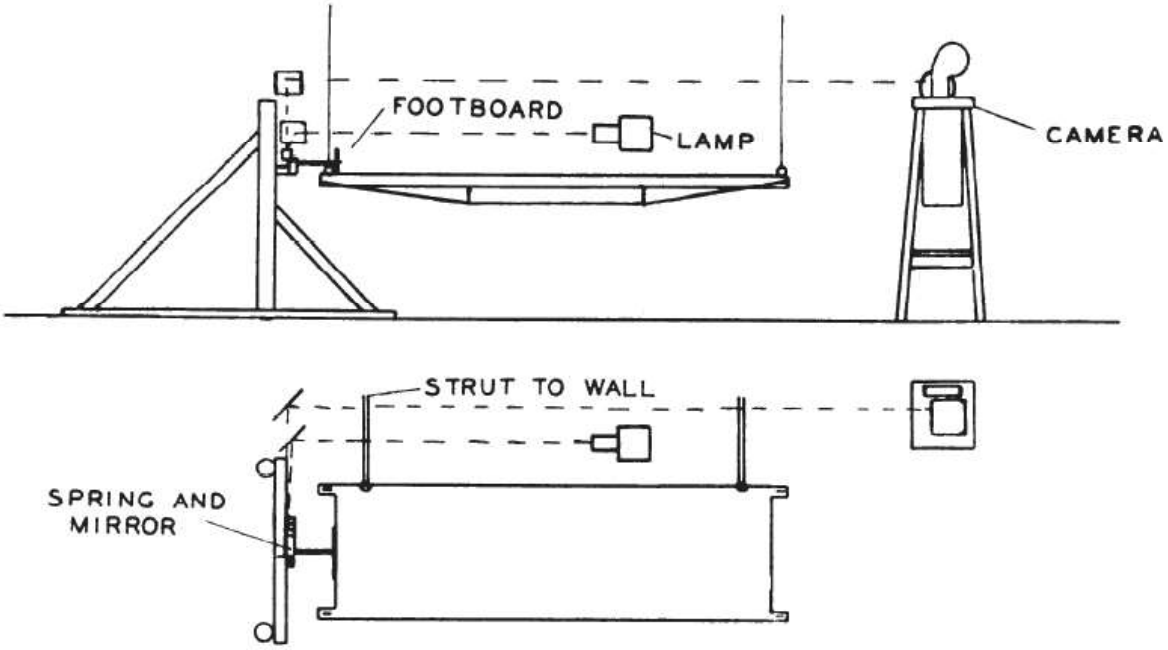

Figure 5: Starr ballistocardiographic instrumentation

2010s, as illustrated in Figure 6 [23].

At that time, signal processing methods were analogic with no other possibility that hand-drawing constructions for heart rate series computing. Vital signs monitoring was indeed time-consuming before the digital electronics emergence. Back in 1952 for example [24], coils and capacitors were still the only filtering techniques among optical and mechanical methods.

1.3.2.2. Recent developments

Recently, with new sensor technologies and digital signal processing, ballistocardiography is gaining a renewed interest [23].

Firstly, instrumentations have completely changed since Starr. New sensor technologies emerged and were applied to ballistocardiography: photoelectric cells and electromagnetic ballistocardiograph in 1949 [25], accelerometers in 1957 [26], pneumatic accelerometers in 1975 [27], capacitive films [28] in 1981, switched-capacitor based instrumentation amplifiers [29], pneumatic pressure sensors [30] in 2000, piezoelectric films [31] in 2003, hydraulic pressure sensor [32] in 2006, MEMS (microelectromechanical systems) accelerometers [33] in 2007 and Fiber Bragg grating [34] in 2012. Sensors have become cheaper and more sensitive throughout those years.

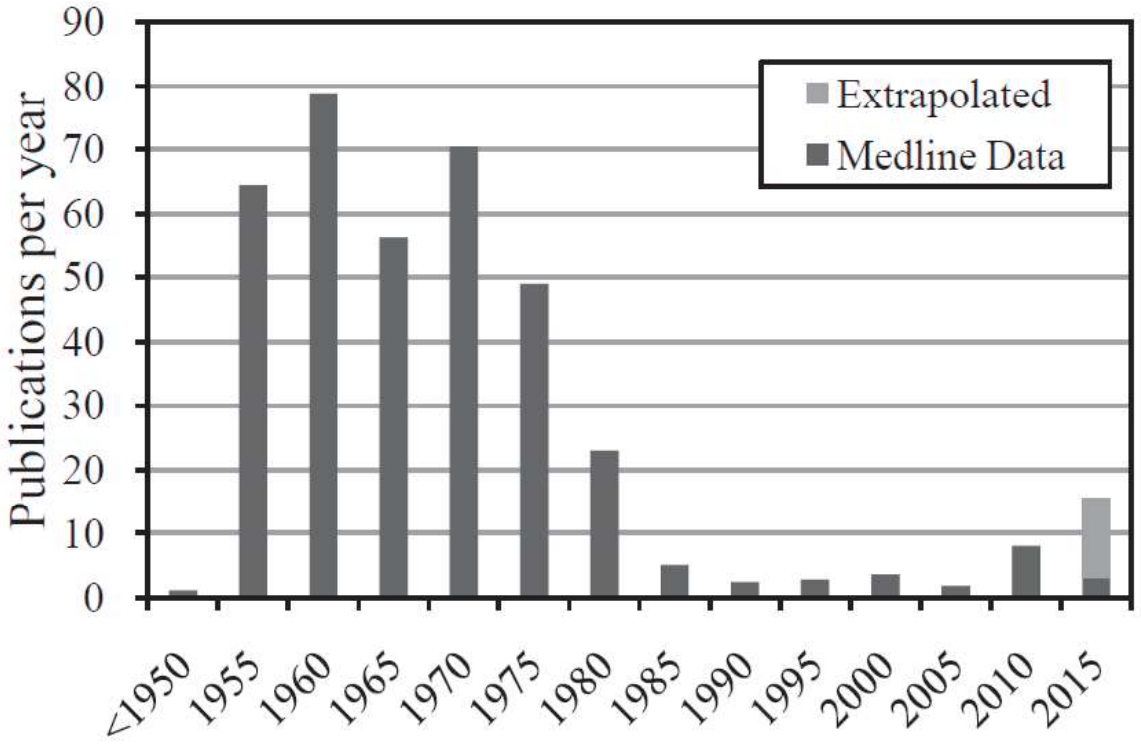

Figure 6: Publication rate of BCG-related research during the 1955-2015 period

Secondly, the emergence of digital processing, wavelet theory, and artificial intelligence has recently been driving the development of BCG systems. Recursive digital

filters such as finite impulse response (FIR) filters have been applied since 1971 for denoising biomedical signals [35]. Detectors of vital signs such as heart rate were first implemented in 1972 [36]. Template matching techniques could successfully detect heartbeats in 1991 [37], with a piecewise linear approximation to remove the respiratory component. Neural networks classified ballistocardiograms for the first time in [38] in 1994. Wavelets were used to filter BCG in 1996 [39]. Clustering methods like k-means and hierarchical clustering were designed to delineate heartbeats in 2011 [40] and 2015 [41] respectively.

1.3.3. Physiological waveforms

1.3.3.1. Cardiac activity

The waveform of ballistocardiogram has been defined by Starr [19] – see Figure 11 - and recently modeled by simulation [13]– see Figure 3. A ballistocardiogram is a succession of heartbeats, segmented in systole marked by IJK fiducial points, and diastole marked by LMN fiducial points. The J peak has usually the biggest amplitude, whereas the LMN fiducial points are not always discernable depending on the instrumentation. This convention is respected throughout this work, except in Section 3.3.2 and Section 3.3.3.

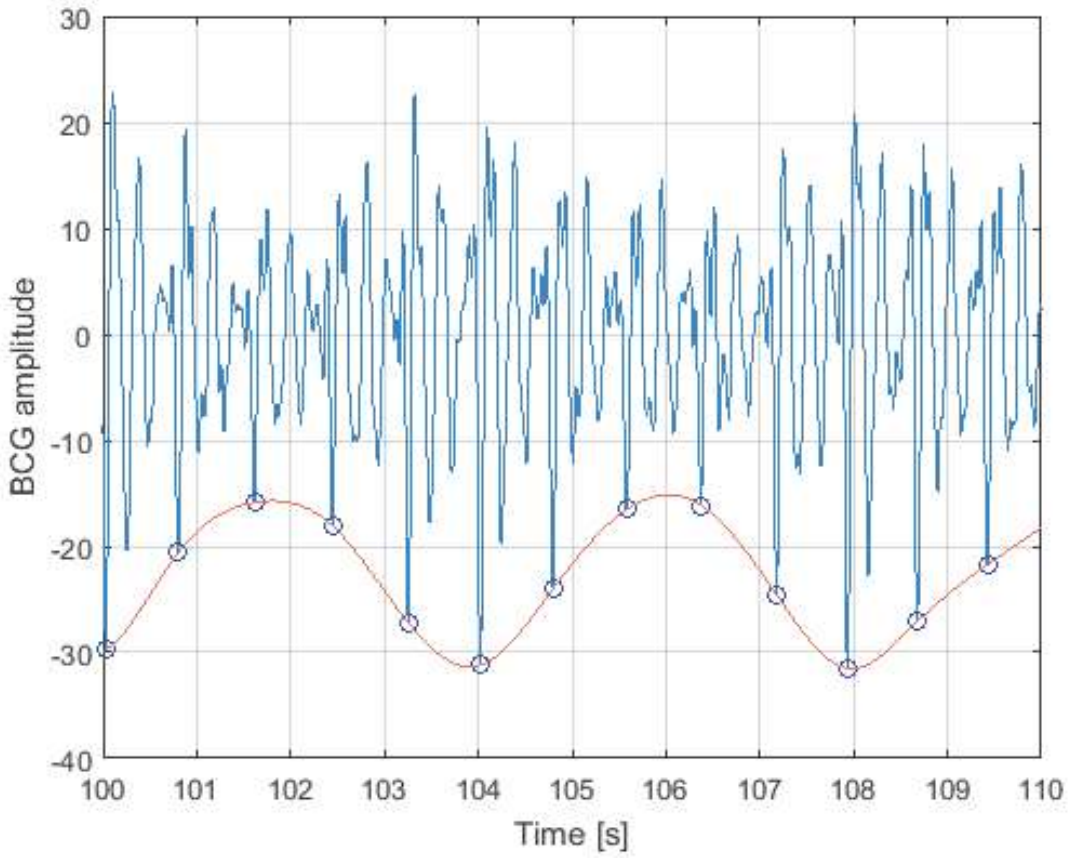

Figure 7: BCG-derived respiration.

1.3.3.2. Respiratory activity

A respiratory component can be found in ballistocardiography in two ways: either a linearly superposed component, that can easily be filtered out; or an amplitude modulating signal of the ballistocardiogram, as in the ECG-derived respiration.

In the latter case, the respiration can be extracted using spline interpolation of J peaks of the ballistocardiograph, as in Figure 7.

1.3.3.3. Autonomic nervous system activity

Heart rate variability is correlated with the autonomic nervous system activity. It is useful for pain monitoring [42] or sleeps studies.

1.3.4. Potential for contactless monitoring and telehealth

Recent developments have made ballistocardiography more portable, cheaper, and more reliable. As a contactless and passive cardiac monitoring method that can be embedded

in mattresses, chairs, or weighing scales, ballistocardiography might become one of the best telehealth devices.

Earlier in 1953 [43], Mandelbaum established, over one hundred acute myocardial infarctions, that BCG could be used for determining myocardial recovery in the 18 months after a heart attack. Pinheiro listed [44] a series of 20th-century-published clinical studies showing physiological troubles that influenced BCG waveforms, especially: coronary artery disease where BCG was a good predictor of appearance and recurrence of myocardial ischemia; mitral stenosis increases the BCG amplitude while aortic stenosis increases it; coarctation of the aorta; myocardial infarction; congestive heart failure. At that time, ballistocardiographs were not automatic and difficult to implement as clinical routine.

More recently, clinical studies have recently shown promising results using ballistocardiography. Inan observed in 2009 [45] on one subject with a premature atrial contraction that the BCG amplitude was correlated to the diastolic filling time. Bruser realized in 2013 [46] proof of concept of atrial fibrillation automated detection on 10 patients with 94% mean sensitivity and 98% mean specificity. Wang used in 2017 [47] BCG to assess the severity of sleep apnea syndromes of 136 patients: he obtained an accuracy of 94% compared to the PSG gold standard. Aydemir showed in 2018 [48] over 36 HF patients that the BCG waveform variability was a significant predictor of decompensation. Finally, Yousefian investigated the use of wearable ballistocardiographs for blood pressure monitoring [49].

1.3.5. Limitations

However, most of these clinical studies are proofs of feasibility concerning a few dozens of patients at most. Limitations of actual BCG systems are detailed in the next paragraphs.

BCG systems still lack reliability and coverage, because they are very sensitive to motion artifacts at home or in the hospital environment.

Most BCG instrumentations are not standardized. Few exceptions exist but are not convenient for telehealth. Starr- and Nickerson-type ballistocardiographs, which are uncomfortable, are not compatible with actual standard medical or home beds. Modern BCG weighing scales are more convenient and can also be standardized but are not passive and need the intervention of either the nurse or the patient, which is likely to undermine patient engagement.

Finally, cardiac outputs of infants and the elderly are weaker than those of adults. However clinical studies often recruit only adults between 19 and 60 years old. For example, over the recent clinical studies presented in the previous section, only two studies were outside that range, with respectively 58±13 years old and 63±18 years old patients [48] [45]. Moreover, few studies [50] [51] focus on pediatric ballistocardiography, where BCG signals, due to low weight and low cardiac contractile force, are noisier than those of adults. For example, the BCG amplitude of a 3kg infant is about 30 times lower for that of an adult [51].

1.4. Research question and methodology

The main research question addressed in this research thesis is stated hereafter: *can ballistocardiography monitor heart conditions of children and the elderly in a clinical context?* The author will focus on passive bed-ballistocardiography.

Secondary questions are also addressed: *how to improve heartbeat detection in ballistocardiography? Can ballistocardiography be standardized on everyone's bed? What are the possible applications of ballistocardiography other than vital signs monitoring?*

During this thesis, neither a BCG signal database nor a commercial ballistocardiograph was available. Therefore, the author had to spend time developing its BCG instrumentation and conducting its clinical experiments from scratch. Even if this was effortful, it brought a very useful complete knowledge of ballistocardiographic systems.

1.5. Outline

The thesis is divided into four chapters, including this general introduction.

Chapter 2 enumerates different instrumentations, sensors, and systems that have been used in the literature for measuring BCG and describes original BCG systems designed by the author. It involves electronics and mechanics.

Chapter 3 explains how vital signs can be processed by the raw physiological signals.

Chapter 4 opens discussion and the perspectives of the future work to achieve.

Chapter 2

2. Instrumentation in ballistocardiography

In this chapter, the ballistocardiograph instrumentations are investigated. As they measure a mechanical phenomenon, the whole mechanical system including the sensor and the bed is defined as a BCG instrumentation. The influence of patient mass is also considered in the mechanical system.

2.1. Benchmark of existing BCG instrumentations

2.1.1. Historical BCG instrumentations

Back in 1952, Scarborough [52] classified bed ballistocardiographs into three categories:

- Starr BCG [19] with a high resonant frequency (10-15 Hz) and undamped mechanical system
- Nickerson BCG [53] with a low resonant frequency (1.5 Hz) and critically damped mechanical system
- Dock BCG [25] which is directly in contact with the body.

2.1.1.1. Starr and Nickerson bed ballistocardiographs

Those beds allow a single degree of mobility, for example, translation in one direction (head-foot, side-to-side, and front-to-back) [14] [18] [54] [55] or rotation around a single axis [56]. The principle is to concentrate the strain energy of the ballistocardiographic force on the measuring sensor, considering the resonant frequency of the mechanical system. Indeed, a human body, and its ballistocardiographic force by extension, have a natural frequency typically comprised between 3 to 7 Hz, depending on the mass and body fat. This degree of mobility of bed BCG is restrained by springs, whose stiffnesses are set so that the weighted bed BCG with a steel dead mass of 75 kg has a resonant frequency different from the

ballistocardiographic force. For instance, the Starr bed BCG has stiffer springs than the Nickerson BCG. The springs' stiffnesses are tuned for every patient, whose mass may vary.

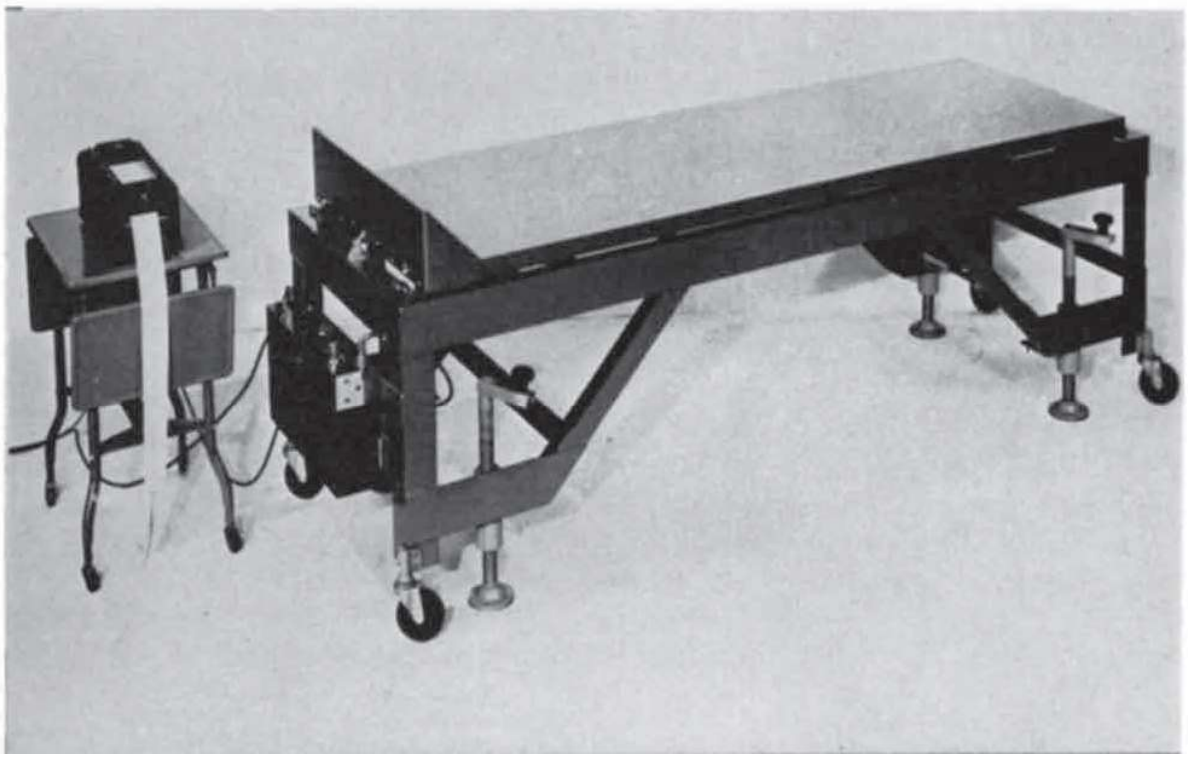

Figure 8: A Starr bed ballistocardiograph

Concerning the degrees of mobility, the ballistocardiographic force is aligned with the orientation of the aortic arch in the bed reference. In the supine position, its main contribution is in the head-foot direction. Nevertheless, it can also contribute to other directions, especially if the patient position changes. Thus, bed BCG with multiple degrees of freedom has also been designed [57] [58].

The effects of the gravity direction on the ballistocardiographic force have also been investigated with a tilt table [55] [59] that moves the patient from supine to standing positions step by step. This work was later continued with zero-gravity experimentations [60].

The analog sensor was at the time either a direct writer on a moving strip, as for early seismometers, or a galvanometer, both recording a body displacement.

The Nickerson bed BCG, compared to the Starr bed BCG, was designed to amplify the early systolic events (G and H waves) and to attenuate the diastolic events (L, M, and N waves) as shown in Figure 11.

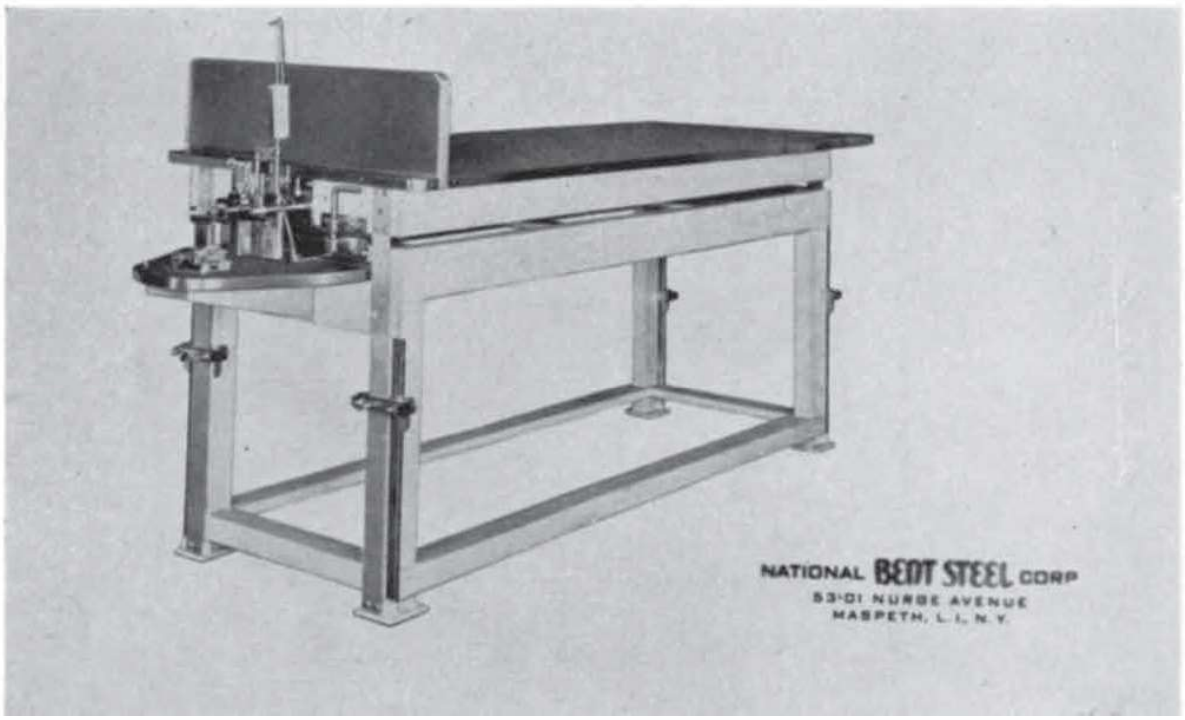

Figure 9: A Nickerson ballistocardiograph

In those two ballistocardiography systems, the ballistocardiographic force is altered through the body and the mattress to the sensor. Thus, it is amplified before analog sensing, for example, 7000 times by an optical system in the original Starr bed BCG [19].

2.1.1.2. Dock ballistocardiograph

Dock ballistocardiographs were designed to broaden the use of ballistocardiograph in the operating room, in the ward, or at home. Instead of including an expensive and bulky bed, they are simpler and portable systems that can be displaced from one bed to another for short exams, as electrocardiographs at that time. They are directly in contact with the patient and do not particularly need high amplifier gains.

In the original publication [25], Dock compared sphygmographic, photocell, and electromagnetic methods involving sensors applied to the vertex of the head. Low- and high-

pass filters were analogically either implemented by rubber pieces for sphygmographic method or capacitors for electromagnetic and photocell methods dimensioned to remove respiratory and motor components from the ballistocardiograms.

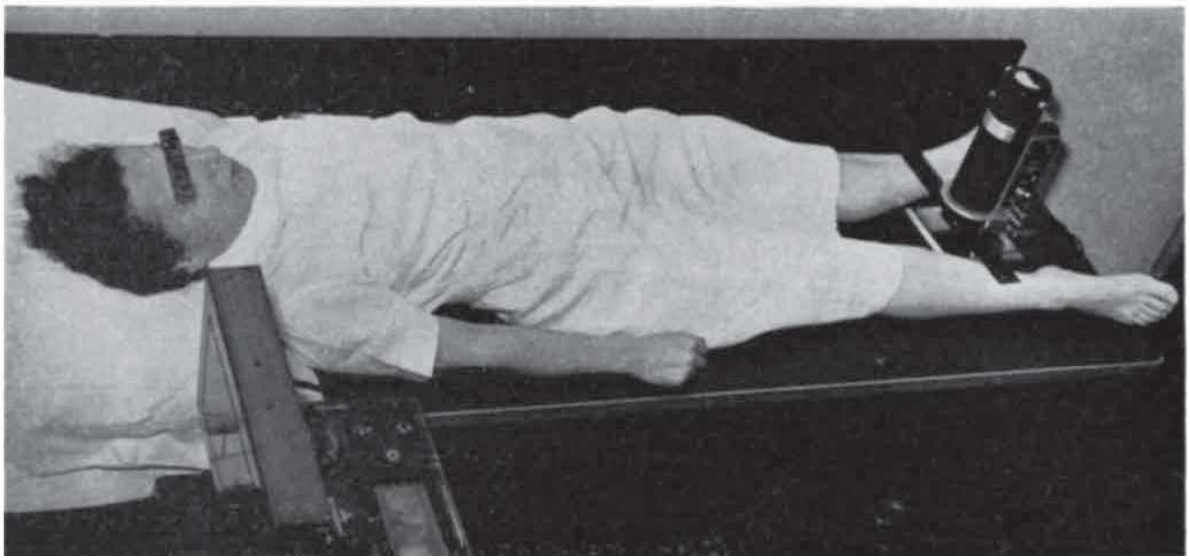

Figure 10: A Dock ballistocardiograph

Dock found that the electromagnetic method was the simplest way to record ballistocardiograms. This was later confirmed with the invention and use of MEMS (Micro-Electro-Mechanical Systems), and capacitive, piezoelectric, and resistive films in most of the recent ballistocardiographs, even if optical and ultrasound methods have also been developed.

The electromagnetic method thus implemented is a magnet moving in a coil that produces voltage changes proportional to the velocity of the movement. Such ballistocardiograms are thus derivative of the conventional Starr ballistocardiograms, and have a quadrature-phase lead (see Figure 11C) that can be reduced by using a capacitor, also needed for the high-pass filtering of the respiratory components anyway.

The Dock ballistocardiographs are calibrated using a pendulum that blows the foot or shoulder of the patient, producing deflections whose amplitudes can be different depending on the patient's morphology or the bed. The ballistocardiograms amplitude is rectified on the amplifier of the direct writer or of the galvanometer.

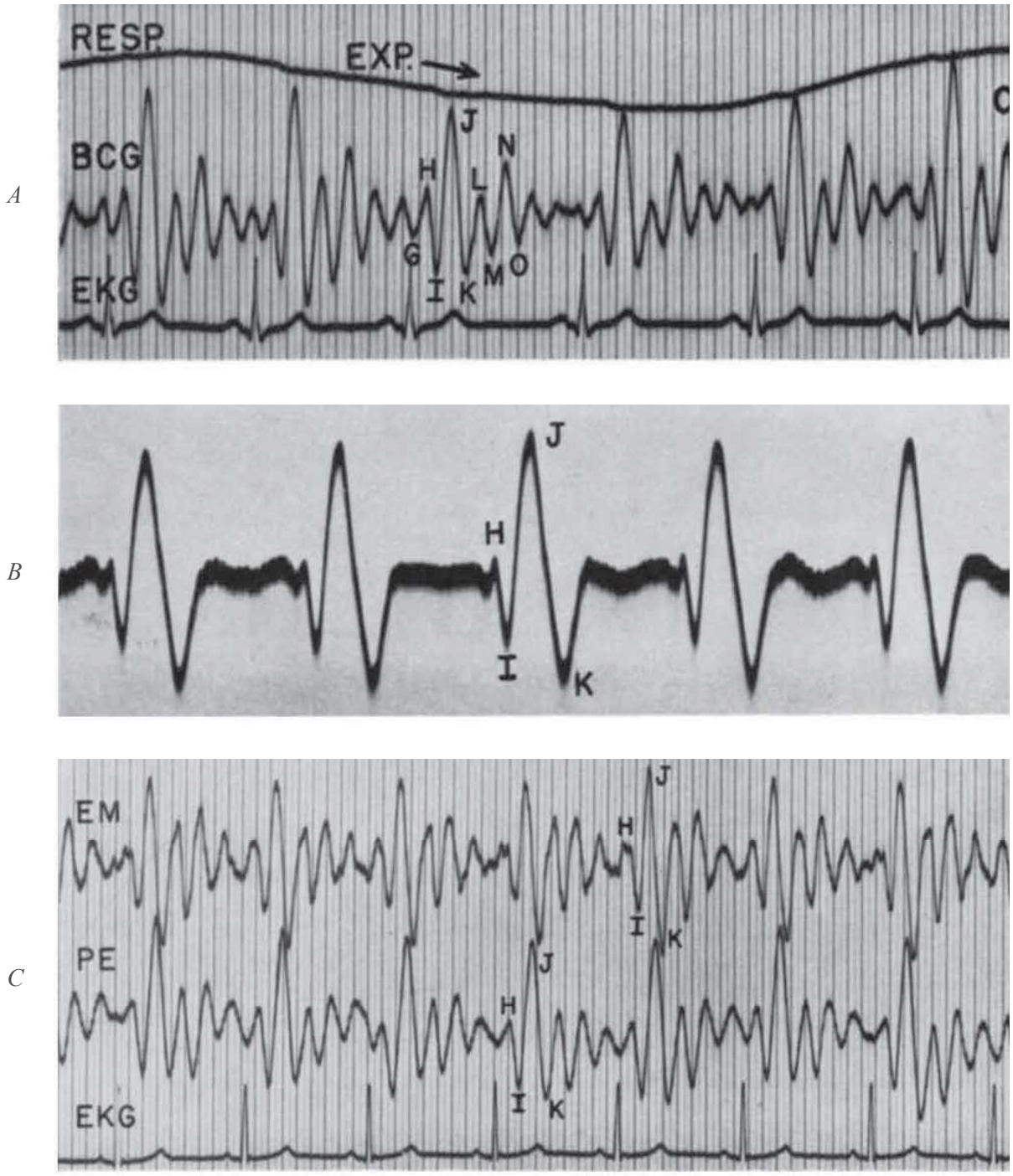

Figure 11: Starr (A) BCG with pneumogram (RESP.) and electrocardiogram (EKG); Nickerson (B) BCG during apnea; Dock (C) ballistocardiograms with electromagnetic (EM) and photoelectric method (PE) methods, and electrocardiogram (EKG) reference. Time divisions are 0.1s-long.

Even if the Dock ballistocardiograph was designed to be portable and adaptable to different beds, its clinical use was restricted to rigid tables without casters, otherwise, the resonant frequency of the bed can mix with the ballistocardiographic force-frequency range. Even if they are simpler and more portable, Dock ballistocardiographs are less patient-

friendly than Starr's and Nickerson's, because the used beds are as rigid, but the measurement is directly in contact with the patient.

Ballistocardiograms recorded with the three historical methods are illustrated in Figure 11. They are often synchronized with other physiological signals such as electrocardiograms and pneumograms, e.g. in Figure 11A. Nickerson ballistocardiograms, propagating in critically damped beds, are delayed and have larger waves than the Starr or Dock ballistocardiograms that are more accurate. To get rid of respiratory modulation, the patient may be asked to stop breathing for a moment, e.g. in Figure 11B. The waves of the signal are annotated following the Starr convention.

Starr, Nickerson, and Dock bed ballistocardiographs permit standardized and repeatable ballistocardiography exams of several minutes. However, even if digitization and digital signal processing could automate the process, they use uncomfortable rigid tables and are inappropriate for long term monitoring.

2.1.2. Recent advances in BCG instrumentations

2.1.2.1. Sensor position

2.1.2.1.1. Beds

Modern bed ballistocardiographs are more comfortable than the Starr, Nickerson, and Dock ballistocardiographs that used rigid tables for short term exams. Contactless, they are particularly well suited for long term physiological monitoring and sleep stages classification at home using heart rate variability, respiratory and actimetry features. Moreover, they are installed once for all: they are also promising for telemedicine. Therefore, this thesis will focus on modern bed ballistocardiographs in the following chapters.

Modern bed ballistocardiographs are here defined as beds offering the same comfort as usual medical or home beds. Concretely, they appeared in 1979 with a capacitive pressure sensor below the mattress, even if the foam mattress was only 5 to 10cm-thick and the bed

frame was a rigid wooden plate [61]. The sensors used in modern bed ballistocardiography are pressure sensors or accelerometers and are detailed in the last subsection.

Concerning the pressure sensors, they are either directly integrated into the bed frame, for example in the legs of the bed frames [62] [63], integrated into the mattress [64] [65], in pillows or cushions [32] [66] [34], in slats [40], or in mattress pads that are placed either below [67] [68] [69] [70] or above [31] the mattress. There are also examples of atmospheric pressure sensors in air-mattresses, e.g. in [71], for very specific usages such as anti-bedsore mattresses.

Concerning accelerometers, they can be placed on or below the bed frame [72], or the mattress [73].

Multi-sensor ballistocardiography is also relevant in beds, because of the large surface of the body. As the pressure is not uniformly distributed in the mattress and the body position moves during the night, sensor arrays provide more robust ballistocardiography than single sensors, eventually using sensor fusion algorithms [74] [65] [75].

2.1.2.1.2. Chairs

Chairs can embed ballistocardiographs as well as mattresses, cushions, or directly integrated into the chair [76]. It can be complementary to bed ballistocardiography for the elderly when they spend most of their time lying or sitting. It is a huge benefit for wheeling chairs and disabled patient physiological monitoring [77].

Vigilance monitoring of pilots in autonomous vehicles is another trendy application [78].

2.1.2.1.3. Weighing scale

While designing specialized Wheatstone bridges circuits for highly sensitive weighing scales with a 4.5g precision, Linear Technology accidentally observed ballistocardiograms in 1990 [29].

An application of weighing scales to ballistocardiography was patented in 1994, but the methods and results were not published [79].

In 2008, Gonzalez-Landaeta modified the instrumentation of an electronic bathroom scale to reach a sensitivity of 0.24 N (see Figure 12), which is enough to measure ballistocardiograms [80]. The principle is to use a low noise AC-coupled instrumentation amplifier in front of the Wheatstone bridge circuit formed by the strain gages.

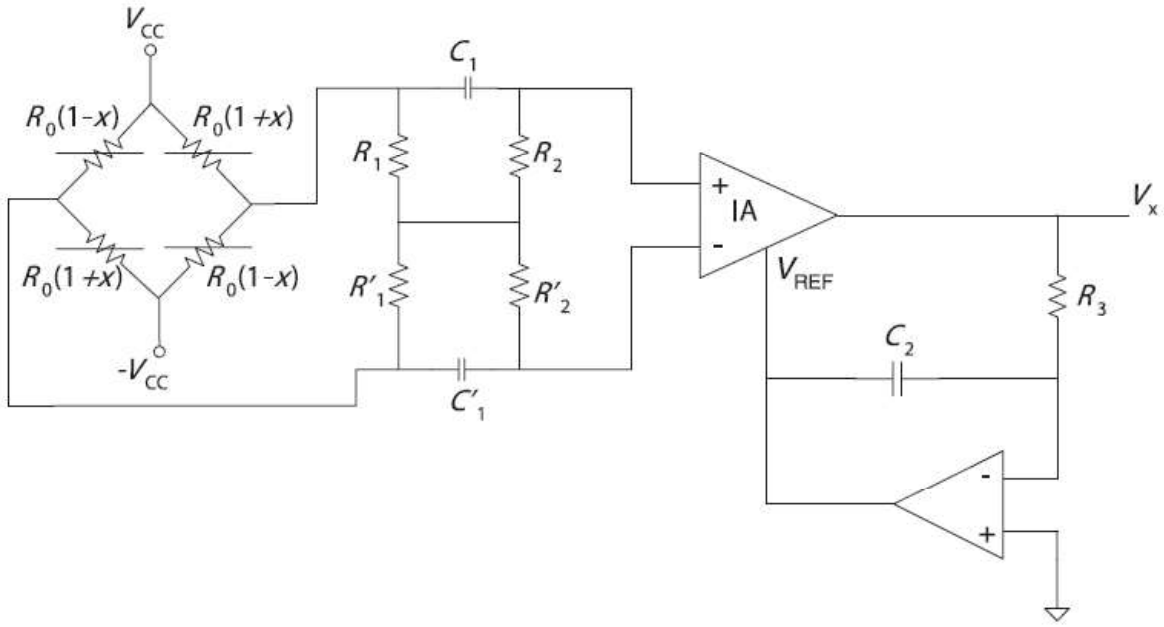

Figure 12: Force sensors connected to the AC-coupled instrumentation amplifier

Most commercial scales, modified with finer strain gages, are suitable for ballistocardiography because their resonant frequency is above 15 Hz, i.e. outside of the ballistocardiograms frequency range, for bodyweights of up to 160 kg [45].

Weighing scale ballistocardiographs also render undistorted ballistocardiogram waveforms so that, combined with feet electrocardiography, it can be used as a blood pressure monitor, with the R-J delay between the R peak of ECG and J peak of BCG correlated to the systolic blood pressure [81].

2.1.2.1.4. Cameras and radars

Cameras have been used in the visible spectrum to detect head motions relative to the ballistocardiographic force [82].

Radars, using the ultrasonic Doppler effect, were successfully investigated for measuring the displacement of the thoracic wall [83] [84].

Impulse Radio Ultra-Wide Band (IR-UWB) radar applications were listed the first time in medicine by Staderini in 2002 [85]; since then, they were applied to ballistocardiography [78] [86].

The advantages of radars and cameras are their long distance to the body which allows easier integration for example in webcams or cars' cabins. However, sensors are usually more expansive than pressure sensors and accelerometers, except for visible spectrum cameras which are more efficient when measuring the skin directly.

2.1.2.1.5. Wearables

Until now, wearables that record ballistocardiography are based on acceleration signal measured by tri-axial MEMS accelerometer, because they are compact and easy-to-integrate in clothes or accessories. They are initially phase-opposed compared to the Starr convention and consequently digitally corrected.

Here is a non-exhaustive list of exotic wearables that records ballistocardiograms: in micro-gravity on the patient back, at the center of mass of the body [87], from the head movement [88], or using an electromagnetic patch on the chest [89] [90]. They can be integrated into clothes [91].

Smart-watches [92] [93] and smart-glasses [94] are also relevant to heart rate estimation using accelerometers.

Landreani [95] reviewed publications that use smartphones' embedded accelerometers have been used directly posed on the thorax for ballistocardiography [96] [97] [98] [99].

Some researchers even succeeded in detecting atrial fibrillation using a smartphone on the chest [100].

Most wearable ballistocardiographs are known to be more accurate than bed BCG since they are not altered during the propagation in the mattress and are close to the patient aortic arch [101]. However, they may be less comfortable and are less relevant for telecare.

2.1.2.2. The technologies of bed ballistocardiograph sensors

2.1.2.2.1. Pressure sensors

In ballistocardiography, pressure sensor use different technologies : pneumatic sensors [71] [67] [70], hydraulic sensors [32], strain gauges [40] [63], film type force sensors [62], micro-bend fiber optic BCG sensor [66] [64] [34], electromagnetic film sensors [65], piezoelectric film sensors [68] or polyvinylidene fluoride (PVDF) sensors [69].

2.1.2.2.2. Acceleration signals

Acceleration signals are measured by MEMS wearables [87] [88] [102] [103] [104]. It happened that the smartphone's embedded inertial measurement units (IMU) are sensitive enough to measure ballistocardiography when the smartphone is on the thorax [95]. It is worth noting that for wearables, the signal amplitude is high enough to use digital accelerometers without baseline analog filtering.

2.1.3. Commercial BCG modules with raw data access

2.1.3.1. Murata SCA11H

The SCA11H BCG sensor is powered through an AC wall adapter and communicates through Wifi. It can operate in two different modes: either a BCG mode where it transmits heart rate, respiratory rate, and heartbeats onsets; or a datalogger mode where it transmits only raw accelerometer data. We will be using the latter mode in this thesis to build the CHArt ballistocardiographic database. Moreover, digital signal processing algorithms used in the BCG mode are proprietary and not clinically validated.

The SCA11H sensor is based on the analog SCA61T accelerometer with a 15 µg/s2/√Hz low noise density [105], as seen in Figure 13. The analog output is AC coupled, anti-aliasing filtered, and amplified before digitization at 1 kHz.

A

B

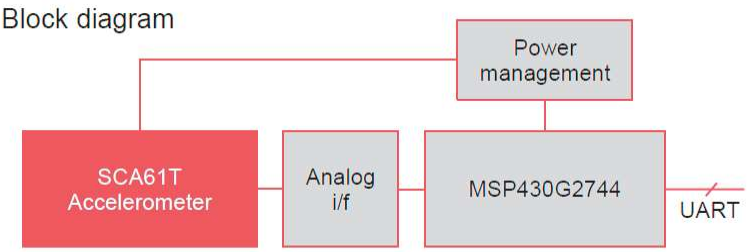

C

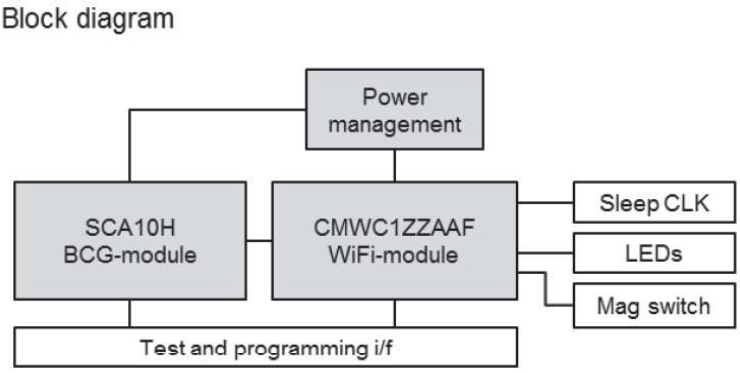

Figure 13: SCA11H sensor (A), SCA11H block diagram (B), SCA10H block diagram (C)

2.1.3.2. EMFIT QS

The EMFIT QS sensor is a pressure sensor based on electromagnetic film [65] that, placed under a mattress as in Figure 15, measures the ballistocardiogram.

Figure 14: EMFIT raw data download interface

Figure 15: Setup of EMFIT QS

It provides clinicians and researchers with respiratory and cardiac components, respectively in the 0.1-3 Hz and the 6-16 Hz frequency ranges. It can only export data of nights or naps longer than 20 minutes.

2.1.4. Related physiological signals

Ballistocardiograms may be confused with other signals which are physiologically close, e.g. seismocardiograms, apexcardiograms, kinetocardiograms, cardiokymograms, phonocardiograms, and vibrocardiograms.

Seismocardiography was probably discovered in 1961 by Bozhenko [106] and detailed by Salerno in 1991 [107]. It involves an accelerometer on the sternum, and can measure several fiducial points during a heartbeat [108], as shown in Figure 16:

- AS, the peak of atrial systole
- MC, the mitral valve closure
- IM, the isovolumic movement, sometimes referred to as IVC, the isovolumetric contraction
- AO, the aortic valve opening
- IC, the isotonic contraction
- RE, the rapid ejection
- AC, the aortic valve closure
- MO, the mitral valve opening
- RF, the rapid filling

It is sometimes confounded with ballistocardiography, though the measurements are different because, in ballistocardiography, only the aortic arch deformation during the ventricular systole is measured.

The apexcardiography was invented in 1878 by Jules-Etienne Marey and is detailed in [109]. This method is now obsolete.

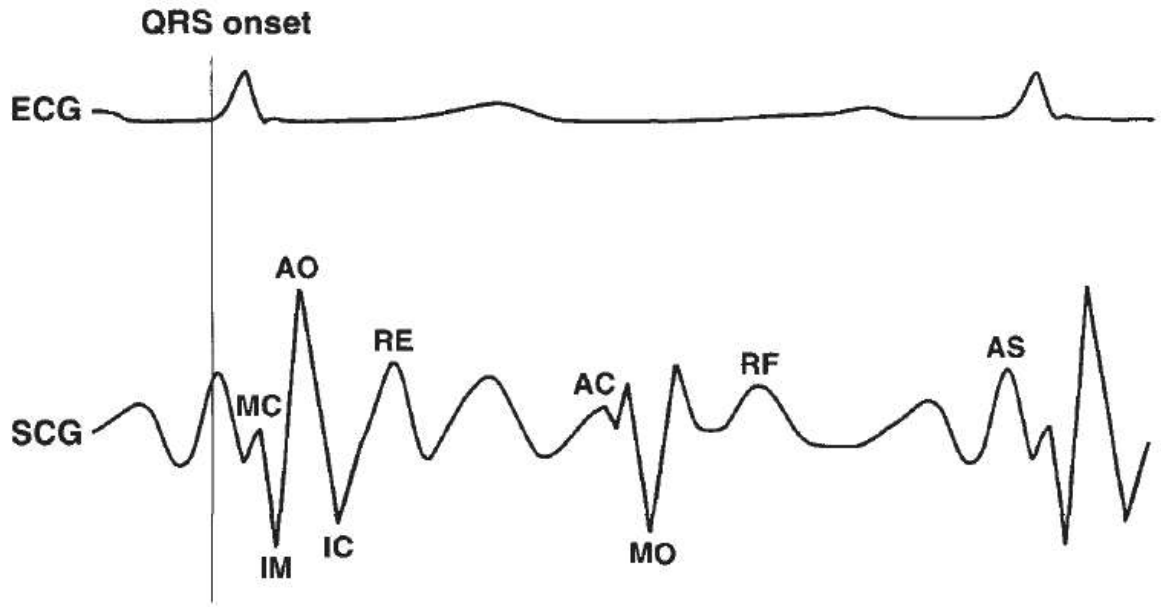

Figure 16: Example of SCG with simultaneous bipolar ECG lead reference from averaged data [108]

The phonocardiography was first imagined by Robert Hooke in his posthumous work published in 1705 [110]: “There may be also a possibility of discovering the internal motions and actions of bodies by the sound they make.” Stethoscopes record the sound of closures and openings of cardiac valves. Nowadays, stethoscopes are digital, cheap, and widely used especially in primary medicine.

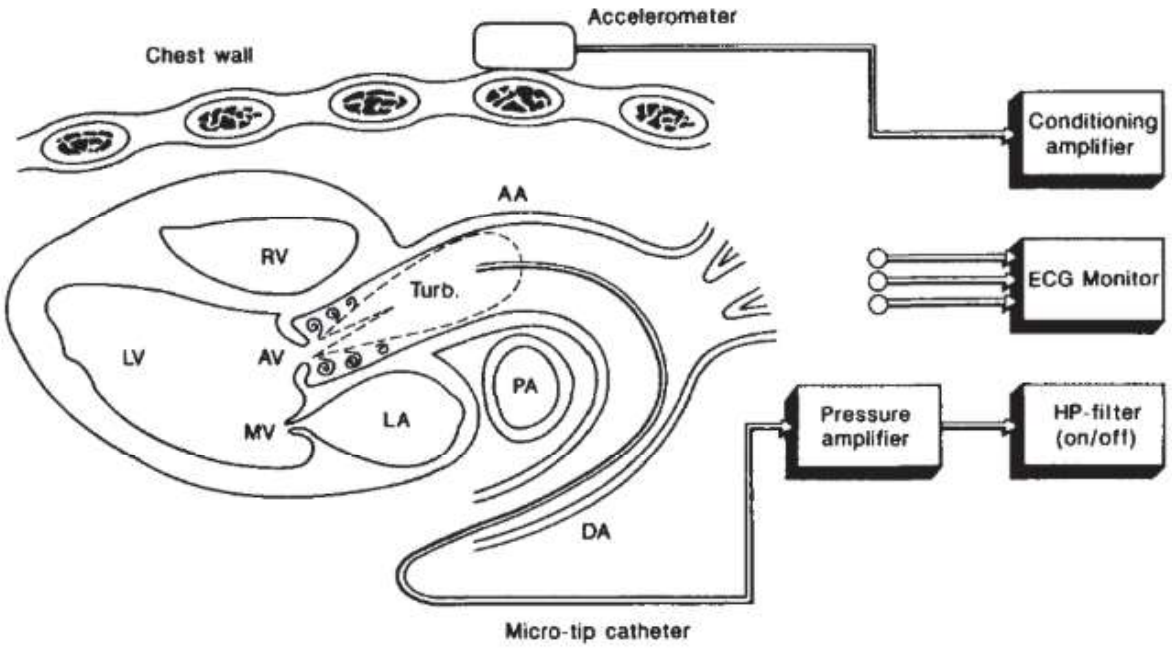

Figure 17: Illustration of a vibrocardiography setup in [111]

Vibrocardiography records the acceleration of the chest wall. Therefore, it is derived and often confounded with seismocardiography. Its origins are not well established, but the method is reviewed by Margaret Down in 1956 [112] and more recently a contactless vibrocardiography was developed using laser interferometry [113].

Other methods similar to ballistocardiography are kinetocardiography, cardiokymography, and vectocardiography.

2.2. Guidelines for designing a BCG accelerometer

Since we could not find any commercial accelerometer module for our BCG experimentations, we decided to design our BCG accelerometer. In this section, we explain how to properly design a BCG accelerometer. The three major guidelines concern the sensor itself, the conditioning circuit, and mechanical integration. The designed BCG accelerometer is named the Fealing BCG module. It is available in three different versions:

- Fealing BCG Wireless module, that communicates via Bluetooth 5 and is powered by a Lithium battery, Figure 18A
- Fealing BCG Biopac module, that communicates and is powered via a DB9 connection on a Biopac MP36R acquisition unit, Figure 18B
- Fealing BCG ST module, that communicates and is powered with an ST Nucleo L476RG prototyping board, Figure 18C.

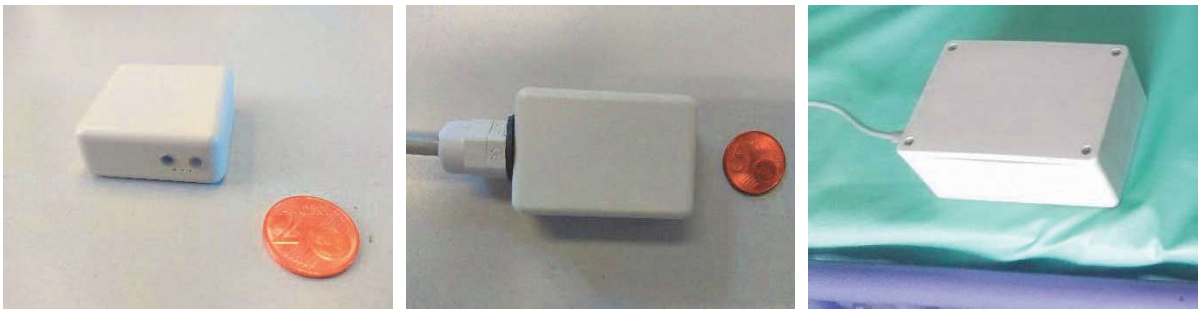

A B C

Figure 18 : Fealing BCG Wireless module (A), Biopac module (B) and ST module (C)

2.2.1. Sensor

The sensor must meet several requirements: the output noise density must be low; it must be small enough; it must be cheap to be used in telemedicine routines.

2.2.1.1. Noise level

The noise density is the square root of the power spectral density of the noise output. It can be expressed in $g/\sqrt{Hz}$ or in $V/\sqrt{Hz}$ depending on the nature of the output. The total output noise in the frequency bandwidth BW is computed by Equation (1).

$$Noise = Noise\_Density . \sqrt{BW . \frac{\pi}{2}} \quad (1)$$

The bandwidth is 25 Hz and the noise must be lower than 0.1 mg, as usually, the BCG measured by bed accelerometers has a 0.1 to 10 mg amplitude. Therefore, the output noise density must be ideally below 16 $\mu g/\sqrt{Hz}$. There is a margin in this value, depending on the BCG amplitude. The selected accelerometers corresponding to this criterion are listed in Table 2. It is worth noting that the Colibrys SI1003 MEMS accelerometer [114], dedicated to seismology, has an impressive 0.7 $\mu g/\sqrt{Hz}$ but is sold at $320/unit, which is not relevant for most ballistocardiographic applications.

Table 2: Benchmark of analog accelerometers, using octopart.com with MOQ>1000 units

Manufacturer	Murata	Analog Devices	ST Microelectronics	Kionix	Units
Model	SCA61T-FAHH1G	ADXL1002	LIS344ALH	KXR94-2050	
Range	0.5	50	2	2	$\pm g$
Sensitivity	4	0.04	0.66	0.66	V/g
Noise density	14	25	50	45	$\mu g/\sqrt{Hz}$
Axes	1	1	3	3	

Price	$ 31.58	$ 40.74	$ 2.20	$ 6.55	USD

Sensitivity is also a requirement, especially for digital accelerometers that already contain a conditioning circuit. However, except for the ADXL355 that reaches 3.9 µg/LSB but is very expensive, most digital accelerometers have too low sensitivity, as shown in Table 3. Consequently, we prefer low noise analog accelerometers whose output can be amplified, unless a mechanical amplification can be performed – see Section 2.4.

Table 3: Benchmark of digital accelerometers, using octopart.com with MOQ>1000 units

Manufacturer	Analog Devices	Kionix	Freescale	Units
Model	ADXL355	KX123-1025	FXLS8471QR1	
Range	2.048	2	2	$\pm g$
Sensitivity	3.9	61.0	244.1	$\mu g/LSB$
	256000	16384	4096	LSB/g
Resolution	20	14	12	bits
Noise density	25	106	99	$\mu g/\sqrt{Hz}$
Price	$ 36.46	$ 1.00	$ 1.43	USD

2.2.1.2. Integration

All the references listed in Table 2 and Table 3 are MEMS with a high compacity, thus can be easily soldered on small PCBs. Even if the ballistocardiographic force often propagates along a single direction, three-axis accelerometers may be preferred, e.g. when the patient shifts his/her position in bed.

2.2.1.3. Cost

Cost is a major concern for telemedicine applications, where nursing homes may have low budgets. Moreover, it is also important to have cost in mind while performing large-scale

experiments. The MEMS must cost less than $10 to be competitive and to allow a commercial price of the BCG module below $100.

Gathering all these requirements, we found that the LIS344ALH was a very good candidate for ballistocardiography [115]: it will be used in the Fealing Wireless and ST BCG modules. The SCA61T, or its SCA100T two-axis version, has the lowest noise and will be used in the Fealing Biopac BCG module for high-quality recordings.

2.2.2. Conditioning circuit

2.2.2.1. Filtering and amplification

Concerning analog accelerometers, the signal must be amplified before digitization. Indeed, the most common analog-to-digital converters (ADC) have a 12 bits resolution. Nowadays, 16 bits resolutions are also common, but 24 bits resolutions are not frequent and reserved for expensive applications. With a 12 bits ADC digitizing the output of an accelerometer with a single power supply of 3.3 V, the resolution equals 806 µV. Equation (2) explains the formula used for this result, according to the IEEE 1241-2010 standard [116]. Applying a sensitivity of 0.66 V/g in the case of the selected LIS344ALH, the resolution is equivalent to 1.22 mg which is insufficient to measure bed accelerometer ballistocardiograms. Typically, the amplification factor should be at least higher than 100, i.e. 40 decibels (dB), to reach the desired resolution.

$$LSB = \frac{FSR}{2^N} \quad (2)$$

However, a baseline wander is present in the output of the accelerometer. Its DC value, ranging from -1 to 1 g, depends on the relative direction to the gravity and on the level of the bedding on which the accelerometer is lying. Thus, this baseline wander can vary in time, e.g. when the patient shifts position. Before amplification, it is important to filter the accelerometer output not to saturate the amplifier output. In this application, the limit between

AC and DC frequency range is 0.05 Hz, corresponding to the lower frequency bound of the respiration activity.

Therefore, the first stage of the conditioning circuit is an active high-pass filter setup with a unity gain and a 0.044 Hz cut-off frequency, according to Equation (3) and Equation (4). These equations are obtained considering a voltage divider circuit under the operational amplifier hypotheses of infinite input impedance and a linear mode. Resistors and capacitors have standardized values, so it is not possible to have 0.05 Hz cut-off frequency exactly. In this circuit, illustrated by Figure 20, the LIS344ALH accelerometer is modeled as a voltage source with a 110 kΩ resistance as in the component datasheet [115]. The common AD8691 instrumentation amplifier is selected for its very low DC offset, very high common-mode rejection ratio, low drift, and low noise [117]. As most microcontroller ADC digitizes only positive voltages, the output is centered around the middle of the full-scale range, or half the power supply V_{cc} returned by the AGND pin.

$$H_1(j\omega) = \frac{V_{U_1}(j\omega) - \frac{V_{cc}}{2}}{V_{acc}(j\omega) - \frac{V_{cc}}{2}} = H_0 . \frac{j\frac{\omega}{2\pi f_0}}{1 + j\frac{\omega}{2\pi f_0}} \tag{3}$$

$$\begin{cases} H_0 = -\dfrac{R_1}{R_{acc}} \\ f_0 = \dfrac{1}{2\pi}\dfrac{1}{R_{acc}C_1} \end{cases} \tag{4}$$

The second stage of the conditioning circuit is the 40-dB amplifier, e.g. a programmable gain amplifier (PGA) whose gain can be tuned by digital pins from 0 to 40 dB. This feature is very useful in noisy conditions where the gain can be dynamically adapted to the signal amplitude. Such a PGA has an inverting operational amplifier structure, as for the LTC6910-1 detailed in Figure 19 [118]. With a 1 kΩ input impedance in the 40-dB setting, it is better preceded by an active filter with zero output impedance, such as in Figure 20, rather

than a passive filter with no impedance adaptation, as the internal resistance of the accelerometer is already high; otherwise, the gain would drop.

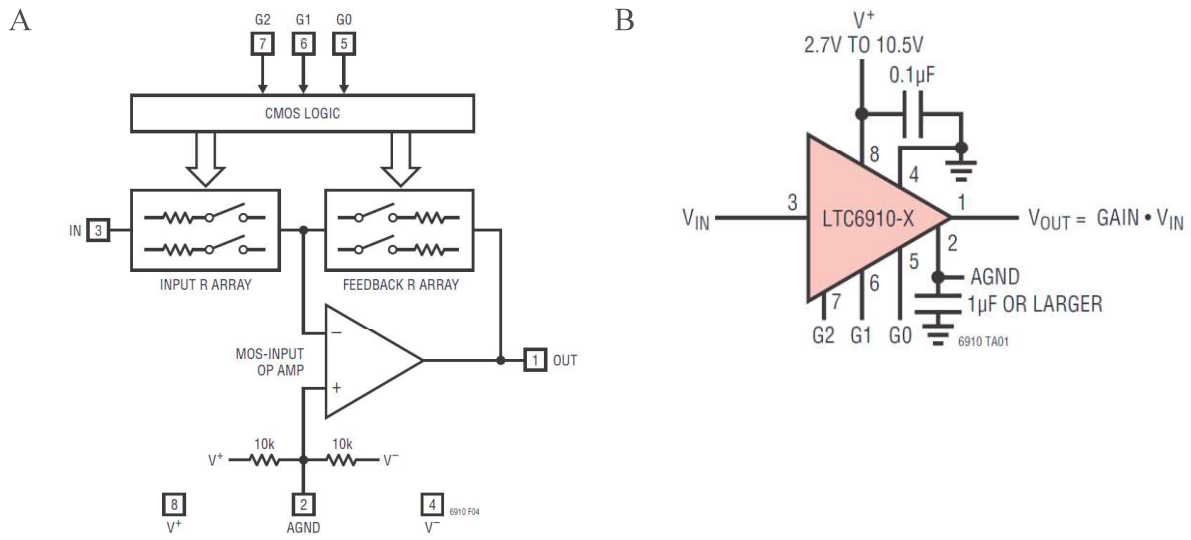

Figure 19: Internal composition and symbolic of the LTC6910 programmable gain amplifier

The final conditioning circuit is shown in Figure 20. It is followed by a first-order low-pass filter with a 66.5 kΩ resistor and a 47 nF capacitor for anti-aliasing and cut the unneeded spectrum part whose frequencies are above 50 Hz. Its Bode diagram, illustrated in Figure 21, confirms the 40 dB gain and the 0.044 Hz cut-off frequency. Moreover, the phase approximately equals zero in the BCG frequency range, i.e. above 1.5 Hz.

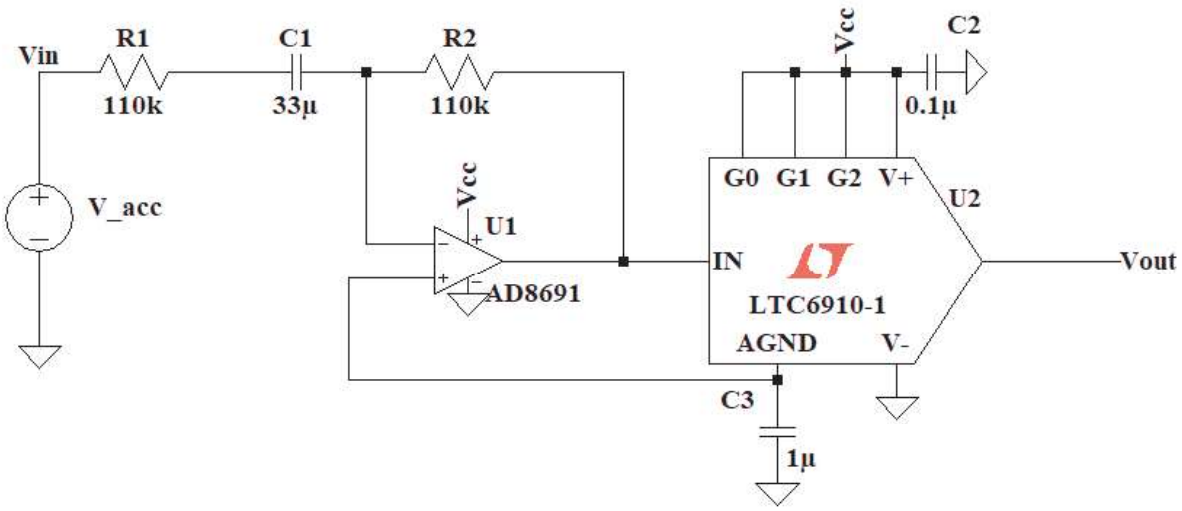

Figure 20: AC coupling with AD8691 and 40dB amplification with LTC6910

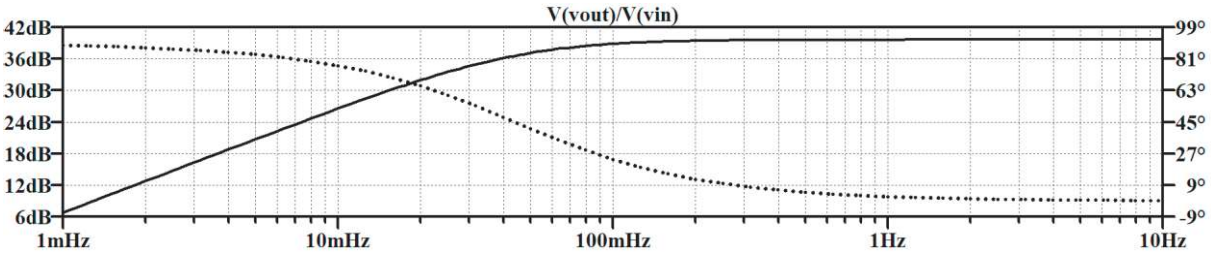

Figure 21: Bode diagram of the transfer function

It is worth noting that some digital accelerometers contain an AC filter, however, the cut-off frequency is not high enough to measure ballistocardiography.

2.2.2.2. Settling time considerations

The AD8691 instrumentation amplifier which is used for AC-coupling could also be used for 40 dB amplification by setting an 11 MΩ resistor in the feedback loop of the inverting circuit - see Figure 22 – rather than separating the filtering and the amplification in two consecutive stages – see Figure 23 [119].

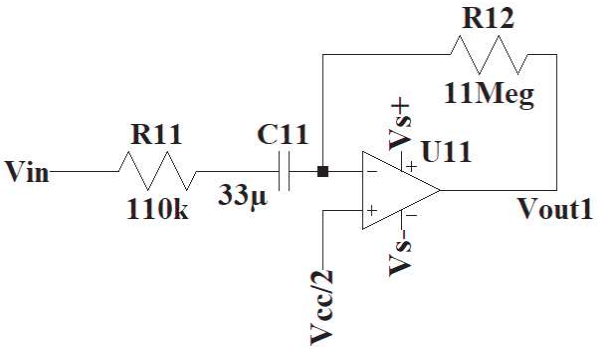

Figure 22: AC filtering and 40 dB amplification on the same stage

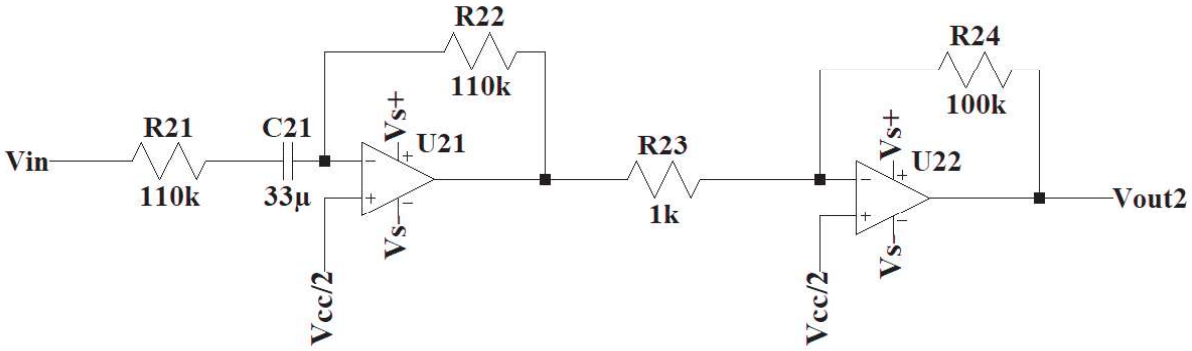

Figure 23: AC filtering and 40 dB amplification on two different stages

However, it has the undesired effect of saturating the capacitor charging current when there is a voltage step, e.g. when the patient shifts position. In Figure 24, we see that the capacitor of the two-stages circuit has a charging peak at -7 µA and reaches a stationary state in less than 20 seconds, whereas the capacitor of the single-stage circuit is immediately saturated to a small deflection. Due to the voltage output saturation, the single-stage capacitor takes 110 seconds to charge enough to stop saturating and reaches a stationary state at approximately 120 seconds, which is 6 times more than in the two-stages circuit and is unacceptable for BCG applications. Consequently, a two-stages circuit separating the filtering and the amplification is selected in Figure 20.

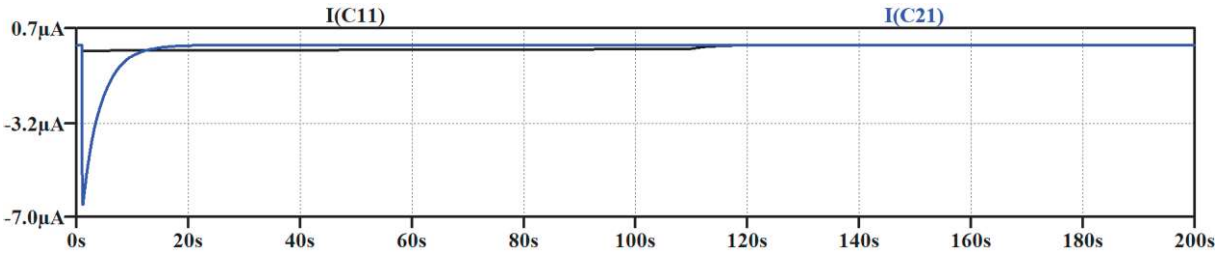

Figure 24: Charging curve of the capacitor after a voltage step from 1.65 V (0 g) to 2.31 V (1 g), using the generator convention.

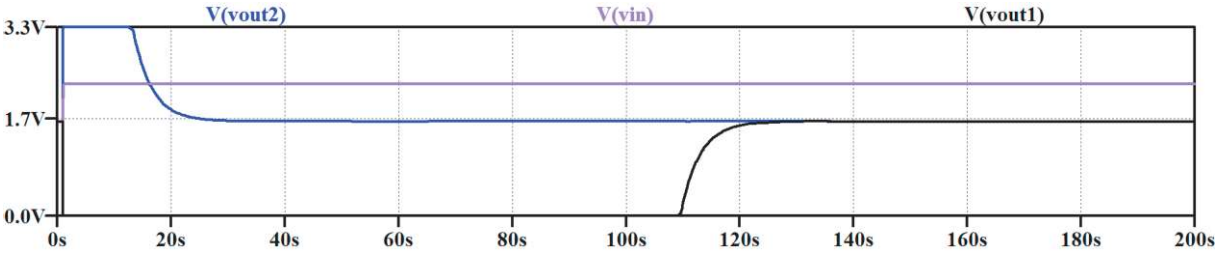

Figure 25: Voltage outputs after a voltage from 1.65 V (0 g) to 2.31 V (1 g)

If higher gains are needed in Figure 20, a small gain of 3 dB to 20 dB can be added to the first filtering stage by slightly increasing the feedback resistor value. This modification will bring capacitor current saturation, which can be acceptable if the gain is limited. Otherwise, adding a third stage for amplification is also an option.

A topology inspired by [120] makes it possible to both reduce the conditioning the circuit to a single-stage with high gain and acceptable settling time. It consists of

automatically switching the gain of the amplifier, when it is close to saturation, to a lower gain. This novel topology is presented in Figure 26. The capacitor can thus charge at high speed, and when it is almost charged, the gain is automatically switched back to its initial value. The automated switch is performed by fast switching diodes instead of the feedback resistor.

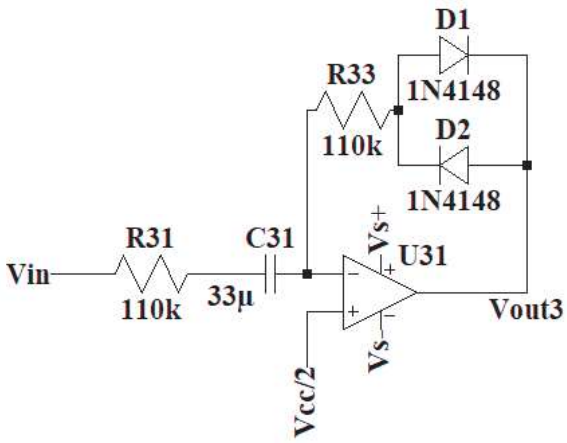

Figure 26: Fast-settling time AC amplifier

Indeed, such diodes can be modeled as a varying resistor with a forward voltage threshold, above which the resistance is very low and below which the resistance is very high. For example, the 1N4148 fast switching diode [121] has a forward voltage threshold at 0 V, where its resistance is 18 MΩ. These values were obtained with a sweep of DC voltage in Figure 27, from -1.0 V to 1.0 V in Figure 28, and from -100 mV to 100 mV in Figure 29.

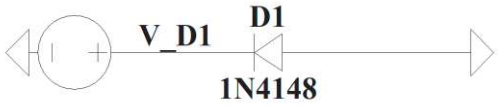

Figure 27: Test of 1N4148 diode.

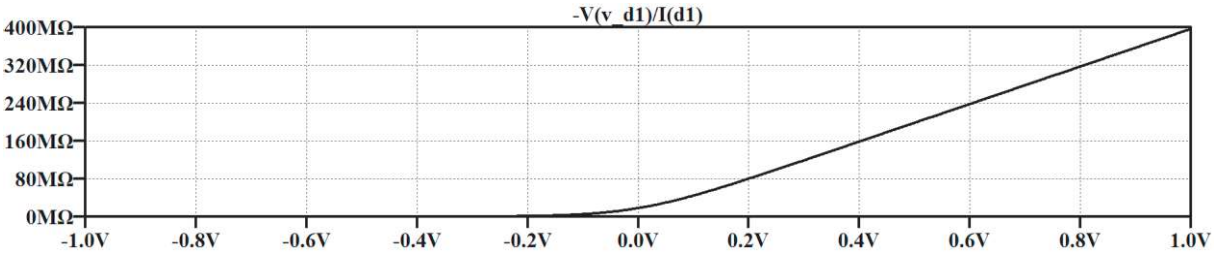

Figure 28: Resistance curve of 1N4148 diode depending on reverse voltage.

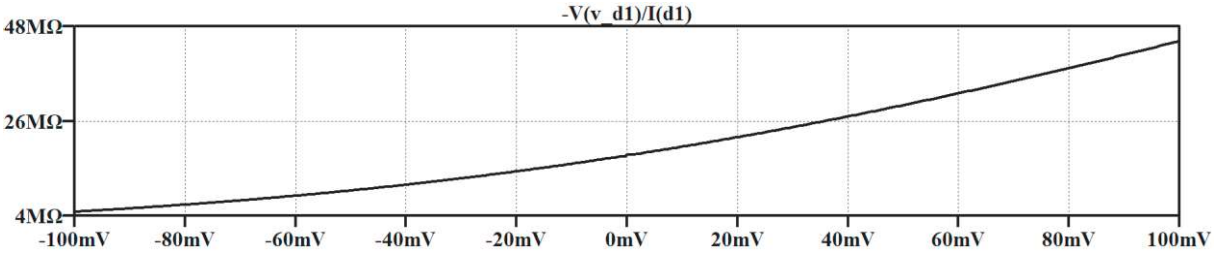

Figure 29: Zoom of the resistance curve of 1N4148 diode depending on reverse voltage.

Antiparallel diodes, when applied a 0 V or with small signals, approximately have a 9 MΩ resistance. It means that the amplifier gain will not exceed $\frac{9M+110k}{110k} = 38\ dB$. This is verified on the Bode diagram of the fast-settling time circuit, illustrated in Figure 30 during a 1mV AC analysis on the LT Spice software.

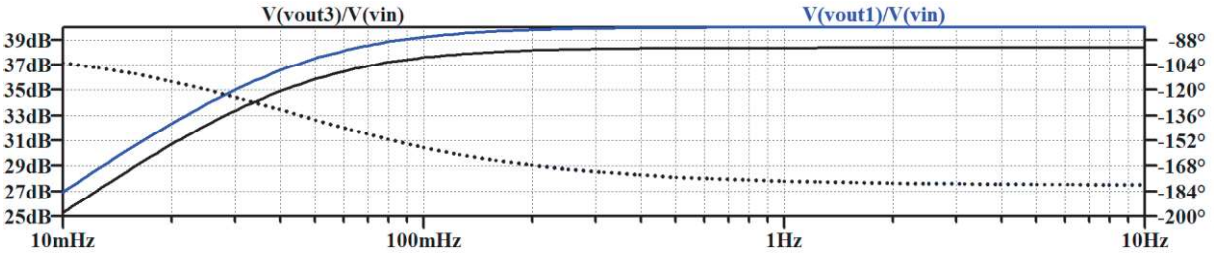

Figure 30: Bode diagram of the fast-settling time AC amplifier compared with the single-stage circuit.

When a large voltage signal happens, one of the diodes, depending on if the signal is higher or lower than $\frac{Vcc}{2}$, passes the current through with a negligible resistor (a few Ohms for the 1N4148 reference) and the feedback resistor takes the value of the 110 kΩ resistor. In this configuration, the amplifier has a unity gain and cannot saturate, allowing the capacitor to fully charge. For example, during a 0 to 1 g step, i.e. a 1.65 to 2.31 V with the LIS344ALH accelerometer, while the D2 diode remains blocked, the D1 diode immediately turn in passing mode, consequently, the amplifier switch to a unity gain amplifier and the capacitor current is

not saturated - see. Once the capacitor is charged, the D1 diode switch back to blocked mode, and the amplifier turns back to a 38 dB gain. This switching functionality keeps the settling time during large signal to 20 seconds, the same as with the two-stages circuit, with a single amplifier.

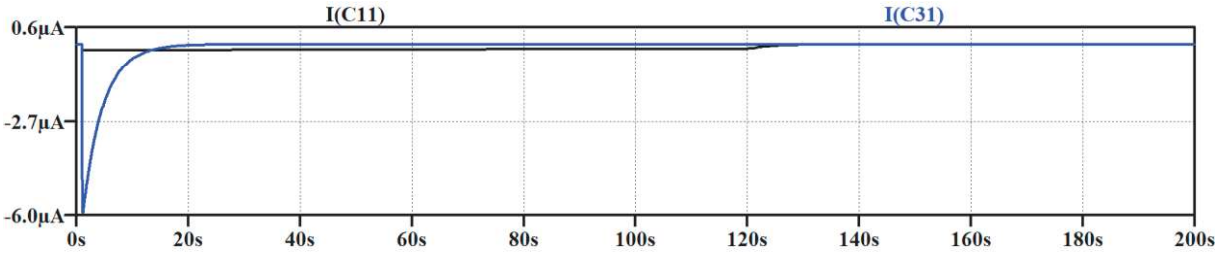

Figure 31: Charging curves of the capacitor after a voltage step, in the single-stage circuit (C11) and in the fast settling time circuit (C31).

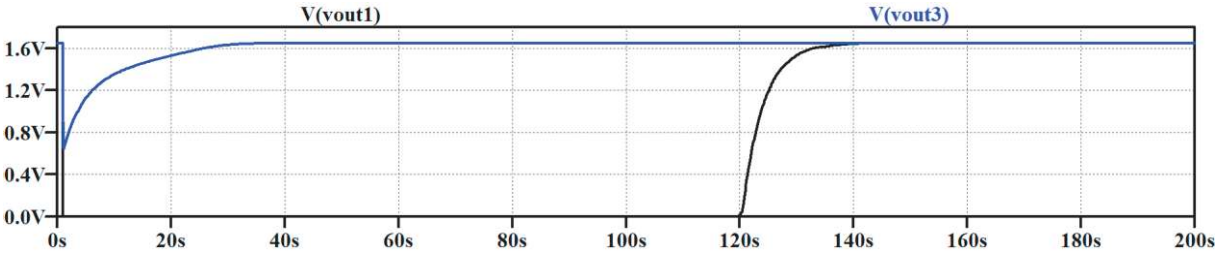

Figure 32: Comparison of the settling times in the single-stage circuit (vout1) and in the fast settling time circuit (vout3).

Later in this thesis, the fast-settling time circuit is not used because it was invented recently; the two-stages circuit with PGA of Figure 20 is used instead.

2.2.2.3. Acquisition unit

Concerning the Fealing Biopac BCG module, the accelerometer output is connected to a Biopac MP36 acquisition unit, illustrated in Figure 33A. This equipment brings very low 9 $nV/\sqrt{Hz}$ input noise density, has hardware AC filters with cut-off frequencies down to 0.05 Hz, very high gains up to 94 dB, a very high resolution with 24 bits with an 8 V full-scale range, and a very high 11 MΩ input impedance [122]. It is adapted for very low amplitude signals such as EEGs and will measure very precisely the BCG sensor output. Moreover, its

DB9 connectors have a +5V power pin and there is no need for external alimentation Figure 33B.

An anti-aliasing filter above 50 Hz is added on the sensor output to minimize noise while sampling over 100 Hz. As the acquisition unit has large dimensions and cannot be embedded in the patient bed, a 2 to 5-meters long shielded coaxial cable links the sensor, which is in the bed to the acquisition unit. It is the major drawback of the Fealing Biopac BCG module, as this cable can bring electromagnetic noise and mechanical noise.

A B

Figure 33: MP36 Biopac and its DB9 connector pinout

Compatibility with the Picoscope 4444 USB oscilloscope was also investigated, as the Biopac MP36 is expensive ($10k compared to $1.5k) and is not always available in our lab. The Picoscope 4444, illustrated in Figure 34, also has DB9 connectors. The pinout is confidential and was hacked, especially the power pin available only if there is a specific resistor between two other pins. It has a 14 bits resolution, no hardware filter, and no amplifier gain: the conditioning circuit detailed in Section 2.2.2.1 must be implemented. Fortunately, the sampling rate can reach 400 MHz which is far enough for a BCG application where a 100 Hz sampling rate is enough

Figure 34: Picoscope 4444 oscilloscope

In these two configurations, a Windows PC is needed for recording, in addition to the Biopac unit and the sensor. It is relevant only in experimental studies with small volunteers' cohorts.

Still, the Fealing BCG module has other advantages such as analog signal synchronization, e.g. for ECG using the analog ECG output of Nihon-Kohden multiparameter scopes in Hôpital Raymond Poincaré. Figure 34 illustrates a setup in a Pediatric Intensive Care Unit (PICU) bed with ECG synchronization.

Figure 35: Fealing Biopac BCG module, with Nihon-Kohden ECG synchronization.

2.2.2.4. Microcontroller

Concerning the Fealing Wireless BCG module and the Fealing ST BCG module, they are interfaced with a 32-bits DSP (digital signal processing) microcontroller. The STM32L476RG was selected for the Fealing ST BCG module because it has low power consumption and intermediate computation resources (Cortex M4), which will be useful for

later applications. For the Fealing Wireless BCG module, the STM32WB55RG was selected, because it adds Bluetooth5 to the previous microcontroller.

These modules' versions need the conditioning circuit previously conceived and detailed in Section 2.2.2.1.

2.2.3. Mechanical integration

2.2.3.1. Position in bed

The BCG modules must be mechanically linked to the bed. More precisely, they must sense the patient's heartbeats, inspirations, and expirations. Usually, we place the sensor on the mattress surface: on the top, as in Figure 36, or on the side.

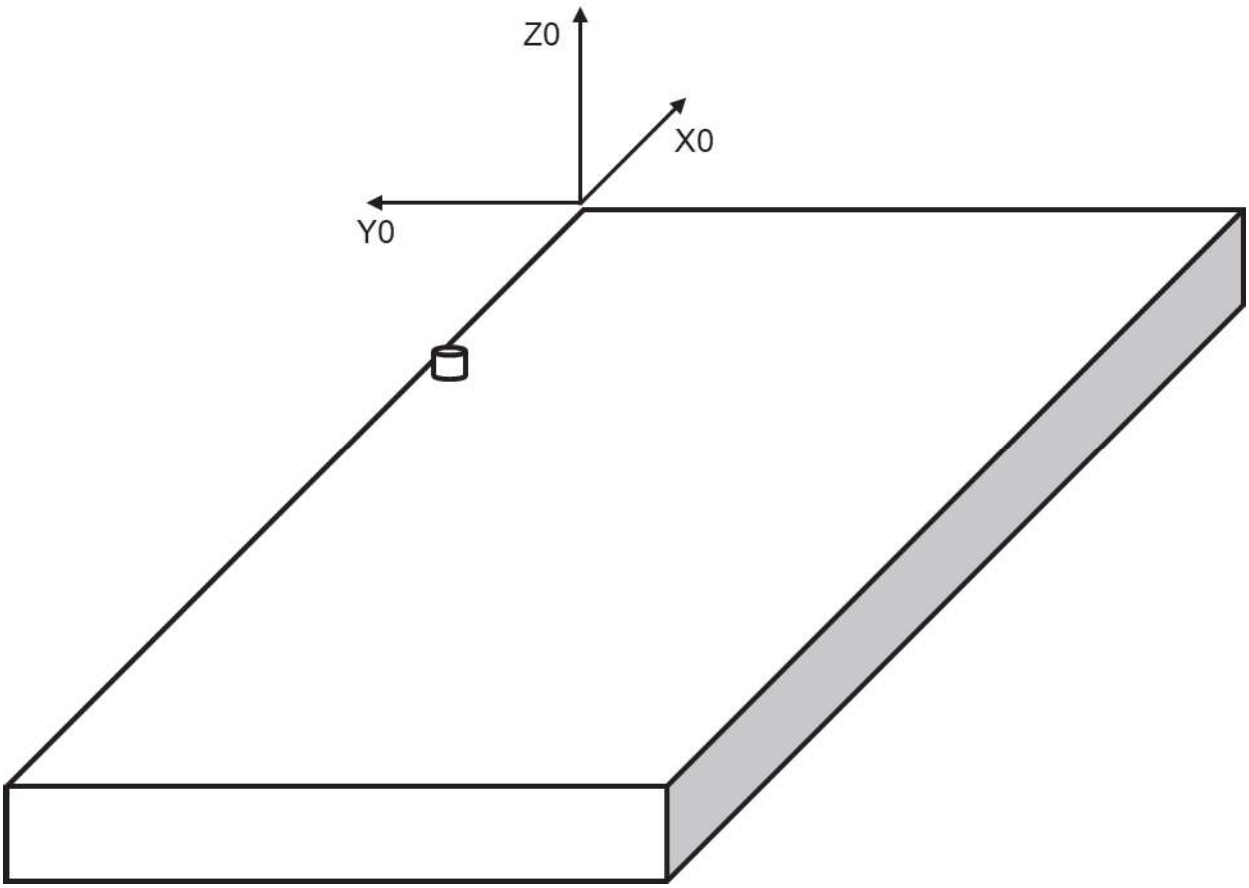

Figure 36: Illustration of the sensor position in the bed. The head of the patient is on the side of the axes origin.

2.2.3.2. Wired connection

For the Fealing Biopac and ST BCG modules, a wired connection to an acquisition unit is necessary for digitizing the sensor output and for power. This wire, transmitting analog information, must be shielded against electromagnetic pollution. However, many coaxial cables are thick and not flexible, which prevents the movement of the module during cardiac or respiration cycles.

We benchmarked several coaxial wires manufactured by AlphaWire [123], shielded and with 3 conductors, adapted for analog BCG transmission, and module powering in Table 4.

Table 4: Benchmark of flexible coaxial cables.

Category	Shield	Part number	Nominal diameter (mm)
EcoCable® Mini	Foil	78103	2.62
EcoFlex® Cable	Braid	79102	5.56
EcoFlex® Cable	Foil+braid	79262	4.55
EcoFlex® PUR Cable	Braid	80102	4.42

We chose the EcoCable Mini 78103 because of its very thin diameter; however, the EcoFlex Pur Cable 80102 will also be tested in the future.

The cable is fixed on the BCG module through a cable gland or a Jack connector.

2.2.3.3. Enclosure

The enclosure needs to be small enough to be integrated into the bed. Hammond Manufacturing enclosures [124] [125] were selected and are illustrated in Figure 18:

- 1551 FGY for the Fealing Biopac BCG module
- 1551 NGY for the Fealing Wireless BCG module
- 1591XXTGY for the Fealing ST BCG module.

Moreover, it must be waterproof for cleaning in the hospital environment.

2.3. The Baby Heartbeat Simulator

2.3.1. The experimental model

A reduced experimental model was first designed to demonstrate the amplification and the filtering principle of the smart BCG front end in a controlled environment.

A  B 

Figure 37: Body lying on a bed (A) and reduced model (B)

The experiment uses a spring-mass model of a baby body lying on a bed, as illustrated in Figure 37. Firstly, the bed is taken from the intensive care unit (Villard reference 505.59). It is made of steel and the security bars were up during the experiment. Secondly, the Pharmaouest polyurethane mattress dimensions are 120x60x10 cm (length x width x height). Thirdly, the weight, representing the thorax, is a steel cylinder of 10cm-wide diameter, and 3.4 kg. The typical average pressure of a thorax lying on a mattress is set at 32 mmHg, which is near the typical 20 - 40 mmHg capillary pressure range [126]. The weight's material is high-density steel. To apply the thorax typical pressure on the spacer fabrics layer, its diameter could not respect the ratio of the reduced model because the cylinder would have been too long and thus unstable.

2.3.2. The cardiac force simulation

Considering the experimental model, the simulated cardiac force should have the characteristics of a BCG. To simplify the model, the cardiac force is simulated by a series of sinusoidal pulses, repeated every second. The average BCG pulse is in the 5 to 10 Hz frequency range and approximately lasts 160 ms and has an approximate 1 N amplitude [13].

To our knowledge, no commercial and compact device can generate such a vibration, consequently, we decided to simulate the cardiac force using a MakeBlock 42BYG stepper motor. It has been previously unbalanced by fixing a 36 g and 3 cm eccentric steel screw on the rotor, as seen in Figure 37B. The centrifugal force equals 1.2 N at 300 rpm or 5 Hz; it can be adjusted to different speeds by updating the weight and position of the eccentric. The stepper motor was initially programmed to generate an average BCG waveform, i.e. pulsed vibrations, by rotating at 300 - 600 rpm during 160 ms every second. However, the stepper motor acceleration is too fast and is stepped at low speed, which generates shocks and noises when the vibration starts and ends. Finally, for practical reasons, the BCG was simulated using the acceleration shocks when the rotor starts rotating. The speed command profile is illustrated in Figure 38.

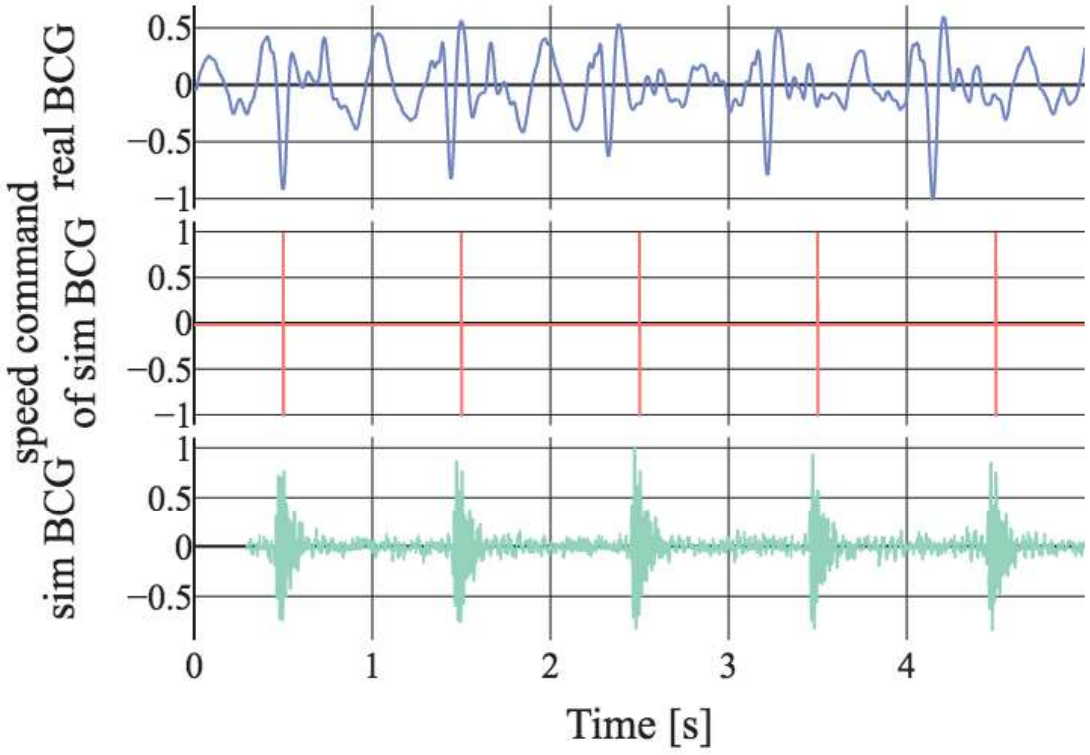

Figure 38: A typical BCG compared to the simulated cardiac force. Signals' amplitudes have been normalized by zero-mean and one-maximal amplitude.

The impulse response of the bed, acting like a damping system, generates noises at the resonance frequency. The simulated vibration differs in the frequency range from the average BCG, and the amplitude has not been investigated. Nevertheless, the demonstration of the underlying principle remains the same.

In parallel, vibrations at different constant frequencies were generated to accurately measure the frequency response of the amplifier.

2.4. Signal amplification for smartphone BCG

2.4.1. Introduction

Analog amplification is required to achieve good detection performance and usually concerns electronics and sensors. However, we observed that the bedding and bed frame

nature alter the propagation of the ejection force to the sensor, especially in case of viscous foam or damping medical beds: the bedding and bed frame mechanical behaviors may have a role on analog amplification.

Using the embedded accelerometer for bed ballistocardiography is enhanced by two factors: the mechanical amplification of the ballistocardiographic force, explained in this section; and more and more sensitive IMUs that are reviewed in the next paragraph.

A review of the smartphone accelerometer resolutions is conducted with three different databases. First, the Phyphox Sensor Database [127] is constituted of 760 different smartphone models submitted by a total of 2325 users, by the time this thesis was written. It has the specifications of the accelerometers used in these smartphones, such as the sampling rate, the resolution, the name, and the manufacturer. During the processing of the database, some smartphones were discarded because specifications were lacking, for example, Apple smartphones. It also provides an estimation of the distribution of the different smartphone models at specific times. Second, the GSMArena (www.gsmarena.com) database gives the release date of many smartphone models. Last, the Mouser database (www.mouser.com) gives finer specification than the Phyphox Sensor Database of every digital accelerometer on the smartphone market, such as the output noise density.

Even if the representativity of the Phyphox database is questionable, it provides good insights for the 2014-2019 period, i.e. the last five years. Indeed, more than 30 devices in the database were released every year in this period, as shown in Figure 39.

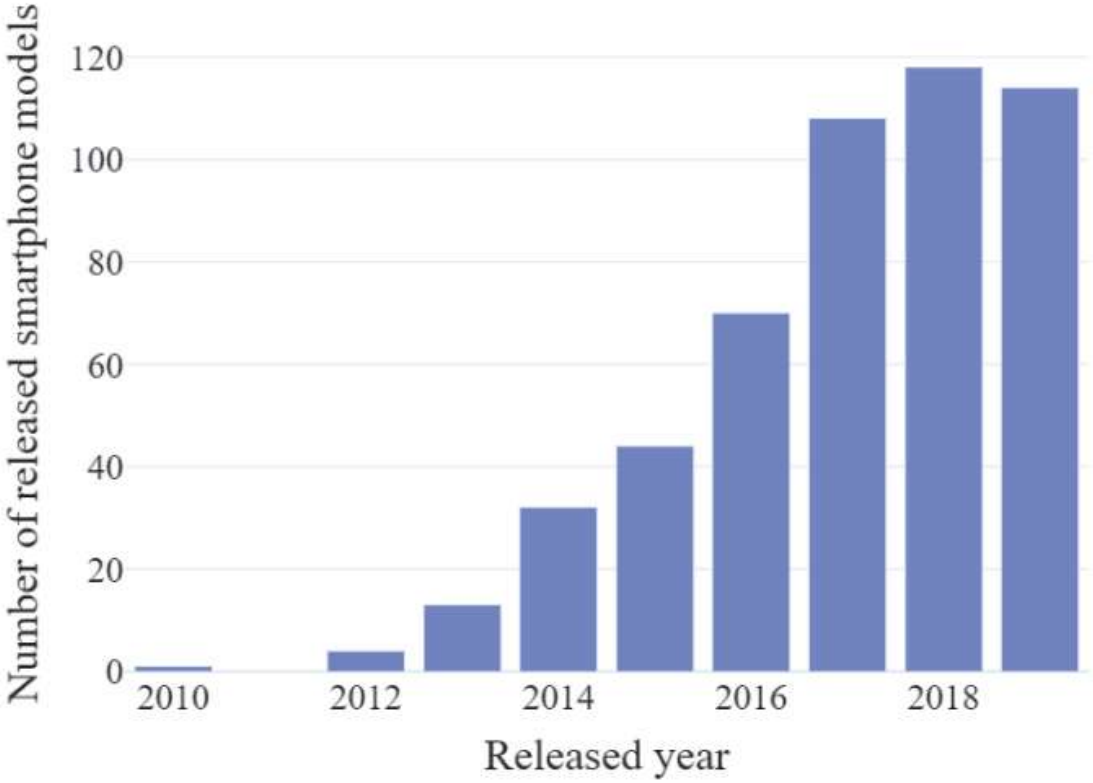

Figure 39: Number of different Android smartphone models released each year and referenced in the Phyphox database.

For every year of the 2014-2019 period, released smartphone models are grouped by their resolution. More and more models are released each year with a resolution of at least 2^{12} LSB/g as shown in Figure 40. In five years, the distribution of larger and equal 2^{12} LSB/g models jumped from 30% to 80%; the distribution of strictly lower than 2^{10} LSB/g models decreased from 40% to 10%.

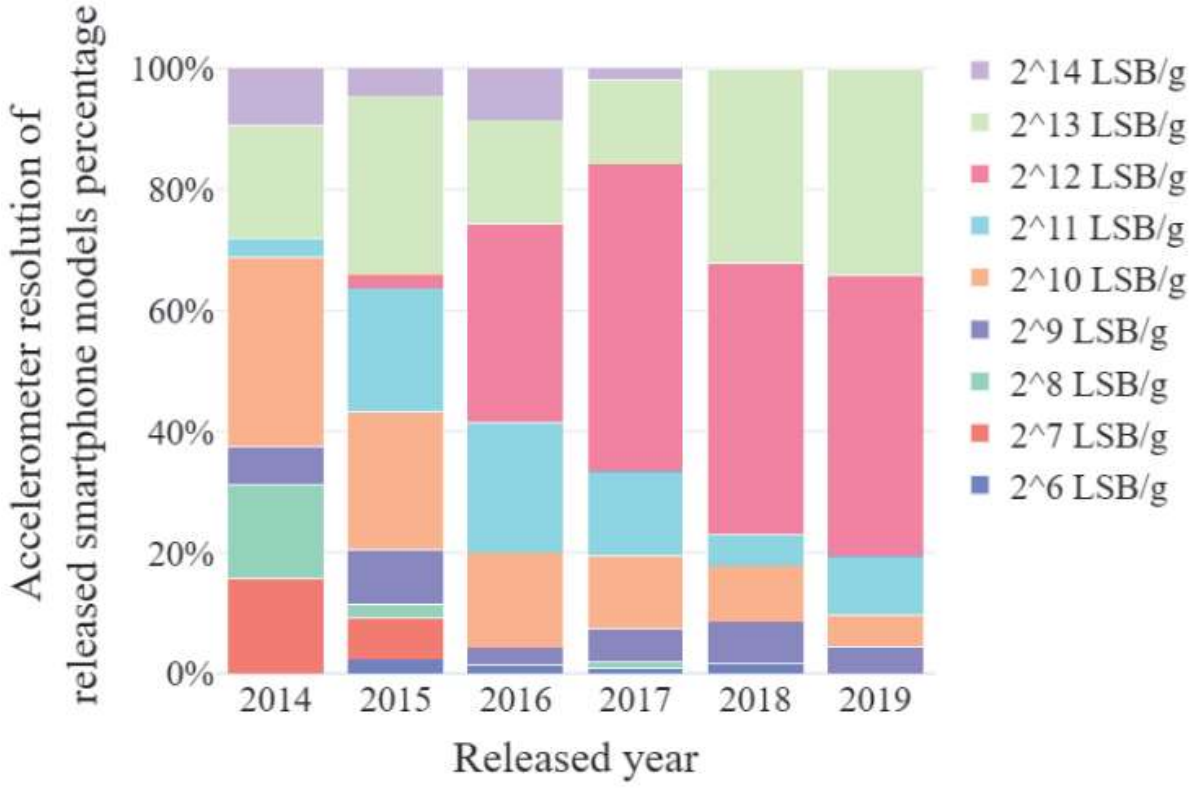

Figure 40: Accelerometer resolution of the different Android smartphone models released each year and referenced in the Phyphox database.

In this context of increasing the sensitivity of smartphone accelerometers, we present bedding designs that amplify the BCG signal.

2.4.2. Bedding waveguide

2.4.2.1. Materials

The bed used for this experimentation is constituted of a slatted solid pine wood Utaker home bed and a firm latex polyurethane Malvik mattress of 200x80 cm dimensions, both Ikea brand products. The bed is equipped with a sensor, detailed in Section 2.2, placed on top and 5 cm away from the mattress side, as shown in Figure 41. This sensor is based on a Murata SCA100T-D02 two-dimensional analog accelerometer with an output noise density as low as 14 $\mu g/\sqrt{Hz}$. The sensor is embedded in an ABS plastic case and linked with a shielded cable to a Biopac MP36R acquisition unit for AC coupling, amplification, and power. The analog output is AC coupled, anti-aliasing filtered and 100 times amplified before digitization at 1 kHz. In this setup, the resolution is as low as 2^{21} LSB/g (least significant bit).

Figure 41: Setup of the bedding waveguide experimentation.

A healthy, 75 kg weight, 25 years-old and 1.90 m tall volunteer and were asked to lie down, still and quiet in the supine position for 2 minutes.

This process is repeated for several configurations of mattress (with or without mattress cover) and the following waveguide beddings: no waveguide, polypropylene (PP) adhesive tape, cotton tape, spacer fabrics. Table 5 illustrates all these configurations. A control sample, without anybody on the bed, is added to measure the noise baseline. Every configuration is repeated thrice to get rid of the bed position variability.

2.4.2.2. Methods

The ultimate goal of the methods is to evaluate the relative performance of the selected waveguide beddings. Figure 42 illustrates the methods.

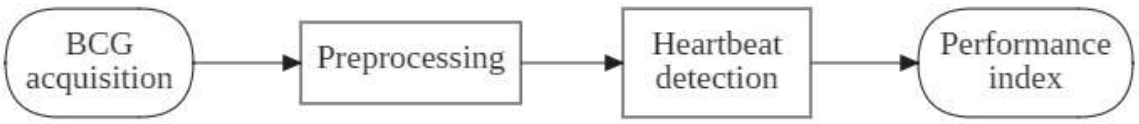

Figure 42: Flowchart of the bedding waveguide methods.

The first minute is discarded from each record to be sure that the volunteer is relaxed and breathes slowly and regularly during the resulting 1-minute-long records. Digital BCG signals are filtered with third-order Butterworth filters, specifically a 25 Hz low-pass filter

and a 2 Hz high-pass filter. They are applied forward and backward to prevent phase distortion. Lastly, the signal is decimated to 200 Hz sampling frequency.

Heartbeats are detected using a dynamic time warping (DTW) template matching algorithm [128], whose steps are reminded in Section 3.3.2. The J peaks of the BCG are set as reference labels for the heartbeats.

The median amplitude of J peaks is a simple performance index, but does not consider two phenomena:

- The amplitude modulation of J peaks during the respiration cycle, as shown in Figure 43
- The non-linearity of the mechanical structure.

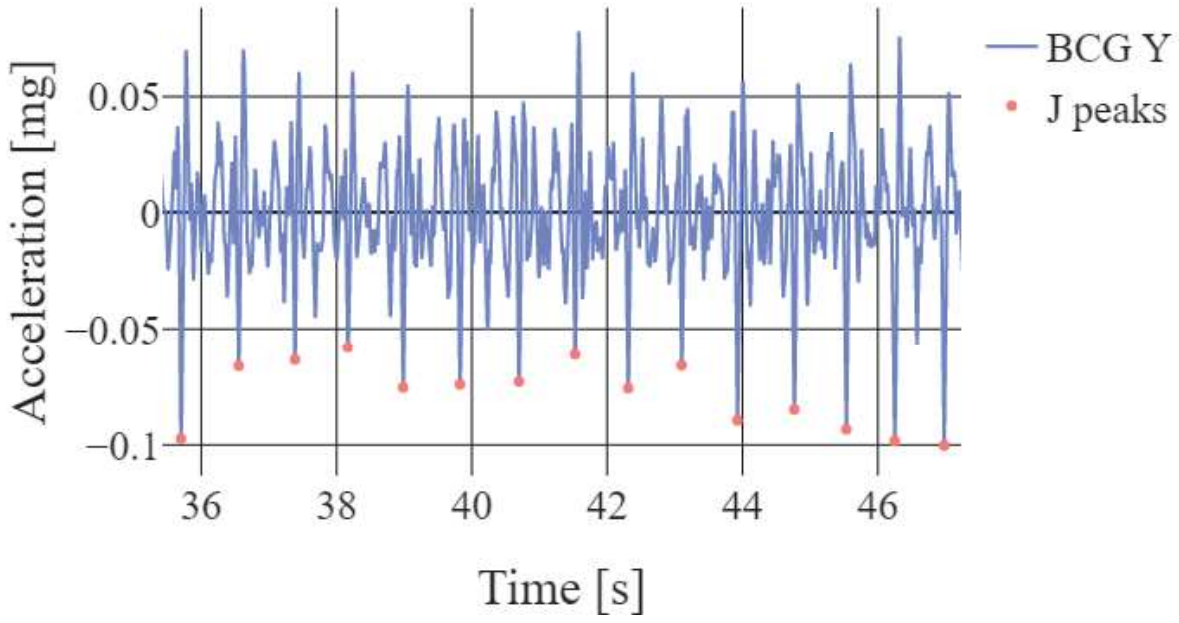

Figure 43: Amplitude modulation of J peaks during respiration.

Consequently, the least detectable J-peaks must be amplified in priority. The first decile of the J-peaks amplitude is selected for every BCG signal. The absolute performance index is the median value of these first deciles over the three records of that configuration. Equation (5) formalizes the definition of the absolute performance index of a waveguide. The relative performance index is defined by Equation (6).

$$\begin{cases} D1_{w_n} = D1\left(\left[BCG_{w_N}[j]\ for\ j\ in\ J_{peaks_{w_n}}\right]\right) \\ PI_{abs_w} = median([D1_{w_N}\ for\ \ 1 \leq N \leq 3]) \end{cases} \quad (5)$$

$$PI_{rel_w} coverconfig = \frac{PI_{abs_w}(cover\ config) - PI_{abs_{w_0}}(coverconfig)}{PI_{abs_{w_0}}(coverconfig)} \quad (6)$$

A performance index is always evaluated with a single axis BCG so that the bedding influence over axis X and Y will be compared.

2.4.2.3. Results

The mattress configuration directly impacts the performance index; moreover, the performance indices are axis dependent. Three main results come out of Figure 44, that ranks the configurations by their Y-axis performance indices.

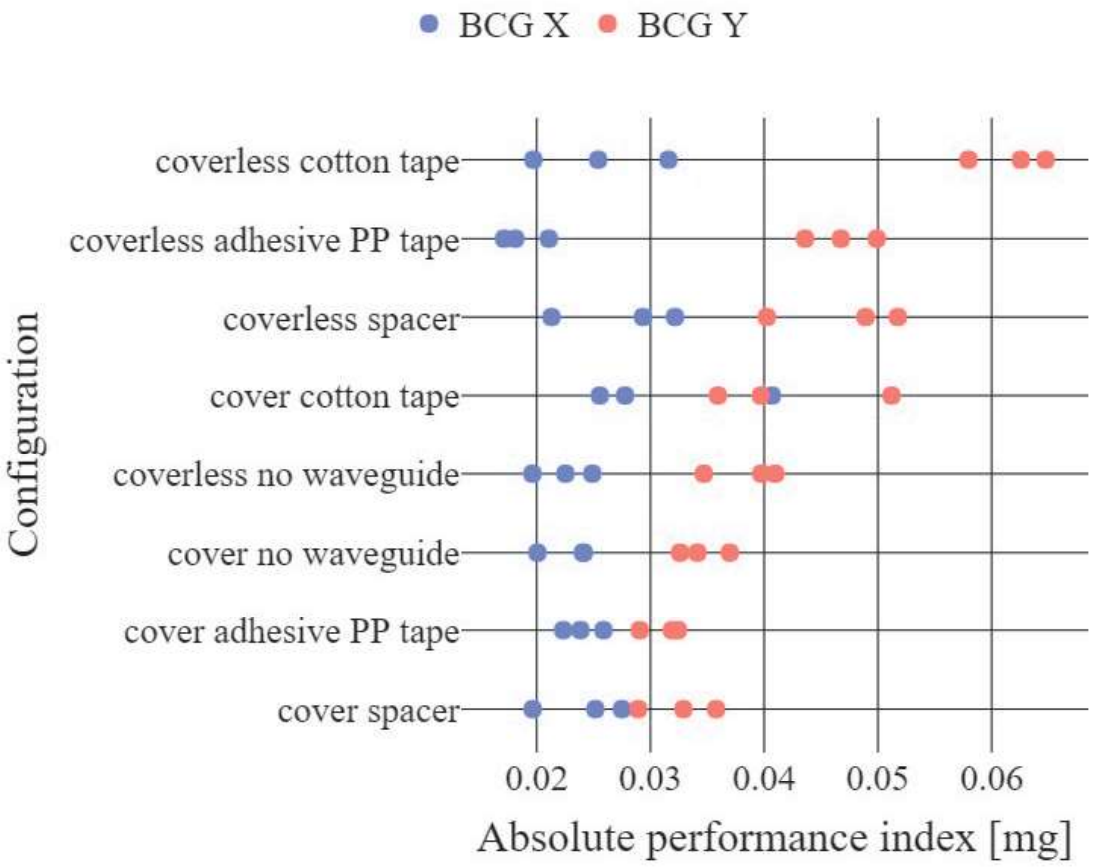

Figure 44: Absolute performance indices of different waveguide configurations.

Firstly, the axis Y better transmits the BCG signal than axis X. This has been verified ($p<0.05$) for every configuration except for {cover+spacer} where $p = 0.053$, and {cover+cotton tape} where $p = 0.171$. Secondly, adding a cover to the mattress configuration alters the BCG signal transmission along axis Y ($p<0.05$), except when no waveguide is used ($p=0.177$). Thirdly, the cotton tape waveguide improves, independently from the mattress configuration, the performance index along the Y-axis, which is not the case of the other waveguides. This has been verified for axis Y with a coverless mattress ($p=0.001$) but not with a covered mattress ($p=0.230$).

Table 5: Absolute performance indices on axis Y.

Wave-guide	No wave-guide	PP adhesive tape	Cotton tape	Spacer fabrics
Without mattress cover	0.04	0.047	0.063	0.049
With mattress cover	0.034	0.032	0.04	0.033

Table 5 and Table 6 respectively summarize the absolute and relative performance indices for Y-axis, which gives the best results.

Table 6: Relative performance indices on axis Y.

Wave-guide	No wave-guide	PP adhesive tape	Cotton tape	Spacer fabrics
Without mattress cover	0.00%	17.60%	57.40%	23.00%
With mattress cover	0.00%	-6.60%	16.30%	-3.60%

2.4.3. Smartphone-based BCG

2.4.3.1. Materials

In this second experimentation, also called the smartphone-based BCG experimentation, the bed and sensor positions are the same as the previous experimentation. This time, the sensor is smartphone-based: it is an LSM6DSM STMicroelectronics digital 3D accelerometer, embedded in a Motorola One phone. In this smartphone configuration, the sampling rate is 200 Hz, the resolution is 2^{12} LSB/g and the output noise density is 90 $\mu g/\sqrt{Hz}$. It is worth noting that these specifications are far worse than the homemade sensor in experimentation 1. The undisclosed Fealing SleepLogger application was used for recording the accelerometer samples and export them on a computer.

Figure 45: Setup of smartphone-based BCG experimentation, with waveguide bedding in orange.

The same adult lies down on the bed, still and quiet in the supine position for a 30 minutes nap, in two different configurations: with the smartphone attached with a Velcro on a waveguide bedding or directly on the mattress cover. The waveguide is comfortable and is not noticed by the subject even after a sleep night. Another sensor is used as a reference: the

EMFIT QS [129] normal pressure sensor, which provides a raw signal export service for naps longer than 20 minutes, in the respiration (0.07-3 Hz) and the heart (1.5-35 Hz) frequency bands.

2.4.3.2. Methods

Motion-free BCG signals are segmented and averaged to zero. The root-mean-square value of sensor signals is computed using the $RMS()$ function. A transfer function is computed as the ratio of the RMS value of smartphone-based sensors upon the RMS of the reference pressure sensor – see Equation (7). The unit of this transfer function is mg/N, with A the acceleration measured by the smartphone along an axis and P the normal pressure measure by the Emfit QS sensor. In Equation (7), the subscript i equals 1 or 2 with or without waveguide; f is the filter for respiratory or cardiac frequency bands.

This method is relevant for longer and noisier segments because heartbeats do not have to be detected and manually checked.

$$H_i(f) = \frac{RMS(f(A_i))}{RMS(f(P))} \tag{7}$$

$$Gain(f) = \frac{H_1(f)}{H_2(f)} \tag{8}$$

The unitless gain is evaluated at the ratio between those transfer functions – see Equation (8). All these equations may depend on the frequency, especially two frequency bands: the respiration and heart frequency bands, previously defined as 0.07-3 Hz and 1.5-35 Hz. Frequency bands are filtered using 2nd order Butterworth filters, which are presumably equivalent to the Emfit QS analog filters.

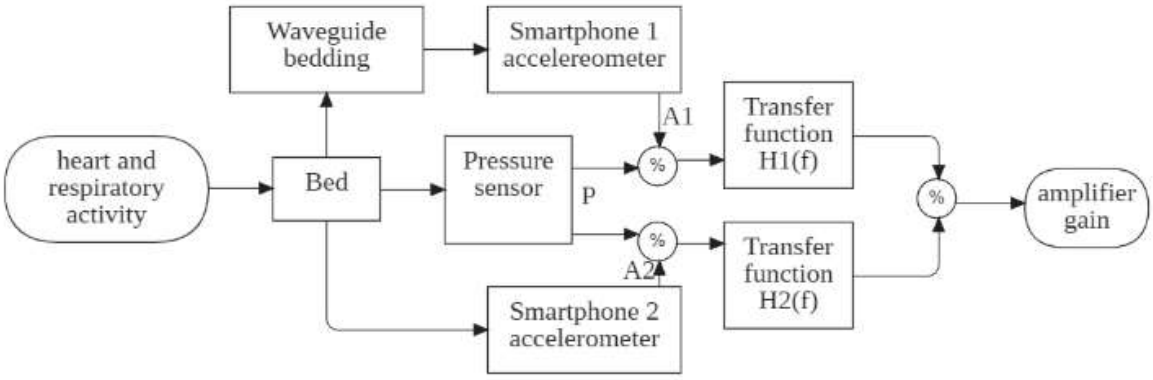

Figure 46: Flowchart of the smartphone-based BCG methods

Ideally, smartphone sensors 1 and 2 record BCG simultaneously; however, the setup is complicated because the waveguide bedding covers the whole width of the mattress. Therefore, two 30 minutes-long naps are recorded: one with (smartphone sensor 1) and one without (smartphone sensor 2) waveguide bedding. For each of these naps, ballistocardiograms are segmented as motion-free segments, with or without presence and with two different frequency bandwidths. The three axes of the accelerometer sensors are investigated.

2.4.3.3. Results

Smartphone-based ballistocardiography is evaluated in Table 7 below. The gain factor is above 3.4 in the heart frequency band on every axis.

Table 7: Smartphone-based ballistocardiography performances depending on the frequency band, the accelerometer axis, and with or without waveguide.

Frequency band	Heart frequency band (1.5-35Hz)			Respiration frequency band (0.07-3Hz)		
Acc axis	X	Y	Z	X	Y	Z
H1 [mg/N]	55.7	63.9	60.2	1.4	1.4	1.6
H2 [mg/N]	14.4	15.9	17.7	0.7	0.8	0.5
Gain []	3.9	4.0	3.4	2.1	1.9	3.1

2.4.4. Conclusion

We tested several waveguide beddings to amplify a BCG signal and found that the cotton tape allows in general better transmission than spacer fabrics or adhesive PP tape. The authors are cautious with the significance of this result because only three records were realized per configuration. More records are needed to confirm the results, and other bed frames and mattresses will need to be investigated.

For a given mattress configuration, some waveguides improve the transmission along Y-axis but alter it along X-axis, e.g. adhesive PP tape on the coverless mattress. Two explanations are plausible: either the waveguide transferred strain from axis X to axis Y, or friction while lying down on the bed rotated the sensor around axis Z. Cameras during the experimentation or simulation will elucidate this phenomenon. The comfort of the waveguide will be quantified in further experiments and through simulation.

Waveguide beddings enable smartphone-based ballistocardiography, thanks to a 3.4 to 4 amplification factor of the smartphone accelerometer signal. This large gain might be explained by the different waveguide material and the wireless sensors using the smartphone. The authors are cautious with these results because experiment 2 has only been conducted once. It has been noticed that when the waveguide is too strained or too relaxed, the amplifier gain may drop. Waveguide optimal nature and tension will be investigated further by mechanical modeling and experimentation. Moreover, the measurements with and without waveguide bedding are not simultaneous, which may add variability. Later, experimentation 2 will be repeated multiple times, with two identical sensors attached simultaneously: one on the left bedside on the waveguide bedding and the other one on the right bedside out of the waveguide bedding.

Finally, the smartphone review shows that accelerometers resolutions of new smartphone models are finer and finer. Resolutions of 2^{14} LSB/g subsisted on the market until

2017, but after a detailed look on the databases, it is because smartphone-accelerometers ranges also get higher. The highest resolution 2^{14} LSB/g models, until 2017, where 16 bits with a ± 2 g range, whereas nowadays manufacturers require at least ± 4 g and up to ± 16 g ranges, which inevitably reduces the accelerometer resolution. Despite all of that, we can expect that new technologies will bring higher resolutions. Noise density is also an important feature, and its evolution will be detailed later.

This study highlights the importance of the bed frame and mattress mechanical behaviors, which are often neglected in BCG systems. It is a step toward a BCG-amplifier mattress with high SNR no matter the bed frame, vibrating environment, and the user, e.g. infants and neonates in the hospital.

2.5. Signal multiplexing for BCG imaging

2.5.1. Introduction

Analog amplification is required to achieve good detection performance. Therefore, it is very sensitive to baseline wander that occurs at a position shift, e.g. from supine to prone position, and needs to be filtered. However, to measure the respiratory activity whose lowest frequency components are about 0.1 Hz [130], the usual high-pass filters are slow to settle and the BCG signal can saturate for several decades of seconds as it will be shown in this thesis. The addition of non-linear components, e.g. commutation diodes in the amplifier feedback loop [116], may help reduce the amplifier settling time, i.e. the time before the end of the saturation, for a few seconds only. Moreover, the individual plus its bed may be considered as a damping system which generates noise at its resonance frequency.

Environmental noises, e.g. nurses walking, ventilation apparatus, or during transportation in a pediatric intensive care unit, can also occur. For the same saturation reasons, these repetitive noises need to be filtered otherwise the monitoring coverage might be lowered.

In this context, we introduce a novel smart BCG front-end which identifies the system resonance frequency, filters the baseline wander and the damping noise, and highly amplifies the BCG signal without saturation after movement.

2.5.2. Materials

The Baby Heartbeat Simulator was used for the experiment and is described in Section 2.3.

2.5.2.1. Electronics components

For measuring the simulated BCG signal, several sensors and electronics components are used. They are listed below and integrated into an ABS enclosure, referenced as 1591XXTGY by Hammond Manufacturing.

The digital signal processor (DSP) is a 32-bit STM32L476, mounted on a Nucleo-L476RG board, whose analog-to-digital converters (ADC) and digital-to-analog converters (DAC) channels have a 12 bits resolution and a 256 Hz sampling rate. The ARM MBED operating system was used with the CMSIS DSP library. A USB port is used for serial communication with a computer and power up the circuit.

The sensor is a LIS344ALH accelerometer with a 50 $\mu g/\sqrt{Hz}$ low noise density and a 0.66 V/g high sensitivity. It is mounted on a STEVAL-MKI015V1 evaluation board, and the FS, PD, and ST pins are grounded. It is powered by a 3.3 V single supply and measures $\pm 2\ g$ accelerations in this configuration. It is oriented such that the Z-axis is in the gravity direction.

The amplifier used is an AD623AN instrumentation amplifier whose gain is adjustable with a resistor and ranges from 0 to 40 decibels (dB). Its voltage reference Vref equals half the accelerometer voltage supply.

2.5.2.2. Mixed-signal front end

A mixed-signal architecture is a topology where an analog signal is digitized by an ADC, filtered on a DSP then synthesized by a DAC [131]. Such circuits have the same advantages as numerical filters, e.g. sharp transition frequency band or fast settling time, and may be associated with an analog amplifier.

In the BCG case, undesired components of the analog acceleration signal have to be filtered before amplification and digitization. The designed architecture, illustrated in Figure 47, removes those undesired components and amplifies the resulting signal using an instrumentation amplifier.

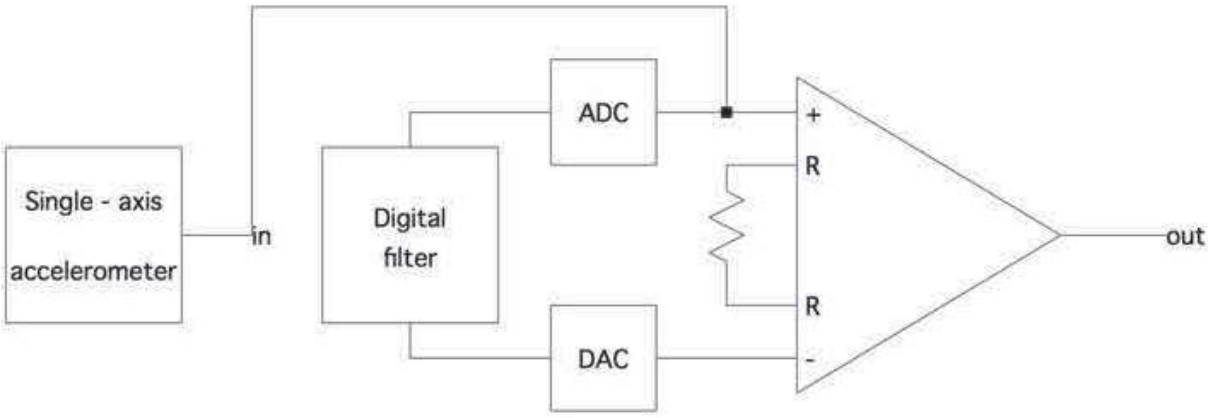

Figure 47: Pseudo-electronic circuit of the front-end

The resulting signal is expressed by Equation (9), where G stands for the gain of the amplifier and f stands for the digital filter.

$$V_{out} = G\,.\,[Vin - f(Vin)] \qquad (9)$$

Similar architectures have been used in bio-signal processing. In 2003, Analog Devices proposed an electrocardiography front-end using the ADuC842 microcontroller with simple stepwise feedback on the AD620 instrumentation amplifier's reference offset pin [132]. In 2004 and more recently, electroencephalography front-end has integrated high-pass filters for baseline wander removal [133] [134]. However, these papers only focused on

baseline wander removal, with a cut-off frequency much less constraining than in the BCG case (5 and 0.05Hz for EEG and BCG respectively).

While synthesizing the feedback signal, a saturation is implemented to respect Equation (10).

$$0 < G.[Vin - f(Vin)] + Vref < 3.3 \tag{10}$$

2.5.2.3. Digital filters and implementation

To remove the undesired signal components, two types of digital linear filters have been investigated: finite impulse response (FIR); and a cascade of second-order infinite impulse response (IIR) filters, defined in Figure 48 and commonly known as a cascade of biquadratic filters. FIR and biquadratic filters are respectively defined by Equation (11) and Equation (12), where n is the sample index, x and y are the input and output signals, N is the number of coefficients, $\{a_n\}$ and $\{b_n\}$ are the feedback and feedforward coefficients.

$$y[n] = b_0.x[n] + \cdots + b_{N-1}.x[n - N + 1] \tag{11}$$

$$y[n] = b_0.x[n] + b_1.x[n-1] + b_2.x[n-2] + a_1.y[n-1] + a_2.y[n-2] \tag{12}$$

By convention, a_0 is set to 1.

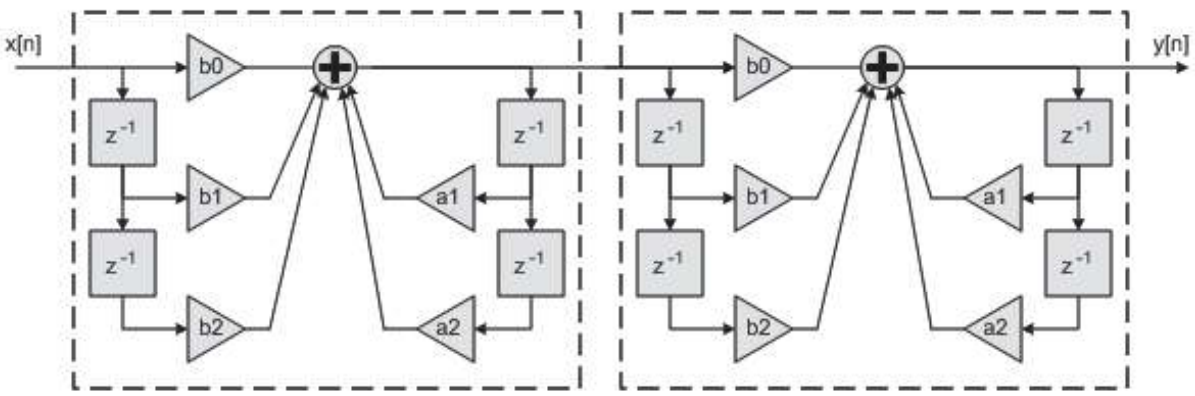

Figure 48: Example of a 4th order IIR filter, a cascade of two biquadratic filters, as implemented by the CMSIS DSP library.

Filter coefficients are computed using the *scipy.signal* Python library on a 64-bits computer. They must be quantified to 32-bits coefficients before being implemented on the DSP, which may generate errors, especially for IIR filters with high constraint filters and very low cut-off frequency. For example, Figure 49 illustrates the quantization of poles for a second-order Butterworth filter with a 0.05 Hz cut-off frequency and a 256 Hz sampling rate.

A

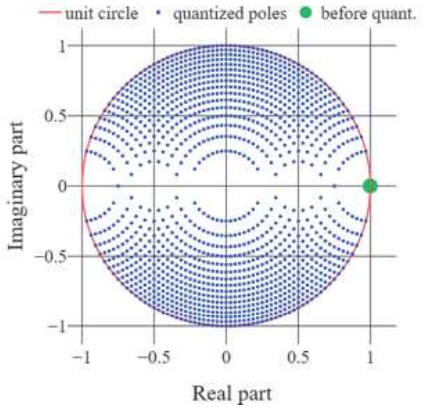

B

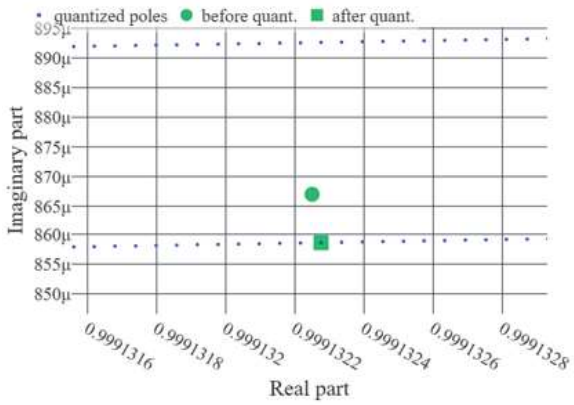

Figure 49: 6 bits poles distribution (A) ; 64 bits to 32 bits quantization of a pole (B).

This coefficient quantization is likely to modify the frequency response of the filter, e.g. the bandpass gain as illustrated in Figure 50 using the same filter as in Figure 49. After quantization, the bandpass gain was systematically corrected to 0 dB using Equation (13).

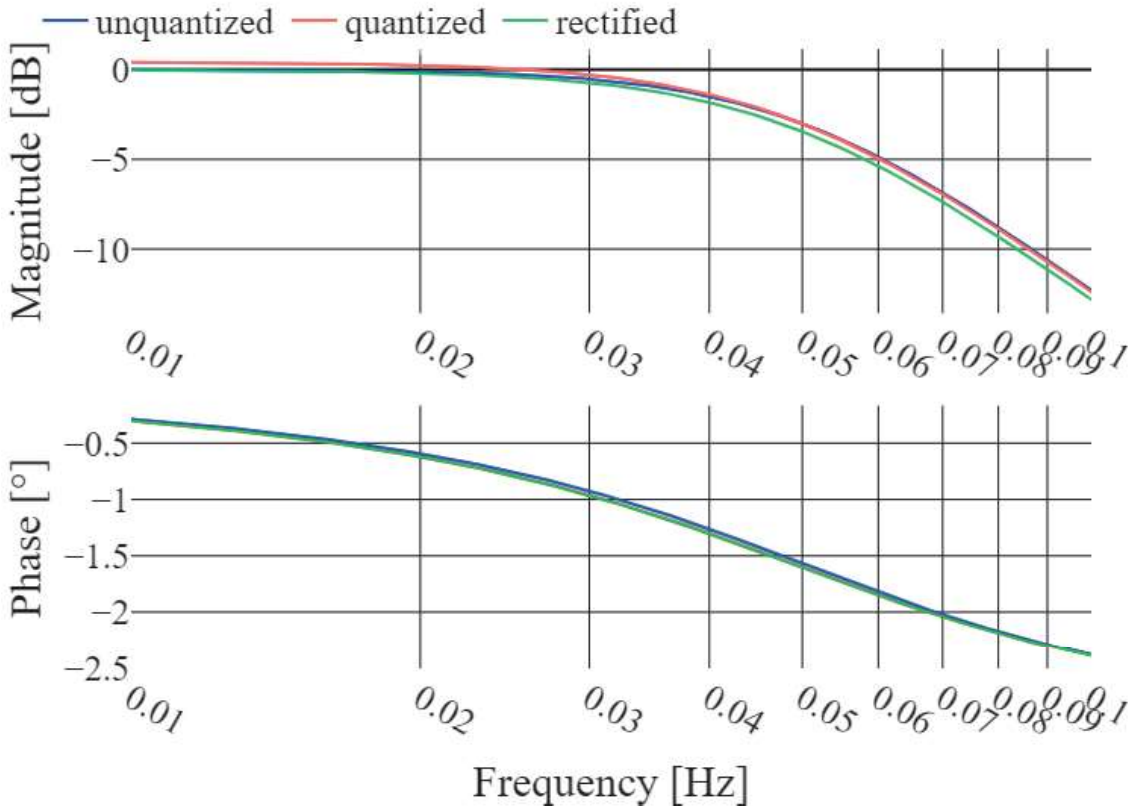

Figure 50: Effect of quantization and passband rectification.

$$b'_n = b_n \frac{\sum a_i}{\sum b_j} \tag{13}$$

The settling time of the filters depends on initialization. The state of the filter is usually initialized to zero: the signal is thus causal. However, the sensor has a rest position that is known or can be estimated. It may be assumed that the accelerometer is laid flat on the mattress which is itself horizontal: the Z-axis should see approximately a +1 g offset value, so 2.31 V in this setting. The filter is initialized considering that the signal is 2.31 V before starting the record.

2.5.3. Baseline wander removal

2.5.3.1. Method

A commonly undesired component of the physiological signal is the baseline wander. It is a low-frequency component that prevents a high gain amplification. In

ballistocardiography, the baseline wander is a voltage offset depending on the body position and weight in the bed. For example, during a patient position shift, the accelerometer orientation and the gravity projection on the accelerometer axes change. We observed that this offset value ranges typically from 0.1 to 0.5 g, for which the amplifier would saturate with $G > 3\,dB$.

The respiration, whose frequency ranges from 0.5 to 1.0 Hz in neonatology [135] and down to 0.1 Hz in geriatrics [130], can be considered either as a part of the baseline wander or as a useful component of the signal. In this work, the respiration is not filtered, consequently, the cut-off frequency of the baseline wander filter is set at 0.05 Hz and f is a low pass filter defined by Equation (9).

In the FIR case, the window method is applied with a Kaiser window of 40 dB minimal attenuation in the passband and a 0.1 Hz transition bandwidth. The resulting FIR filter has 5716 coefficients. In the IIR case, a second-order Butterworth filter, chosen because of its maximally flat response in the passband, is designed and repeated twice to sharpen the transition. In this work, the selected filter is this fourth-order IIR filter, because the FIR filter is too computation-expensive for the microcontroller.

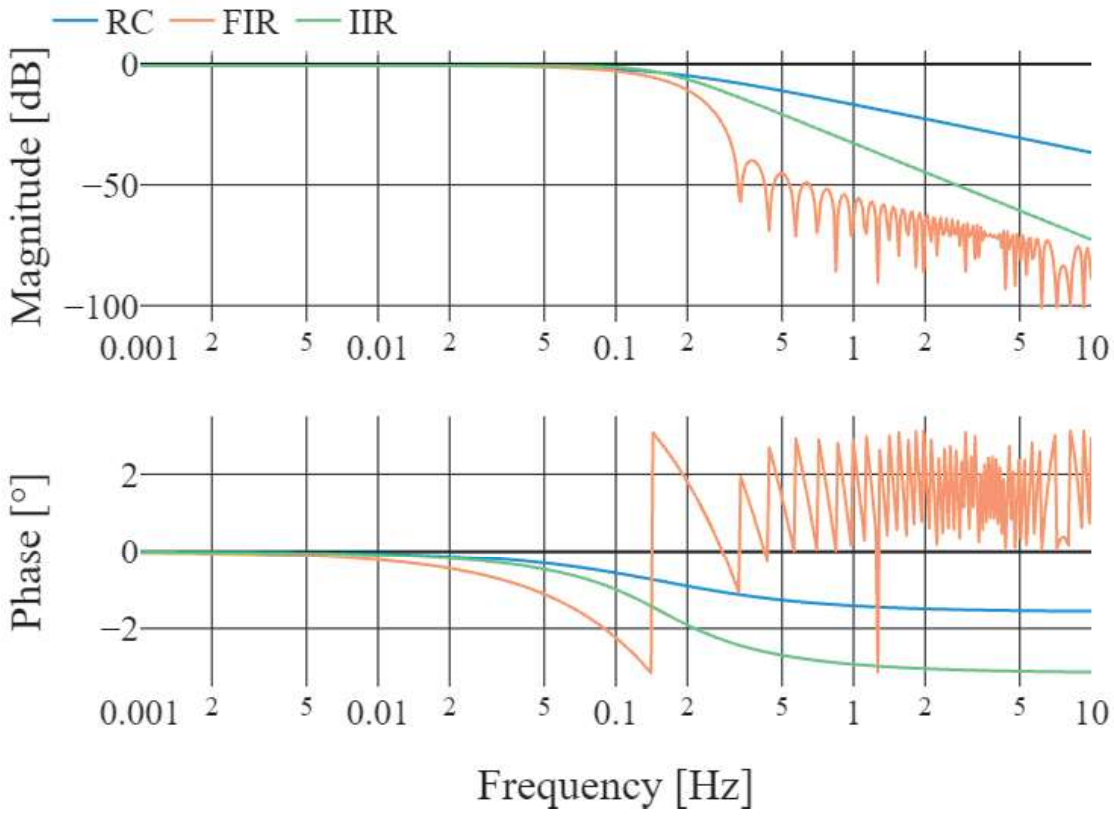

Figure 51: Frequency responses of the lowpass equivalent of the designed filters and the typical analog RC filter.

Figure 51 illustrates the responses of the designed FIR and IIR filters low pass equivalent. They are compared to a typical first-order resistor-capacitor (RC) filter with the same cut-off frequency.

Furthermore, a gain of 21 dB is set in the experiment. The high-pass equivalent filter finally has the following numerator and denominators in

Table 8. It is defined by Equation (14), Equation (15), and Equation (16).

$$V_{out} = g(Vin) \tag{14}$$

$$a'_n = a_n \tag{15}$$

$$b'_n = G.(a_n - b_n) \tag{16}$$

Table 8: Numerators and denominators of the high-pass equivalent filter.

a0	1

a1	-1.9982646
a2	0.99826604
b0	11.183295
b1	-22.3472
b2	11.163904

2.5.3.2. Results

The IIR filter succeeds in filtering the baseline wander, and it is removed by the amplifier. At steady state, the maximal peak to peak amplitude of the pulses is ten times higher on the output than on the input. Figure 52: Illustration of baseline wander removal with 21 dB amplification. Figure 52 is an illustration of the signal before and after the amplifier with pulses amplitude below the noise level.

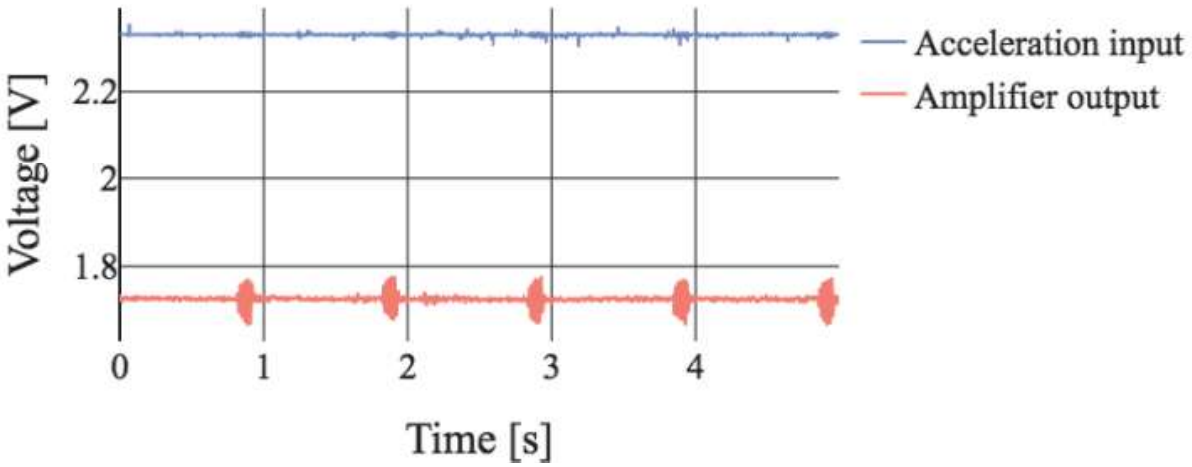

Figure 52: Illustration of baseline wander removal with 21 dB amplification.

Using this filter, vibrations at different constant frequencies are generated and the measured accelerations are compared before and after filtering and amplification by their root-mean-square values. The experimental frequency response is compared to the designed filter in Figure 53.

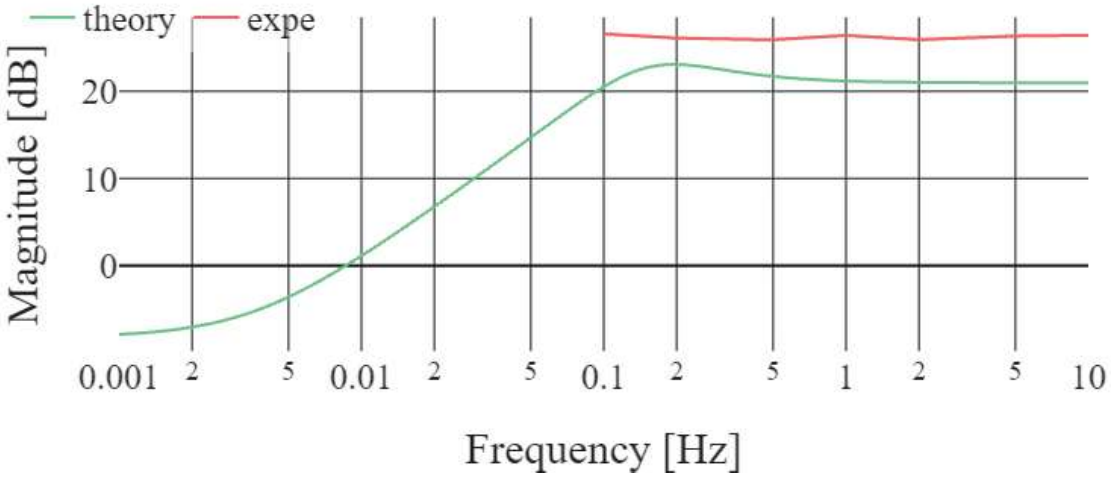

Figure 53: Comparison of frequency responses for a 21 dB gain, quantized IIR versus experimental points

2.5.3.3. Settling time comparison

Signals were recorded at different initialization settings. Figure 54 is a superposition of two signals at different times, with 0 V and 2.31 V offset initialization. When the state of the filter is initialized at 0 V, the amplifier can saturate for decades of seconds, which is not the case if the offset is well estimated.

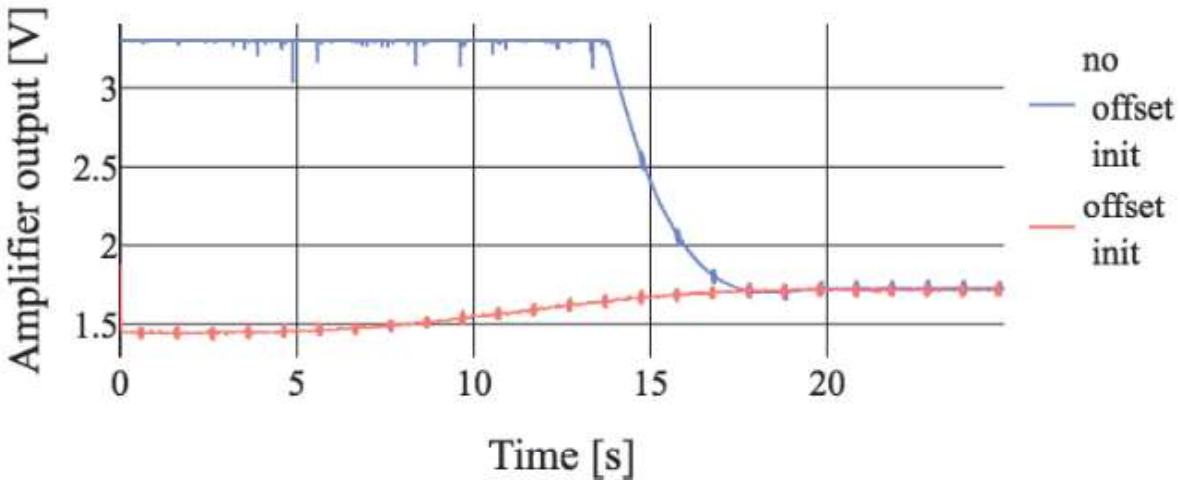

Figure 54: Effect of offset initialization on settling time.

The settling time depends on offset initialization, as illustrated in Figure 55.

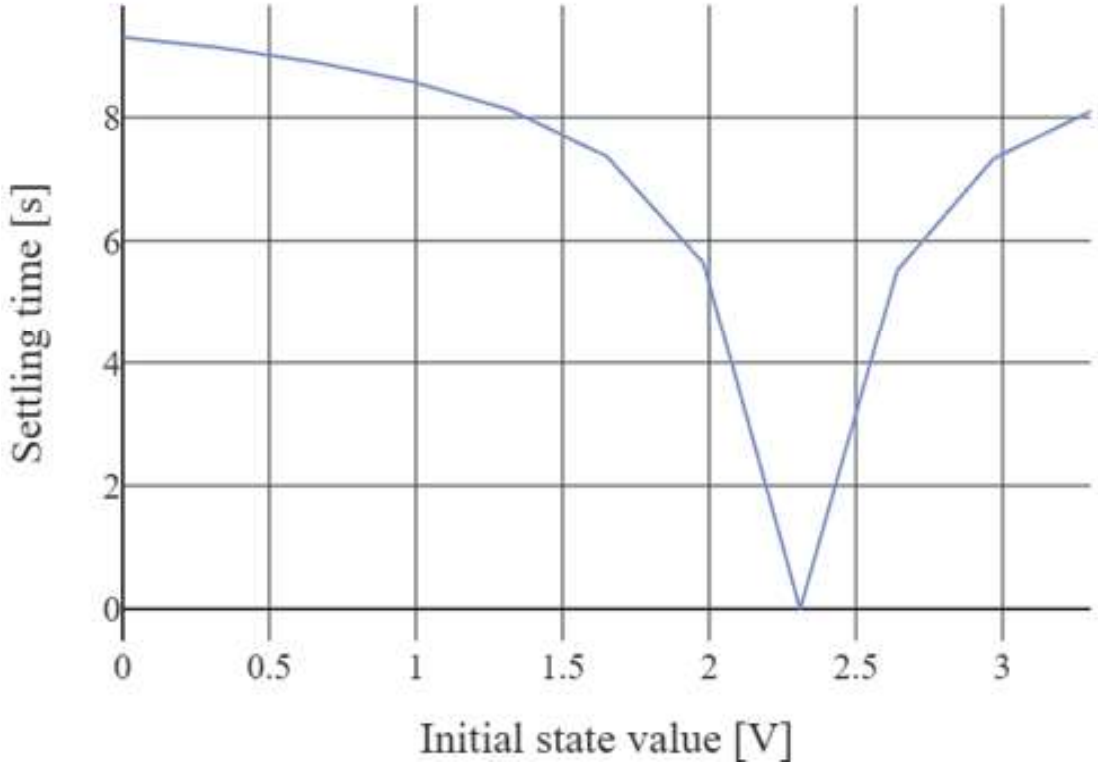

Figure 55: Settling times for different offset initialization with a 21 dB amplification.

2.5.4. Noise frequency identification and filtering

2.5.4.1. Method

The noise frequency is identified and filtered using the embedded algorithm detailed in Figure 56, where the signal stands for the amplified signal.

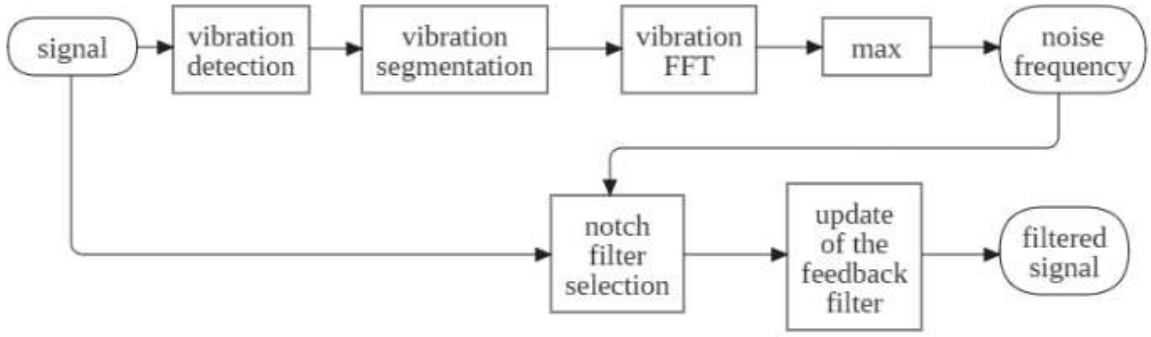

Figure 56: Noise frequency identification and filtering pseudo-algorithm.

The vibration detection step is parametrized by a voltage threshold, hereafter referred to as threshold, over which the vibration is detected. The vibration starts there and has a fixed duration. The power spectral density of the segmented vibration is computed by the

microcontroller. Its maximum is located at the noise frequency so that it is outside the BCG frequency range, otherwise, the heartbeats in the BCG signal would be distorted or filtered.

Several notch filters, with Q=0.707 quality factors, have been previously computed using the *scipy.signal* library outside the microcontroller. The notch filter whose frequency is the closest to the noise frequency is selected and added to the IIR baseline wander filter.

2.5.4.2. Results

The threshold and duration were set at 1.5% of the baseline wander and 0.25 seconds respectively. The noise was generated by pulsed vibration, i.e. the simulated BCG. The noise frequency determined by the microcontroller is approximately 68 Hz, as can be seen in Figure 57. This is the resonant frequency of the damping system.

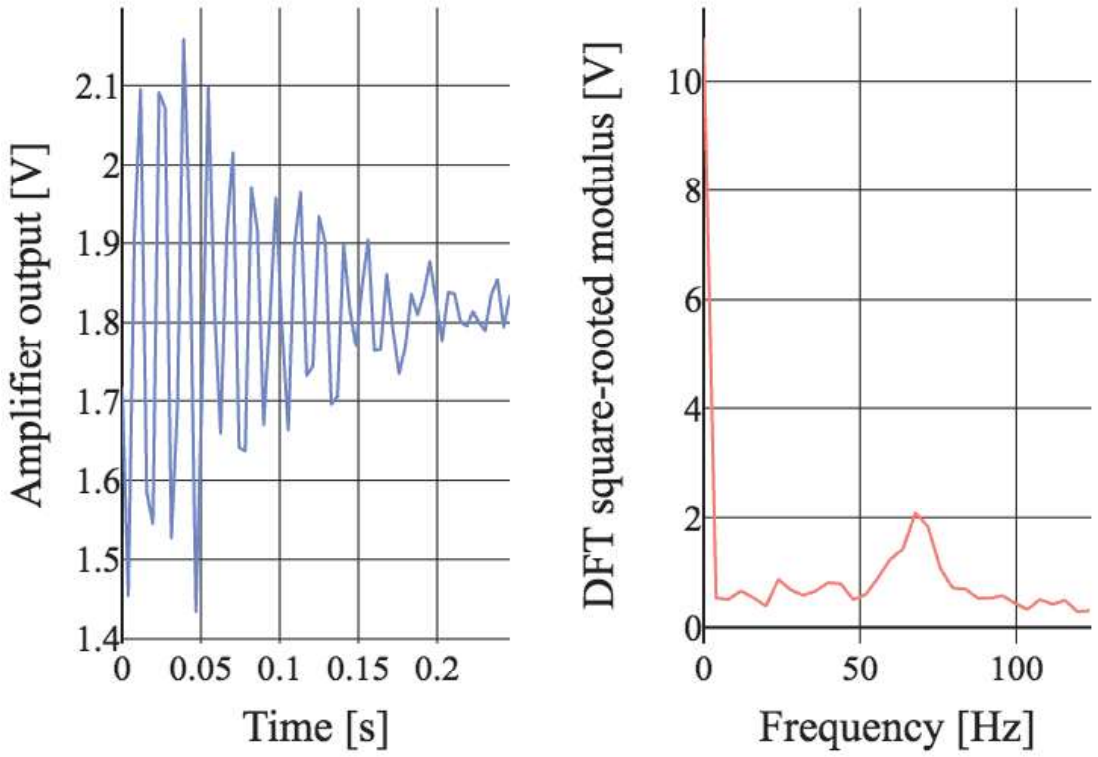

Figure 57: Example of a simulated BCG pulse and its single-sided frequency spectrum computed by the microcontroller.

A notch filter was then selected by the algorithm illustrated in Figure 56 to filter the identified noise frequency.

2.5.5. Conclusion

This work introduced a novel smart BCG front-end which identifies the system resonance frequency, filters the baseline wander and the damping noise, and amplifies the BCG signal without saturation after patient movement.

During the experimentations, a limited 21 dB gain was used for illustrating the principle of the smart BCG front-end. Higher gains resulted in noisy signals and saturation, due to the use of prototyping boards rather than a specific electronics circuit with a proper ground plane. In the future, an amplifier with a higher gain will be designed and tested on real patients.

Compared to usual BCG instrumentations, this conditioning circuit has a lower settling time and a sharper frequency transition. The principle of a smart BCG front-end has been demonstrated; it opens possibilities for medical, real-time, and low-cost applications.

Chapter 3

3. Digital signal processing in ballistocardiography

Ballistocardiograms contain much physiological information: the motor, respiratory and cardiac activities, and sleep cycles. Since the patients are likely to get out of bed at night, it may be important to detect occupancy as well. A typical ballistocardiogram is illustrated in Figure 58 with different periods: movement, absence, and presence. In presence segments, the ballistocardiogram contains vital signs such as respiratory and heart rates, or fiducial points of respiratory and cardiac activities, that need to be detected by specific algorithms.

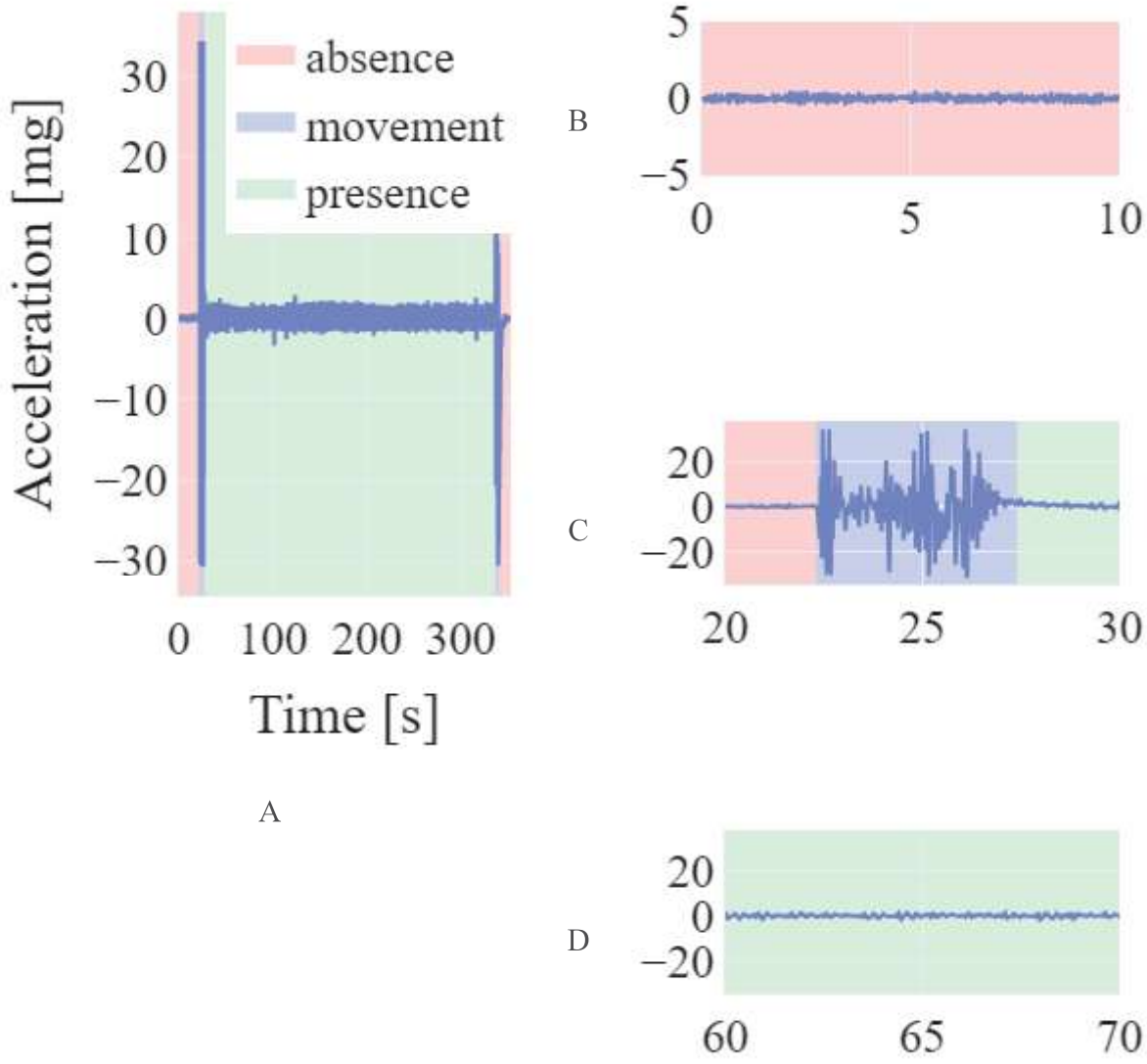

Figure 58: Typical ballistocardiogram (A) with absence (B), movement (C), and presence (phases).

In this chapter, we introduce ballistocardiographic databases that were acquired during this thesis, as no public database was available – see Section 3.1. A typical digital signal processing workflow is illustrated in Figure 59, for motion-free BCG segmentation – see Section 3.2 - and heart and respiratory rates detection - see Section 3.3. In each of these sections, we will review the existing digital signal processing algorithms, and detail novel algorithms that we developed to detect the physiological information contained in ballistocardiograms.

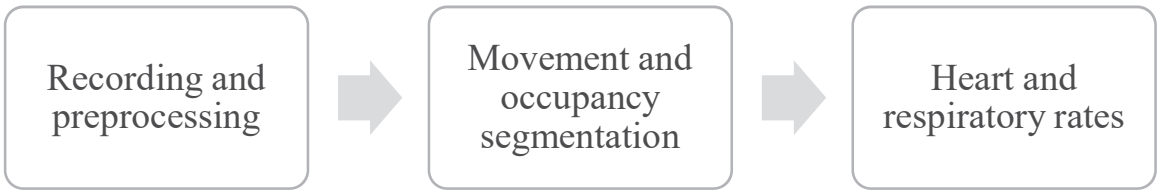

Figure 59: Workflow of BCG digital signal processing algorithms.

3.1. Recording and preprocessing of ballistocardiographic databases

Before developing digital signal processing algorithms for segmenting ballistocardiograms and detecting vital signs, databases were recorded. The databases presented in this section contain raw ballistocardiograms and reference vital signs. The reference vital signs were obtained either with reference instrumentation (e.g. ECG) or with labels that were manually checked by two experts. For example, the I, J, and K fiducial points of the raw ballistocardiograms were computed using [128] and annotated in the databases. Reference heart rate series are reconstructed using these annotations.

These databases are stored in a private server in the standardized EDF format [136], which was developed in 1992 and improved in 2002 for storing efficiently polygraphic databases.

All the processes for these data acquisitions have been validated by an ethical commission in conformity with the European data legislation.

The databases are summarized in Table 9.

Table 9: Summary of the BCG databases.

Database	CHArt	LSI	Ollie	R2P2
Number of patients	27	336	130	40
Age	Adults	Mostly children	Adults	Neonates
Number of records per patient	1	1	183	1
Length of records	20-50 min	35 seconds	1 night	1 night
Ballistocardiograph	Murata SCA11H	Fealing Biopac BCG module	Ollie	Fealing Wireless BCG module
Other signals	No	No	PSG and other BCG for ≈ 30 patients	Clinical ECG and SPO2
Status	Complete	Complete	Started	Starts in 09/2020

In the next sections, those databases are described.

3.1.1. CHArt

The CHArt ballistocardiographic database was acquired in one of the Ecole Pratique des Hautes Etudes offices. Healthy adults volunteering employees of the laboratory were asked to rest for 20 to 50 minutes at lunch break, in a supine position. We used an MM0 3000 [137] medical bed and an MMO Aerospacer overlay [138]. A Murata SCA11H BCG sensor - see Section 2.1.3.1 - was placed on top of the overlay, in the head-to-foot direction. The materials are shown in Figure 60.

27 volunteers were accidentally not asked to stay still and quiet. Therefore, many records were polluted by motion artifacts and were discarded from the database. In the end, the CHArt database includes 10 healthy adults for 20- to 50-minutes long records.

A B C

Figure 60: MMO 3000 medical bed (A), Aerospacer mattress (B) and SCA11H sensor on overlay (C)

3.1.2. LSI

This acronym stands for “La Science Infuse”, a one-week long event of the Cité des Sciences et de l’Industrie in Paris, France, which aims at vulgarizing science to the public. Volunteers, recruited among the public, were asked to lie down and quiet in the supine position for 35 seconds.

Figure 61 shows the setup of the experimentation during the LSI database acquisition. The Fealing Biopac BCG module is used for ballistocardiogram recordings in the left-right direction – see Section 2.2. For pedagogical purposes, ballistocardiograms were displayed in real-time on a screen and another visitor, usually a friend or a relative of the volunteer, was asked to clap his hands in front of a microphone as soon as a “W” waveform, i.e. a heartbeat, appeared on the ballistocardiogram. The ballistocardiograph and microphone were synchronously acquired on a BIOPAC MP36 unit, detailed in Section 2.2.2.3.

The bed used for this experimentation is constituted of a slatted solid pine wood Ikea® Sniglar infant home bed and a firm latex polyurethane Tediber® Tedi mattress of 70x140 cm dimensions. The sensor is placed on top and 5 cm away from the mattress side.

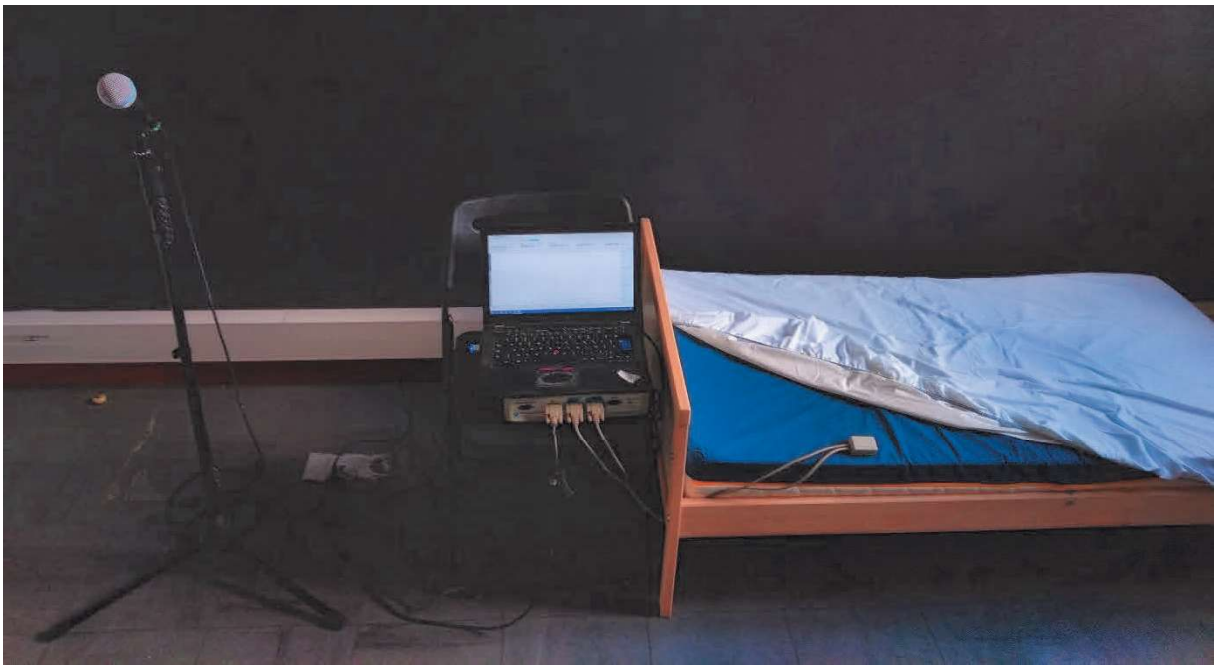

Figure 61: Setup for the LSI database acquisition

Only children were originally targeted for this study, with parental consent; however, accompaniers and adult visitors were also willing to take part in the study. The authors found it interesting to recruit them and compare adults with children BCG in further physiological studies. For subjects taller than 140 cm, the bed size was not appropriate, and legs were uncomfortably out of the bed. That did not seem to alter the quality of the recording, as long as the subjects were still.

In total, 336 subjects were recorded; however, many records were discarded because signals were polluted by motion artifacts as children had difficulties in concentrating not to move or talk. In the end, 40 subjects are included, with ages ranging from 8 to 74.

3.1.3. Ollie

The Ollie database is related to the name of a Fealing product, consisting of a bedding waveguide amplifier to be put around the mattress as in Figure 45. Every night, the volunteer attaches his or her phone on the waveguide magnet and runs a recording with the Ollie application. The first mobile app version of Ollie is named SleepLogger: the two interfaces

are shown in Figure 62. It is only available on iOS and in French via TestFlight for beta testing.

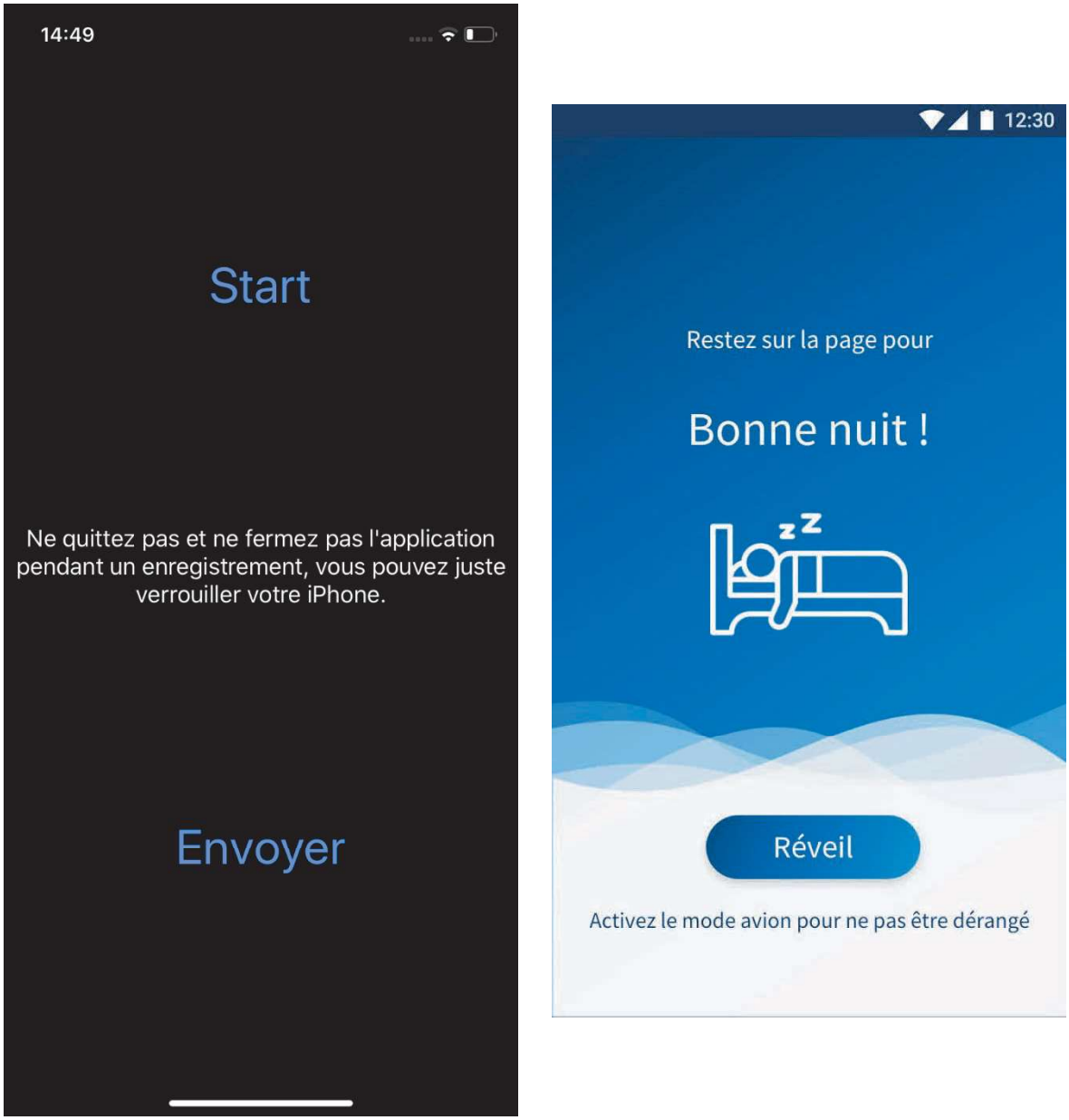

A B

Figure 62: Recording page on SleepLogger (A) and Ollie (B) mobile applications

When possible, an EMFIT QS BCG sensor is used for recording raw ballistocardiograms and vital signs and compare them with the Ollie system. A sleep study on 30 athletes is also about to be conducted with this system and reference polysomnographic

measurements with Dreem headbands and more traditional portable polysomnographs in the Institut National du Sport, de l'Expertise et de la Performance (INSEP).

Until today, five persons have been recorded their nights for a week with this setup. Besides the INSEP part of the Ollie database, Fealing is launching a research program to record ballistocardiograms of 100 volunteers for 6 months in ecological conditions.

3.1.4. R2P2

The R2P2 database is related to the "Réanimation Pédiatrique de l'hôpital Raymond Poincaré", the pediatric intensive care unit (PICU) that hosts this database acquisition in Garches, France. The objective of the initial study is to confront BCG measurements of healthy and diseased neonates to the ECG and SPO2 clinical measurements, to see if BCG is relevant for neonatal physiological monitoring in the hospital environment. Figure 35 and illustrates the setup used: the Fealing Biopac BCG module is synchronized with the SPO2 and the ECG analog outputs from the Nihon-Kohden multiparameter scope.

Figure 63: Setup of R2P2 database acquisition

The study will begin in September 2020 at Assistance Publique des Hôpitaux de Paris. 40 neonates will be recruited from the patients hospitalized for at least one night in the PICU.

3.1.5. Preprocessing

Before further processing, such as motion and occupancy segmentation and vital signs detection, all the signals contained in the previous databases need to be pre-processed. They are filtered with third-order Butterworth filters, specifically a 25 Hz low-pass filter and a 2 Hz high-pass filter. They are chosen because of their flat bandpass and are applied forward and backward to prevent phase distortion. A 25 Hz cut-off frequency for the low-pass filter is indeed the limit not to distort the signal and affect the RJ time intervals [139].

3.1.6. Signal-to-noise ratio

All the signals in the databases are qualified by their signal-to-noise ratio (SNR), which helps quantify the noise in heartbeats measured by ballistocardiographs. This metrics is very important as the BCG signal may be noisy, in case of movement artifacts or external vibrations.

The signal-to-noise ratio of physiological signals is uneasy because of their spectral variabilities. In the literature, several papers address this issue with a focus on ballistocardiography. They are computed after heartbeat detection.

In [140], the sample correlation coefficient as defined in Equation (17) and is used for SNR estimation in Equation (18).

$$r = \frac{\frac{1}{L}\sum_{n=1}^{L}\left(x_j[n] - \overline{x_j}\right)\left(x_k[n] - \overline{x_k}\right)}{\sqrt{\frac{1}{L}\sum_{n=1}^{L}\left(x_j[n] - \overline{x_j}\right)^2 \frac{1}{L}\sum_{n=1}^{L}\left(x_k[n] - \overline{x_k}\right)^2}} \quad (17)$$

$$SNR_r = \mathrm{A}\frac{r}{1-r} + B \; with \begin{cases} A = \exp\left(\frac{-2}{L-3}\right) \\ \mathrm{B} = -\frac{1}{2}\left(1 - \exp\left(\frac{-2}{L-3}\right)\right) \end{cases} \quad (18)$$

In [141], a noise-free signal is generated and compared to the signal using Equation (19).

$$\mathrm{SNR}(\boldsymbol{x}) = \frac{\sum_{n=0}^{N-1}(\tilde{x}[n])^2}{\sum_{n=0}^{N-1}(\tilde{x}[n] - x[n])^2} \quad (19)$$

3.1.7. ECG synchronization

Some of the signals, e.g. in the R2P2 database, in the previous databases, are synchronized with reference physiological signals such as ECG.

A

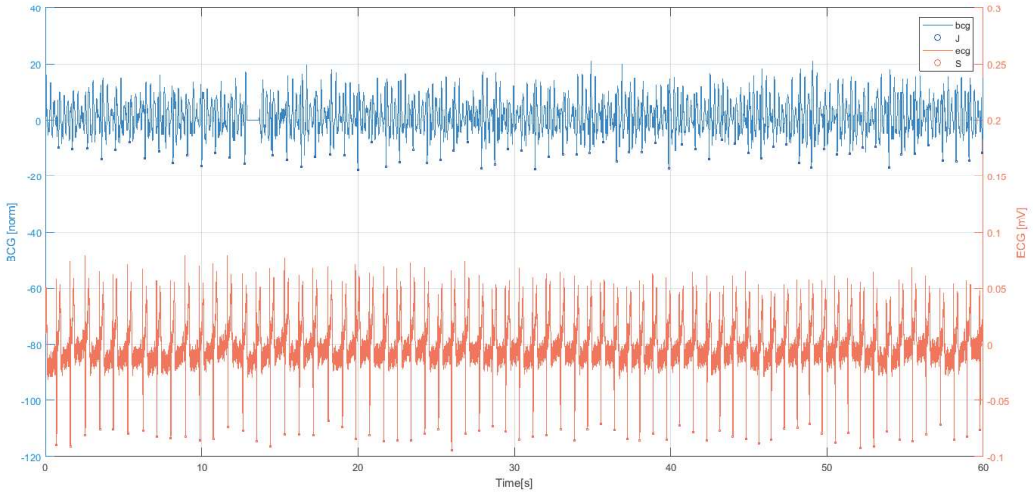

B

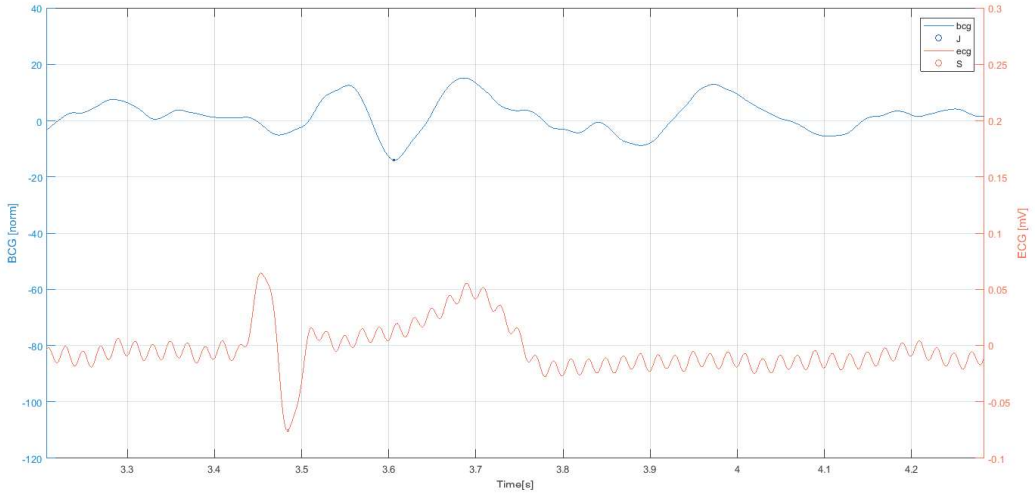

Figure 64: Synchronization of the Biopac ECG with the Murata SCA11H BCG

Synchronizing signals that are digitized on acquisition units that do not share the same clock is often an issue in signal processing. One of the ways to synchronize such signals or channels is to generate an event that can be read on both channels. In the case of ballistocardiograms and electrocardiograms, quick pressure on the electrode will induce a motion artifact that will also appear in a ballistocardiogram. Figure 64 shows a one-minute long BCG using the SCA11H Murata sensor thus synchronized with ECG, acquired on the Biopac MP36.

Delays between heartbeats measured by both channels are consistent with the literature: approximately 130 ms between the QRS complex of the ECG and the J peak of the BCG.

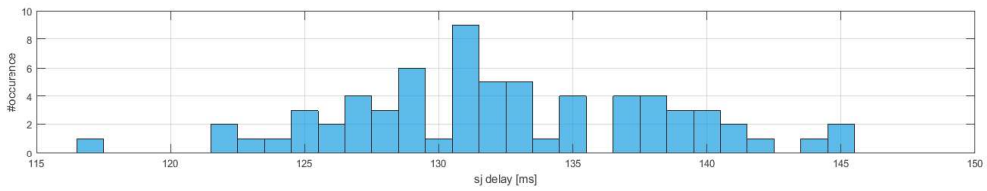

Figure 65: SJ delays distribution in a 1-minute long recording.

For recordings longer than one hour, it is also important to take care of the sampling frequency drift that is likely to be different on two different acquisition units. Thus, it seems necessary to regularly generate synchronization events.

Another way is to correlate information in the signal, e.g. heart rate series derived on the one hand by ECG, on the other hand by BCG. This will be used later, e.g. with the Fealing Wireless BCG module.

3.2. Movement and occupancy segmentation

After having recorded and preprocessed the signals, they are segmented by their motion and occupancy characteristics following the signal processing workflow of Figure 59.

The motor activity is useful to monitor neuromotor or sleep pathologies, e.g. epilepsy or parasomnias. More generally on healthy patients, it is correlated to certain sleep phases and is used for evaluating hypnograms during actimetry exams [142] [143]. Moreover, movements are artifacts that may saturate ballistocardiograms, which must often be segmented into motion-free periods to detect physiological signs such as heartbeats and heart rate.

Therefore, movements must be detected before any other physiological parameter in raw ballistocardiograms. In the next sections, the state of the art algorithms for motion and occupancy segmentation are detailed – see Section 3.2.1; then typical features for clustering and classification are listed – see Section 3.2.2; novel algorithms are developed in Section 3.2.3; finally state of the art and novel algorithms are compared on the databases listed in Section 3.1.

3.2.1. State of the art

In this section, the algorithms of the literature for motion and occupancy segmentation are detailed: the fixed threshold, the signal variance, derivatives, and signal amplitude and noise reference methods.

3.2.1.1. Fixed threshold

Detecting movements in ballistocardiography is not a challenge, as many algorithms have already been developed in actigraphy.

In actigraphy, time series are divided into fixed-size epochs on which the motor activity is quantified by one of the following metrics: TAT or time above threshold, ZCM or zero-crossing mode, and PIM or proportional-integral mode, respectively defined by Equation (20), Equation (21) and Equation (22). There are multiple ways to estimate zero-crossing; only an algebraic approach is explained here [144]. Before these computations, accelerometer raw data are usually band-pass filtered from 0.25 Hz to 2-3 Hz, which defines the following $x(t)$ time series.

$$TAT(t, threshold) = \int_{t-T/2}^{t+T/2} y(u)du$$
$$with\ y(t) = \begin{cases} 1\ if\ x(t) \geq threshold \\ 0\ elsewhere \end{cases} \quad (20)$$

$$ZCM(t) = \int_{t-T/2}^{t+T/2} w(u)du\ \ with\ w(t)$$
$$= \begin{cases} 1\ if\ \dfrac{d^2(x-|x|)}{dt^2}\dfrac{d^2(x+|x|)}{dt^2} = 0 \\ 0\ elsewhere \end{cases} \quad (21)$$

$$PIM(t) = \int_{t-T/2}^{t+T/2} x(u)du \quad (22)$$

A

B

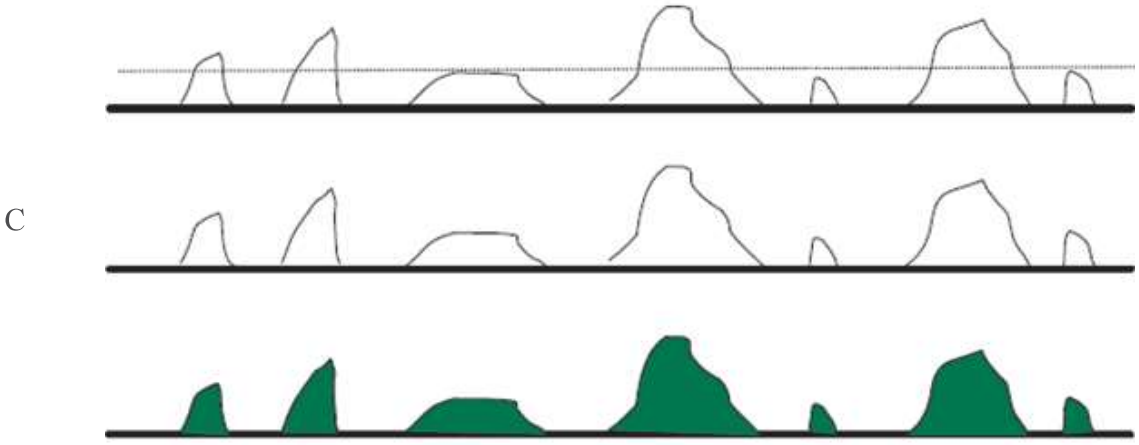

Figure 66: Illustration of the most common actigraphy metrics : TAT or time above threshold (A), ZCM or zero crossing mode (B), PIM or proportional integral mode (C)

These three metrics are illustrated in Figure 66. In the TAT method, the threshold for detecting movement is commonly 0.1 to 0.2 g: a basic algorithm segmenting movement when the BCG raw data exceed this threshold is a good start. However, compared to actigraphs, ballistocardiographs are not worn at the user's hand so the measured acceleration might be attenuated. Nevertheless, calibration is likely to overcome this issue and permit fixed-threshold movement detection.

Fixed-threshold motion artifacts detection methods have also been widely used in ballistocardiography [145] [146] [46], though they might not be perfectly detected, even in case of manual calibration.

The threshold can also apply to the amplitude range, i.e. the difference between the minimum and the maximum amplitude of the signal in a moving window [147].

The distribution f of the data x, filtered in the 0.5 to 25 Hz range to remove respiratory components, is different between motion-free and motion-polluted segments as seen in Figure 67; this distribution difference can be exploited to detect motion artifacts [148]. Alivar showed in 2017, through a sequential detection algorithm, that 1-second long BCG segments could be classified in one of those categories using the Neyman-Pearson test of

Equation (23) hypotheses, where (μ_0, σ_0) and (μ_1, σ_1) are the mean and standard deviation of the fitted Gaussian distribution of motion-free and motion-polluted segments respectively.

$$\begin{cases} H_0: f(x) = \dfrac{1}{\sigma_0\sqrt{2\pi}} e^{-\frac{1}{2}(\frac{x-\mu_0}{\sigma_0})^2} \\ H_1: f(x) = \dfrac{1}{\sigma_1\sqrt{2\pi}} e^{-\frac{1}{2}(\frac{x-\mu_1}{\sigma_1})^2} \end{cases} \tag{23}$$

The log-likelihood ratio LLRT is defined by Equation (24) for every 1-second long BCG segment x, where N is the number of samples in x. Two thresholds A and B, defined in Equation (25), help classify this segment into a motion-free category when $LLRT(x) \leq B$, motion-polluted category when $LLRT(x) > A$ or motion-unknown category when $B < LLRT(x) \leq A$.

$$LLRT(x) = \log\frac{p(\boldsymbol{x}; H_1)}{p(\boldsymbol{x}; H_0)} = N.log\left(\frac{\sigma_0}{\sigma_1}\right) + \frac{\sum_{i=1}^{N}(x_i - \mu_0)^2}{2\sigma_0^2} - \frac{\sum_{i=1}^{N}(x_i - \mu_1)^2}{2\sigma_1^2} \tag{24}$$

$$\begin{cases} A = \log\left(\dfrac{desired\_sensitivity}{1 - desired\_specificity}\right) \\ B = \log\left(\dfrac{1 - desired\_sensitivity}{desired\_specificity}\right) \end{cases} \tag{25}$$

Setting the desired sensitivity and specificity to 90%, the sequential detection algorithm from Alivar performs motion detection with actual sensitivity and specificity of 97%. However, the dataset includes a single child and is prone to inter-individual variability.

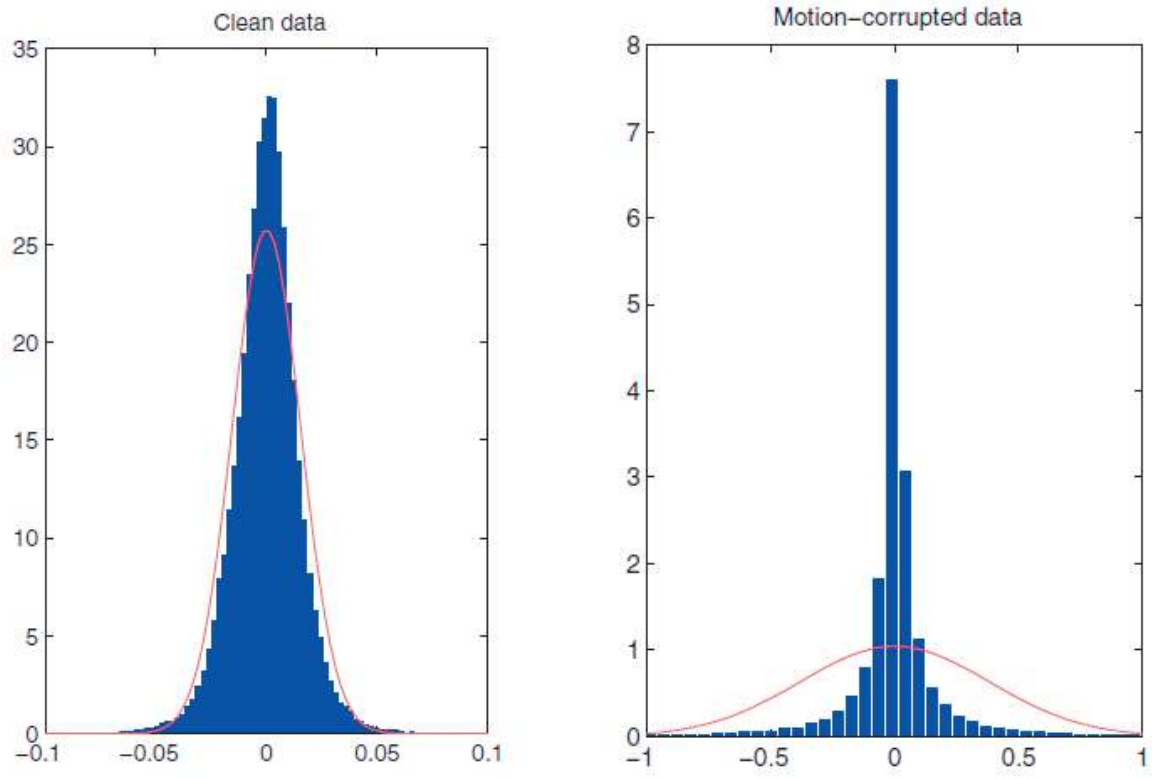

A B

Figure 67: Amplitude distribution of motion-free (A) and motion-polluted (B) ballistocardiograms of an individual [148]

The fixed signal method is interesting but lacks robustness for motion segmentation.

3.2.1.2. Signal variance

The fixed-threshold method has been extended to the signal variance over sliding time windows. The duration of this window is typically set from 1 [149] to 4-5 seconds [65] [150]. In the latter reference, the threshold is precisely fixed at the standard deviation of the whole ballistocardiogram: if the standard deviation of a 5-seconds long segment exceeds the global standard deviation, the segment is classified as a motion-polluted segment.

Pino proposed in 2015 to compute two metrics T1 and T2, defined by Equation (26) and Equation (27), that mix mean, standard deviation, minimum and maximum at every 1-second long segment x. If T1(x) is greater than T2(x), the segment x will be detected as a motion-polluted segment [149].

$$T1(x) = \frac{max(x) + min(x)}{2} \tag{26}$$

$$T2(x) = mean(x) + 1.1std(x) \tag{27}$$

Watanabe relies more on the standard deviation of an envelope of 51.2 seconds-long segments, with 0 to 1 normalization of the ballistocardiogram over the whole night [70].

Alivar also tested in 2017 to fit the variance distribution of 1-second long segments to exponential models [148], as seen in Figure 68. The exponential probability functions are parametrized by the λ_0 and λ_1 rate parameters for motion-free and motion-polluted segments respectively. A Neyman-Pearson test is run for each window to find which of the Equation (28) hypotheses are realized, with y the standard deviation of the 1-second long segment x and f the density probability function of the variance of those segments.

$$\begin{cases} H_0 : f(y) = \lambda_0 e^{-\lambda_0 . y} \\ H_1 : f(y) = \lambda_1 e^{-\lambda_1 . y} \end{cases} \tag{28}$$

Setting the desired specificity to 99.5%, the desired sensitivity for motion detection is expressed by $e^{-\lambda_1 . \tau}$ with a threshold $\tau = -\lambda_0 . ln(1 - specificity)$ on the variance, above which the segment x is detected as motion-polluted. With such a setting, the Neyman-Pearson algorithm from Alivar performs motion detection with a 95% sensitivity and a specificity of 94%. Again, the dataset includes a single child and is prone to inter-individual variability.

For detection motion in PPG, Krishnan also uses a Neyman-Pearson decision rule but with Gaussian distribution of other features [151]: time-domain skewness time-domain kurtosis, and frequency-domain kurtosis. Skewness and kurtosis, i.e. the third and fourth standardized moments, of a segment x are defined by Equation (29) and Equation (30), with μ and σ the mean and standard deviation of x, and E the expectation operator.

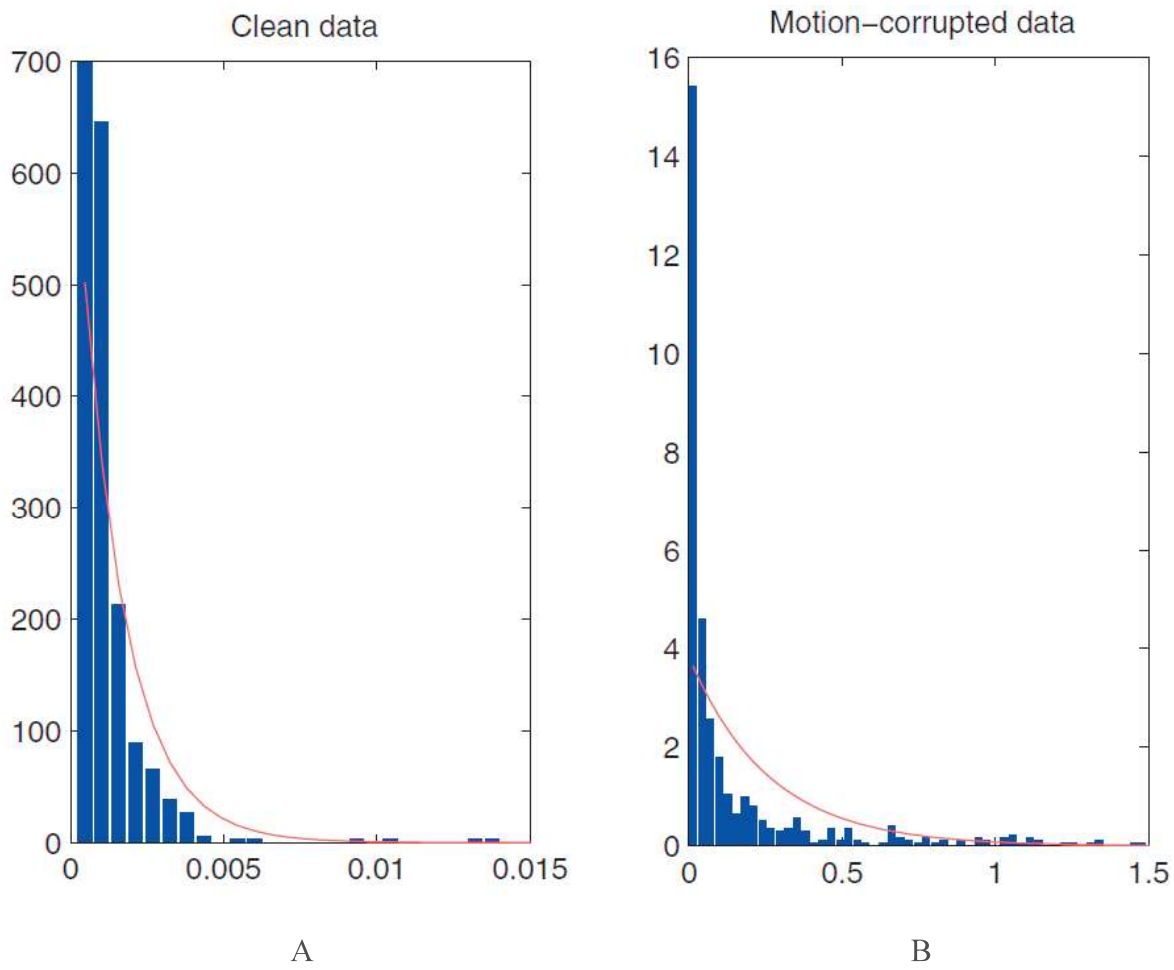

Figure 68: Variance distribution of motion-free (A) and motion-polluted (B) of 1-second long ballistocardiograms of an individual [Alivar2017]

$$skweness = E\left[\left(\frac{x-\mu}{\sigma}\right)^3\right] \quad (29)$$

$$kurtosis = E\left[\left(\frac{x-\mu}{\sigma}\right)^4\right] \quad (30)$$

These tests are fused with a quadratic-phase coupling test using the Varshney-Chair, which produces 91% sensitivity and 94% specificity over three healthy subjects' recordings.

3.2.1.3. Derivatives and signal amplitude

Instead of using signal variance or fixed threshold, derivatives and signal amplitude can be used for motion detection.

Aubert computes an activity index with the signal energy and time-derivatives, but its formula is not detailed at all [129]. This activity index is used, with minimum motion duration constraints, to segment the ballistocardiogram into motion-free intervals.

Denoising algorithms have been proposed for ECG such as linear filtering [152], wavelet denoising [153], and Bayesian filtering methods [154]; however, those physiological signals are much less sensitive to mechanical noise than ballistocardiograms, which are unusable for heartbeat measurements during movement.

3.2.1.4. An external sensor as a noise reference

Finally, one last literature example is to use an external sensor, which is robust but more complicated than a single ballistocardiogram to setup.

Several examples of movement detection or movement cancellation in ballistocardiogram come from bathroom scales ballistocardiograph experiments.

In [155], a noise reference seismic sensor near the modified scale measures vibrations and segments noise-free intervals in the ballistocardiogram.

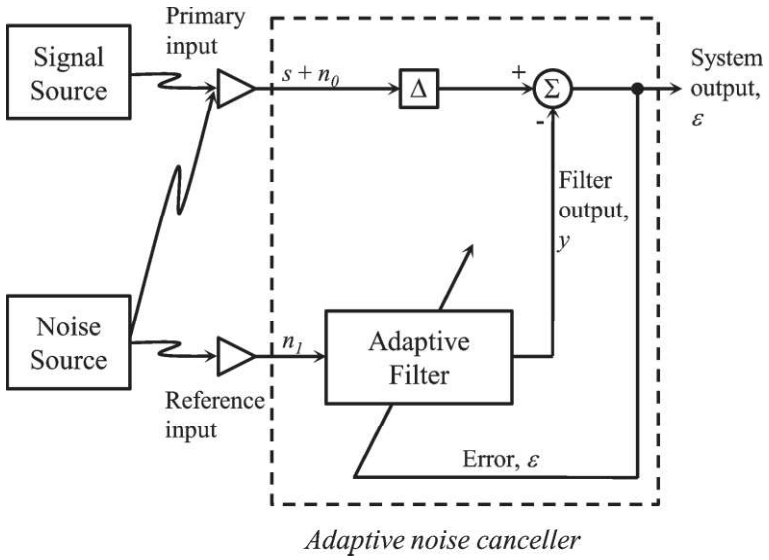

Figure 69: Adaptive noise cancellation using a noise sensor, with n1 the noise measured by the noise sensor, s the ballistocardiogram and n0 the noise measured by the ballistocardiograph

In [156], a lower-leg electromyogram (EMG) serves a movement reference: its root mean square values (RMS) are evaluated on a 10-seconds long moving window and normalized to zero mean and unity variance. Segments having a normalized RMS variance larger than unity are classified as motion-polluted segments.

3.2.2. Features

First and before applying algorithms to the entire databases presented in Section 3.1, we use the ballistocardiogram example illustrated in Figure 70. It was obtained with the CHArt database setup, detailed in Section 3.1.1, with a different measurement protocol though: the patient was asked to lie down 10-20 seconds after the start, stay still and quiet for 5 minutes, then get out of the bed. Thus, the ballistocardiogram contains the three phases that can be observed during a night: absence, movement, and presence. Presence and absence are considered to be motion-free intervals.

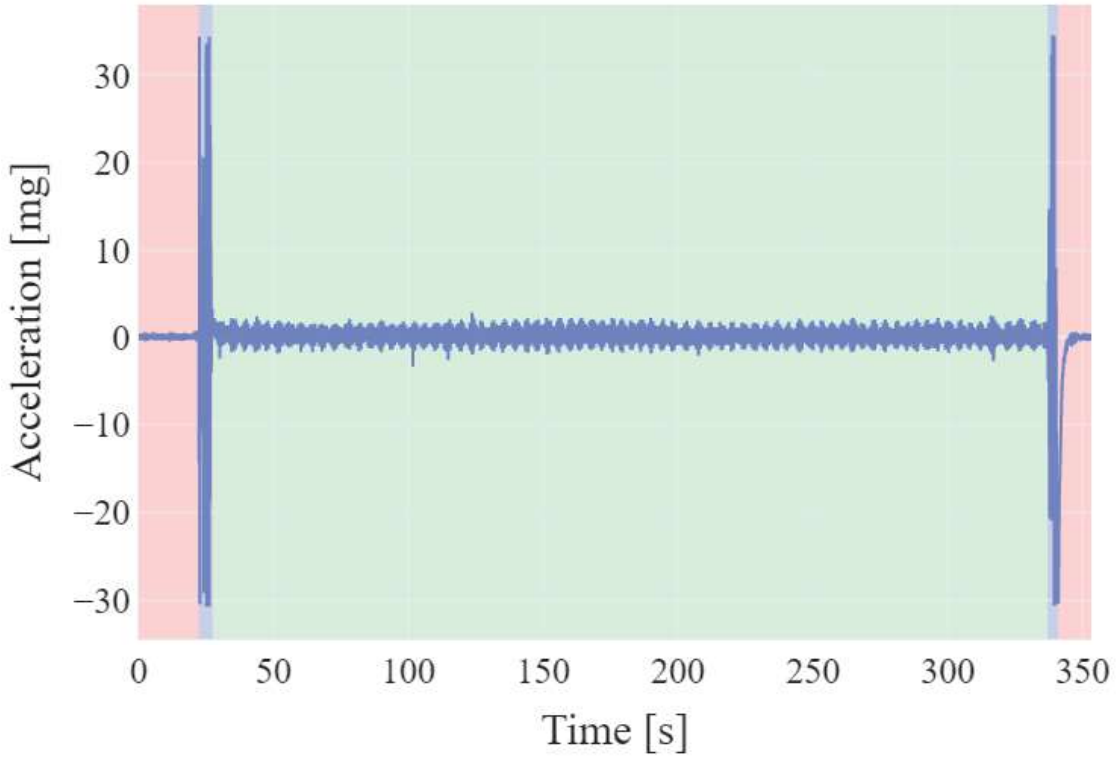

Figure 70: Typical ballistocardiogram with absence (red), movement (blue), and presence (green) phases.

Before detecting cardiac or respiratory events in the ballistocardiogram, it is necessary to select only the intervals that contain presence information. The first step in this process is to segment the movements in the ballistocardiogram, as illustrated in Figure 71.

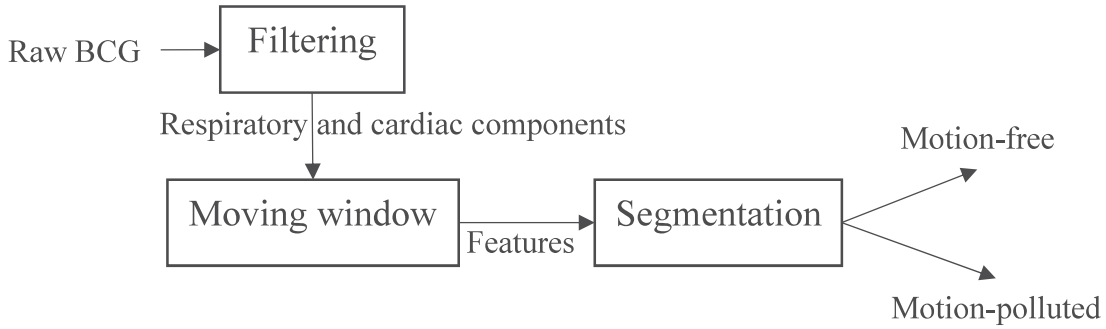

Figure 71: Motion segmentation process.

3.2.2.1. Respiratory envelope

The features that were first selected are the moving mean and standard deviation of the ballistocardiogram respiratory component. Experimentally, this component has indeed varying amplitude and offset, respectively corresponding to standard deviation and mean, through the three different phases.

The respiratory information is contained in the low-frequency range, from 0.1 to 0.5 Hz. However, the AC coupling of the ballistocardiograph may have sometimes a higher cut-off frequency, e.g. in the SCA11H used in this example, and linear filtering of the raw ballistocardiogram is insufficient. To overcome this issue, the BCG is amplitude-demodulated twice. It can be indeed modeled as a sinusoidal carrier with a high frequency modulating signal (cardiac component) and a low frequency modulating signal (respiratory component). In Equation (31), h_r and h_c are the modulation indices of the respiratory and cardiac modulating signal: they typically equal to 0.5. Their frequencies are identified by ω_r and ω_c: they have physiological bounds depending on the patient.

$$BCG(t) = \frac{BCG_{max}}{4}[1 + h_r cos(\omega_r t)][1 + h_c cos(\omega_c t)]cos(\omega_0 t) \quad (31)$$

The BCG could be fitted to the twice AM modulation model; we will simply use it to justify the following non-linear filtering method, by applying twice an envelope detector to the ballistocardiogram.

First, as explained in Section 3.1.5, the raw BCG is preprocessed by a 3rd order Butterworth filter, applied forward and backward to preserve the zero-phase delay:

- A low-pass filter with 25 Hz cut-off frequency
- A high-pass filter with 3 Hz cut-off frequency.

Second, the cardiac component is extracted as a respiratory-modulated component by an envelope detector, using the Hilbert method with a filter length corresponding to 500 ms.

Third, the respiratory component is extracted from the previous cardiac component, using a finding peaks method with a 500-ms minimum delay between heartbeats. The envelopes are illustrated in Figure 72 and Figure 73. Only the lower envelope is considered at each envelope detection step.

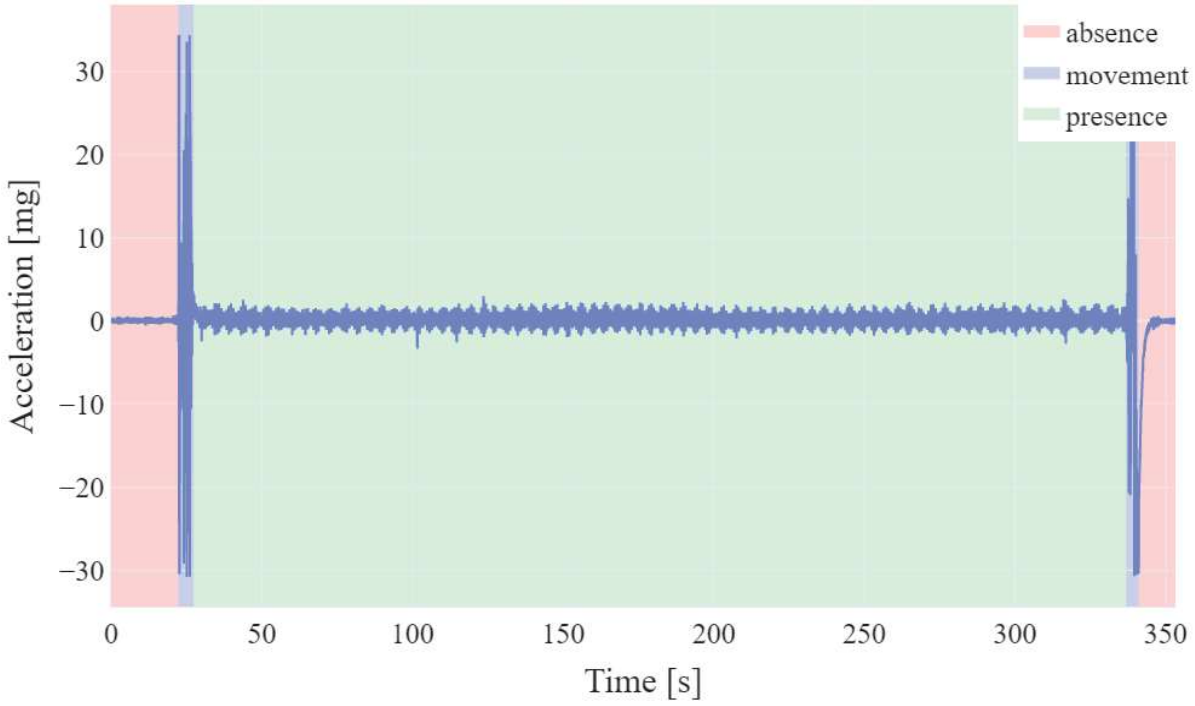

Figure 72: Cardiac and respiratory envelopes detection in the example BCG.

Fourth, a 10-second long moving window with 90% overlapping is used to compute the respiratory standard deviation and mean of each segment. The coefficient of variation is computed according to Equation (32).

$$c_v(x) = \frac{\sigma(x)}{\mu(x)} \tag{32}$$

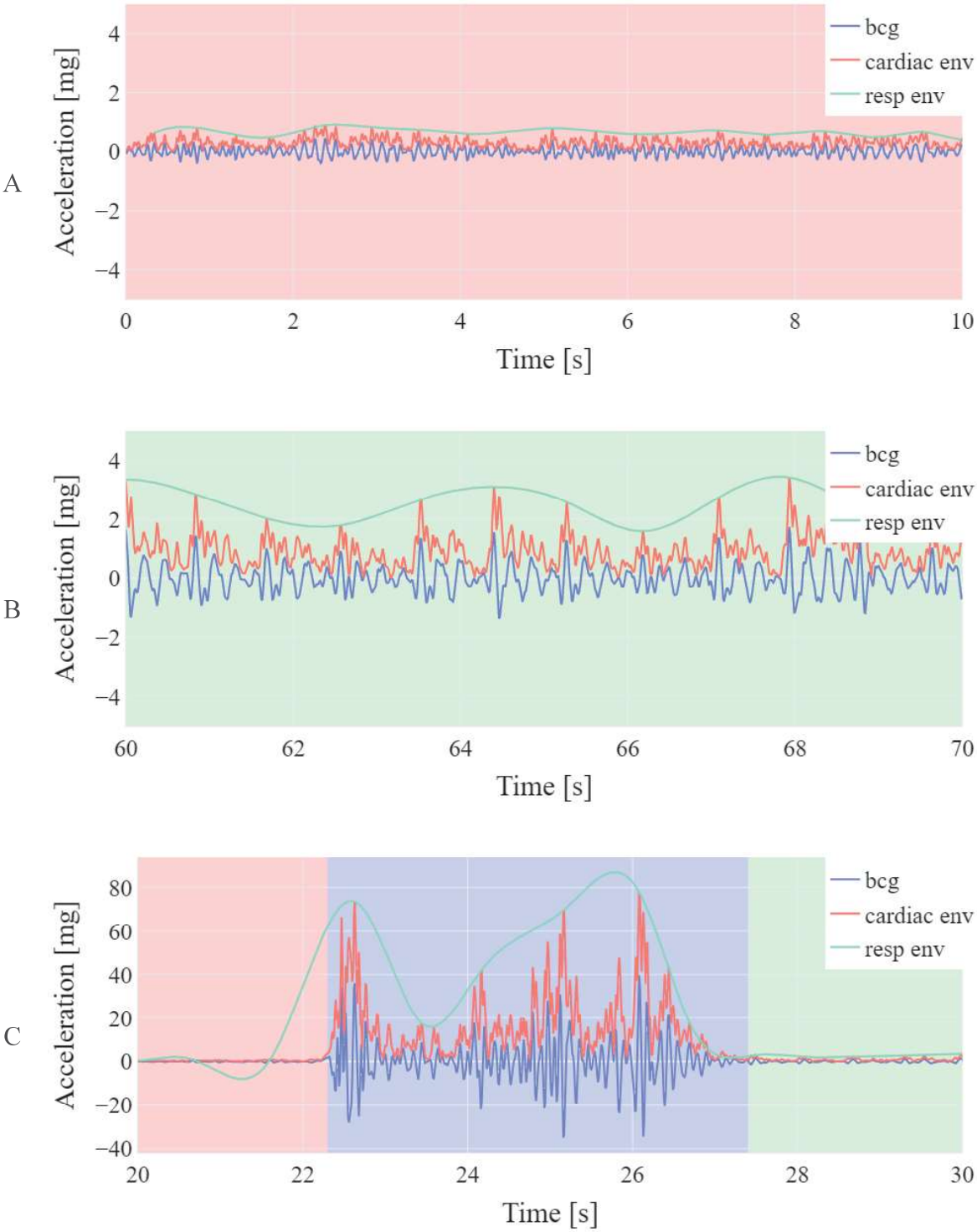

Figure 73: Cardiac and respiratory envelopes detection during presence, absence and movement phases of the BCG example.

Finally, a logarithmic function is applied to these features, which are then z-score normalized over the whole recording according to Equation (33). They are illustrated and labeled in Figure 74.

$$z\_score(x) = \frac{x - \mu(x)}{\sigma(x)} \tag{33}$$

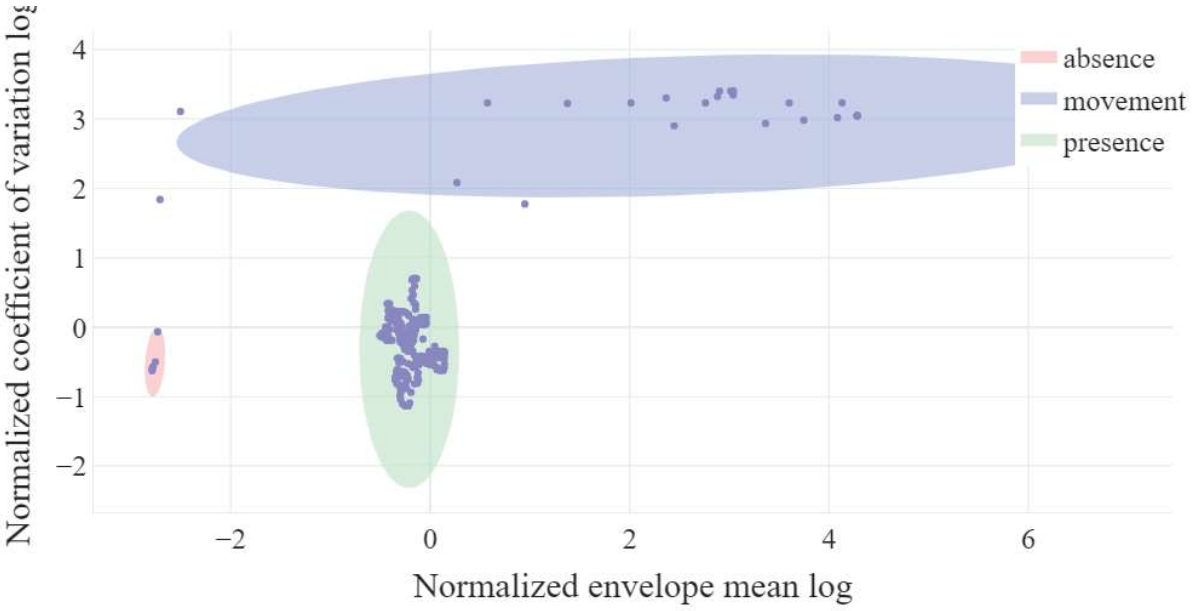

Figure 74: Respiratory standard deviation and mean features of the segmented ballistocardiogram.

3.2.2.2. Ballistocardiogram power spectral density

Spectral features of ballistocardiograms can be used for motion and occupancy segmentation. In this section, the power spectral density along time provides new insights on the signal content.

An estimation of the power spectral density is given by the Welch method [157], that computes the periodogram, i.e. the Fast Fourier Transforms of the auto-correlation function, of overlapping windows; the periodograms are averaged altogether to get an estimate of the PSD. The chosen sliding window is a Tukey window a 50% shape parameter α, as defined in Equation (34).

$$w[n] = \begin{cases} \frac{1}{2}\left[1 - \cos\left(\frac{2\pi}{\alpha}\frac{n}{N}\right)\right], & 0 \le n < \frac{\alpha}{2}N \\ 1, & \frac{\alpha}{2}\mathrm{N} \le n \le (1 - \frac{\alpha}{2})N \\ \frac{1}{2}\left[1 - \cos\left(\frac{2\pi}{\alpha}\left(1 - \frac{n}{N}\right)\right)\right], & (1 - \frac{\alpha}{2})N < n \le N \end{cases} \quad (34)$$

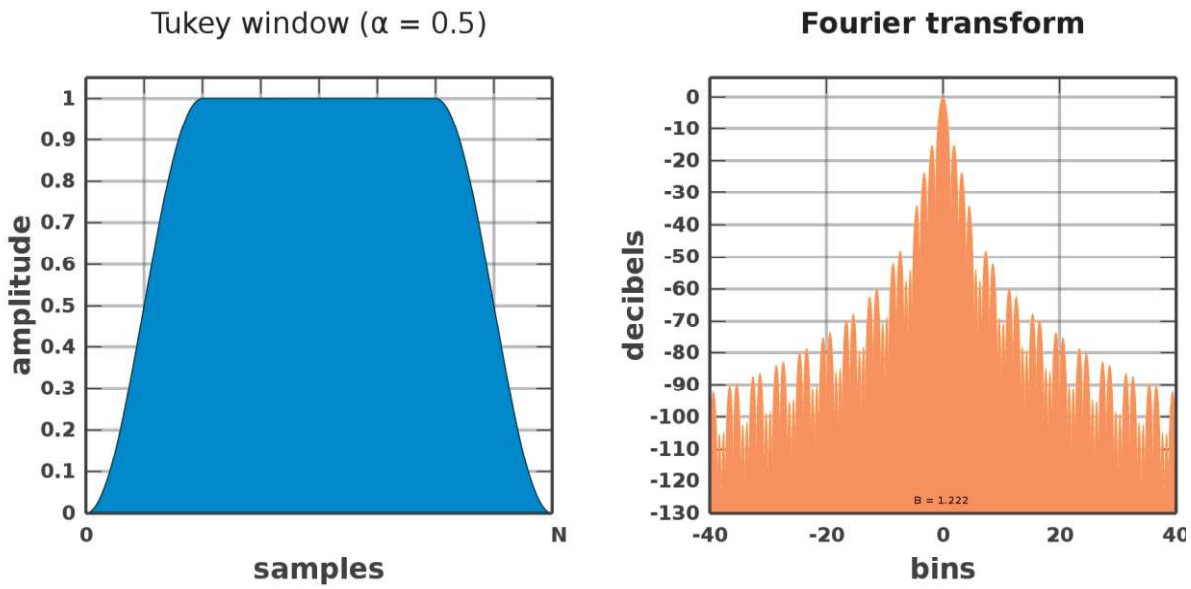

A B

Figure 75: A Tukey window with a 50% shape parameter in the time (A) and frequency (B) domains.

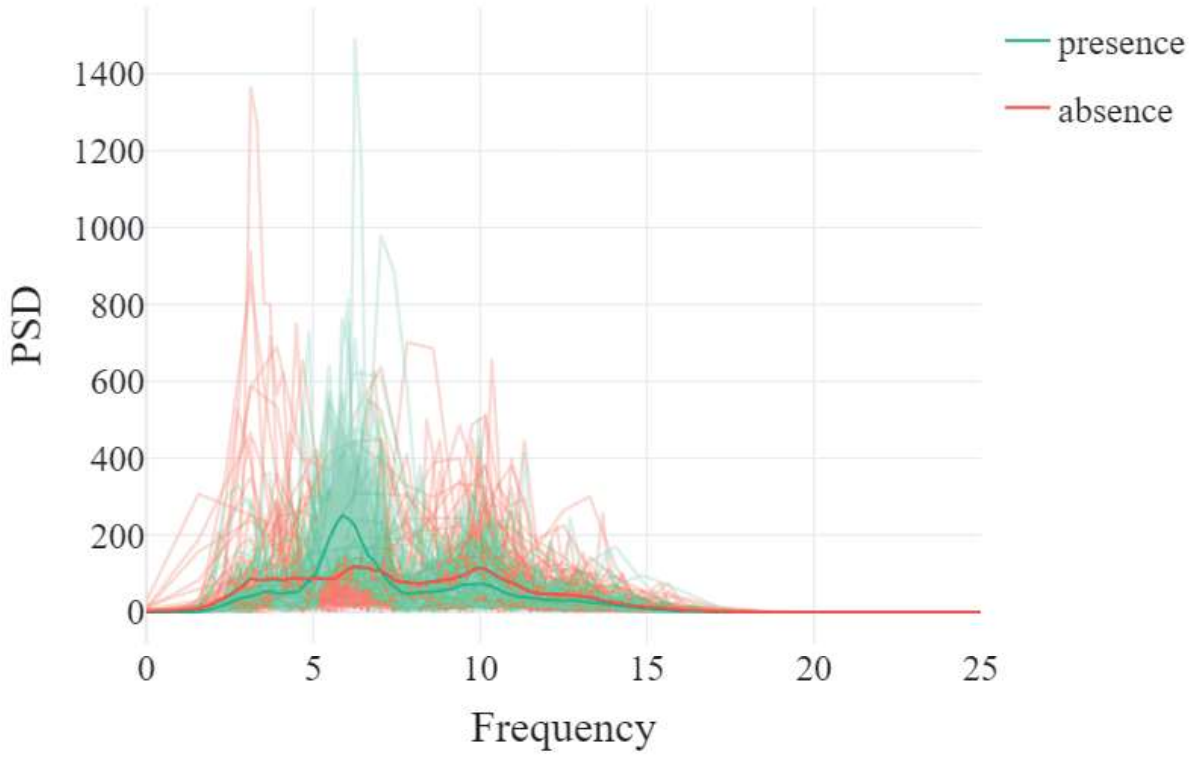

Figure 76: Power spectral density of BCG segments during the presence and absence phases. The average PSDs of each phase are darkened.

The Tukey window, or tapered cosine window, represents a tradeoff between the rectangular window, e.g. a Tukey window with a 0% shape parameter, and the Hann window, e.g. a Tukey window with a 100% shape parameter. With a 5.12-seconds length, the periodograms and thus the Welch PSD of each segment approximately have a 0.2 Hz frequency step which is enough in this application. The overlapping is set at 50%, which means that two consecutive segments share the same abscissa over half a window duration.

The spectrogram is the succession of the Welch PSD for every segment obtained by sliding the predefined window. The power spectral densities (PSD) of BCG segments have different shapes depending on the segment phase: motion, presence, or absence. Figure 76: Power spectral density of BCG segments during the presence and absence phases. The average PSDs of each phase are darkened. Figure 76 shows these different shapes by averaging the spectrogram of a ballistocardiogram during presence and absence. It is worth

noting there is a fundamental frequency in the ballistocardiogram frequency range for the presence segments only, which will be later used for classification.

3.2.2.3. The amplitude of the cardiac envelope fundamental frequency

The cardiac envelope computed in Section 3.2.2.1 using the Hilbert transform has a power spectral density that contains the cardiac modulating signal of the ballistocardiogram. Therefore, it can be used to estimate the heart rate, as the fundamental frequency of its power spectrum density, or better, the instantaneous heart rate using the spectrogram. The PSD maximum amplitude of the cardiac envelope can be used as a feature for motion, absence, and presence classification.

Moreover, the mean of the segmented cardiac envelope is another useful feature for movement and occupancy classification: it is correlated to the standard deviation of the ballistocardiogram.

3.2.3. Classification

Using the previously defined features, absence, presence, and movement segments can be classified. Usually, as movement segments have a much greater signal amplitude than presence and absence movement, movement is segmented first; then, on motion-free segments, absence and presence are segmented. The hierarchical clustering with iterative Mahalanobis distance algorithm is an exception and can directly segment the signal into the three desired segments.

3.2.3.1. Fixed threshold

As the signal oscillates much more during movement than during absence or presence phases, and as the features have been normalized, a fixed zero threshold on the respiratory standard deviation, i.e. the Y-axis of Figure 74, is generally enough to segment movement. If

movement phases have a too low proportion in the recording duration, the z-score normalization of the respiratory features may need to use mean and standard deviation of other recordings.

3.2.3.2. Agglomerative hierarchical clustering with Euclidean distance

An agglomerative hierarchical clustering algorithm was used to cluster presence and absence phases on motion-free BCG segments using the Euclidean distance between their power spectral densities. This feature is detailed in Section 3.2.2.2. The Euclidean distance is relevant when the signal intra-variability is low.

Agglomerative hierarchical clustering consists of computing a matrix $D = \left(d_{ij}\right)$ of the observations pairwise distance. Here, each observation is the power spectral density of a 5.12-second long BCG segment. The distance is set as the Euclidean distance in Equation (35).

$$d_{ij} = \sqrt{\sum_{k=1}^{N} (PSD_i(k) - PSD_j(k))^2} \quad (35)$$

Each observation is initialized as a cluster. Iteratively, the two nearest clusters are agglomerated in a dendrogram such as in Figure 77, where the leaves of the clustering tree are the initial observations.

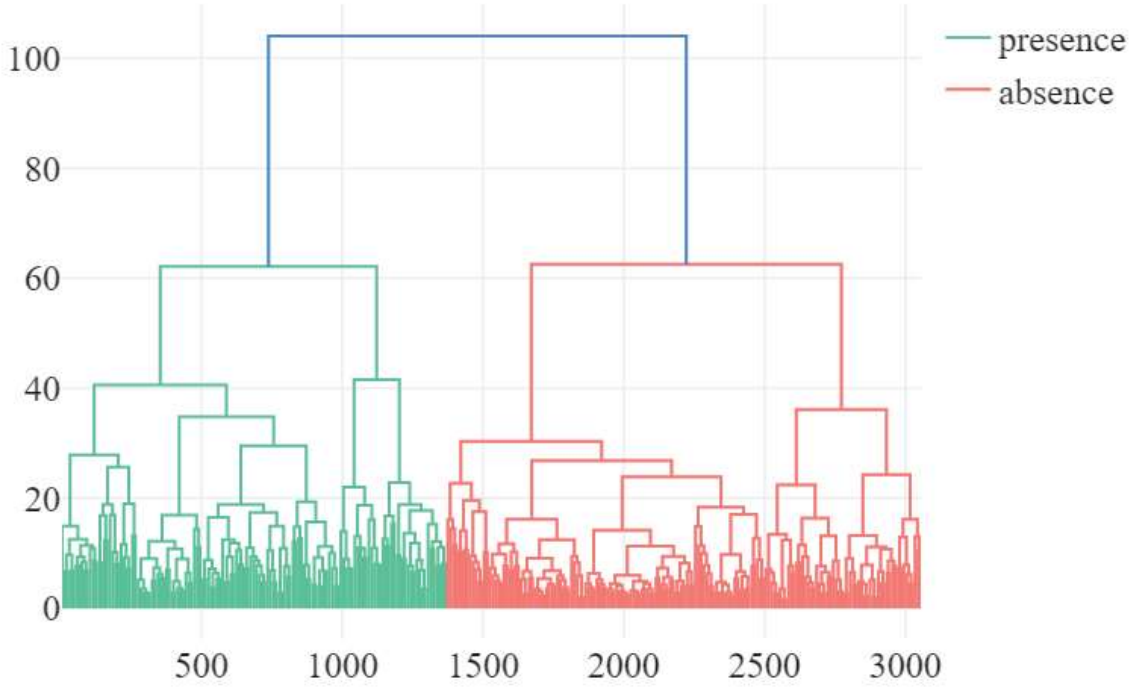

Figure 77: Dendrogram of hierarchical clustering of presence and absence on motion-free segments.

The distance $\delta(u, v)$ between two clusters u and v can be assessed by different linkage methods, e.g. single, complete, average, or ward. These linkage methods are defined in Equation (36), Equation (37), Equation (38), and Equation (39), where u is the newly joined cluster consisting of clusters t and s, v is an unused cluster in the tree, and $|*|$ is the cardinality operator. In this section, the ward linkage method is selected, as it minimizes the intra-cluster variance.

$$\delta_{single}(u, v) = \min_{i \in u, j \in v} d_{ij} \tag{36}$$

$$\delta_{complete}(u, v) = \max_{i \in u, j \in v} d_{ij} \tag{37}$$

$$\delta_{average}(u, v) = \frac{1}{|u| * |v|} \sum_{i \in u, j \in v} d_{ij} \tag{38}$$

$$\delta_{ward}(u,v) = \sqrt{\begin{matrix}\frac{|v|+|s|}{|v|+|s|+|t|}\delta_{ward}(v,s)^2 \\ +\frac{|v|+|t|}{|v|+|s|+|t|}\delta_{ward}(v,t)^2 \\ -\frac{|v|}{|v|+|s|+|t|}\delta_{ward}(s,t)^2\end{matrix}} \quad (39)$$

This information is stored in a linkage matrix with as many rows as iterations. A row of the linkage matrix, corresponding to an iteration, contains the indices of the clusters to agglomerate, their distance according to the linkage method, and the number of original observations in the newly formed cluster.

3.2.3.3. Hierarchical clustering with iterative Mahalanobis linkage

Mahalanobis distance explained below, is useful to cluster elongated shapes. Figure 74 shows the features of the respiratory envelope component of movement, absence, and presence of ballistocardiogram segments. Those features seem to follow two-dimensional gaussian distributions.

Euclidean distance, using the k-means clustering or agglomerative hierarchical clustering, is not well suited for such distribution. Figure 78 shows that Euclidean distance gathers presence and absence clusters without considering the elongated shape of the movement cluster. However, Euclidean distance usually does not make any clustering error until 10 clusters in our dataset.

The Mahalanobis distance is defined by Equation (40) with $f_i = \begin{pmatrix} mean(resp_i) \\ std(resp_i) \end{pmatrix}$ the feature vector of the ith BCG segment and V a covariance matrix, usually the covariance matrix of the dataset. In our case, the covariance matrix is re-evaluated at each iteration step of the hierarchical clustering for every cluster, and the Mahalanobis distance is pairwise computed from the point of view of each cluster.

$$d_{mahal_{ij}}(V) = \sqrt{(f_i - f_j)V^{-1}(f_i - f_j)^T} \quad (40)$$

A

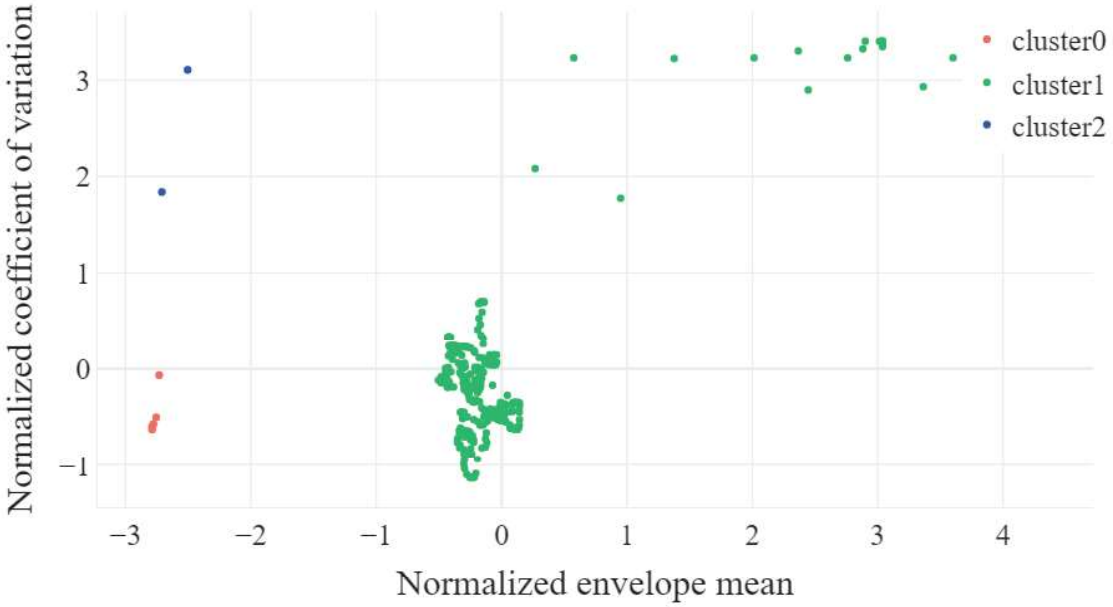

B

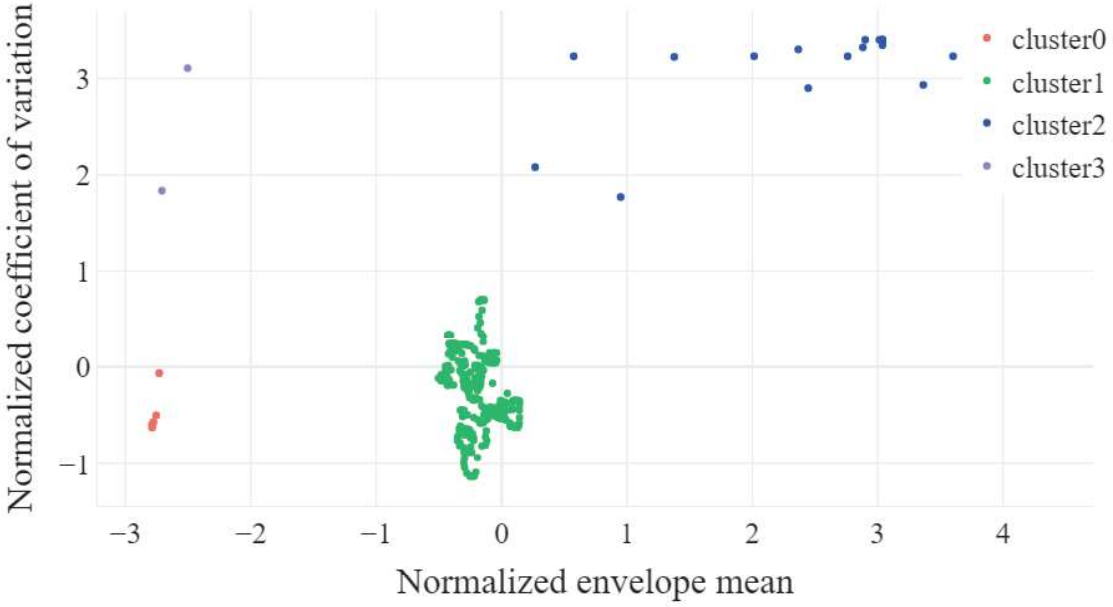

Figure 78 : Hierarchical clustering with Euclidean distance and single linkage, for three (A) and four (B) clusters.

More simply, a new linkage method, called iterative Mahalanobis linkage (IML), is developed and specified by Equation (41).

$$\delta_{IML}(u,v) = \frac{1}{|u| * |v|} \sum_{i \in u, j \in v} \min_{k \in (u,v)} (d_{mahal_{ij}}(V_k))) \quad (41)$$

The resulting clustering on the BCG example is illustrated in Figure 79, in which the covariance matrix of the motion, presence, and movement clusters is highlighted by ellipses in a blue-yellow color scale.

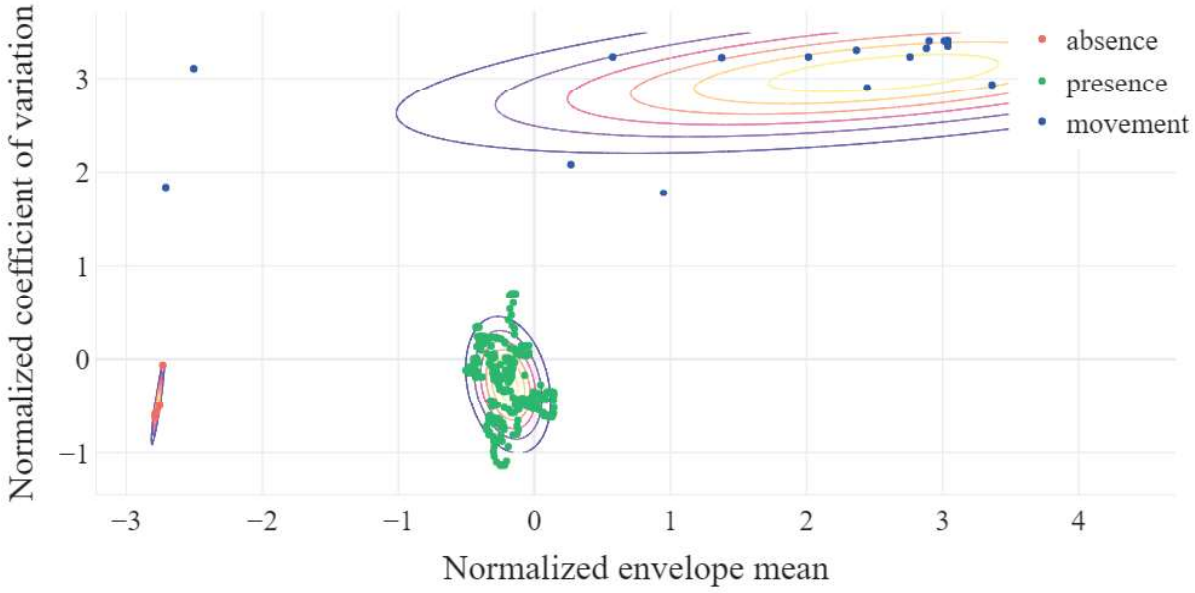

Figure 79: Iterative Mahalanobis linkage clustering.

3.2.3.4. Gaussian mixture models

As the amplitude distribution of signals follows normal laws, gaussian mixture models (GMM) are used to cluster motion-free BCG segments into absence or presence categories. The amplitude of the cardiac envelope fundamental frequency detailed in Section 3.2.2.3 is used as a clustering feature, as well as the mean amplitude of the cardiac envelope.

A GMM is defined by Equation (42), with K mixtures, x the features vector and N its size, $\boldsymbol{\mu_i}$, $\mathbf{V_i}$ and ϕ_i the mean, covariance and weight of the ith mixture. In our case, the observation features are fitted to the GMM by the expectation-maximization algorithm, where the model parameters are randomly initialized and then refined after each iteration step that assigns observations to their most probable mixture components.

$$f(x) = \sum_{i=1}^{K} \phi_i \frac{1}{(2\pi)^{N/2}|\mathbf{V}_i|^{1/2}} \exp\left[-\frac{1}{2}(\boldsymbol{x}-\boldsymbol{\mu}_i)^{\top}\mathbf{V}_i^{-1}(\boldsymbol{x}-\boldsymbol{\mu}_i)\right] \quad (42)$$

3.2.3.5. Hidden Markov model clustering

Another algorithm developed in this thesis is a gaussian Hidden Markov model (HMM) that takes the respiratory envelope as an observation sequence and estimates the supposed underlying state sequence. The original idea came from the amplitude distribution of ballistocardiogram samples illustrated in Figure 67, which show different variance between motion-free and motion-polluted distributions. However, those distributions have the same means, which can make it difficult to cluster them. Using the respiratory component samples rather than the ballistocardiogram samples overcomes this issue, by shifting the means of the distributions of Figure 67.

The HMM, illustrated in Figure 80, has two states that emit respiratory envelope samples according to the previously cited gaussian distributions. In practice, the state sequence can directly segment the signal into motion-free and motion-polluted categories.

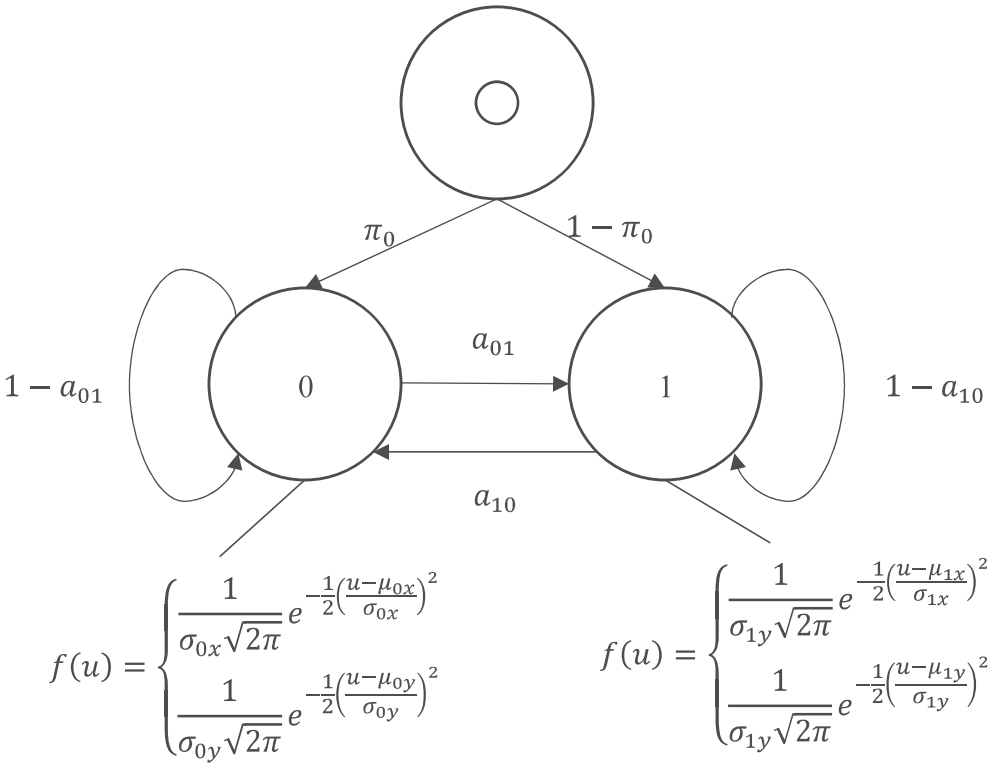

Figure 80: HMM motion clustering

A gaussian mixture model with two mixture components could be used to cluster the motion-free and motion-polluted distributions; however, the HMM brings transition constraints which fits more with the actual ballistocardiogram.

The motion-free and motion-polluted states are identified by 0 and 1 subscripts, respectively. The respiratory mean and standard deviation are identified by x and y subscripts, respectively. The initial state distribution Π and the transition matrix *A* are defined by Equation (43) and Equation (44).

$$\Pi = \begin{pmatrix} \pi_0 \\ \pi_1 \end{pmatrix} \tag{43}$$

$$A = \begin{pmatrix} a_{00} & a_{01} \\ a_{10} & a_{11} \end{pmatrix} \tag{44}$$

3.2.4. Benchmark of the literature and developed methods

The previous methods have >95% specificity and sensibility for movement and occupancy detection on the databases detailed in Section 3.1.

Figure 81 shows an example of movement clustering with the IML method presented in Section 3.2.3.3.

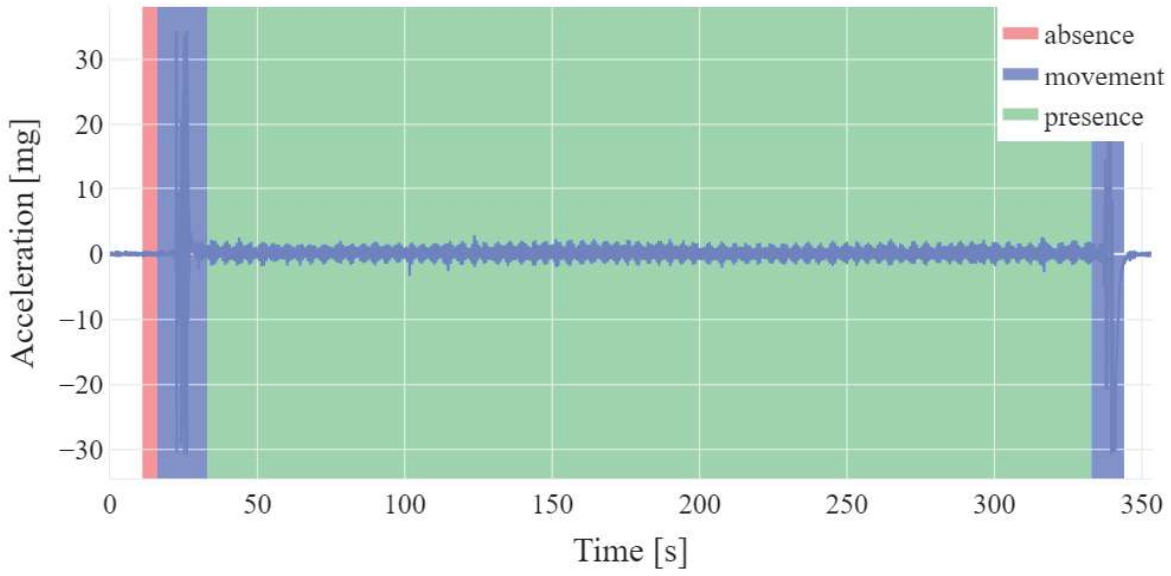

Figure 81: Hierarchical clustering of occupancy with Mahalanobis distance.

Figure 82 shows an example of motion clustering using the HMM method, with the same features as for the IML method.

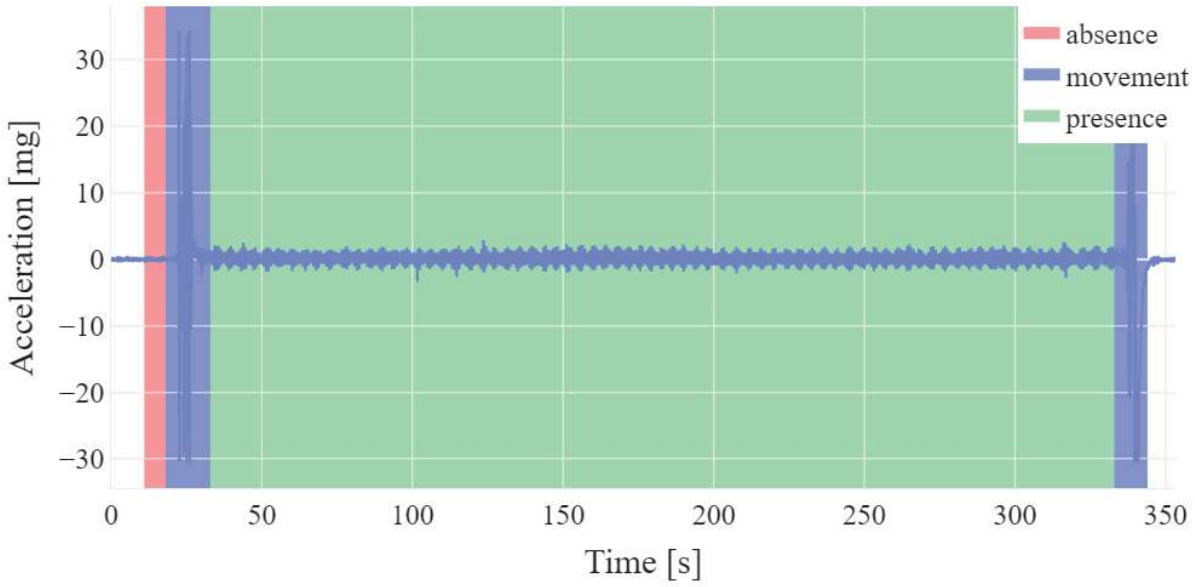

Figure 82: HMM motion clustering of occupancy with HMM method.

3.3. Heart and respiratory rates measurement

The motion-free presence ballistocardiograms are segmented using the methods explained in Section 3.2. They are visually checked by two experts. On those BCG segments, vital signs such as the heart and respiratory rates can be measured. In this section, we mainly focus on heart rate detection; however, the developed methods can be applied for respiratory rate detection as well.

The main concern in BCG digital processing for vital signs detection is the signal noise and variability, which are much more important than in ECG – see Figure 83.

A

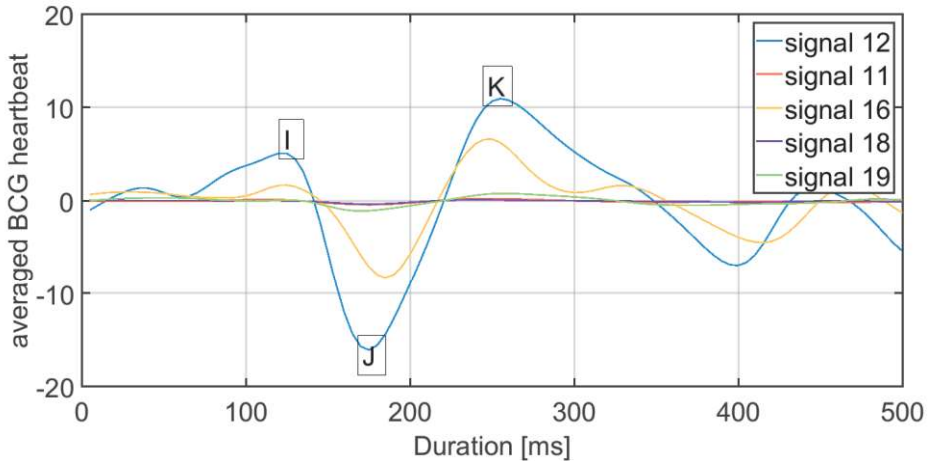

B

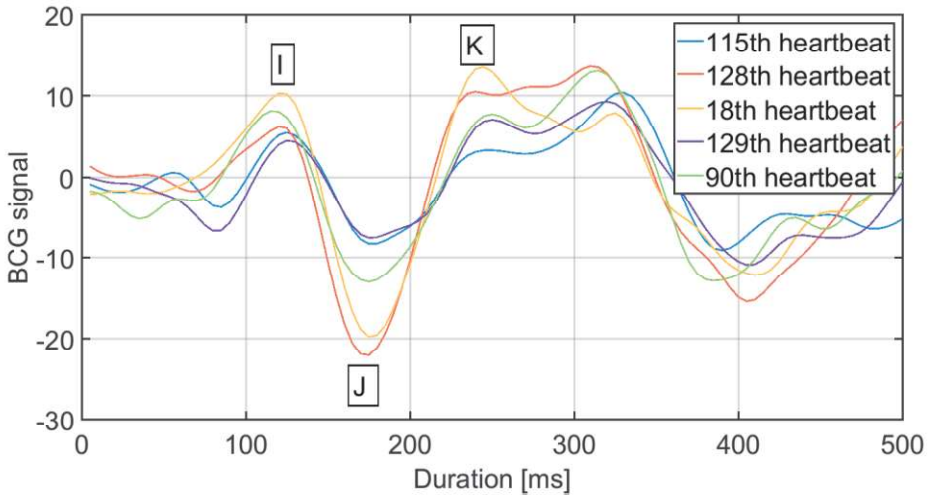

Figure 83: A superposition of averaged heartbeats from different patients (A) and heartbeats from one patient (B) that show inter- and intra-variabilities.

In this section, the state of the art and newly developed algorithms are presented.

3.3.1. State of the art

Specific digital signal processing algorithms have been developed for detecting heartbeats, beat-to-beat heart rate, and heart rate variability (HRV) in BCG signals using time-domain or time-frequency domain methods. Sprager benchmarked several algorithms for heartbeat detection but found better results in PCG than in BCG [64].

3.3.1.1. The estimate of the average heart rate

For many applications that do not require heart rate variability information, the average heart rate over a period is useful enough.

Figure 84 compares spectrograms with a 15-second long window of synchronous ballistocardiograms and electrocardiograms.

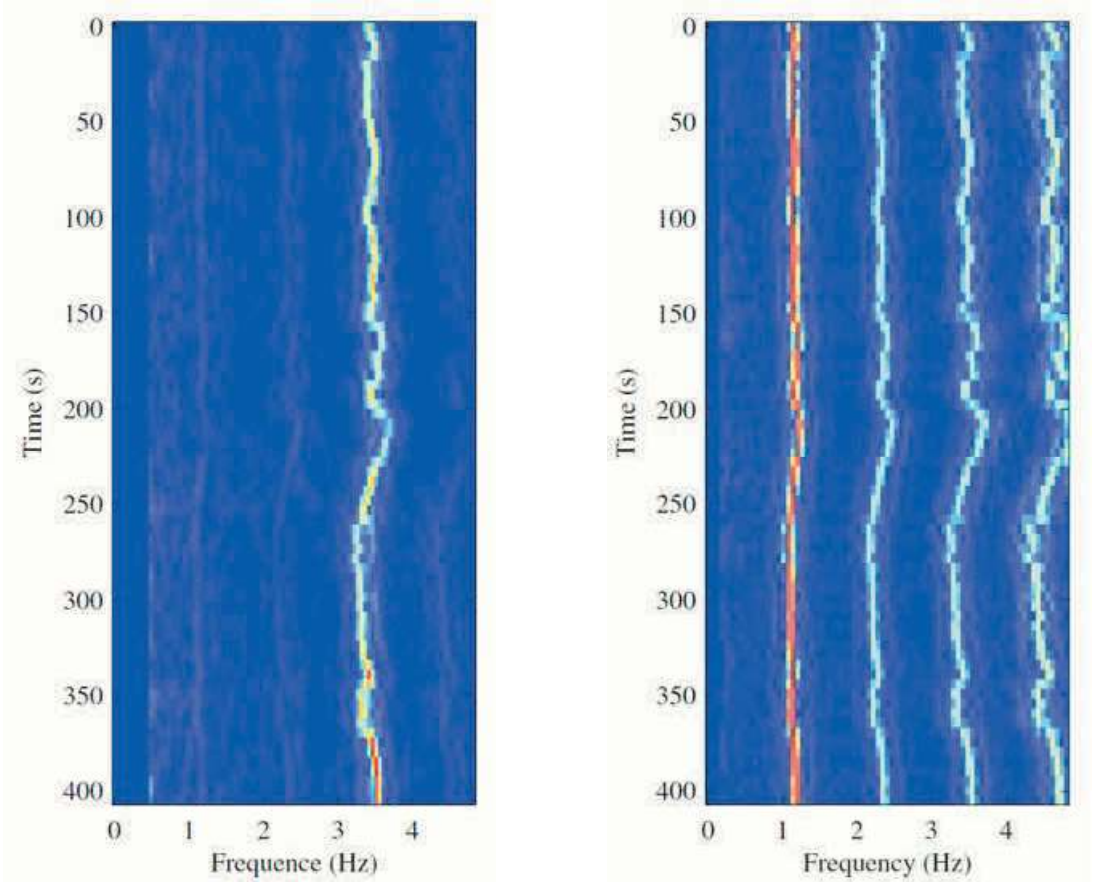

A B

Figure 84: Spectrograms of a synchronous ballistocardiogram (A) and electrocardiogram (B) [66]

Zhu observed that contrary to the electrocardiogram, the ballistocardiogram has a fundamental frequency that is different from the heart rate. He associates this fundamental frequency of the ballistocardiogram to the third harmonic of the heart rate. In this method, the average heart rate is thus estimated by dividing by 3 the fundamental frequency of the ballistocardiogram.

The short-term Fourier transform can also be applied to a signal envelope, i.e. cardiac modulating signal, to regularly estimate the averaged heart rate [158].

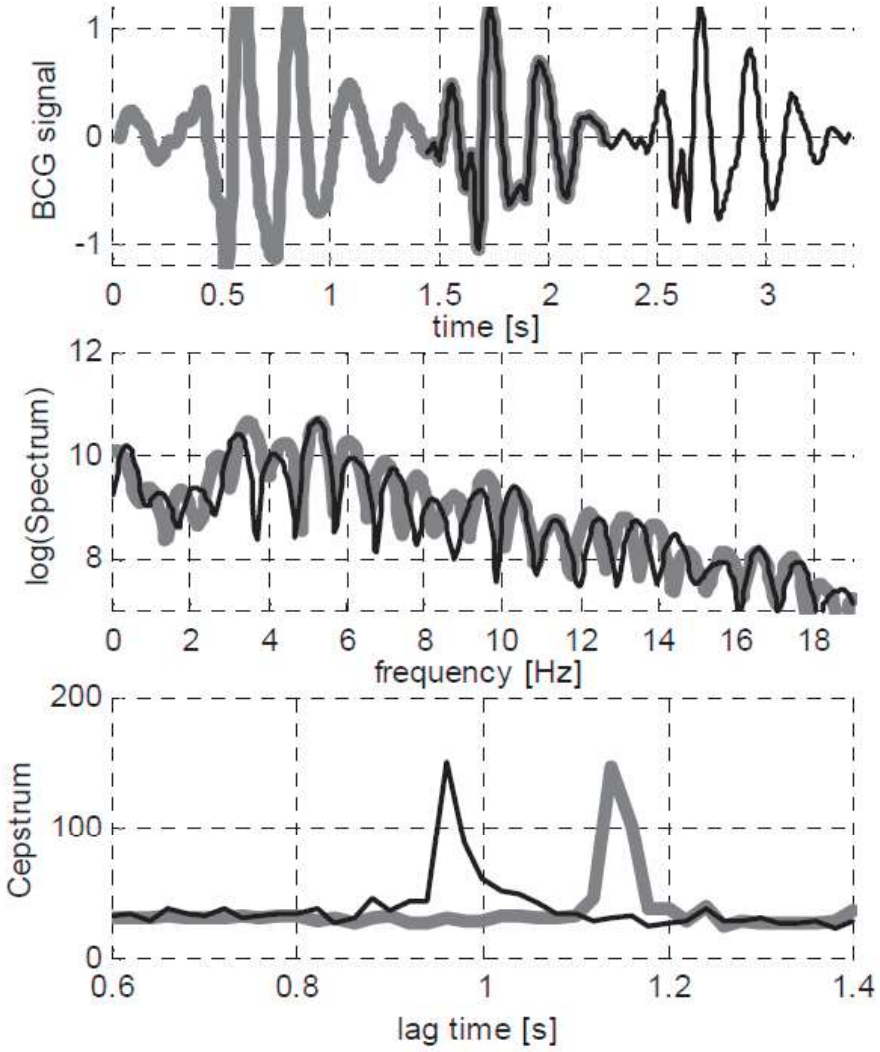

Figure 85: Two consequent heartbeat interval periods and corresponding spectra and cepstra [65].

An adaptive window cepstrum method is explained in [65]: a short-term real cepstrum transform, as defined by Equation (45) with $\mathcal{F}$ the Fourier transform and x the windowed BCG, can be applied on the ballistocardiogram with an adaptive window that covers two heartbeats. The cesptra of two windows with different inter-beat interval are illustrated in Figure 85 and show the potential of this method for estimating an average heart rate.

$$C_r = \mathcal{F}^{-1}\{\log(|\mathcal{F}\{x\}|)\} \tag{45}$$

3.3.1.2. *Instantaneous heart rate*

For arrhythmias or heart rate variability applications, e.g. sleep studies, the instantaneous heart rate is necessary: heartbeats have to be detected one by one, and heart rate is computed by Equation (46) where HR and BB is the heart rate (in beats per minute or bpm) and beat-to-beat delay (in ms) series, fs the BCG sampling frequency and n_i the index of the i[th] heartbeat. The HR and BB series are linearly interpolated between two heartbeats, e.g. to uniformize their sampling frequencies.

$$HR(n_i) = 60.\frac{1}{BB(n_i)} = 60.fs.\frac{1}{n_i - n_{i-1}} \tag{46}$$

3.3.1.3. *Pan-Tompkins*

The reference Pan-Tompkins algorithm for R peaks detection [159] in ECG performs is difficult to apply to J-peak detection in BCG. Figure 86 shows an implementation of this method on the moving window integrated BCG. The algorithm performs best on the filtered signal; however, this signal is distorted which tends to average the heart rate.

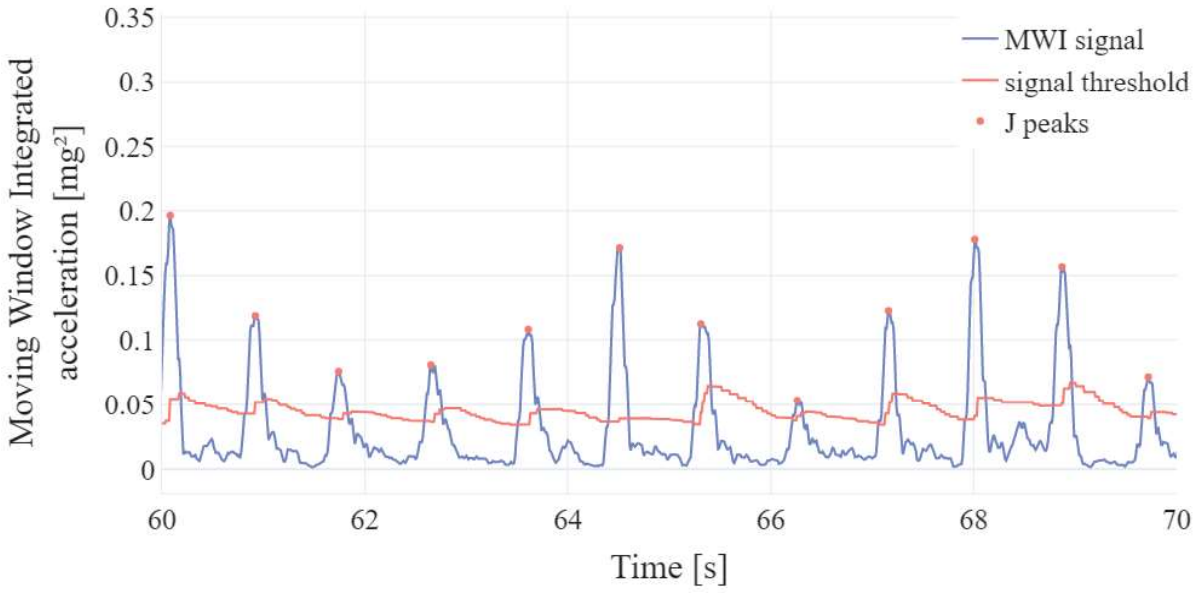

Figure 86: Dual threshold as implemented in [159] of the Moving Window Integrated BCG.

The Pan-Tompkins method is part of several segmentation methods used to detect QRS complexes in electrocardiograms [160] [161] [162] [163] [164]. Those methods will be benchmarked on our databases in later works.

3.3.1.4. Distance adaptive threshold

Heartbeats can be detected among a set of local maxima and decision rules based on the delays between these maxima [63]. Using a peak searching algorithm with a distance constraint can show heartbeats clusters on a Poincaré plot, depending on the distance parameter setting. Figure 87 shows, for three distance parameters of the peak searching algorithm, the resulting detections on the right and Poincaré plots on the left.

Poincaré plots map $\binom{BB(n-1)}{BB(n)}$ points in a two-dimensional space. On beat-to-beat series, they form a Gaussian cluster with a diagonal covariance matrix. Consequently, they are useful for arrhythmias detection, where two consecutive beat-to-beat intervals can be very different and appear as an outlier point on the Poincaré plot.

From A to C in Figure 87, the distance parameter of the peak searching algorithm is increased. In Figure 87A (distance = 0.2 s), a vertical cross-cluster appears and is centered on 0.27 s, which is related to the third harmonic of the heart rate mentioned in Section 3.3.1.1. Increasing the distance parameter, e.g. in Figure 87B to 0.65 s, leads to a diagonal covariance Gaussian cluster centered on 0.8 seconds, related to the average heart rate of this BCG segment.

As shown in Figure 87C, the distance parameter is insufficient to correctly detect heartbeats, as it does not limit the maximum distance between heartbeats: some peaks are missed (outliers of the diagonal covariance Gaussian distribution in the Poincaré plot) and should be searched back by the algorithm to improve its sensitivity.

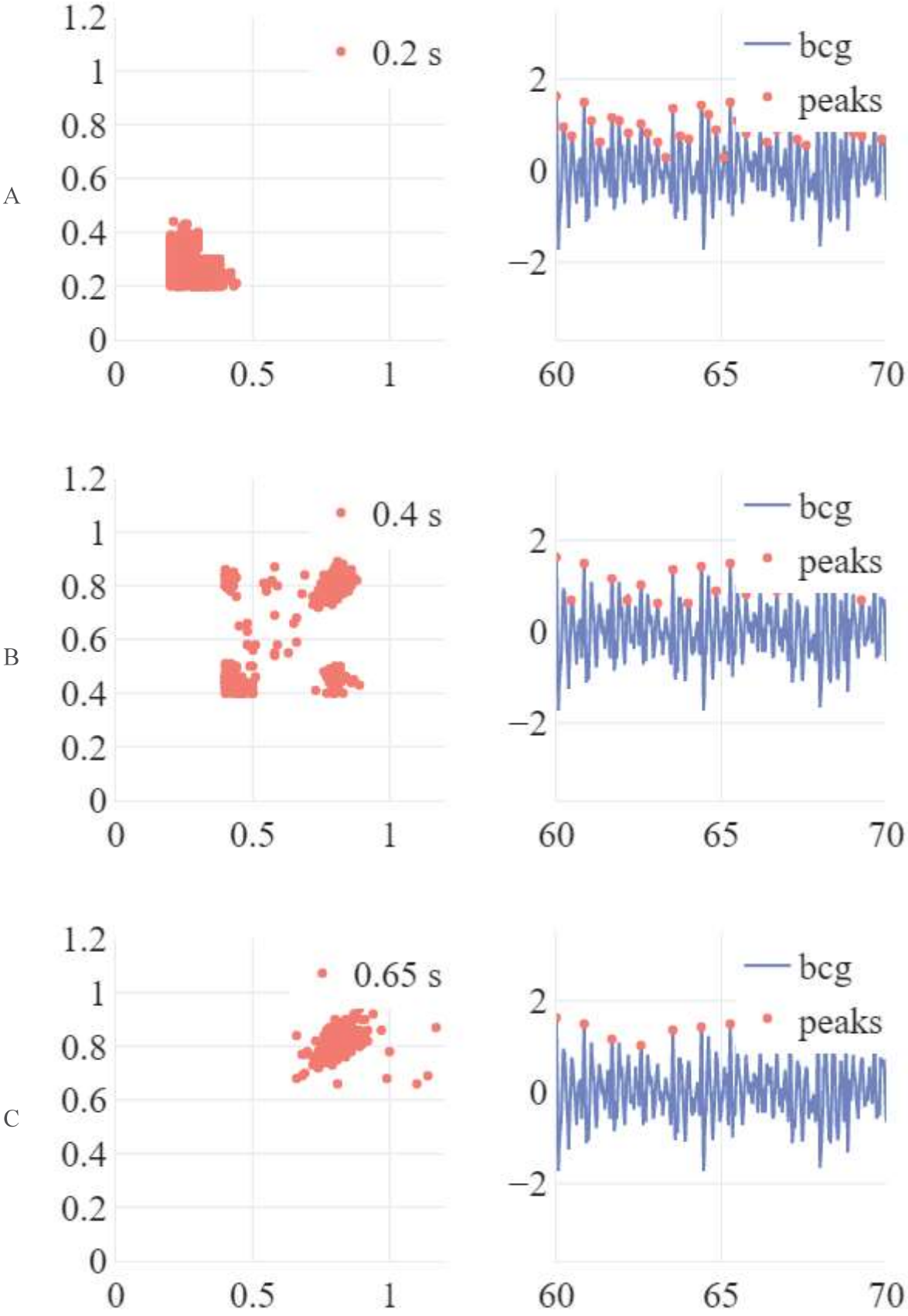

Figure 87: Iterations of the distance adaptive threshold clustering: 0.2 s (A), 0.4 s (B), 0.65 s (C)

3.3.1.5. Time features clustering

The fiducial points of a ballistocardiogram waveform have specific shapes that can be identified by several parameters. Figure 88A shows parameters used in [40], for example, the prominences and widths of a peak and the following peaks. After principal component analysis, fiducial points can be clustered by the k-means algorithm, as in Figure 88B.

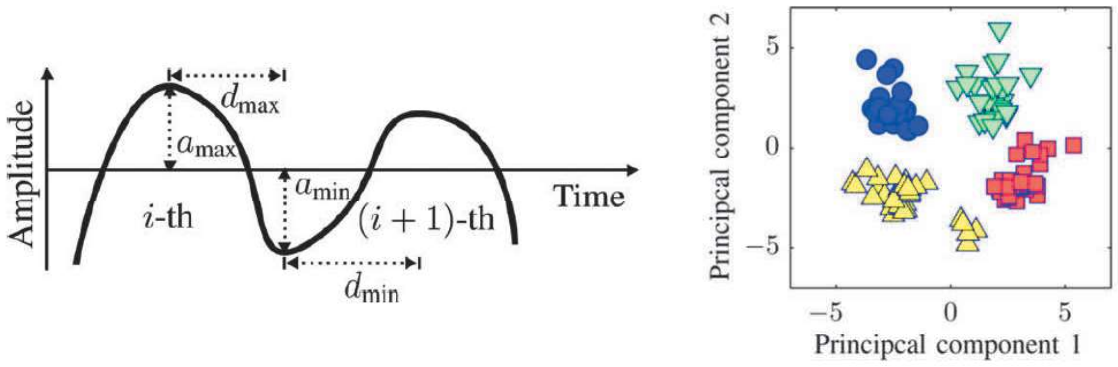

A B

Figure 88: Times features of local maxima (A) and clustering after PCA (B) in [40].

We detected such synchronization points and plotted feature vectors representing local extrema in the BCG signal in the (prominence, distance) space, where the distance is understood as the distance delay between a local extremum and the synchronization point.

After a logarithmic transformation, those extrema can be clustered using k-means, as shown in Figure 89. The appropriate number of clusters is selected by optimizing the average silhouette. The fiducial points clusters are identified by their respective prominence and delays; for example, the highest prominence cluster centroid indicates the J peak cluster.

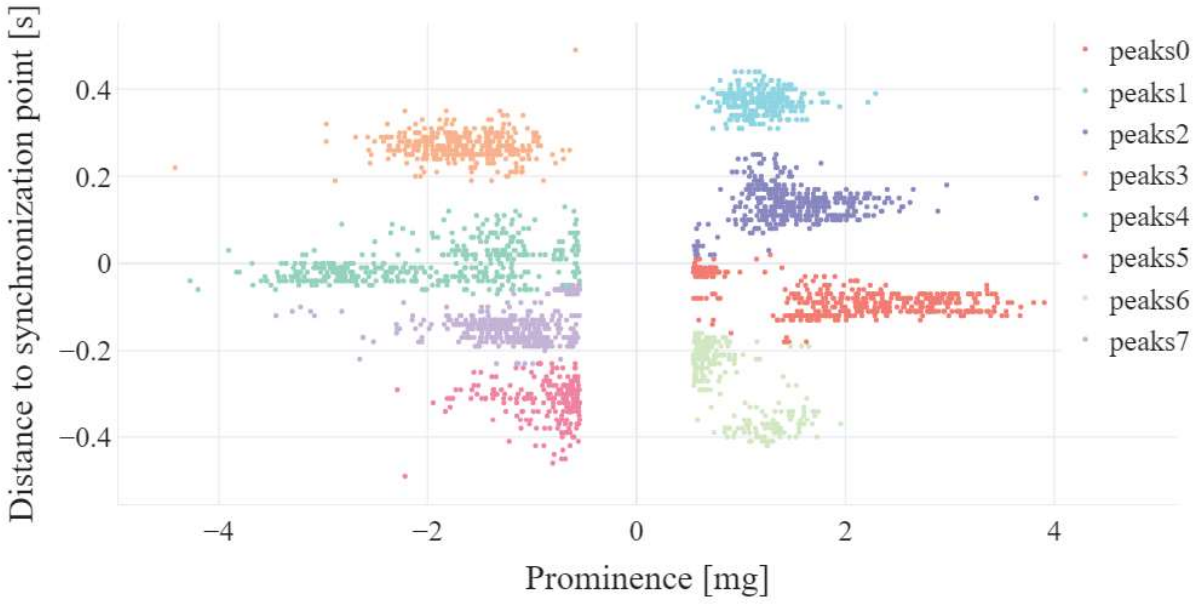

Figure 89: Clustering of local extrema of the BCG in the (prominence, distance to beat reference) space.

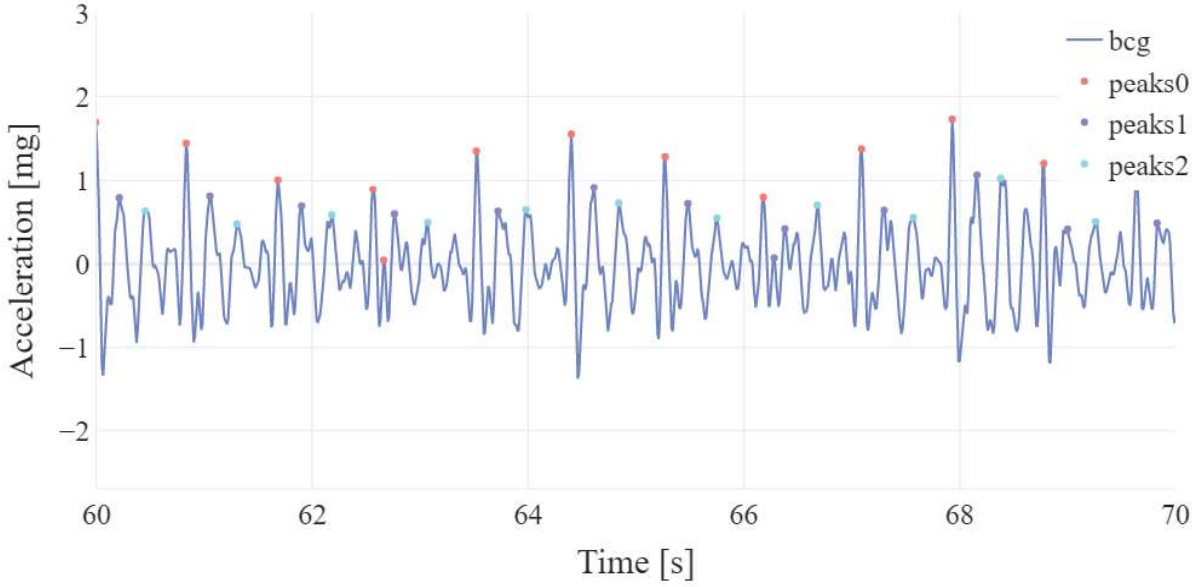

Figure 90: Peak clusters used to detect fiducial points.

The trajectory of fiducial points in a two-dimensional space such as in [40] is useful if clusters are not perfectly separated. When extrema are far from their cluster centroid, the previous and next points are overlooked: if they respectively belong to the previous and next cluster, the extremum is confirmed in its cluster, otherwise, its belonging is reevaluated. Figure 91 illustrates this so-called trajectory that needs to be corrected.

A blind segmentation algorithm, BSeg++, finds synchronization points, i.e. local maxima of a narrow band-pass filtered BCG in the 1-2 Hz frequency range [165]. The local minima of the raw BCG, in the neighborhood of those synchronization points, are identified as I peaks. Local maxima in a specific neighborhood before and after those I peaks are identified by H and J peaks, respectively.

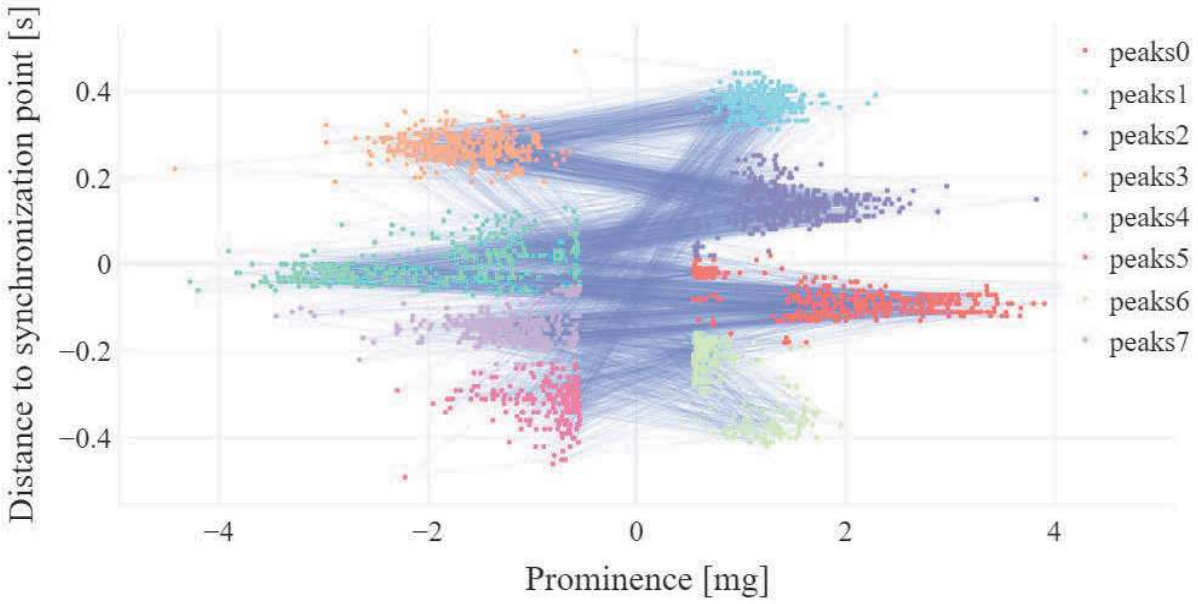

Figure 91: Trajectory of the clustered fiducial points.

3.3.1.6. Wavelets detector

Wavelet analysis has been used a little in BCG signal processing.

In 1996, wavelet multiresolution combined with a single feedforward neural network could classify normal, hypertension, and heart attack ballistocardiograms [39]. However, it was no used as a heartbeat detector. Akhbardeh improved the classification performance with compact support Daubechies wavelet and two hidden layers [166].

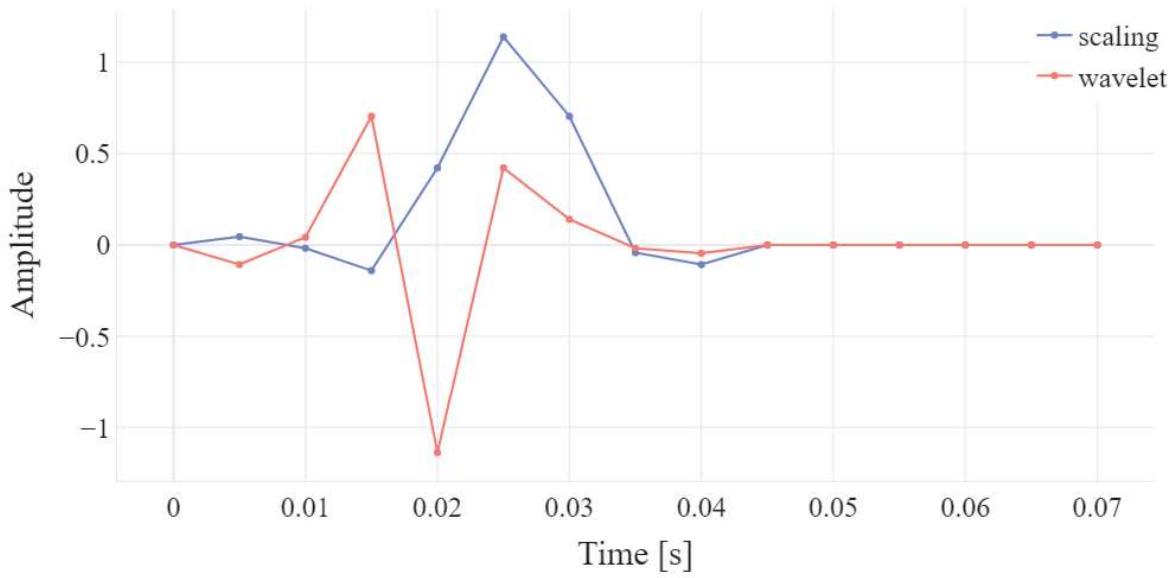

Figure 92: Sym4 wavelet and scaling approximated functions at the first decomposition level.

Jin used in 2009 wavelets to denoise ballistocardiogram and applies an adaptive threshold to detect heartbeats [167].

The Sym4 wavelet introduced in Figure 92 was used to generate a BCG scalogram, i.e. a time-frequency representation at different wavelet scales. A BCG scalogram example is illustrated in Figure 93. Heartbeats patterns are easily recognized in this image. The advantages of symlet wavelets are their symmetries.

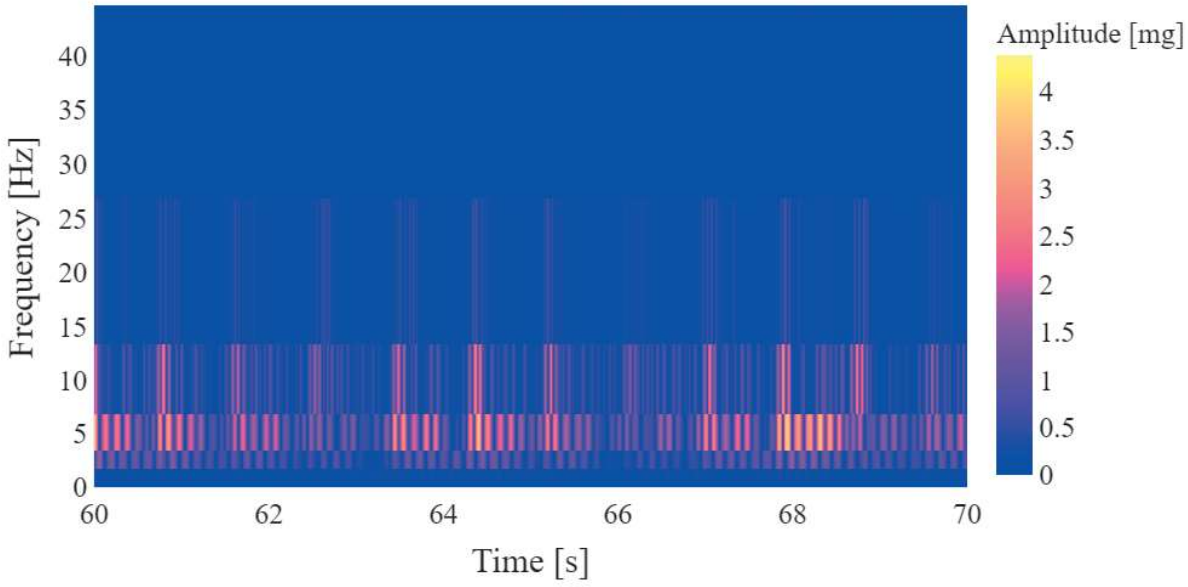

Figure 93: BCG scalogram example with the Sym4 wavelet

As a narrow band-pass filter equivalent, the detail coefficient which has the highest variance is selected. Thus, a single scale with a narrow frequency range is selected and its envelope can be extracted by the Hilbert method – see Figure 94.

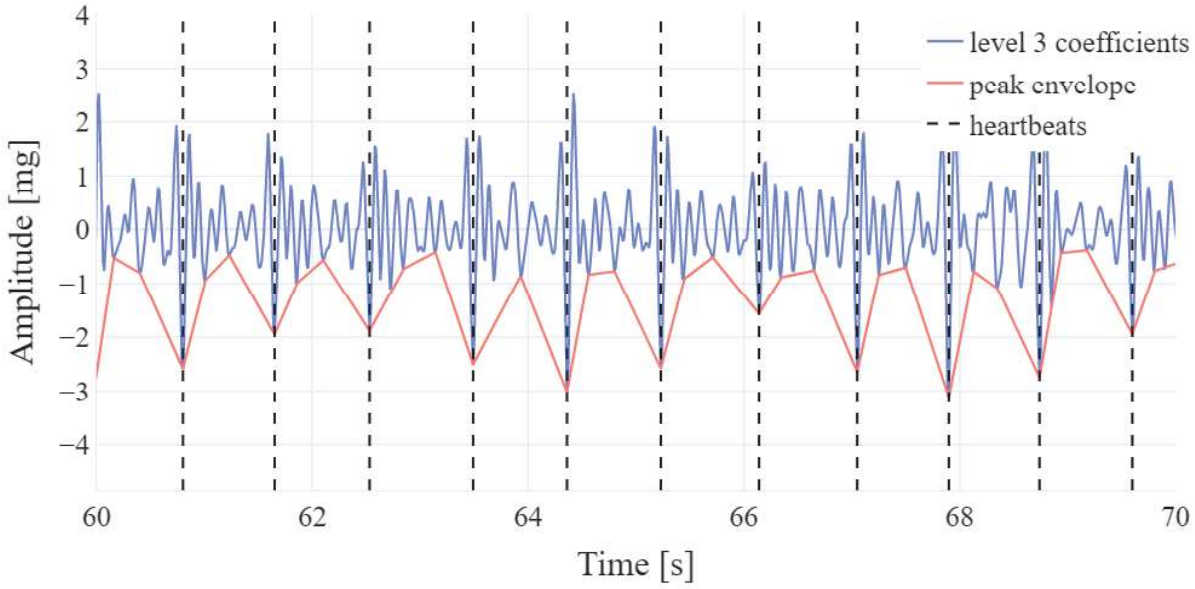

Figure 94: Envelope extraction on a wavelet coefficient.

A threshold can be used to detect heartbeats on this simplified waveform.

3.3.1.7. Template matching

In template matching methods, a heartbeat shape is modeled and cross-correlated to the signal. The heartbeat shape can be estimated manually [37] [153] or automatically [40][41].

However, the cross-correlation function may be difficult to threshold because of the amplitude of the IJK complex. The cross-correlation function R is defined by Equation (47), with T the template of length N and x the ballistocardiogram.

Figure 95A illustrates the cross-correlation of a ballistocardiogram with a heartbeat template. As the ballistocardiogram is amplitude-modulated by the respiration, the cross-correlation oscillates and may be uneasy to threshold. A normalized cross-correlation $\tilde{R}$, as defined by Equation (48), Equation (50) and Equation (51), gets rid of most of the amplitude variability as shown in Figure 95B.

A

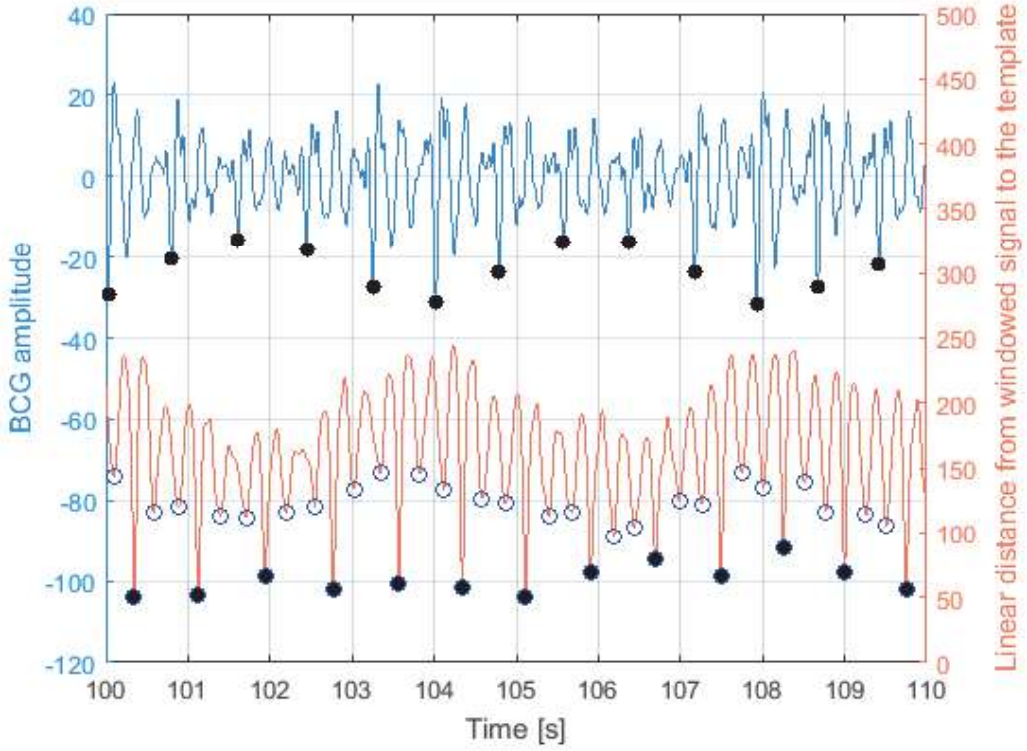

B

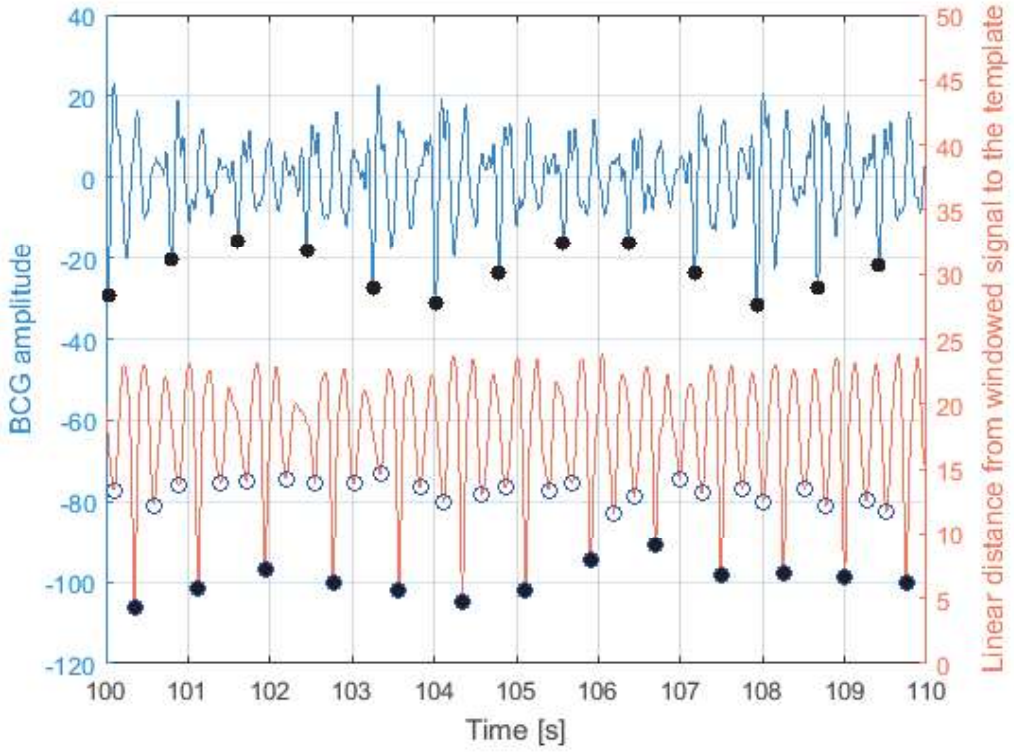

Figure 95: Brute (A) vs normalized (B) correlation coefficient and heartbeat detection.

$$R(n) = \sum_{m=0}^{N} T(m) \cdot x\left(n + m - \frac{N}{2}\right) \tag{47}$$

$$\tilde{R}(n) = \frac{\sum_{m=0}^{N} \tilde{T}(m) \cdot \tilde{x}\left(n + m - \frac{N}{2}\right)}{\sqrt{\sum_{m=0}^{N} \tilde{T}(m)^2 \cdot \sum_{m=0}^{N} \tilde{x}\left(n + m - \frac{N}{2}\right)^2}} \tag{48}$$

$$HR(n_i) = 60.\frac{1}{BB(n_i)} = 60.\frac{1}{n_i - n_{i-1}} \text{ bpm} \tag{49}$$

$$\tilde{T}(m) = T(m) - \underset{0 \le k < N}{\text{mean}}\, T(k) \tag{50}$$

$$\tilde{x}(m) = x(m) - \underset{0 \le k < N}{\text{mean}}\, x(m + k) \tag{51}$$

3.3.2. Dynamic Time Warping

We present a new method to detect heartbeats based on a template matching algorithm improved by DTW and heartbeat normalization [128]. The resulting detection is robust to noise and heartbeats variability. The method has been tested against the CHArt database.

In this section, as well as in Section 3.3.3, the J peak corresponds to the minimum amplitude of heartbeats.

The ultimate goal of the methods is to accurately detect heartbeats in BCG, for heart rate and HRV analyses. Before the detection algorithm, motion-free BCG signals were manually isolated. In this work, we focus on these signals. Figure 96 illustrates the methods.

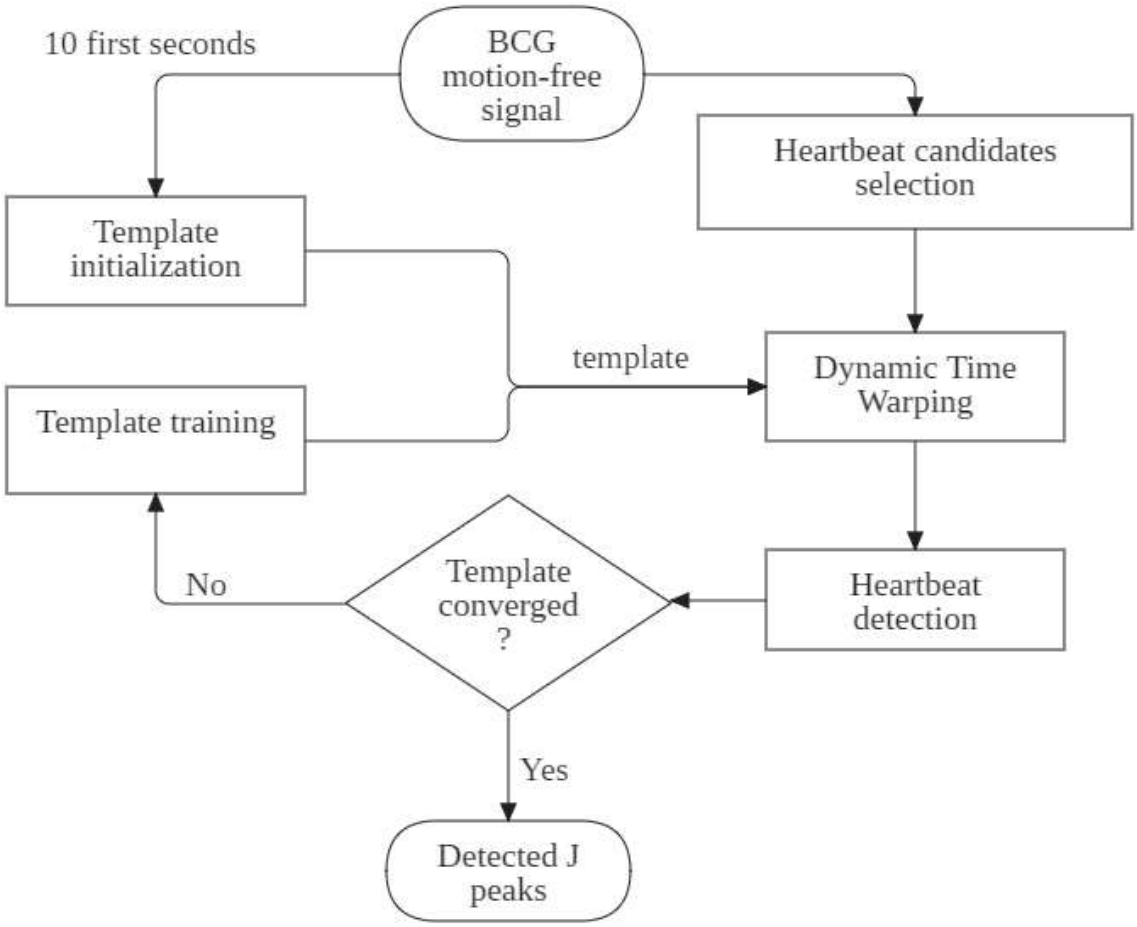

Figure 96: Flowchart of the DTW template matching algorithm.

3.3.2.1. Template initialization

In template matching methods, a template helps recognize similar patterns in the signal; it is often defined manually. In our case, a heartbeat template is automatically initialized for each participant in the following manner. An envelope detection algorithm based on a Hilbert transform is applied on the ten first motion-free seconds of the BCG signal. Local minima, spaced by a minimum delay Δt depending on an $\widetilde{HR}$ estimate of the heart rate, are detected. The $\widetilde{HR}$ estimate equals 60 times the fundamental frequency of the BCG envelope's Fast Fourier Transform. Segments, starting from one of these local minima to another one, are very likely to include one heartbeat each and are thus called inter-beat intervals IBI. Global minima of IBIs are probably J peaks, as illustrated in Figure 97.

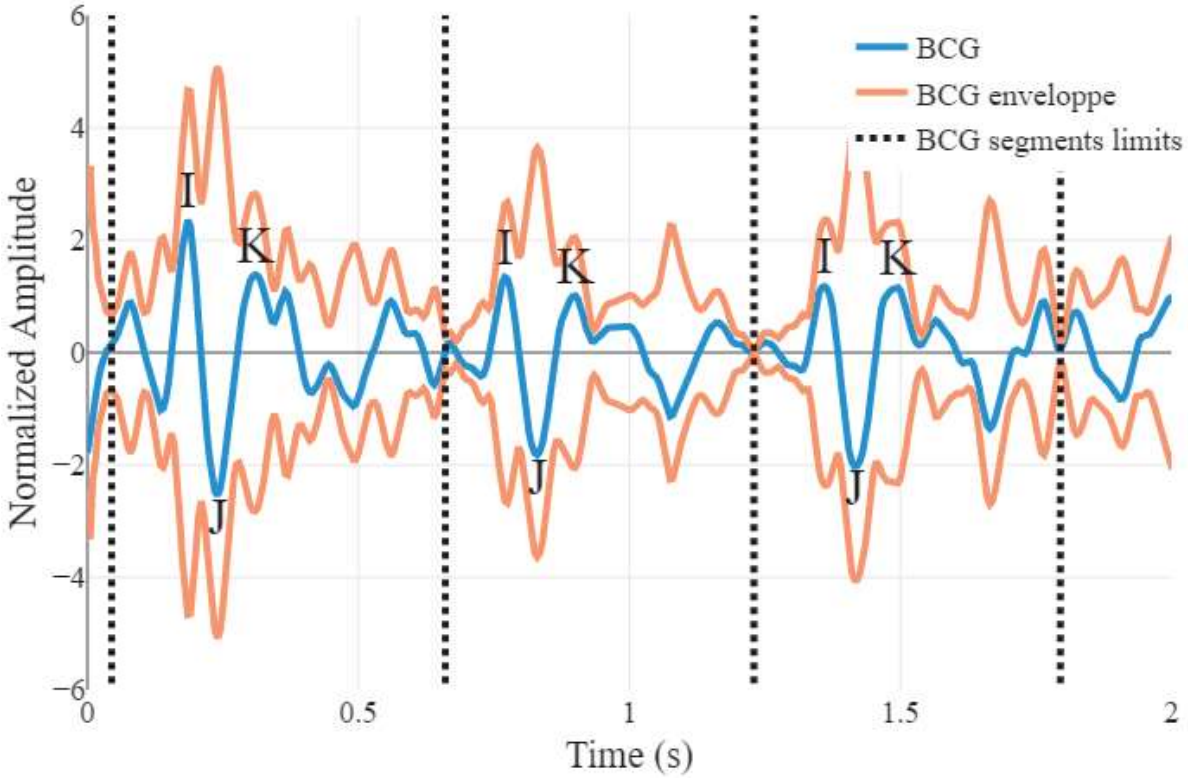

Figure 97: BCG envelope detection and segmentation.

In Figure 98, IBIs are J peaks synchronized, z-score normalized, and averaged altogether. Normalizing IBIs is necessary to preserve the shape of heartbeats and to overcome amplitude variability issues. The initial heartbeat template is parametrized by its length L and the J peak index i_J.

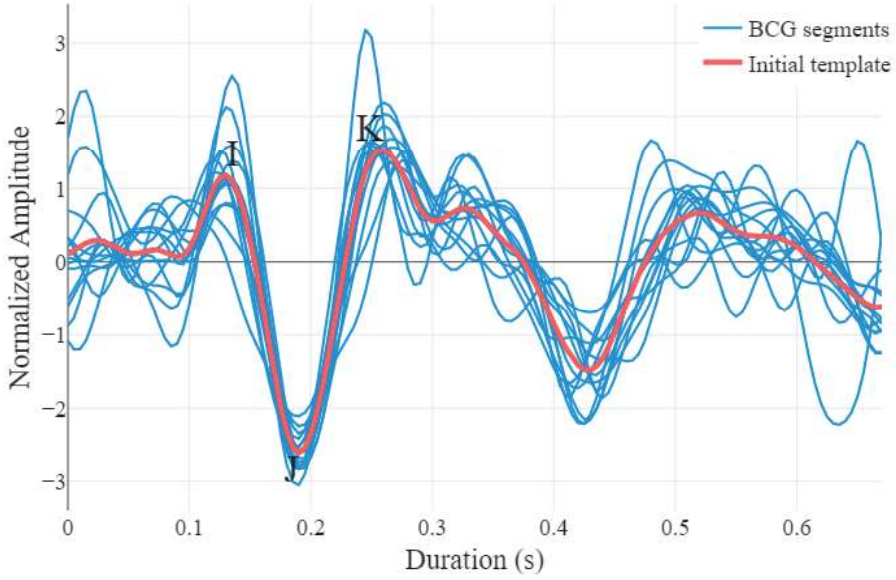

Figure 98: Initialization of the template.

3.3.2.2. Heartbeat candidates selection

To recognize patterns similar to the initialized template, the BCG signal is sliced into L-long IBIs called heartbeat candidates. Local minima of the BCG signals are detected as potential J peaks of heartbeat candidates. Heartbeat candidates are IBIs shortened to LL with J peak at index i_Ji$_J$. There are potentially about 25 heartbeat candidates per second because the low-pass cut off frequency is 25 Hz; features like the minimum distance between peaks or minimum height of peaks can help reduce the number of candidates.

3.3.2.3. Dynamic Time Warping

Heartbeat candidates must be compared with the template in such a way that time variability issues are overcome. Dynamic Time Warping (DTW) is a method for measuring similarity between two time-series which are globally or locally delayed. By aligning the sequences in time, DTW is independent of the non-linear time variability of the sequences. It is widely used for pattern recognition in time series. It has been used in BCG for evaluating the potential changes in the signal induced by different respiratory patterns and posture [168].

Optimization, in terms of normalization, endpoints weighting, and warping constraint has been performed [169]. Firstly, the initial template and heartbeat candidates are z-score normalized and multiplied by a tapered cosine window to smooth endpoints and force a zero value. Secondly, the width of the warping path is constrained to 5 samples by a Sakoe-Chiba band, which corresponds to 25 ms of local delays. In fact, as the maximum frequency of the signal is limited to 25 Hz, adjacent local minima are minimally spaced by 40 ms. If time-warping were longer than this delay, heartbeat candidates might be confounded. Figure 99 illustrates a warping between a heartbeat candidate and the template.

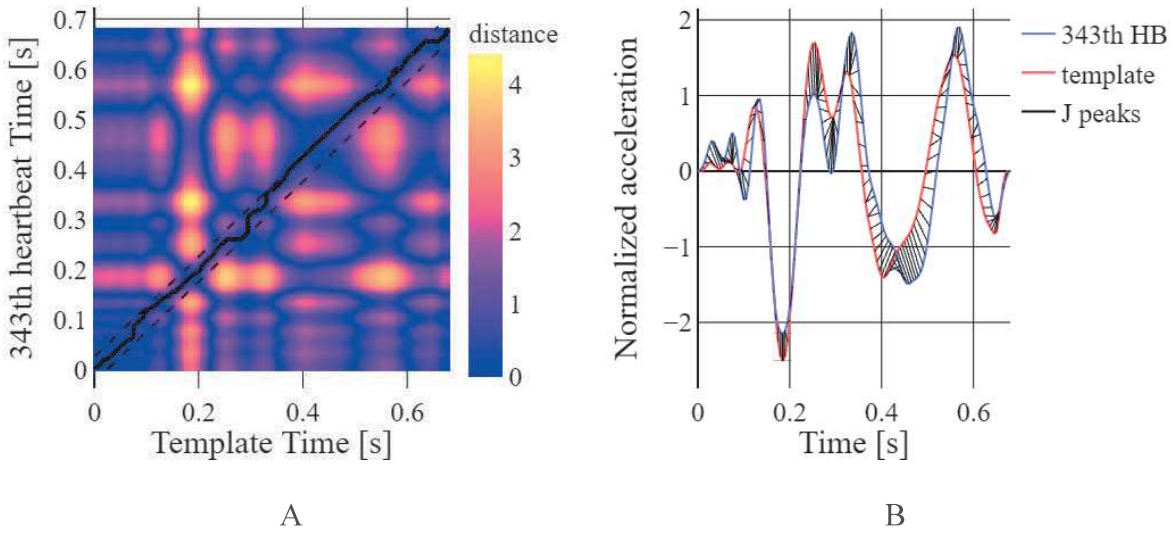

Figure 99: Pairwise Euclidean distance matrix of a heartbeat candidate and the template (A), and warping of the two waveforms (B).

3.3.2.4. Heartbeat detection

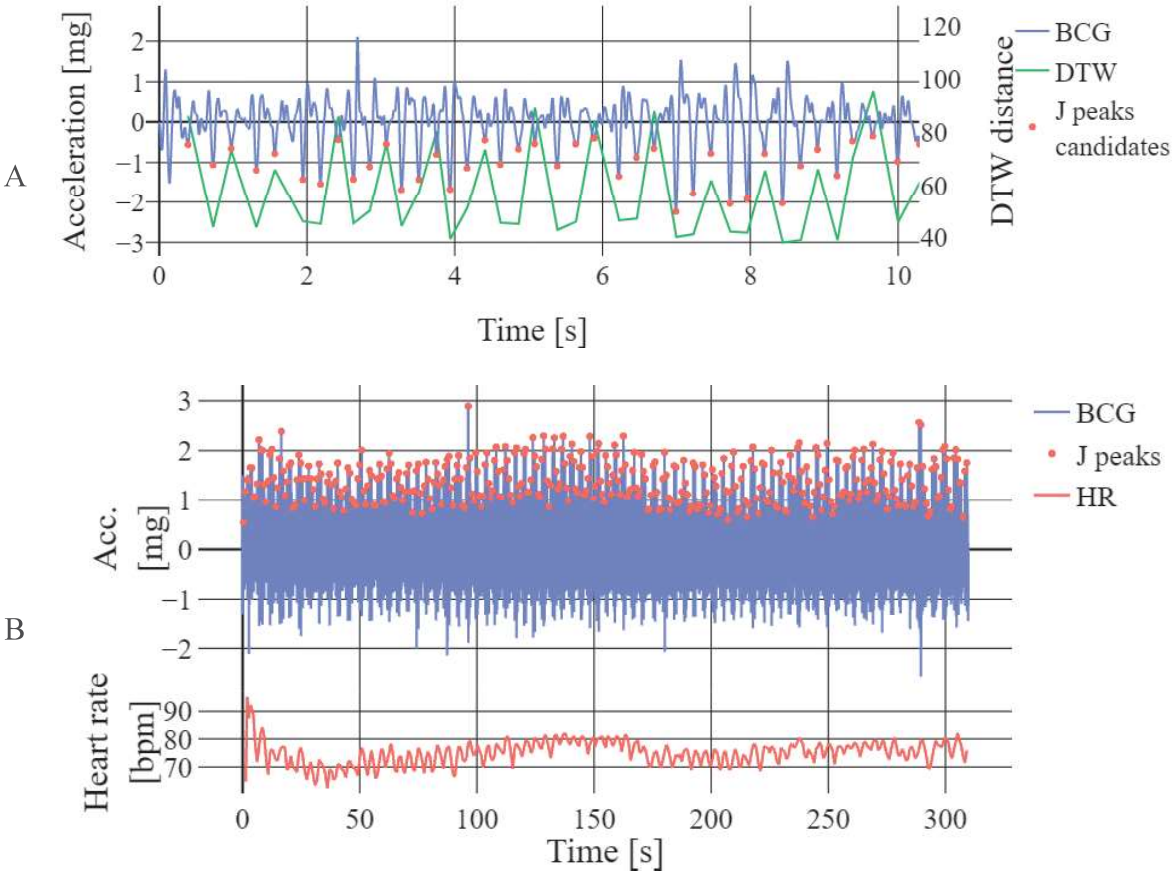

Figure 100: DTW distance of local minima with the template and heartbeat detection (A), and heart rate measurement (B).

Heartbeat candidates are sorted in a buffer by their DTW distance with the template. Starting from the smallest DTW distance, heartbeats candidates are discarded from the buffer as soon as they are closer in time than Δt to a heartbeat candidate with smaller DTW distance. Beat-to-beat delays, heart rate series, and HRV are computed from J peak position of the remaining heartbeat candidates. Figure 100 illustrates the heartbeat detection in this algorithm.

3.3.2.5. Template training

The initial template is an average of IBIs synchronized with their probable J peaks for the ten first seconds. Its shape may differ from actual heartbeats, consequently, the template must be refined. In the template training step, IBIs are updated with the new detected J peaks and the trained template is the average of IBIs synchronized with these J peaks. The previous steps of optimization, DTW execution, and heartbeat detection are then iterated to make sure that no false positive or false negative occurred when the template differed from actual heartbeats. Iterations are executed until the template converges (two iterations are generally enough for a ten-second-long BCG signal). An example is given in Figure 101.

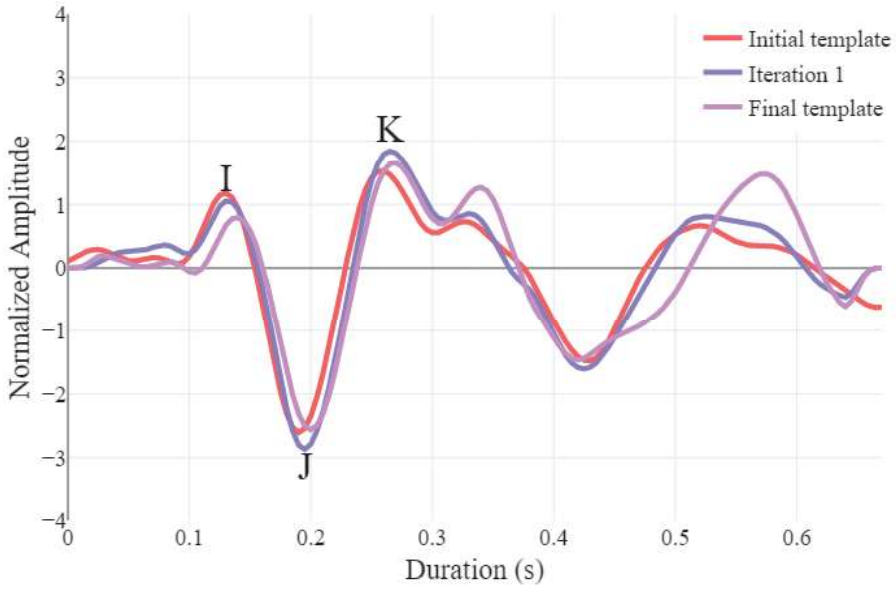

Figure 101: Refinement of the template.

3.3.2.6. Results and discussion

The DTW template matching algorithm presented in this work has been tested on the CHArt BCG database described in Section 3.1.1. A medical expert manually checked every heartbeat using dedicated data visualization software. A detected heartbeat is classified as a true positive only if its J peak is at the same location as the J peak of a real heartbeat. Overall records (M = 14139 real heartbeats), false positives (FP), true positives (TP), and false negatives (FN) are reported in Table 10. Specificity was not computed because true negatives are ill-defined.

Table 10: Truth table for detection of heartbeats.

M = 14139	Heartbeat	No heartbeat
Detected	TP = 13523	FP = 433
Undetected	FN = 616	

The overall sensitivity and positive predictivity are 95.6 % and 96.8 % respectively, with records' SNR ranging from 2.0 to 14.6. If we separate records whose SNR are lower than 3 (four records) from those higher than 3 (six records), sensitivity and positive predictivity will be 85.3% and 88.5% in the noisiest case; 98.7 % and 99.2 % in the second case. Figure 102 shows the influence of the SNR on the sensitivity and positive predictivity.

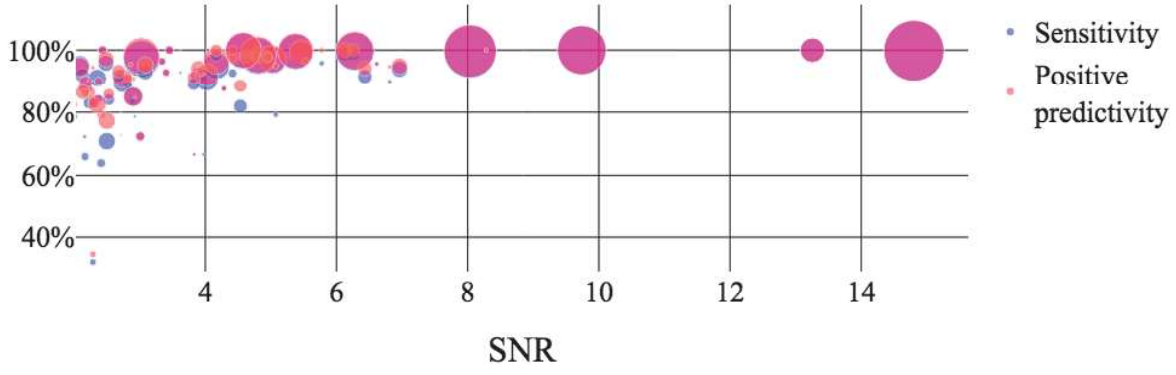

Figure 102: SNR of BCG segments and their corresponding sensitivities and positive predictivities. Bullet size is proportional to segments' durations.

We presented a template matching method for automatically detecting and determining the shape of heartbeats in BCG signals, which solves amplitude and time variability issues by dynamic time warping and normalization. This algorithm was successfully tested on a database with varying conditions of noise.

Synchronized gold standard physiological measurements such as ECG were missing, so detected heartbeats were checked manually. This process is tedious especially in noisy conditions where it is difficult to manually label heartbeats. Moreover, the heartbeat detection step of the algorithm forces a minimum delay between two consecutive heartbeats based on an estimation of the average heart rate. This strong assumption might be locally refined using Short-Term Fourier Transform depending on the length of the signal. Besides, as heartbeats are selected by their ascending DTW distance with the template, one badly labeled heartbeat often leads to multiple false positives in its neighborhood; this issue could be solved by adding features for the heartbeat detection step.

3.3.3. Hidden Markov Models

Another way to non-linearly model the signal is to use Hidden Markov models. Many physiological signals, due to their pseudo-periodicity, tend to be well modeled by Gaussian Hidden Markov Models (HMM). For example, ECG signals might be modeled as a recurrent sequence of states P, Q, R, S, T peaks, which generate voltages amplitude that follow different gaussian laws and have different durations [170] [171] [172] [173]. Seismocardiograms, i.e. cardiac signals measured by the thoracic acceleration, have also be modeled using a different architecture with more states [174] to measure beat-to-beat intervals. Due to similarities between SCG and BCG signals, this last method could be applied to BCG. However, it has several drawbacks. Firstly, it does not detect heartbeats but only delays between heartbeats because no state is associated with a fiducial point. Secondly, it is patient-specific and needs

manual annotations for every new subject to train the HMM. Thirdly, it is computationally expensive because of the high number of states, typically hundreds.

In this context, we present a new method, inspired by [174], to detect BCG heartbeats based on a patient-independent HMM and a model reduction algorithm. The resulting detection is robust to noise and heartbeats variability. The CHArt database was used to test detection performances.

In the next sections, the methods are divided into three: the patient-dependent HMM, the HMM reduction, and the patient-independent HMM. The first subsection explains how a BCG signal may be modelled by a Gaussian HMM, with a focus on initialization and training, to detect heartbeats. The second subsection explains how a patient-dependent HMM may be reduced to lower the computation cost of the heartbeat detection algorithm. The third subsection explains how a patient-independent HMM may be designed to detect heartbeats of new subjects in a supervised manner.

In this section, as well as in Section 3.3.2, the J peak corresponds to the minimum amplitude of heartbeats.

3.3.3.1. Theory of Hidden Markov Models

Before going into the details of the methods, here is a quick reminder of HMM notions. An HMM is a Markov model, i.e. a stochastic model for randomly changing processes, with an underlying or hidden state sequence [175]. The random process or observation sequence $y = \{y_t\}_{t \leq L}$ is here a L long motion-free ballistocardiogram. The associated state sequence is noted $x = \{x_t\}_{t \leq L}$. The HMM architecture, called one-way sequential Gaussian HMM, is illustrated in Figure 104 with N possible states, where N depends on the sampling frequency. Every fiducial point, for example, the J peak, corresponds to a specific state. The remaining states correspond to intermediates states between fiducial

points; in particular, the state 1 corresponds to the longest pause between two heartbeats, typically the heart diastole.

The HMM also depends on four other parameters: the initial state probability π defines the starting state probability – Equation (52); the state transition matrix A defines the probability of going from one state to another one – Equation (53); the emission probabilities, i.e. the mean μ and the standard deviation σ, defines the gaussian probability density function of observations in every state – Equation (55). In these equations, $P(\alpha|\beta)$ is the probability of α given β.

$$\pi = \{\pi_i\}_{i\leq N} = \{P(x_0 = i)\}_{i\leq N} \tag{52}$$

$$A = \{A_{ij}\}_{i,j\leq N} = \{P(x_t = j|x_{t-1} = i)\}_{i,j\leq N}\ \forall t \leq L \tag{53}$$

$$(\mu,\sigma) = \{(\mu_i,\sigma_i)\ |P(y_t|x_t = i) = \frac{1}{\sigma_i\sqrt{2\pi}} e^{-\frac{1}{2}\left(\frac{y_t-\mu_i}{\sigma_i}\right)^2}\ \forall t \leq L\}_{i\leq N} \tag{55}$$

$$HR(n_i) = 60.\frac{BB(n_i)}{n_i - n_{i-1}} = 60.\frac{f_s}{n_i - n_{i-1}} \tag{54}$$

3.3.3.2. *Patient dependent HMM*

In this subsection, the authors focus on a single L long motion-free BCG, such that $\frac{L}{f_s} > 10$ s, which is the observation sequence y.

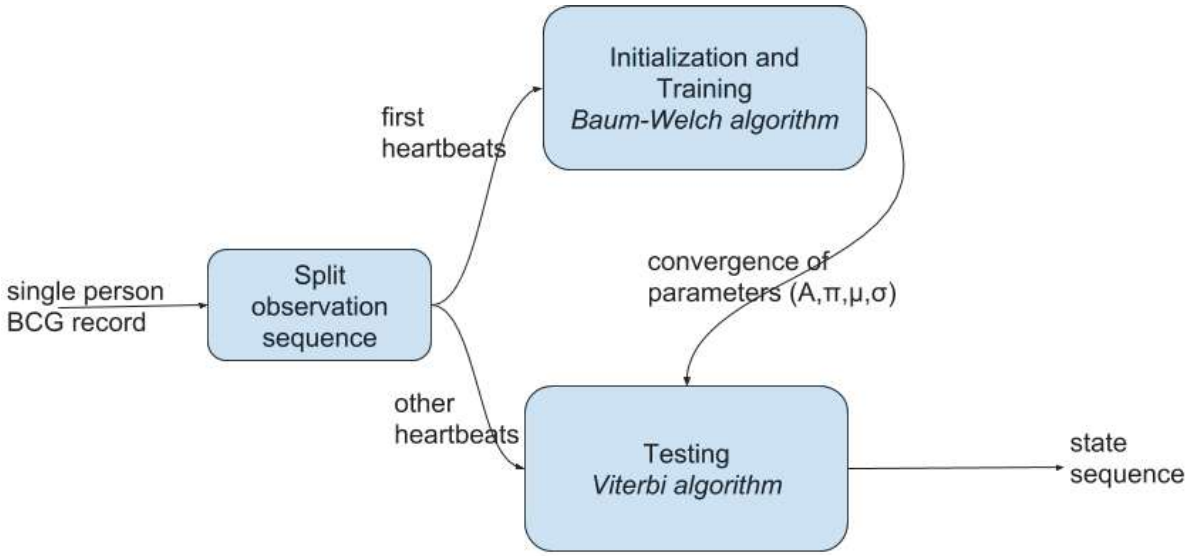

Figure 103: Pseudo algorithm of the patient dependent HMM.

The observation is split in a training test, used for initializing then training the HMM, and a testing set used for state sequence estimation and heartbeat detection. Figure 103 illustrates the pseudo algorithm of this patient-dependent HMM design.

3.3.3.3. Initialization

The N, A, π, μ, σ parameters of the HMM are firstly initialized, as shown in Figure 105. According to the chose one-way sequential HMM architecture, the matrix transition is zeroed except the main diagonal coefficients which are set to a low probability, empirically 2 % as recommended in [128], and the first upper diagonal coefficients plus the (N,1) coefficient which are set to the 98 % complementary high probability – see Equation (56).

$$A = \begin{pmatrix} 0.98 & 0.02 & 0 & \cdots & \cdots & 0 \\ 0 & 0.02 & 0.98 & \ddots & \ddots & \ddots \\ \vdots & 0 & 0.02 & 0.98 & \ddots & \ddots \\ \vdots & \ddots & \ddots & \ddots & \ddots & \ddots \\ 0 & \ddots & \ddots & \ddots & 0.02 & 0.98 \\ 0.98 & \ddots & \ddots & \ddots & 0 & 0.02 \end{pmatrix} \tag{56}$$

$$\pi = \begin{pmatrix} \frac{1}{N} & \cdots & \frac{1}{N} \end{pmatrix} \tag{57}$$

The first row of the transition matrix, corresponding to state 1 i.e. the diastole, has inverted coefficients so 98 % on the main diagonal and 2 % on the first upper diagonal. In the case of a Markov chain, such a transition matrix would imply that on one hand, the most probable and shortest duration of crossing state 2 to state N through intermediate states is $t_{2N} = \frac{N-1}{f_s}$; on the other hand, the most probable duration of crossing state 1 to state 2, i.e. the diastole duration, is $t_{12} = \frac{\frac{\ln(0.02)}{\ln(0.98)}}{f_s} \sim 0.97$ s (where $\ln(\alpha)$ is the natural logarithm of α) which is in the diastole duration's order of magnitude.

The number of states is empirically set at $N = 100 + 1 = 101$, as recommended in [174]. It is related to the maximal measurable heart rate, here set at rest to 120 beats per minute (bpm) i.e. a 0.5 s long beat-to-beat interval. Indeed, this setting implies that the

shortest duration of a heartbeat is $t_{2N} = 0.5$ s. We noticed that HMM trained with N < 80 generally gives bad heartbeat detection results.

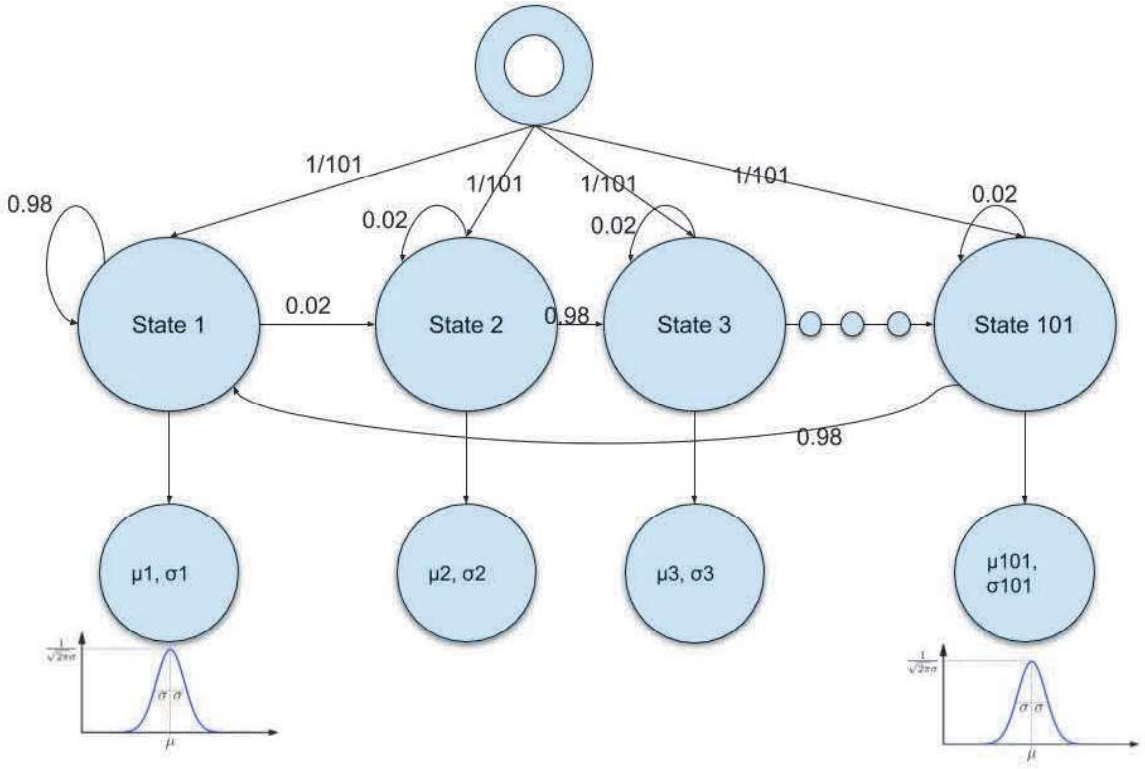

Figure 104: HMM architecture and initial parameters.

The initial state probability π is uniform in order not to assume any prior knowledge of when starts the first heartbeat – see Equation (57).

The emission probabilities μ and σ are initialized as the average and standard deviation of the estimated heartbeats in the training sequence. An envelope detection algorithm based on a Hilbert transform is applied to the BCG signal. Local minima, spaced by a minimum delay depending on a $\widetilde{HR}$ estimate of the heart rate, are detected. This $\widetilde{HR}$ estimate equals 60 times the fundamental frequency of the BCG envelope's Fast Fourier Transform. The $n_{HBtrain}$ segments starting from one of these local minima to another one are very likely to include one heartbeat each and are thus called inter-beat intervals IBI or beat-to-beat intervals. The global minima of these intervals must be J peaks, as illustrated in Figure

97. Then, the heartbeats $\{HBtrain_i\}_{i \leq n_{HBtrain}}$ are restricted to a limited length N with their J peak references synchronized and at the same J_{peak} index – see Equation (58). In the end, the emission probabilities μ and σ are initialized using the Equation (59).

$$\begin{cases} HBtrain_{p_t} = HBtrain_{q_t} \; for \; t = J_{peak} \\ len(HBtrain_p) = len(HBtrain_q) \end{cases} \forall p, q \leq n_{HBtrain} \tag{58}$$

$$\begin{cases} \pi_i = \dfrac{1}{n_{HBtrain}} \displaystyle\sum_{p=1}^{n_{HBtrain}} HBtrain_{p_i} \\ \sigma_i = \sqrt{\dfrac{1}{n_{HBtrain}} \displaystyle\sum_{p=1}^{n_{HBtrain}} (HBtrain_{p_i} - \pi_i)^2} \end{cases} \tag{59}$$

To sum up, the estimation of heartbeats uses the same method as template initialization in Section 3.3.2.1, except that heartbeats are not normalized before averaging.

3.3.3.4. Training

The training of the initial HMM is operated on the training set, i.e. the first ten seconds of the BCG signal. The Baum-Welch algorithm [175] is an expectation-maximization algorithm that, when iterated, finds a local maximum likelihood which means the convergence of the HMM parameters. Equation (60) formulates one iteration step. In Figure 105, the HMM converges after ten iterations of the Baum-Welch algorithm.

$$\left(\hat{A}, \hat{\pi}, \hat{\mu}, \hat{\sigma}\right) = \underset{A,\pi,\mu,\sigma}{\text{arglocalmax}} \, P(y|A, \pi, \mu, \sigma) \tag{60}$$

$$\hat{x} = \underset{x}{\text{arglocalmax}} \, P(x|(y, A, \pi, \mu, \sigma)) \tag{61}$$

In this example, the IJK complex is manually labeled for the μ parameter because it is the template of the training set heartbeats: $J_{peak} = 35$ corresponds to the state of occurrence of J peaks.

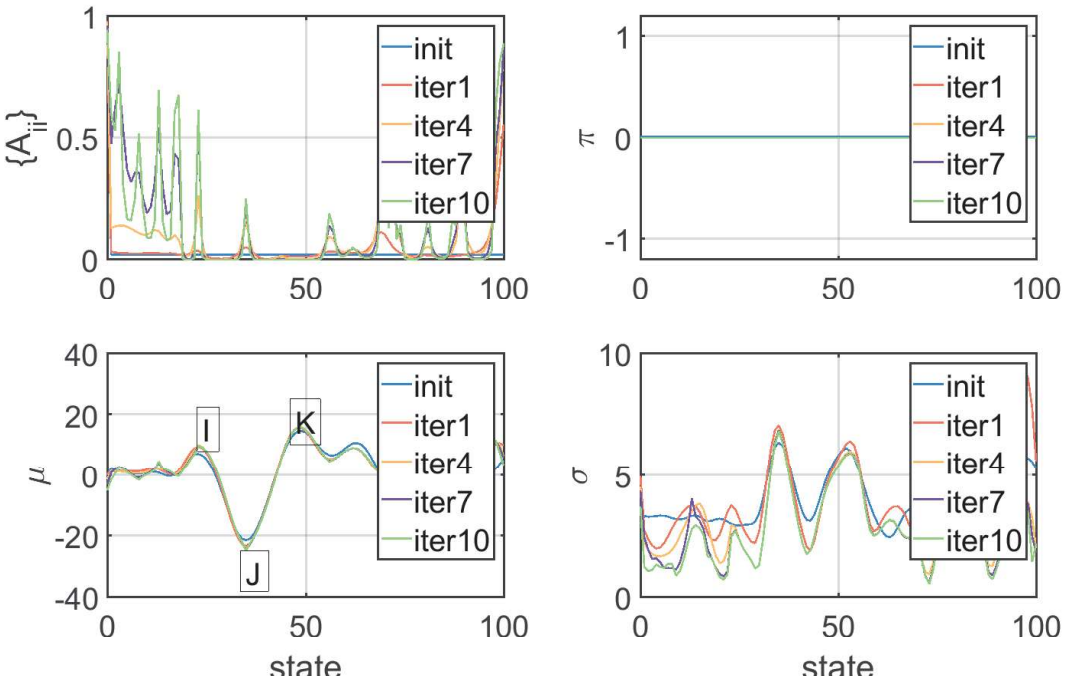

Figure 105: Training of HMM parameters on the ten first seconds, through iterations of the Baum-Welch algorithm.

However, it is also visible for the other parameters, for example, the diagonal coefficients of the transition matrix where the J_{peak} the state has a higher probability (25 %) of looping rather than going to the next state compared to its neighbors (< 2 %).

3.3.3.5. Testing and heartbeat detection

Heartbeat detection is operated on the testing set, i.e. the observation sequence after ten seconds. The Viterbi algorithm [175] finds the most probable state sequence, called the Viterbi path, underlying the given observation sequence and the HMM parameters. The Viterbi path is formulated by Equation (61) and illustrated in Figure 106. The periodicity of the state sequence reflects the periodicity of heartbeats: starting from now, the heart rate can be estimated.

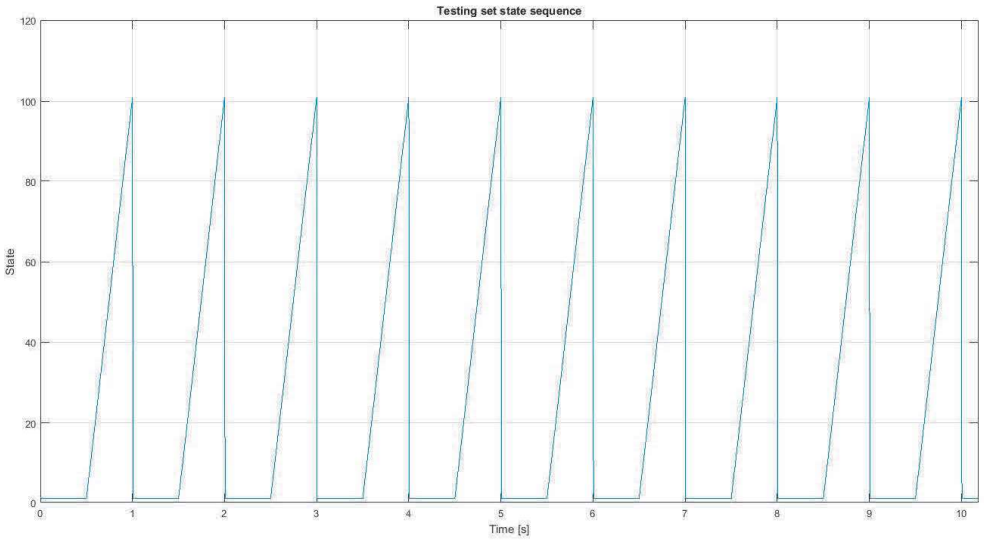

Figure 106: Viterbi path of a 10-s long observation sequence in the testing set.

However, heartbeat detection needs a few more information, for example, which state corresponds to J_{peak}. This is resolved by finding the global minimum of the μ parameter of the trained HMM because it is the template of heartbeats in the training set and this section's convention implies that the J peak corresponds to the minimum amplitude of heartbeats. In the example taken along this section, $J_{peak} = 35$.

Finding the i samples where $x_i = J_{peak}$ is not enough to detect heartbeats, because there are often consecutive states in the state sequence, especially $x_i = x_{i+1} = \cdots = x_j = J_{peak}\ for\ i < j$. This is due to high values of the diagonal coefficients of the transition matrix and the standard deviation of the emission probability function for specific states included the J_{peak} state as seen in Figure 105. In those cases, the index of the minimum in the observation sequence of such consecutive J_{peak} states is defined as the only heartbeat reference, as stated in Equation (62) where $HB_{p_{ref}}$ stands for the index of the detected J peak or reference in the p[th] heartbeat and I_{HBtest_p} the sample interval corresponding to the p[th] heartbeat.

$$HB_{p_{ref}} = \underset{i \in I_{HB_p}}{\operatorname{argmin}}\, y_i | (x_i = J_{peak}) \tag{62}$$

In the end, heartbeat references are refined by finding the index of the minimum observations in a 0.1-s long window neighborhood of the heartbeat references found using Equation (62). Figure 111 illustrates the result of heartbeats detection using a patient-dependent HMM.

The other peaks can be detected following the same procedure, but it will not be detailed in this thesis.

3.3.3.6. Robust HMM reduction

To lower the complexity and reduce the computation time, the number of states of the trained HMM may be reduced by different techniques. To our knowledge, we developed two novel techniques, dedicated to BCG signals, to reduce HMM. They are based on the same iterative process: reduce the longest consecutive states interval of μ that does not contain any extrema – see Figure 107, then run the Baum-Welch algorithm. The states corresponding to extrema, i.e. J peak, and the state 1 corresponding to the diastole are not reduced. We developed two techniques: robust HMM reduction and fast HMM reduction.

The Robust HMM reduction algorithm reduces the HMM state by state and runs one Baum-Welch iteration between two states reduction. At every step, it repeats the following procedure:

- Identify the longest consecutive states interval of μ
- Find in this interval the state with the biggest transition matrix diagonal coefficient
- Find this state's neighbor with the biggest transition matrix diagonal coefficient and fuse these two states.
- Run a Baum-Welch iteration.

The fusion f of two consecutive states is defined for vectors in Equation (63) and matrices in Equation (64), given j the lowest index state (to fuse with index j+1) and orders p and q of approximation. In this thesis, a first-order approximation is chosen: $p, q \in \{0,1\}$.

$$f: u, k \rightarrow v \; with \begin{cases} v_i = \dfrac{u_k + u_{k+1}}{2} \; if \; i = k \\ v_i = u_i \; for \; i < k \\ v_i = u_{i+1} \; for \; i > k \end{cases} \tag{63}$$

$$f: M, k \rightarrow M' with$$

$$\begin{cases} M'_{i,i+1} = \sum_{p,q} M_{i,i+1} M_{i+1,i+2} M_{i,i}^{p} M_{i+1,i+1}^{q} \; if \; i = k \\ M'_{i,i} = 1 - M'_{i,i+1} \; if \; i = k \\ M'_{i,j} = M_{i,j} \; if \; i,j < k \\ M'_{i,j} = M_{i+1,j+1} \; if \; i,j > k \end{cases} \tag{64}$$

This algorithm stops running when μ is only constituted of extrema. The advantage of this method is its robustness: the shape of the HMM parameters is similar from one step to another, thanks to the Baum-Welch iteration at every step. However, it is time-consuming.

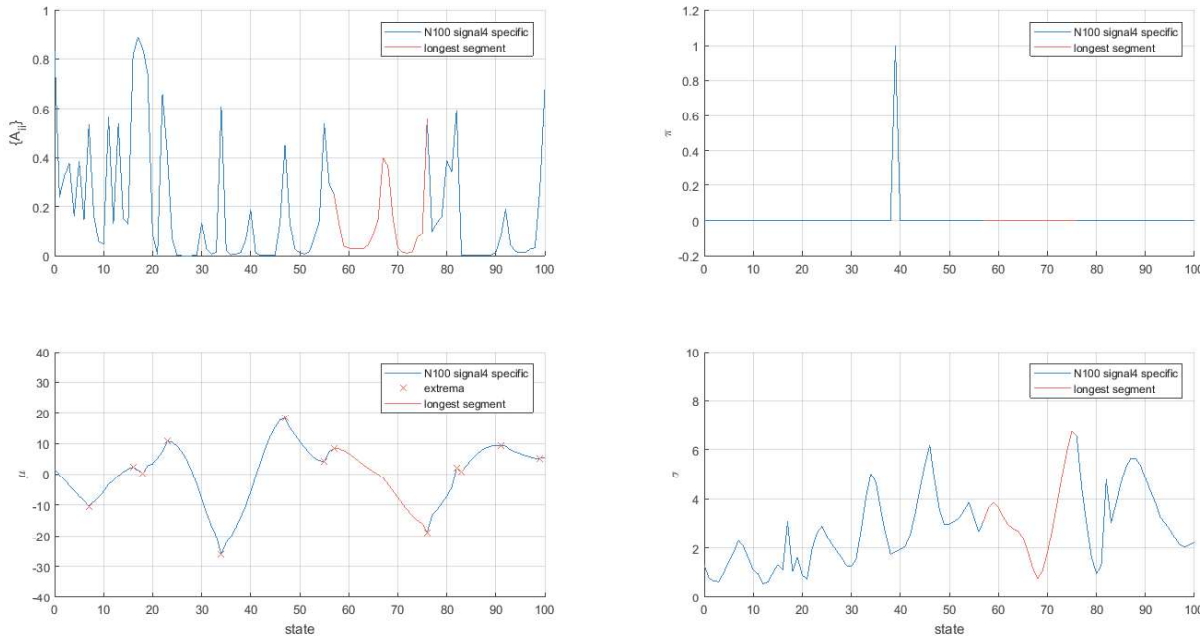

Figure 107: Identification of the longest consecutive states interval to be reduced.

3.3.3.7. Fast HMM reduction

The Fast HMM reduction algorithm is faster than the previous algorithm because it reduces multiple consecutive states before running multiple iterations of the Baum-Welch algorithm.

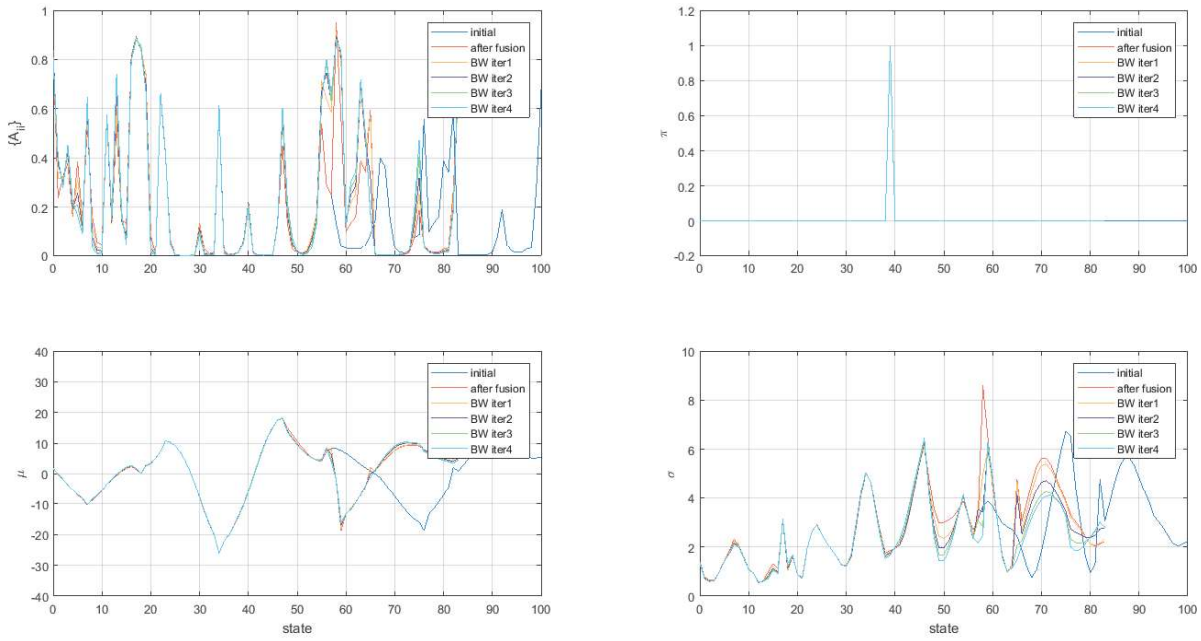

Figure 108: Reduction of the longest consecutive states' interval using the Fast HMM reduction algorithm.

At every step it runs the following process:

- Identify the longest consecutive states interval of μ
- Fuse all the states of this interval
- Run multiple iterations of the Baum-Welch algorithm until convergence.

The fusion algorithm is slightly different and will not be detailed here. Figure 108 illustrates the first iteration of the Fast HMM reduction algorithm. Again, this algorithm stops running when μ is only constituted of extrema. The advantage of this method is its rapidity: globally, it needs fewer Baum-Welch iteration steps than the Robust HMM reduction algorithm. However, it tends to be also less robust. This is better suited for low noise BCG signals.

3.3.3.8. Patient-independent HMM

The previous section focused on how to design a specific HMM, trained on a motion-free BCG. As factors influencing the waveform of a heartbeat BCG are mostly patient-dependent, we will now focus on a patient-independent HMM.

The algorithm in Figure 109 illustrates the patient-independent HMM.

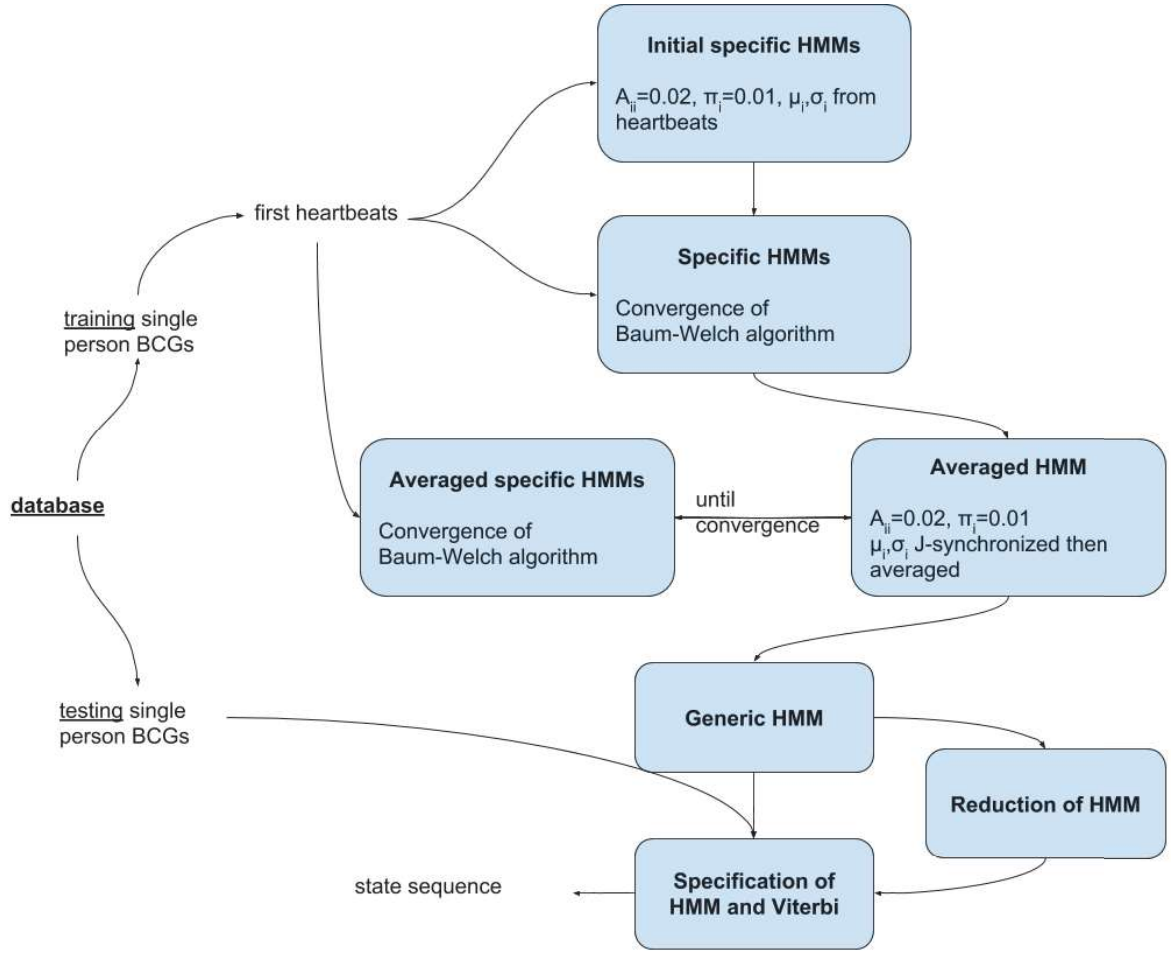

Figure 109: Training of a generic heartbeat model for supervised learning.

The training set is now constituted of the motion-free BCG of some patients of the database; the motion-free BCG of the other patients are put in the testing set. The specific hidden Markov models of the training patients are initialized and trained using the previously defined patient-dependent HMM algorithm. An averaged HMM is then initialized: μ and σ parameters are computed using Equation (59) with the μ in place of $HBtrain$; A and π using Equation (56) and Equation (57) respectively. It is then trained using the same training method as in the patient-dependent HMM algorithm, illustrated in Figure 105, with the new training set.

The resulting generic HMM can be specified, without further initialization, to any patient in the testing set: the initialization step of the patient-dependent HMM design can be

skipped. Optionally, it can also be reduced using either the Robust HMM reduction algorithm or the Fast HMM reduction algorithm, to limit the computation time, as shown in

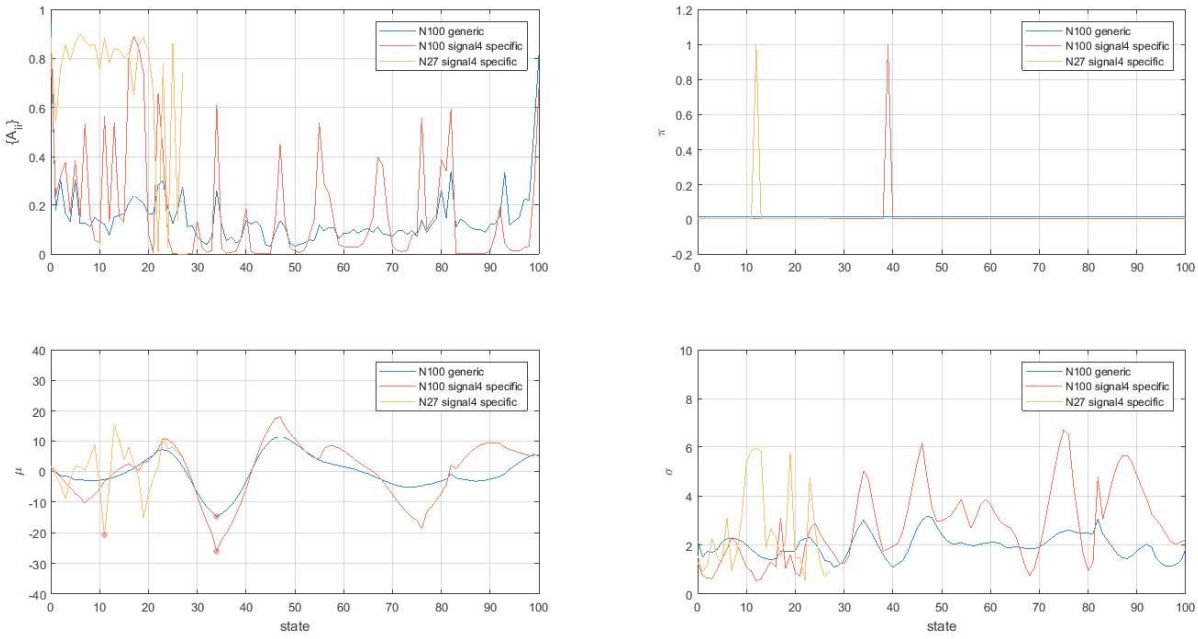

Figure 110: Patient-specific HMM computed from a patient independent HMM and reduced using the Robust HMM reduction algorithm.

3.3.3.9. Performance

The patient-dependent HMM and patient-independent HMM algorithms, with or without the optional Robust or Fast HMM reduction algorithms presented in this work, have been tested on the CHArt database. Performances are being processed and compared to other algorithms.

A

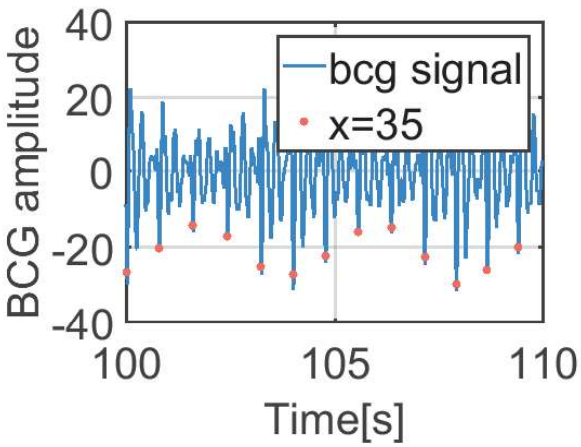

B

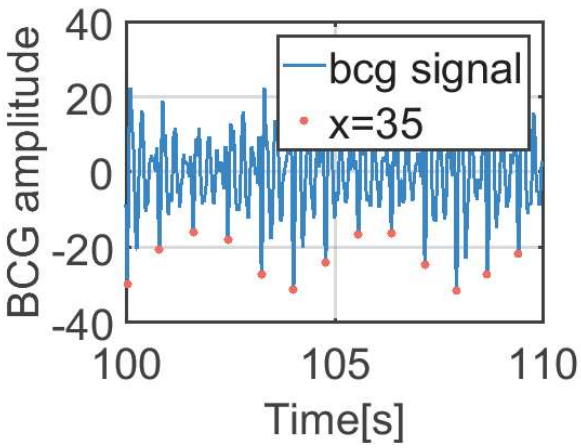

Figure 111: Result of heartbeat detection using a patient-dependent HMM before (A) and after (B) refinement.

Figure 111 shows the results of a patient-dependent HMM without reduction, before and after refinement. Figure 112 shows the heartbeat detection result using a patient-dependant HMM and the associated beat-to-beat series.

A

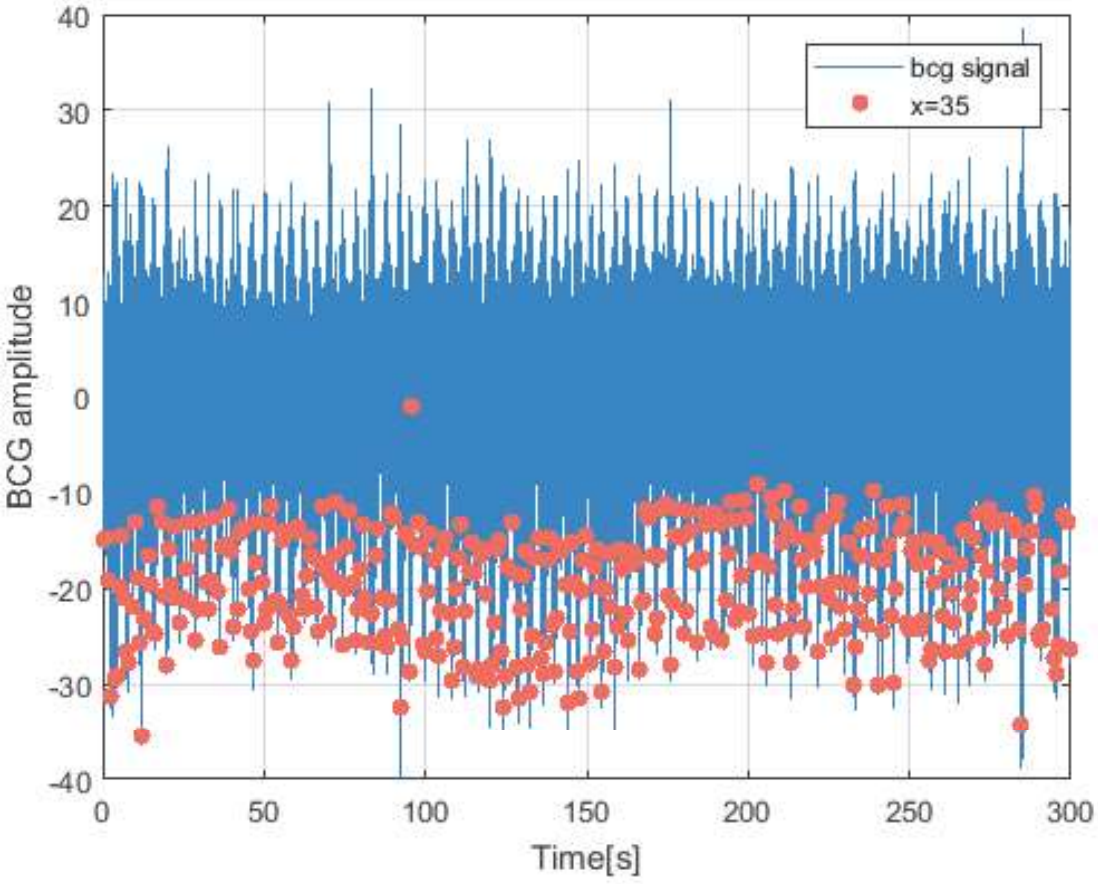

B

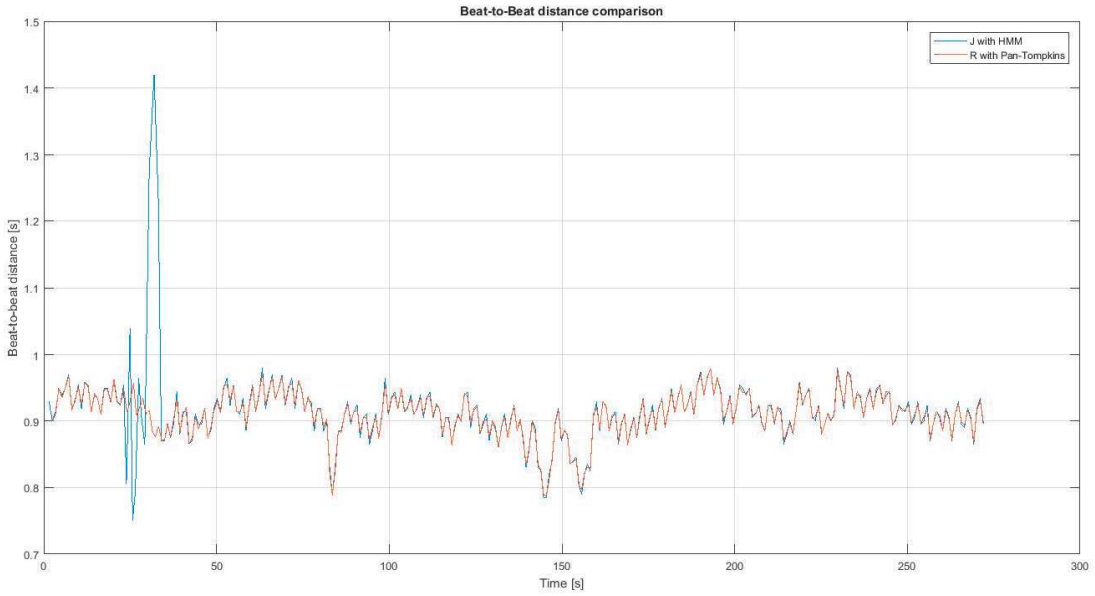

Figure 112: HMM heartbeat detection (A) and beat-to-beat series after refinement (B)

3.3.3.10. Delay of computation

The optional reduction step decreases the computation time of training (Baum-Welch iterations) and testing, either the Viterbi algorithm or labeling heartbeats, as shown in Figure 113.

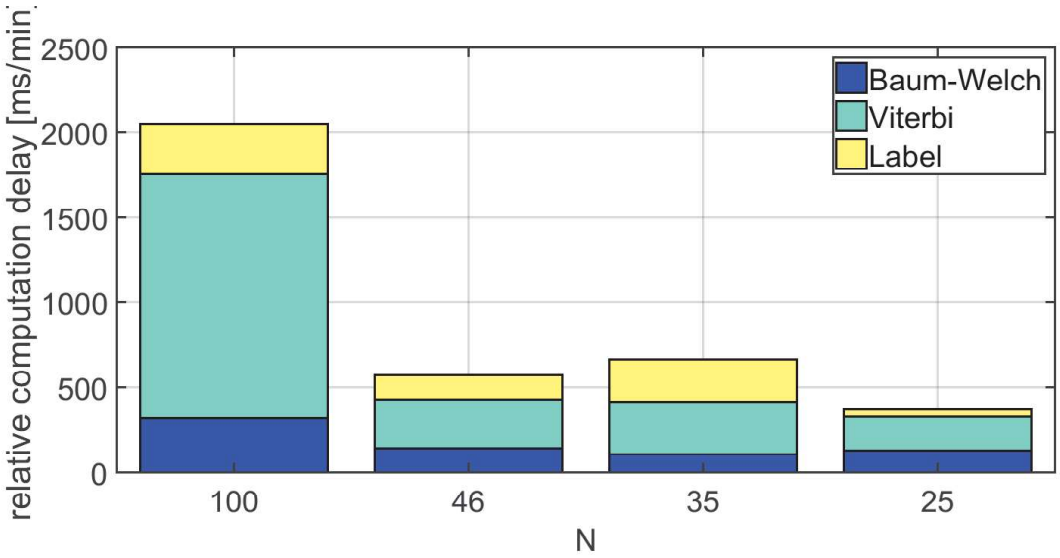

Figure 113: Computation time of the training and testing of a patient-dependent HMM with Robust HMM reduction depending on the HMM number of states.

The computation time was measured on a Thinkpad T400 portable computer and Cython libraries. This figure shows the advantages of decreasing the number of states in the Hidden Markov model in terms of computation time.

3.3.4. U-Net Neural network

Another way to non-linearly model a ballistocardiogram is by using neural networks. Neural networks have been used to detect and classify heartbeats and fiducial points in ECG signals [176]. Convolutional neural networks have been applied to detect IJK segments in BCG, with a rather low accuracy of 88% [177]. U-Net, a recent neural network architecture, has achieved impressive results for ECG delineation [178], with up to 99.9% F1 score for QRS segmentation and a small dataset. This method is applied to BCG heartbeat detection in this work.

In this context, we introduce a new method to segment IJK complexes and detect heartbeats in BCG based on a U-Net model. This method is tested on the LSI database.

3.3.4.1. U-Net architecture

The role of the neural network is to take BCG records as inputs and find for every record sample its probability of belonging to the IJK class or not.

The neural network for segmenting the records is based on a U-Net architecture [179], with two symmetric paths and mono-dimensional inputs. It is parametrized with the same settings as in [178], which proved to be efficient for electrocardiogram delineation.

On the left side of Figure 114, the contraction path or encoder finds what information is present in the record. It is constituted of row repetitions, where one row includes two sequential convolution layers ($kernel\_size = 9$, $strides = 1$ and same padding), with batch normalization and ReLU activation. Sixteen filters are used for the first convolution layers.

Each row is followed by a MaxPooling layer which subsamples the data with $pool\_size = 2$, and the filter numbers of the convolution layers in the rows are doubled.

On the right side, the role of the expanding path or decoder is to localize this information in the record. It is constituted of row repetitions, where one row includes two sequential convolution layers ($kernel\_size = 9$, $strides = 1$ and same padding), with batch normalization and ReLU activation. Each row is preceded by a concatenation layer, fed by a transposed convolution layer (with $kernel\_size = 8$, $strides = 2$ and same padding) following the previous row, and the output of the corresponding encoded row.

In the expanding path, the number of filters of the convolution layers is divided by two, row after row.

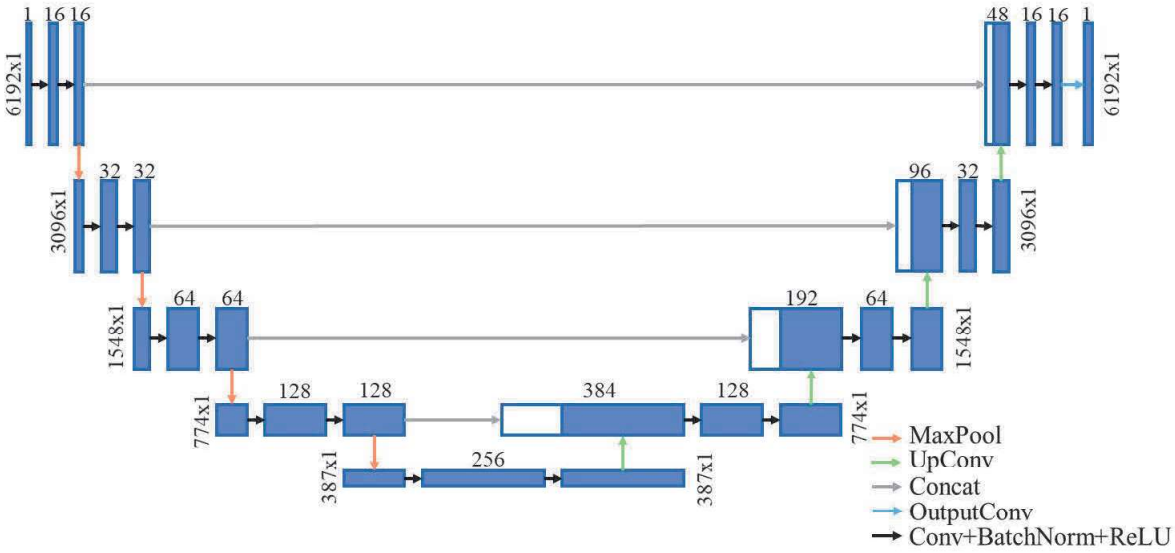

Figure 114: Neural network architecture, inspired by an electrocardiogram delineation U-Net [168].

In this architecture, the input length must be multiples of two power the number of subsampling steps, e.g. 16. BCG records are thus shortened to 6192 samples which approximately corresponds to 30 seconds long records. In the end, i.e. on the top right side of Figure 114, a convolution layer (one filter, $kernel\_size = 1$, $strides = 1$ and valid padding) and a sigmoid activation function are used to find the probability of belonging to class IJK or not.

This neural network is trained using a binary entropy loss and an Adam optimizer, which is a stochastic gradient descent algorithm based on adaptive estimates of first and lower-order moments [180]. The training set includes 30 random BCG records from the 40 selected records of the database; models are trained 50 times over the training set. This process is repeated 30 times, and the model that produces the best test F1 score is kept.

To see if the neural network has not been overfitted, the loss curve along epochs is examined in Figure 115A. The precision-recall curve also gives useful hints about the U-Net ability to segment IJK, in Figure 115B. Typical trends of these curves are observed. The F1 score for IJK segmentation with the U-Net approximately equals 95%.

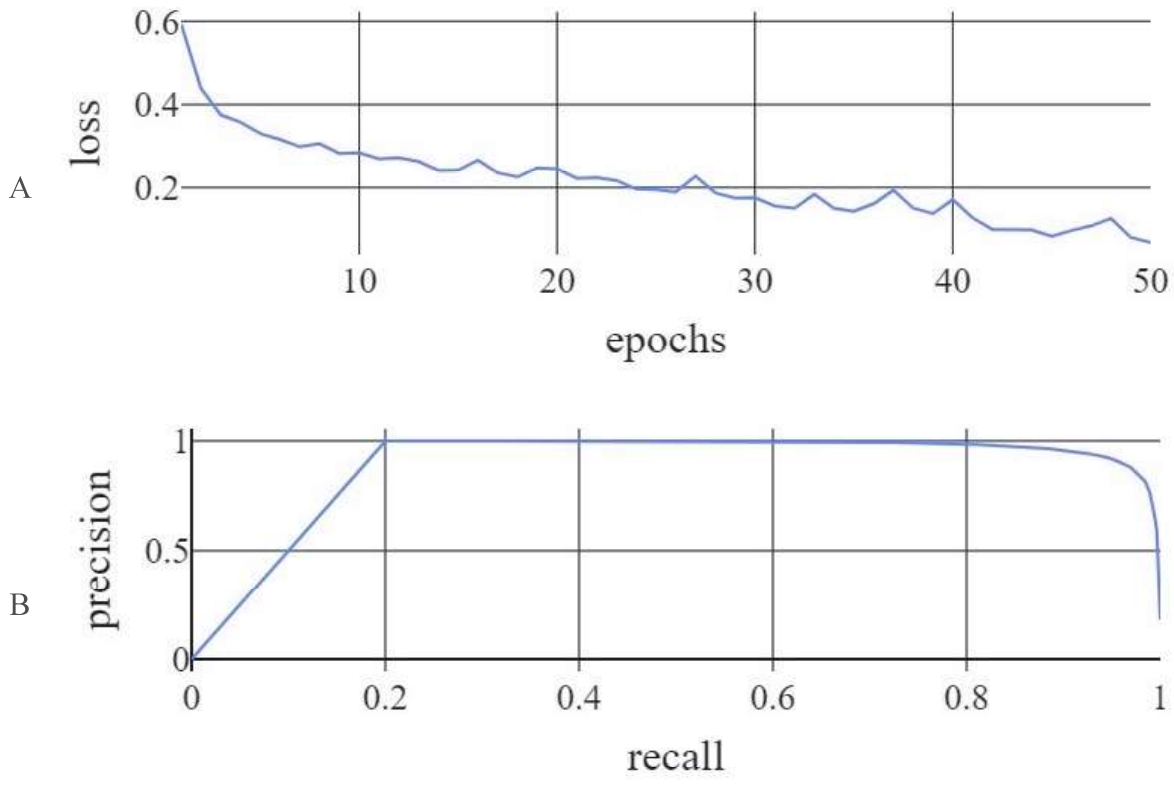

Figure 115: Binary entropy losses after epochs of training for IJK segmentation (A) and precision-recall curve for IJK segmentation by trained the U-Net (B)

3.3.4.2. Heartbeat detection algorithm

The most obvious algorithm to detect heartbeats from the output of the previously defined U-Net model is to segment IJK in the records as the samples where this class probability is the greater, then find the index of the most extreme value, i.e. maximum or minimum depending on the convention. This ideal algorithm makes the strong assumption that IJK segments are well distinguished in BCG records by the neural network, which may not always be the case because of noise.

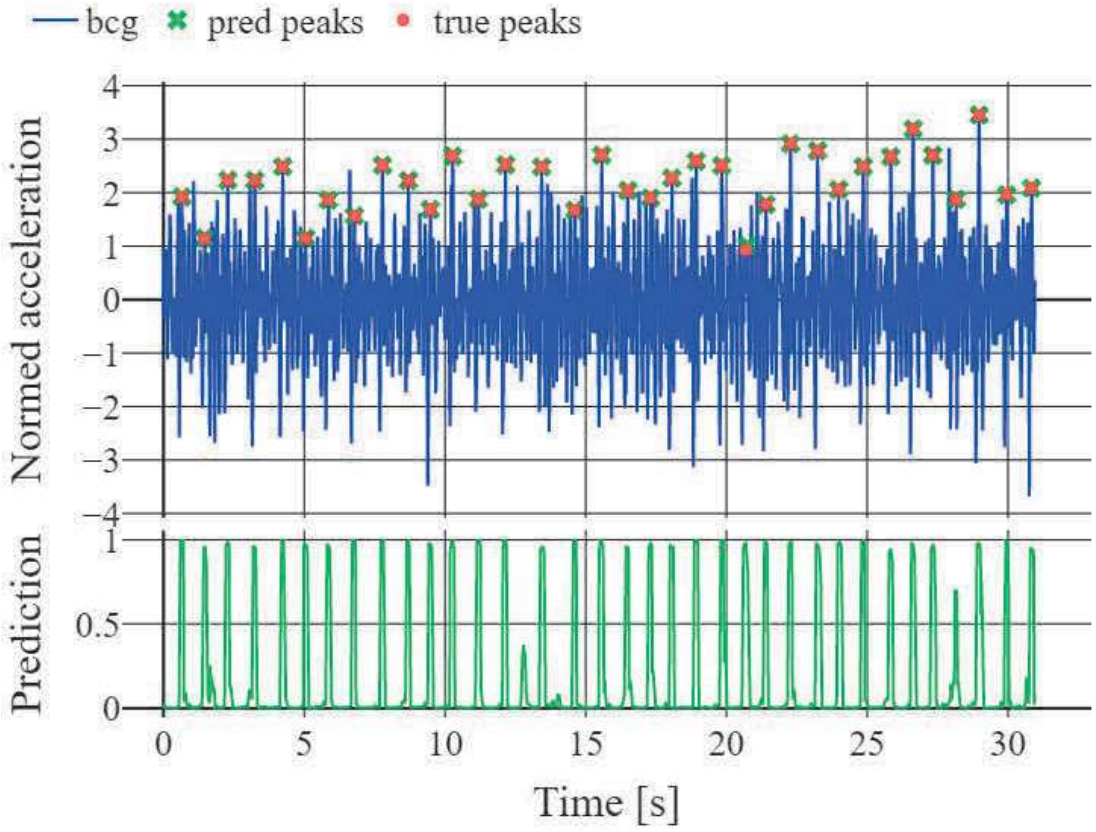

Figure 116: Example of heartbeat detection on a BCG signal with the U-Net output IJK prediction probability

A more robust approach is designed, where peaks in the neural network outputs are detected even if their height (IJK probability) is lower than 0.5. Those samples have higher probabilities than their neighbors to be part of IJK segments. Samples in the half-height width regions of the peaks are classified as IJK segments, and J peaks, i.e. heartbeats reference, are

detected as IJK segments global extrema. A minimal distance criterion for the peak finding algorithm is added to prevent non-physiological effects, e.g. resting heart rates higher than 120 beats per minute for healthy adults.

The most important performance values are heartbeat detection rates, in terms of precision and recall. An error tolerance of 150 ms on the location of heartbeats is added.

Figure 116 illustrates, on a testing record, the IJK probability of each sample, and the predicted labels by the heartbeat detection algorithm. The mean heart rate error is another performance index, based on the comparison of linear interpolations of true and predicted heart rate series. It is defined in Equation (65), where HR_{true_i} and $HR_{predicted_i}$ stand respectively for the ith sample of the linear interpolated true heart rate and predicted heart rate series; L=6192 is the number of samples in one BCG record.

$$HRerror = \frac{1}{L}\sum_{i=0}^{L}\left|HR_{true_i} - HR_{predicted_i}\right| \quad (65)$$

The performances of the heartbeat detection algorithm based on U-Net IJK segmentation on the CHArt database, are reported in Table 11.

Table 11: Statistics and HR error

set	precision	recall	F1 score	Mean HR error
test	92.1 %	80.9 %	85.7 %	5.7 bpm
train	94.2 %	92.6 %	92.9 %	3.1 bpm

3.3.4.3. Discussion

This algorithm introduced a new way to detect heartbeats in ballistocardiography that learns the heart rate physiological periodicity and heartbeats variabilities with good

performances. U-Net is relevant for this task, as it allows an intermediate segmentation step that helps to detect heartbeats in further steps.

This study has several issues that will need to be addressed in further studies. First, the recruitment process changed during the experiment, so all the materials were not adapted for adults, e.g. the children's bed. The experiment will be repeated and split between adults and children, who will use an adapted bed size. Second, many records have been discarded because of movement artifacts, consequently, the measurement protocol will be revised, for example, records' duration will be increased. If this revision is not enough to get BCG motion free segments in every record, the hardware will also be revised. Third, hyperparameters settings have been inspired by an existing electrocardiogram delineation U-Net [178]; hyperparameter optimization could be interesting to improve the BCG heartbeat detection accuracy.

Other improvements such as data augmentation and multi-class segmentation, based on the other fiducial points present in BCG, must also be investigated.

Chapter 4

4. General discussion and future perspectives

Ballistocardiographic instrumentations have been developed to amplify ballistocardiograms and record several databases. Due to the limited number of records used for Section 2.4 and Section 2.5. The performances obtained with the novel amplifiers will need to be comforted by other experiments.

Several algorithms for movement and occupancy segmentation, as well as heartbeat detection, have been detailed in this document. In further work, those algorithms will be systematically benchmarked against the reference algorithms of the literature, on all the recorded databases. Thus, the best algorithms will be quantitatively selected.

These algorithms will be tested on the acquired databases to determine if a medical-grade RPM device can be designed using ballistocardiography.

This work will be continued with applications on imagery, telehealth, neonatal care, and sleep studies.

Consolidated list of references

[1] F. Toutlemonde, "Les établissements de santé," 2019 ed., DREES, Ed., Paris, France, 2019.

[2] A. Alwan, Global Status Report on Noncommunicable Diseases 2010, World Health Organization, 2011.

[3] M. Chassang and A. Gautier, "Les Maladies Chroniques, Avis du Conseil économique, social et environnemental," 2019.

[4] M. Visscher, A. King, A. M. Nie, P. Schaffer, T. Taylor, D. Pruitt, M. J. Giaccone, M. Ashby and S. Keswani, "A Quality-Improvement Collaborative Project to Reduce Pressure Ulcers in PICUs," *Pediatrics,* vol. 131, p. e1950–e1960, 5 2013.

[5] A. A. Alwani and Y. Chahir, "Neonatal events recognition using LBP descriptor and wavelet thresholding technique," in *2014 International Conference on Multimedia Computing and Systems (ICMCS)*, 2014.

[6] A. Broderick and D. Lindeman, "Scaling telehealth programs : lessons from early adopters.," *The Commonwealth Fund,* 1 2013.

[7] S. I. Chaudhry, J. A. Mattera, J. P. Curtis, J. A. Spertus, J. Herrin, Z. Lin, C. O. Phillips, B. V. Hodshon, L. S. Cooper and H. M. Krumholz, "Telemonitoring in Patients with Heart Failure," *New England Journal of Medicine,* vol. 363, p. 2301–2309, December 2010.

[8] S. I. Chaudhry, Y. Wang, J. Concato, T. M. Gill and H. M. Krumholz, "Patterns of Weight Change Preceding Hospitalization for Heart Failure," *Circulation,* vol. 116, p. 1549–1554, October 2007.

[9] M. K. Ong, P. S. Romano, S. Edgington, H. U. Aronow, A. D. Auerbach, J. T. Black, T. D. Marco, J. J. Escarce, L. S. Evangelista, B. Hanna, T. G. Ganiats, B. H. Greenberg, S. Greenfield, S. H. Kaplan, A. Kimchi, H. Liu, D. Lombardo, C. M. Mangione, B. Sadeghi, B. Sadeghi, M. Sarrafzadeh, K. Tong and G. C. Fonarow, "Effectiveness of Remote Patient Monitoring After Discharge of Hospitalized Patients With Heart Failure," *JAMA Internal Medicine,* vol. 176, p. 310, 3 2016.

[10] D. Peretz, A. Arnaert and N. N. Ponzoni, "Determining the cost of implementing and operating a remote patient monitoring programme for the elderly with chronic conditions: A systematic review of economic evaluations," *Journal of Telemedicine and Telecare,* vol. 24, p. 13–21, 9 2016.

[11] A. Maeder, N. Poultney, G. Morgan and R. Lippiatt, "Patient Compliance in Home-Based Self-Care Telehealth Projects," *Journal of Telemedicine and Telecare,* vol. 21, p. 439–442, 11 2015.

[12] A.-S. Grenouilleau, "Stimulateurs cardiaques conventionnels," Saint-Denis, France, 2009.

[13] C.-S. Kim, S. L. Ober, M. S. McMurtry, B. A. Finegan, O. T. Inan, R. Mukkamala and J.-O. Hahn, "Ballistocardiogram: Mechanism and Potential for Unobtrusive Cardiovascular Health Monitoring," *Scientific Reports,* vol. 6, 8 2016.

[14] J. W. Gordon, "Certain Molar Movements of the Human Body produced by the Circulation of the Blood," *Journal of Anatomy and Physiology,* vol. 11, pp. 533-536, 1877.

[15] Y. Henderson, "The Mass-Movements of the Circulation as shown by a Recoil Curve," *American Journal of Physiology-Legacy Content,* vol. 14, p. 287–298, 9 1905.

[16] C. B. Heald and W. S. Tucker, "Recoil Curves as Shown by the Hot-Wire Microphone," *Proceedings of the Royal Society of London. Series B, Containing Papers of a Biological Character,* vol. 93, p. 281–298, 1922.

[17] G. Angenheister and E. Lau, "Seismographische Aufnahmen der Herztätigkeit," *Die Naturwissenschaften,* vol. 16, p. 513–515, 6 1928.

[18] E. Abramson, "Die Rückstoßkurve des Herzens (Kardiodynamogramm)," *Skandinavisches Archiv Für Physiologie,* vol. 66, p. 191–224, 7 1933.

[19] I. Starr, A. J. Rawson, H. A. Schroeder and N. R. Joseph, "Studies on the Estimation of Cardiac Output in Man, and of Abnormalities in Cardiac Function, from the Heart's Recoil and the Blood's impacts : the Ballistocardiogram," *American Journal of Physiology-Legacy Content,* vol. 127, p. 1–28, 7 1939.

[20] W. B. Fye, "A History of the origin, evolution, and impact of electrocardiography," *The American Journal of Cardiology,* vol. 73, p. 937–949, 5 1994.

[21] I. Edler and C. H. Hertz, "The Use of Ultrasonic Reflectoscope for the Continuous Recording of the Movements of Heart Walls.," *Proceeding of the Royal Physiographic Society at Lund,* vol. 24, 3 1954.

[22] P. C. Lauterbur, "Image Formation by Induced Local Interactions: Examples Employing Nuclear Magnetic Resonance," *Nature,* vol. 242, p. 190–191, 3 1973.

[23] L. Giovangrandi, Member, IEEE, O. T. Inan, Member, IEEE, R. M. Wiard and Student, "Ballistocardiography – A Method Worth Revisiting," in *33rd Annual International Conference of the IEEE EMBS Boston, Massachusetts USA, August 30 - September 3, 2011*, 2011.

[24] J. E. Smith and S. Bryan, "The Low Frequency Velocity Measurement Ballistocardiograph," *Circulation,* vol. 5, p. 892–902, 6 1952.

[25] W. Dock and F. Taubman, "Some technics for recording the ballistocardiogram directly from the body," *The American Journal of Medicine,* vol. 7, p. 751–755, 12 1949.

[26] T. J. Reeves, W. B. Jones and L. L. Hefner, "Design of an Ultra Low Frequency Force Ballistocardiograph on the Principle of the Horizontal Pendulum," *Circulation,* vol. 16, p. 36–42, 7 1957.

[27] B. M. Wright, "A Portable Ballistocardiograph," *Bibliotheca Cardiologica,* pp. 72-75, 1975.

[28] J. Alihanka, K. Vaahtoranta and I. Saarikivi, "A new method for long-term monitoring of the ballistocardiogram, heart rate, and respiration," *American Journal of Physiology-Regulatory, Integrative and Comparative Physiology,* vol. 240, p. R384–R392, 5 1981.

[29] J. Williams, "Bridge Circuits : Marrying Gain and Balance," 1990.

[30] K. Watanabe and H. Watanabe, "Study on the Non-Restrictive Vital Bio-Measurement by the Air Mattress Methods," *Transactions of the Society of Instrument and Control Engineers,* vol. 36, p. 894–900, 2000.

[31] F. Wang, M. Tanaka and S. Chonan, "Development of a PVDF Piezopolymer Sensor for Unconstrained In-Sleep Cardiorespiratory Monitoring," *Journal of Intelligent Material Systems and Structures,* vol. 14, p. 185–190, 3 2003.

[32] X. Zhu, W. Chen, T. Nemoto, Y. Kanemitsu, K. Kitamura, K. Yamakoshi and D. Wei, "Real-Time Monitoring of Respiration Rhythm and Pulse Rate During Sleep,"

IEEE Transactions on Biomedical Engineering, vol. 53, p. 2553–2563, 12 2006.

[33] P. Castiglioni, A. Faini, G. Parati and M. D. Rienzo, "Wearable Seismocardiography," in *2007 29th Annual International Conference of the IEEE Engineering in Medicine and Biology Society*, 2007.

[34] L. Dziuda, F. W. Skibniewski, M. Krej and J. Lewandowski, "Monitoring Respiration and Cardiac Activity Using Fiber Bragg Grating-Based Sensor," *IEEE Transactions on Biomedical Engineering,* vol. 59, p. 1934–1942, 7 2012.

[35] P. A. Lynn, "Recursive digital filters for biological signals," *Medical & Biological Engineering,* vol. 9, p. 37–43, 1 1971.

[36] J. R. Cox, F. M. Nolle and R. M. Arthur, "Digital analysis of the electroencephalogram, the blood pressure wave, and the electrocardiogram," *Proceedings of the IEEE,* vol. 60, p. 1137–1164, 1972.

[37] B. H. Jansen, B. H. Larson and K. Shankar, "Monitoring of the Ballistocardiogram and with the Static and Charge Sensitive and Bed," in *IEEE Transactions On Biomedical Engineering*, 1991.

[38] X. Yu, D. Dent, F. of Design and Techndogv, "Neural Networks in Ballistocardiography(BCG) Using FPGAs," in *The Institution of Electrical Engineers*, 1994.

[39] X. Yu, "A Wavelet and Multiiresolution and Neural and Network System and for BCG and Signal and Analysis," in *1996 IEEE TENCON - Digital Signal Processing Applications*, 1996.

[40] C. Bruser, K. Stadlthanner, S. de Waele and S. Leonhardt, "Adaptive Beat-to-Beat Heart Rate Estimation in Ballistocardiograms," *IEEE Transactions on Information Technology in Biomedicine,* vol. 15, p. 778–786, 9 2011.

[41] J. Paalasmaa, H. Toivonen and M. Partinen, "Adaptive heartbeat modeling for beat-to-beat heart rate measurement in ballistocardiograms," *IEEE journal of biomedical and health informatics,* vol. 19, p. 1945–1952, 2015.

[42] B. M. Appelhans and L. J. Luecken, "Heart rate variability and pain: Associations of two interrelated homeostatic processes," *Biological Psychology,* vol. 77, p. 174–182, 2 2008.

[43] H. Mandelbaum and R. A. Mandelbaum, "Studies Utilizing the Portable Electromagnetic Ballistocardiograph," *Circulation,* vol. 7, p. 910–915, 6 1953.

[44] O. P. Eduardo Pinheiro and P. Girão, "Theory and Developments in an Unobtrusive Cardiovascular System Representation: Ballistocardiography," in *The Open Biomedical Engineering Journal*, 2010.

[45] O. T. Inan, M. Etemadi, R. M. Wiard, L. Giovangrandi and G. T. A. Kovacs, "Robust ballistocardiogram acquisition for home monitoring," *Physiological Measurement,* vol. 30, p. 169–185, 1 2009.

[46] C. Bruser, J. Diesel, M. D. H. Zink, S. Winter, P. Schauerte and S. Leonhardt, "Automatic Detection of Atrial Fibrillation in Cardiac Vibration Signals," *IEEE Journal of Biomedical and Health Informatics,* vol. 17, p. 162–171, 1 2013.

[47] Z. Wang, X. Zhou, W. Zhao, F. Liu, H. Ni and Z. Yu, "Assessing the severity of sleep apnea syndrome based on ballistocardiogram," *PLoS ONE,* vol. 12, pp. 1-24, 4 2017.

[48] V. B. Aydemir, J. Fan, S. Dowling, O. T. Inan, J. M. Rehg and L. Klein, "Ballistocardiography for Ambulatory Detection and Prediction of Heart Failure Decompensation," *Journal of Cardiac Failure,* vol. 24, p. S116, 8 2018.

[49] P. Yousefian, S. Shin, A. Mousavi, C.-S. Kim, R. Mukkamala, D.-G. Jang, B.-H. Ko, J. Lee, U. K. Kwon, Y. H. Kim and J.-O. Hahn, "The Potential of Wearable Limb Ballistocardiogram in Blood Pressure Monitoring via Pulse Transit Time," *Scientific Reports,* vol. 9, July 2019.

[50] W. K. Lee, H. Yoon, D. W. Jung, S. H. Hwang and K. S. Park, "Ballistocardiogram of baby during sleep," in *2015 37th Annual International Conference of the IEEE Engineering in Medicine and Biology Society (EMBC)*, 2015.

[51] M. Erkinjuntti, K. Vaahtoranta, J. Alihanka and P. Kero, "Use of the SCSB method for monitoring of respiration, body movements and ballistocardiogram in infants," *Early Human Development,* vol. 9, p. 119–126, 2 1984.

[52] W. R. Scarborough, F. W. Davis, B. M. Baker, R. E. Mason and M. L. Singewald, "A review of ballistocardiography," *Am Heart J.,* vol. 44, pp. 910-46, 12 1952.

[53] J. L. Nickerson and H. J. Curtis, "The Design of the Ballistocardiograph," *American Journal of Physiology-Legacy Content,* vol. 142, p. 1–11, 8 1944.

[54] I. Starr and A. J. Rawson, "The Vertical Ballistocardiograph; Experiments on the Changes in the Circulation on Arising; with a Further Study of Ballistic Theory," *American Journal of Physiology-Legacy Content,* vol. 134, p. 403–425, 8 1941.

[55] V. E. Krahl, "The Electric Strain Gauge Ballistocardiograph," *American Heart Journal,* vol. 39, p. 161–173, 2 1950.

[56] K. R. Reissmann and E. G. Dimond, "Torsion Ballistocardiography: With Special Reference to Patterns in Surgically Amenable Cardiovascular Diseases," *Circulation,* vol. 8, p. 585–599, 10 1953.

[57] W. F. Hamilton, P. Dow and J. W. Remington, "The Relationship Between the Cardiac Ejection Curve and the Ballistocardiographic Forces," *American Journal of Physiology-Legacy Content,* vol. 144, p. 557–570, 9 1945.

[58] J. R. Braunstein, C. E. Oelker and R. C. Gowdy, "Design of a Two-Dimensional Ballistocardiograph," *Journal of Clinical Investigation,* vol. 29, p. 1219–1226, 9 1950.

[59] R. W. Wilkins, "A Tilting Ballistocardiograph," *American Heart Journal,* vol. 26, p. 351–354, 9 1943.

[60] W. C. Hixson and D. E. Beischer, "Biotelemetry of the triaxial ballistocardiogram and electrocardiogram in a weightless environment," 1964.

[61] J. Alihanka and K. Vaahtoranta, "A static charge sensitive bed. A new method for recording body movements during sleep," *Electroencephalography and Clinical Neurophysiology,* vol. 46, p. 731–734, 6 1979.

[62] A. Vehkaoja, S. Rajala, P. Kumpulainen and J. Lekkala, "Correlation approach for the detection of the heartbeat intervals using force sensors placed under the bed posts," *Journal of Medical Engineering & Technology,* vol. 37, p. 327–333, June 2013.

[63] B. H. Choi, G. S. Chung, J.-S. Lee, D.-U. Jeong and K. S. Park, "Slow-wave sleep estimation on a load-cell-installed bed: a non-constrained method," *Physiological Measurement,* vol. 30, p. 1163–1170, 10 2009.

[64] S. Sprager and D. Zazula, "Heartbeat and Respiration Detection From Optical Interferometric Signals by Using a Multimethod Approach," *IEEE Transactions on Biomedical Engineering,* vol. 59, p. 2922–2929, 10 2012.

[65] J. M. Kortelainen and J. Virkkala, "FFT averaging of multichannel BCG signals from bed mattress sensor to improve estimation of heart beat interval," in *2007 29th Annual International Conference of the IEEE Engineering in Medicine and Biology Society*, 2007.

[66] Y. Zhu, H. Zhang, M. Jayachandran, A. K. Ng, J. Biswas and Z. Chen, "Ballistocardiography with fiber optic sensor in headrest position a feasibility study and a new," in *35th Annual International Conference of the IEEE EMBS Osaka, Japan, 3 - 7 July, 2013*, 2013.

[67] D. C. Mack, D. C. Mack, J. T. Patrie, P. M. Suratt, R. A. Felder and M. Alwan, "Development and Preliminary Validation of Heart Rate and Breathing Rate Detection Using a Passive, Ballistocardiography-Based Sleep Monitoring System," *IEEE Transactions on Information Technology in Biomedicine,* vol. 13, p. 111–120, 1 2009.

[68] J. Paalasmaa, M. Waris, H. Toivonen, L. Leppäkorpi and M. Partinen, "Unobtrusive Online Monitoring of Sleep at Home," in *34th Annual International Conference of the IEEE EMBS San Diego, California USA, 28 August - 1 September, 2012*, 2012.

[69] C. Wang, "The Segmented Dynamic Time Warping Algorithm for Beat-to-Beat Heart Rate Estimation based on Ballistocardiogram Signals," *Journal of Fiber Bioengineering and Informatics,* vol. 6, p. 415–425, 6 2013.

[70] K. Watanabe, T. Watanabe, H. Watanabe, H. Ando, T. Ishikawa and K. Kobayashi, "Noninvasive Measurement of Heartbeat, Respiration, Snoring and Body Movements of a Subject in Bed via a Pneumatic Method," *IEEE Transactions on Biomedical Engineering,* vol. 52, p. 2100–2107, December 2005.

[71] Y. Chee, J. Han, J. Youn and K. Park, "Air mattress sensor system with balancing tube for unconstrained measurement of respiration and heart beat movements," *Physiological Measurement,* vol. 26, p. 413–422, 4 2005.

[72] X. Feng, M. Dong, P. Levy and Y. Xu, "Non-contact Home Health Monitoring Based on Low-Cost High-Performance Accelerometers," in *2017 IEEE/ACM International Conference on Connected Health: Applications, Systems and Engineering Technologies (CHASE)*, 2017.

[73] S. Nurmi, T. Saaresranta, T. Koivisto, U. Meriheinä and L. Palva, "Validation of an Accelerometer Based BCG Method for Sleep Analysis," Aalto University; Aalto-yliopisto, 2016.

[74] C. Bruser, A. Kerekes, S. Winter and S. Leonhardt, "Multi-channel optical sensor-array for measuring ballistocardiograms and respiratory activity in bed," in *2012 Annual International Conference of the IEEE Engineering in Medicine and Biology Society*, 2012.

[75] J. M. Kortelainen, M. van Gils and J. Pärkkä, "Multichannel Bed Pressure Sensor for Sleep Monitoring," in *Proceedings of the 39th Computing in Cardiology, 2012*, 2012.

[76] T. Koivistoinen, S. Junnila, A. Varri and T. Koobi, "A new method for measuring the ballistocardiogram using EMFi sensors in a normal chair," in *The 26th Annual*

International Conference of the IEEE Engineering in Medicine and Biology Society.

[77] O. A. Postolache, P. M. B. S. Girao, J. Mendes, E. C. Pinheiro and G. Postolache, "Physiological Parameters Measurement Based on Wheelchair Embedded Sensors and Advanced Signal Processing," *IEEE Transactions on Instrumentation and Measurement,* vol. 59, p. 2564–2574, 10 2010.

[78] S. Leem, F. Khan and S. Cho, "Vital Sign Monitoring and Mobile Phone Usage Detection Using IR-UWB Radar for Intended Use in Car Crash Prevention," *Sensors,* vol. 17, p. 1240, May 2017.

[79] "Method and apparatus for measuring quantities relating to the cardiac activity of a person". Patent WO1994006348A1, 1994.

[80] R. González-Landaeta, O. Casas and R. Pallàs-Areny, "Heart rate detection from an electronic weighing scale," *Physiological Measurement,* vol. 29, p. 979–988, July 2008.

[81] J. H. Shin, K. M. Lee and K. S. Park, "Non-constrained monitoring of systolic blood pressure on a weighing scale," *Physiological Measurement,* vol. 30, p. 679–693, June 2009.

[82] G. Balakrishnan, F. Durand and J. Guttag, "Detecting Pulse from Head Motions in Video," in *2013 IEEE Conference on Computer Vision and Pattern Recognition*, 2013.

[83] L. Guohua, W. Jianqi, Y. Yu and J. Xijing, "Study of the Ballistocardiogram signal in life detection system based on radar," in *2007 29th Annual International Conference of the IEEE Engineering in Medicine and Biology Society*, 2007.

[84] O. Postolache, P. S. Girao, R. N. Madeira and G. Postolache, "Microwave FMCW Doppler radar implementation for in-house pervasive health care system," in *2010 IEEE International Workshop on Medical Measurements and Applications*, 2010.

[85] E. M. Staderini, "UWB radars in medicine," *IEEE Aerospace and Electronic Systems Magazine,* vol. 17, p. 13–18, 2002.

[86] F. Khan, A. Ghaffar, N. Khan and S. H. Cho, "An Overview of Signal Processing Techniques for Remote Health Monitoring Using Impulse Radio UWB Transceiver," *Sensors,* vol. 20, p. 2479, April 2020.

[87] P.-F. Migeotte, Q. Deliere, J. Tank, I. Funtova, R. Baevsky, X. Neyt and N. Pattyn, "3D-ballistocardiography in microgravity: Comparison with ground based recordings," in *2013 35th Annual International Conference of the IEEE Engineering in Medicine and Biology Society (EMBC)*, 2013.

[88] D. D. He, E. S. Winokur and C. G. Sodini, "A continuous, wearable, and wireless heart monitor using head ballistocardiogram (BCG) and head electrocardiogram (ECG)," in *2011 Annual International Conference of the IEEE Engineering in Medicine and Biology Society*, 2011.

[89] E. Hyun, S. Noh, C. Yoon and H. C. Kim, "Patch type integrated sensor system for measuring electrical and mechanical cardiac activities," in *2014 IEEE Sensors Applications Symposium (SAS)*, 2014.

[90] A. Barleanu, M. Hagan, O. Geman and I. Chiuchisan, "Wearable Ballistocardiography system for heartbeat detection," in *2016 International Conference and Exposition on Electrical and Power Engineering (EPE)*, 2016.

[91] G. López, V. Custodio and J. I. Moreno, "LOBIN: E-Textile and Wireless-Sensor-Network-Based Platform for Healthcare Monitoring in Future Hospital Environments," *IEEE Transactions on Information Technology in Biomedicine,* vol. 14, p. 1446–1458, November 2010.

[92] J. Hernandez, D. McDuff and R. Picard, "BioWatch: Estimation of Heart and Breathing Rates from Wrist Motions," in *Proceedings of the 9th International Conference on Pervasive Computing Technologies for Healthcare*, 2015.

[93] M. Kaisti, T. Panula, J. Leppänen, R. Punkkinen, M. J. Tadi, T. Vasankari, S. Jaakkola, T. Kiviniemi, J. Airaksinen, P. Kostiainen, U. Meriheinä, T. Koivisto and M. Pänkäälä, "Clinical assessment of a non-invasive wearable MEMS pressure sensor array for monitoring of arterial pulse waveform, heart rate and detection of atrial fibrillation," *npj Digital Medicine,* vol. 2, May 2019.

[94] J. Hernandez, Y. Li, J. Rehg and R. Picard, "BioGlass: Physiological Parameter Estimation Using a Head-mounted Wearable Device," in *Proceedings of the 4th International Conference on Wireless Mobile Communication and Healthcare - "Transforming healthcare through innovations in mobile and wireless technologies"*, 2014.

[95] F. Landreani and E. G. Caiani, "Smartphone accelerometers for the detection of heart rate," *Expert Review of Medical Devices,* vol. 14, p. 935–948, November 2017.

[96] S. Kwon, J. Lee, G. S. Chung and K. S. Park, "Validation of heart rate extraction through an iPhone accelerometer," in *2011 Annual International Conference of the IEEE Engineering in Medicine and Biology Society*, 2011.

[97] J. Hernandez, D. J. McDuff and R. W. Picard, "Biophone: Physiology monitoring from peripheral smartphone motions," in *2015 37th Annual International Conference of the IEEE Engineering in Medicine and Biology Society (EMBC)*, 2015.

[98] F. Landreani, A. Martin-Yebra, C. Casellato, E. Pavan, C. Frigo, P.-F. Migeotte and E. G. Caiani, "Feasibility study for beat-to-beat heart rate detection by smartphone\textquotesingles accelerometers," in *2015 E-Health and Bioengineering Conference (EHB)*, 2015.

[99] F. Landreani, A. Martin-Yebra, C. Casellato, C. Frigo, E. Pavan, P.-F. Migeotte and E. G. Caiani, "Beat-to-beat heart rate detection by smartphone's accelerometers: Validation with ECG," in *2016 38th Annual International Conference of the IEEE Engineering in Medicine and Biology Society (EMBC)*, 2016.

[100] O. Lahdenoja, M. Pankaala, T. Koivisto, T. Hurnanen, Z. Iftikhar, S. Nieminen, T. Knuutila, A. Saraste, T. Kiviniemi, T. Vasankari and J. Airaksinen, "Atrial Fibrillation Detection via Accelerometer and Gyroscope of a Smartphone," *IEEE Journal of Biomedical and Health Informatics,* vol. 22, p. 108–118, January 2018.

[101] A. Wiens, M. Etemadi, L. Klein, S. Roy and O. T. Inan, "Wearable ballistocardiography: Preliminary methods for mapping surface vibration measurements to whole body forces," in *2014 36th Annual International Conference of the IEEE Engineering in Medicine and Biology Society*, 2014.

[102] E. S. Winokur, D. D. He and C. G. Sodini, "A wearable vital signs monitor at the ear for continuous heart rate and Pulse Transit Time measurements," in *2012 Annual International Conference of the IEEE Engineering in Medicine and Biology Society*, 2012.

[103] G. K. Prisk, S. Verhaeghe, D. Padeken, H. Hamacher and M. Paiva, "Three-dimensional ballistocardiography and respiratory motion in sustained microgravity.," *Aviation, space, and environmental medicine,* vol. 72, no. 12, p. 1067–1074, December 2001.

[104] A. D. Wiens and O. T. Inan, "Accelerometer body sensor network improves systolic time interval assessment with wearable ballistocardiography," in *2015 37th Annual International Conference of the IEEE Engineering in Medicine and Biology Society (EMBC)*, 2015.

[105] "Datasheet - The SCA61T inclinometer series".

[106] B. S. Bozhenko, "Seismocardiography - a new method in the study of functional conditions of the heart.," *Terapevticheskii arkhiv,* vol. 33, p. 55—64, September 1961.

[107] D. M. Salerno and J. Zanetti, "Seismocardiography for Monitoring Changes in Left Ventricular Function during Ischemia," *Chest,* vol. 100, p. 991–993, October 1991.

[108] R. S. Crow, P. Hannan, D. Jacobs, L. Hedquist and D. M. Salerno, "Relationship between Seismocardiogram and Echocardiogram for Events in the Cardiac Cycle," *American Journal of Noninvasive Cardiology,* vol. 8, p. 39–46, 1994.

[109] E. M. I. L. I. O. Tafur, L. S. Cohen and H. D. Levine, "The Normal Apex Cardiogram," *Circulation,* vol. 30, p. 381–391, September 1964.

[110] R. Hooke, "The Posthumous Works of Robert Hooke," Richard Waller, 1705, p. 39.

[111] J. M. Hasenkam, "Advances in Hemodynamics and Hemorheology," T. V. How, Ed., T. V.How, 1996, pp. 325-372.

[112] M. Down, "Vibrocardiography-A Study of Vibrations in the Normal Heart," *Australasian Annals of Medicine,* vol. 5, p. 54–61, February 1956.

[113] U. Morbiducci, L. Scalise, M. D. Melis and M. Grigioni, "Optical Vibrocardiography: A Novel Tool for the Optical Monitoring of Cardiac Activity," *Annals of Biomedical Engineering,* vol. 35, p. 45–58, November 2006.

[114] "SI1000 - Preliminary Datasheet - Single axis analog accelerometer," 2019.

[115] "LIS344ALH - MEMS inertial sensorhigh performance 3-axis ±2/±6g ultracompact linear accelerometer," 2008.

[116] "IEEE Standard for Terminology and Test Methods for Analog-to-Digital Converters," *IEEE Std 1241-2010 (Revision of IEEE Std 1241-2000),* pp. 1-139, 2011.

[117] "AD8691/AD8692/AD8694 - Low Cost, Low Noise, CMOS,RRO Operational Amplifiers," 2013.

[118] "LTC6910-1/LTC6910-2/LTC6910-3 - Digitally ControlledProgrammableGain Amplifiers in SOT-23," 2017.

[119] T. Greena, P. Semig and C. Wells, "Analog Engineer’s Circuit Cookbook:Amplifiers," 2 ed., Texas Instrument, 2019, pp. 113-116.

[120] T. Greena, P. Semig and C. Wells, "Analog Engineer’s Circuit Cookbook:Amplifiers," 2 ed., Texas Instrument, 2019.

[121] "1N91x, 1N4x48, FDLL914,FDLL4x48 - Small Signal Diode," 2017.

[122] "MP System Hardware Guide," 2020.

[123] "EcoGen™Wire and Cable," 2018.

[124] "Coffrets portatifs miniatures en plastique ABS 1551 Series," 2020.

[125] "Boîtiers en plastique ABS tout usage avec douilles-entretoises pour cartesde circuit imprimé 1591XX Series," 2020.

[126] C. Turnage-Carrier, K. M. McLane and M. A. Gregurich, "Interface Pressure Comparison of Healthy Premature Infants With Various Neonatal Bed Surfaces," *Advances in Neonatal Care,* vol. 8, p. 176–184, June 2008.

[127] S. Staacks, S. Hütz, H. Heinke and C. Stampfer, "Advanced tools for smartphone-based experiments: phyphox," *Physics Education,* vol. 53, p. 045009, 5 2018.

[128] G. Cathelain, B. Rivet, S. Achard, J. Bergounioux and F. Jouen, "Dynamic Time Warping for Heartbeat Detection in Ballistocardiography," in *2019 Computing in Cardiology Conference (CinC)*, 2019.

[129] X. L. Aubert and A. Brauers, "Estimation of vital signs in bed from a single unobtrusive mechanical sensor: Algorithms and real-life evaluation," in *2008 30th Annual International Conference of the IEEE Engineering in Medicine and Biology Society*, 2008.

[130] A. Rodríguez-Molinero, L. Narvaiza, J. Ruiz and C. Gálvez-Barrón, "Normal Respiratory Rate and Peripheral Blood Oxygen Saturation in the Elderly Population," *Journal of the American Geriatrics Society,* vol. 61, p. 2238–2240, December 2013.

[131] W. Kester, Mixed-signal design seminar : mastering the mix in signal processing, Norwood, MA: Analog Devices, 1991.

[132] E. Company-Bosch and E. Hartmann, *ECG Front-End Design is simplified with microconverter. Analog Device Inc,* 2003.

[133] M. Mojarradi, T. Johnson, M. Ortiz, T. Cunningham and R. Andersen, "Low-Cutoff, High-Pass Digital Filtering of Neural Signals," 2004.

[134] R. Muller, S. Gambini and J. M. Rabaey, "A 0.013 mm², 5 μW, DC-Coupled Neural Signal Acquisition IC With 0.5 V Supply," *IEEE Journal of Solid-State Circuits,* vol. 47, p. 232–243, January 2012.

[135] S. Reuter, C. Moser and M. Baack, "Respiratory Distress in the Newborn," *Pediatrics in Review,* vol. 35, p. 417–429, October 2014.

[136] B. Kemp, A. Värri, A. C. Rosa, K. D. Nielsen and J. Gade, "A simple format for exchange of digitized polygraphic recordings," *Electroencephalography and Clinical Neurophysiology,* vol. 82, p. 391–393, May 1992.

[137] "MMO 3000 - Community Ultra-Low Bed".

[138] "Medstrom AeroSpacer Range Brochure," 2017.

[139] J. Gomez-Clapers, A. Serra-Rocamora, R. Casanella and R. Pallas-Areny, "Uncertainty factors in time-interval measurements in ballistocardiography," in *19th Symposium IMEKO TC 4 Symposium and 17th IWADC Workshop*, S. l, 2013.

[140] C. McCall, Z. Stuart, R. M. Wiard, O. T. Inan, L. Giovangrandi, C. M. Cuttino and G. T. A. Kovacs, "Standing ballistocardiography measurements in microgravity," in *2014 36th Annual International Conference of the IEEE Engineering in Medicine and Biology Society*, 2014.

[141] C. H. Antink, F. Schulz, S. Leonhardt and M. Walter, "Motion Artifact Quantification and Sensor Fusion for Unobtrusive Health Monitoring," *Sensors,* vol. 18, p. 38, December 2017.

[142] S. Ancoli-Israel, R. Cole, C. Alessi, M. Chambers, W. Moorcroft and C. P. Pollak, "The Role of Actigraphy in the Study of Sleep and Circadian Rhythms," *Sleep,* vol. 26, p. 342–392, 5 2003.

[143] T. Blackwell, S. Redline, S. Ancoli-Israel, J. L. Schneider, S. Surovec, N. L. Johnson, J. A. Cauley and K. L. Stone, "Comparison of Sleep Parameters from Actigraphy and Polysomnography in Older Women: The SOF Study," *Sleep,* vol. 31, p. 283–291, 2 2008.

[144] G. Fedele, F. Chiaravalloti and C. Join, "An algebraic derivative-based approach for the zero-crossings estimation," in *2009 17th European Signal Processing Conference*, 2009.

[145] D. Heise and M. Skubic, "Monitoring pulse and respiration with a non-invasive hydraulic bed sensor," in *2010 Annual International Conference of the IEEE Engineering in Medicine and Biology*, 2010.

[146] K. Niizeki, I. Nishidate, K. Uchida and M. Kuwahara, "Unconstrained cardiorespiratory and body movement monitoring system for home care," *Medical & Biological Engineering & Computing,* vol. 43, p. 716–724, November 2005.

[147] Z. Chen, J. T. Teo, S. H. Ng, X. Yang, B. Zhou, Y. Zhang, H. P. Loo, H. Zhang and M. Thong, "Monitoring respiration and cardiac activity during sleep using microbend fiber sensor: A clinical study and new algorithm," in *2014 36th Annual International Conference of the IEEE Engineering in Medicine and Biology Society*, 2014.

[148] A. Alivar, C. Carlson, A. Suliman, S. Warren, P. Prakash, D. Thompson and B. Natarajan, "Motion Detection in Bed-Based Ballistocardiogram to Quantify Sleep Quality," in *GLOBECOM 2017 - 2017 IEEE Global Communications Conference*, 2017.

[149] E. J. Pino, J. A. P. Chavez and P. Aqueveque, "Noninvasive ambulatory measurement system of cardiac activity," in *2015 37th Annual International Conference of the IEEE Engineering in Medicine and Biology Society (EMBC)*, 2015.

[150] L. Rosales, "Heartbeat Detection from a Hydraulic Bed Sensor Using a Clustering Approach," in *34th Annual International Conference of the IEEE EMBS San Diego, California USA, 28 August - 1 September, 2012*, 2012.

[151] R. Krishnan, B. Natarajan and S. Warren, "Analysis and detection of motion artifact in photoplethysmographic data using higher order statistics," in *2008 IEEE International Conference on Acoustics, Speech and Signal Processing*, 2008.

[152] J. S. Paul, M. R. Reddy and V. J. Kumar, "A transform domain SVD filter for suppression of muscle noise artefacts in exercise ECG\textquotesingles," *IEEE Transactions on Biomedical Engineering,* vol. 47, p. 654–663, May 2000.

[153] M. Ayat, M. B. Shamsollahi, B. Mozaffari and S. Kharabian, "ECG denoising using modulus maxima of wavelet transform," in *2009 Annual International Conference of the IEEE Engineering in Medicine and Biology Society*, 2009.

[154] R. Sameni, M. B. Shamsollahi, C. Jutten and G. D. Clifford, "A Nonlinear Bayesian Filtering Framework for ECG Denoising," *IEEE Transactions on Biomedical Engineering,* vol. 54, p. 2172–2185, December 2007.

[155] O. T. Inan, M. Etemadi, B. Widrow and G. T. A. Kovacs, "Adaptive Cancellation of Floor Vibrations in Standing Ballistocardiogram Measurements Using a Seismic Sensor as a Noise Reference," *IEEE Transactions on Biomedical Engineering,* vol. 57, p. 722–727, 3 2010.

[156] O. T. Inan, G. T. A. Kovacs and L. Giovangrandi, "Evaluating the Lower-Body Electromyogram Signal Acquired From the Feet As a Noise Reference for

Standing Ballistocardiogram Measurements," *IEEE Transactions on Information Technology in Biomedicine,* vol. 14, p. 1188–1196, 9 2010.

[157] P. Welch, "The use of fast Fourier transform for the estimation of power spectra: A method based on time averaging over short, modified periodograms," *IEEE Transactions on Audio and Electroacoustics,* vol. 15, p. 70–73, June 1967.

[158] D. Friedrich, X. L. Aubert, H. Führ and A. Brauers, "Heart Rate Estimation on a Beat-to-Beat Basis via Ballistocardiography - A hybrid Approach," in *32nd Annual International Conference of the IEEE EMBS Buenos Aires, Argentina, August 31 - September 4, 2010*, 2010.

[159] J. Pan and W. J. Tompkins, "A Real-Time QRS Detection Algorithm," *IEEE Transactions on Biomedical Engineering,* Vols. BME-32, p. 230–236, 3 1985.

[160] W. Engelse and C. Zeelenberg, "A single scan algorithm for QRS detection and feature extraction," *IEEE Comp. in Cardiology,* vol. 6, pp. 37-42, 1979.

[161] P. Hamilton, "Open source ECG analysis," in *Computers in Cardiology*, 2002.

[162] I. I. Christov, "Real time electrocardiogram QRS detection using combined adaptive threshold," *BioMedical Engineering OnLine,* vol. 3, p. 28, 2004.

[163] M. Elgendi, M. Jonkman and F. D. Boer, "Frequency bands effects on QRS detection," in *Proceedings of the Third International Conference on Bio-inspired Systems and Signal Processing*, 2010.

[164] V. Kalidas and L. Tamil, "Real-time QRS detector using Stationary Wavelet Transform for Automated ECG Analysis," in *2017 IEEE 17th International Conference on Bioinformatics and Bioengineering (BIBE)*, 2017.

[165] A. Akhbardeh, B. Kaminska and K. Tavakolian, "BSeg++: A modified Blind Segmentation Method for Ballistocardiogram Cycle Extraction," in

Proceedings of the 29th Annual International Conference of the IEEE EMBS, 2007.

[166] A. Akhbardeh, S. Junnila, M. Koivuluoma, T. Koivistoinen and A. Värri, "Evaluation of Heart Condition based on Ballistocardiogram Classification using Compactly Supported Wavelet Transforms and Neural Networks," in *Proceedings of the TB3.4 2005 IEEE Conference on Control Applications Toronto, Canada, August*, 2005.

[167] J. Jin, X. Wang, S. Li and Y. Wu, "A Novel Heart Rate Detection Algorithm in Ballistocardiogram Based on Wavelet Transform," in *2009 Second International Workshop on Knowledge Discovery and Data Mining*, 2009.

[168] A. Martín-Yebra, F. Landreani, C. Casellato, E. Pavan, P.-F. Migeotte, C. Frigo, J. P. Martínez and E. G. Caiani, "Evaluation of respiratory- and postural-induced changes on the ballistocardiogram signal by time warping averaging," *Physiological Measurement,* vol. 38, p. 1426–1440, 6 2017.

[169] A. Mueen and E. Keogh, "Extracting Optimal Performance from Dynamic Time Warping," in *Proceedings of the 22nd ACM SIGKDD International Conference on Knowledge Discovery and Data Mining*, 2016.

[170] D. A. Coast, R. M. Stern, G. G. Cano and S. A. Briller, "An approach to cardiac arrhythmia analysis using hidden Markov models," *IEEE Transactions on Biomedical Engineering,* vol. 37, p. 826–836, 1990.

[171] N. P. Hughes, L. Tarassenko and S. J. Roberts, "Markov Models for Automated ECG Interval Analysis," in *Advances in Neural Information Processing Systems 16*, S. Thrun, L. K. Saul and B. Schölkopf, Eds., MIT Press, 2004, p. 611–618.

[172] R. V. Andreao, B. Dorizzi and J. Boudy, "ECG signal analysis through hidden Markov models," *IEEE Transactions on Biomedical Engineering,* vol. 53, p. 1541–1549, 8 2006.

[173] Koski, "Modelling ECG signals with hidden Markov models," 1996.

[174] J. Wahlstrom, I. Skog, P. Handel, F. Khosrow-khavar, K. Tavakolian, P. K. Stein and A. Nehorai, "A Hidden Markov Model for Seismocardiography," *IEEE Transactions on Biomedical Engineering,* 2017.

[175] L. R. Rabiner, "A tutorial on hidden Markov models and selected applications in speech recognition," *Proceedings of the IEEE,* vol. 77, p. 257–286, 1989.

[176] J. Camps, B. Rodriguez and A. Minchole, "Deep Learning Based QRS Multilead Delineator in Electrocardiogram Signals," in *2018 Computing in Cardiology Conference (CinC)*, 2018.

[177] H. Lu, H. Zhang, Z. Lin and N. S. Huat, "A Novel Deep Learning based Neural Network for Heartbeat Detection in Ballistocardiograph," in *2018 40th Annual International Conference of the IEEE Engineering in Medicine and Biology Society (EMBC)*, 2018.

[178] V. Moskalenko, N. Zolotykh and G. Osipov, "Deep Learning for ECG Segmentation," in *Studies in Computational Intelligence*, Springer International Publishing, 2019, p. 246–254.

[179] O. Ronneberger, P. Fischer and T. Brox, "U-Net: Convolutional Networks for Biomedical Image Segmentation," in *Lecture Notes in Computer Science*, Springer International Publishing, 2015, p. 234–241.

[180] D. P. Kingma and J. Ba, "Adam: A Method for Stochastic Optimization," in *3rd International Conference on Learning Representations, ICLR 2015, Conference Track Proceedings*, San Diego, CA, USA, 2015.

[181] O. T. Inan, "Recent Advances in Cardiovascular Monitoring Using Ballistocardiography," in *34th Annual International Conference of the IEEE EMBS San Diego, California USA, 28 August - 1 September, 2012*, 2012.

[182] O. T. Inan, "Non-invasive Measurement of Valsalva-induced Hemodynamic Changes on a Bathroom and Scale Ballistocardiograph," in *3 0th Annual International IEEE EMBS Conference Vancouver, British Columbia, Canada, August 20-24, 2008*, 2008.

[183] X. Zhang, W. Kou, E. I.-C. Chang, H. Gao, Y. Fan and Y. Xu, "Sleep stage classification based on multi-level feature learning and recurrent neural networks via wearable device," *Computers in Biology and Medicine,* vol. 103, p. 71–81, 12 2018.

[184] J. M. Zanetti, M. O. Poliac and R. S. Crow, "Seismocardiography: Waveform Identification and Noise Analysis," in *IEEE*, 1992.

[185] Y. Yao, C. Bruser, U. Pietrzyk, S. Leonhardt, S. van Waasen and M. Schiek, "Model-Based Verification of a Non-Linear Separation Scheme for Ballistocardiography," *IEEE Journal of Biomedical and Health Informatics,* vol. 18, p. 174–182, 1 2014.

[186] J. Yao, S. Tridandapani, C. A. Wick and P. T. Bhatti, "Seismocardiography-Based Cardiac Computed Tomography Gating Using Patient-Specific Template Identification and Detection," *IEEE Journal of Translational Engineering in Health and Medicine,* vol. 5, p. 1–14, 2017.

[187] T. V. Y. Yao and M. Schiek, "Signal Separation for Ballistocardiography via Locally Projective Noise Reduction," in *M. Long (Ed.): World Congress on Medical Physics and Biomedical Engineering, IFMBE Proceedings 39, pp. 501–504, 201*, 2013.

[188] A. D. Wiens and O. T. Inan, "A novel system identification technique for improved wearable hemodynamics assessment," *IEEE Transactions on Biomedical Engineering,* vol. 62, p. 1345–1354, 2015.

[189] M. Weenk, H. van Goor, B. Frietman, L. J. L. P. G. Engelen, C. J. H. M. van Laarhoven, J. Smit, S. J. H. Bredie and T. H. van de Belt, "Continuous monitoring of vital signs using wearable devices on the general ward: pilot study," *JMIR mHealth and uHealth,* vol. 5, p. e91, 7 2017.

[190] O. Wasz-Höckert, The Infant Cry: A Spectrographic and Auditory Analysis, Spastics International Medical Publications, 1968.

[191] V. Tuzcu, "Dynamic Time Warping As a Novel Tool in Pattern Recognition of ECG Changes in Heart Rhythm Disturbances," in *200 5 IEEE International Conference on Systems, Man and Cybernetics Waikoloa, Hawaii October 10-12, 2005*, 2005.

[192] K. Tavakolian, B. Kaminska, A. Vaseghi and H. Kennedy-Symonds, "Respiration analysis of the sternal Ballistocardiograph signal," in *2008 Computers in Cardiology*, 2008.

[193] J. H. Shin, "Automatic Ballistocardiogram (BCG) Beat Detection Using a Template and Matching Approach," in *30th Annual International IEEE EMBS Conference Vancouver, British Columbia, Canada, August 20-24, 2008*, 2008.

[194] Y. Sereda, S. Alekseev, A. Koneva, R. Kataev and G. Osipov, *ECG Segmentation by Neural Networks: Errors and Correction,* 2018.

[195] M. D. Rienzo, Member, IEEE, P. Meriggi, E. Vaini, P. Castiglioni and F. Rizzo, "24h Seismocardiogram Monitoring in Ambulant Subjects," in *34th Annual International Conference of the IEEE EMBS San Diego, California USA, 28 August - 1 September, 2012*, 2012.

[196] O. Postolache, P. S. Girao and G. Postolache, "New Approach on Cardiac Autonomic Control Estimation Based on BCG Processing," in *2007 Canadian Conference on Electrical and Computer Engineering*, 2007.

[197] E. Pinheiro, O. Postolache and P. Girao, "Method for segmentation of cardiac signals based on four parameter sine fitting," in *2011 IEEE EUROCON - International Conference on Computer as a Tool*, 2011.

[198] J. Palotti, R. Mall, M. Aupetit, M. Rueschman, M. Singh, A. Sathyanarayana, S. Taheri and L. Fernandez-Luque, "Benchmark on a large cohort for sleep-wake classification with machine learning techniques," *npj Digital Medicine,* vol. 2, 6 2019.

[199] J. Paalasmaa, "A respiratory latent variable model for mechanically measured heartbeats," *Physiological Measurement,* vol. 31, p. 1331–1344, 8 2010.

[200] B. Ngai, K. Tavakolian, A. Akhbardeh, A. P. Blaber, B. Kaminska and A. Noordergraaf, "Comparative Analysis of Seismocardiogram Waves with the Ultra-Low Frequency Ballistocardiogram," in *31st Annual International Conference of the IEEE EMBS Minneapolis, Minnesota, USA, September 2-6, 2009*, 2009.

[201] M. Migliorini, A. M. Bianchi, D. Nistico, J. Kortelainen, E. Arce-Santana, S. Cerutti and M. O. Mendez, "Automatic sleep staging based on ballistocardiographic

signals recorded through bed sensors," in *2010 Annual International Conference of the IEEE Engineering in Medicine and Biology*, 2010.

[202] P.-F. Migeotte, J. Tank, N. Pattyn, I. Funtova, R. Baevsky, X. Neyt and G. K. Prisk, "Three dimensional ballistocardiography: Methodology and results from microgravity and dry immersion," in *2011 Annual International Conference of the IEEE Engineering in Medicine and Biology Society*, 2011.

[203] P.-F. Migeotte, L. Lejeune, Q. Deliere, E. Caiani, C. Casellato, J. Tank, I. Funtova, R. Baevsky, G. K. Prisk and P. van de Borne, "Three dimensional Ballistocardiogram and Seismocardiogram: What do they have in common?," in *2014 36th Annual International Conference of the IEEE Engineering in Medicine and Biology Society*, 2014.

[204] P.-F. Migeotte, S. D. Ridder, J. Tank, N. Pattyn, I. Funtova, R. Baevsky, X. Neyt and G. K. Prisk, "Three dimensional ballisto- and seismo-cardiography: HIJ wave amplitudes are poorly correlated to maximal systolic force vector," in *2012 Annual International Conference of the IEEE Engineering in Medicine and Biology Society*, 2012.

[205] A. Massaro, V. Maritati, N. Savino, A. Galiano, D. Convertini, E. D. Fonte and M. D. Muro, "A Study of a Health Resources Management Platform Integrating Neural Networks and DSS Telemedicine for Homecare Assistance," *Information,* vol. 9, p. 176, 7 2018.

[206] Y. Makihara, M. R. Aqmar, N. T. Trung, H. Nagahara, R. Sagawa, Y. Mukaigawa and Y. Yagi, "Phase Estimation of a Single Quasi-Periodic Signal," *IEEE Transactions on Signal Processing,* vol. 62, p. 2066–2079, 4 2014.

[207] X. Long, P. Fonseca, J. Foussier, R. Haakma and R. M. Aarts, "Sleep and Wake Classification With Actigraphy and Respiratory Effort Using Dynamic Warping," *IEEE Journal of Biomedical and Health Informatics,* vol. 18, p. 1272–1284, 7 2014.

[208] W. Lee, H. Yoon, C. Han, K. Joo and K. Park, "Physiological Signal Monitoring Bed for Infants Based on Load-Cell Sensors," *Sensors,* vol. 16, p. 409, 3 2016.

[209] Y. Lavner, R. Cohen, D. Ruinskiy and H. Ijzerman, "Baby cry detection in domestic environment using deep learning," in *2016 IEEE International Conference on the Science of Electrical Engineering (ICSEE)*, 2016.

[210] O. T. I. Laurent Giovangrandi, "Preliminary Results from BCG and ECG Measurements in the Heart Failure and Clinic," in *34th Annual International Conference of the IEEE EMBS San Diego, California USA, 28 August - 1 September, 2012*, 2012.

[211] M. Krej, L. Dziuda and F. W. Skibniewski, "A Method of Detecting Heartbeat Locations in the Ballistocardiographic Signal From the Fiber-Optic Vital Signs Sensor," *IEEE Journal of Biomedical and Health Informatics,* vol. 19, p. 1443–1450, 7 2015.

[212] A. Koutseff, D. Reby, O. Martin, F. Levrero, H. Patural and N. Mathevon, "The acoustic space of pain: cries as indicators of distress recovering dynamics in pre-verbal infants," *Bioacoustics,* vol. 27, p. 313–325, 6 2017.

[213] S.-E. Kim, M. K. Behr, D. Ba and E. N. Brown, "State-space multitaper time-frequency analysis," *Proceedings of the National Academy of Sciences,* vol. 115, p. E5–E14, 12 2017.

[214] C.-S. Kim, A. M. Carek, R. Mukkamala, O. T. Inan and J.-O. Hahn, "Ballistocardiogram as proximal timing reference for pulse transit time measurement: Potential for cuffless blood pressure monitoring," *IEEE Transactions on Biomedical Engineering,* vol. 62, p. 2657–2664, 2015.

[215] F. Khosrow-Khavar, K. Tavakolian, A. P. Blaber, J. M. Zanetti, R. Fazel-Rezai and C. Menon, "Automatic annotation of seismocardiogram with high-frequency precordial accelerations," *IEEE journal of biomedical and health informatics,* vol. 19, p. 1428–1434, 2015.

[216] J. M. Kelly, R. E. Strecker and M. T. Bianchi, "Recent Developments in Home Sleep-Monitoring Devices," *ISRN Neurology,* vol. 2012, p. 1–10, 2012.

[217] W. Karlen, C. Mattiussi and D. Floreano, "Improving actigraph sleep/wake classification with cardio-respiratory signals," in *2008 30th Annual International Conference of the IEEE Engineering in Medicine and Biology Society*, 2008.

[218] S. Junnila, "A Wireless and Ballistocardiographic Chair," in *Proceedings of the 28th IEEE SaEP6.6 EMBS Annual International Conference New York City, USA, Aug 30-Sept*, 2006.

[219] S. Junnila, A. Akhbardeh, A. Varri and T. Koivistoinen, "An EMFi-film sensor based ballistocardiographic chair: performance and cycle extraction method," in *IEEE Workshop on Signal Processing Systems Design and Implementation, 2005.*.

[220] O. T. Inan, M. Etemadi, R. M. Wiard, G. T. A. Kovacs and L. Giovangrandi, "Non-invasive measurement of Valsalva-induced hemodynamic changes on a bathroom scale Ballistocardiograph," in *2008 30th Annual International Conference of the IEEE Engineering in Medicine and Biology Society*, 2008.

[221] O. T. Inan, P.-F. Migeotte, K.-S. Park, M. Etemadi, K. Tavakolian, R. Casanella, J. Zanetti, J. Tank, I. Funtova, G. K. Prisk and M. D. Rienzo, "Ballistocardiography and Seismocardiography: A Review of Recent Advances," *IEEE Journal of Biomedical and Health Informatics,* vol. 19, p. 1414–1427, 7 2015.

[222] O. T. Inan, "Recent advances in cardiovascular monitoring using ballistocardiography," in *2012 Annual International Conference of the IEEE Engineering in Medicine and Biology Society*, 2012.

[223] O. T. Inan, M. Etemadi, R. M. Wiard, G. T. A. Kovacs and L. Giovangrandi, "Novel methods for estimating the ballistocardiogram signal using a simultaneously acquired electrocardiogram," in *2009 Annual International Conference of the IEEE Engineering in Medicine and Biology Society*, 2009.

[224] O. T. Inan, M. Etemadi, A. Paloma, L. Giovangrandi and G. T. A. Kovacs, "Non-invasive cardiac output trending during exercise recovery on a bathroom-scale-based ballistocardiograph," *Physiological Measurement,* vol. 30, p. 261–274, 2 2009.

[225] S. Hersek, B. Semiz, M. M. H. Shandhi, L. Orlandic and O. T. Inan, "A Globalized Model for Mapping Wearable Seismocardiogram Signals to Whole-Body Ballistocardiogram Signals Based on Deep Learning," *IEEE Journal of Biomedical and Health Informatics,* p. 1–1, 2019.

[226] Z. He, J. Niu, J. Ren, Y. Shi and W. Zhang, "A Deep Learning Method for Heartbeat Detection in ECG Image," in *Lecture Notes in Electrical Engineering*, Springer Singapore, 2019, p. 356–363.

[227] J. Gomez-Clapers, A. Serra-Rocamora, R. Casanella and R. Pallas-Areny, "Towards the standardization of ballistocardiography systems for J-peak timing measurement," *Elsevier - Measurement,* vol. 58, p. 310–316, 12 2014.

[228] M. A. García-González, A. Argelagós-Palau, M. Fernández-Chimeno and J. Ramos-Castro, "A Comparison of Heartbeat Detectors for the Seismocardiogram," in *Computing in Cardiology*, 2013.

[229] M. Etemadi, O. T. Inan, L. Giovangrandi and G. T. A. Kovacs, "Rapid Assessment of Cardiac Contractility on a Home Bathroom Scale," *IEEE Transactions on Information Technology in Biomedicine,* vol. 15, p. 864–869, 11 2011.

[230] H. Danker-Hopfe, P. Anderer, J. Zeitlhofer, M. Boeck, H. Dorn, G. Gruber, E. Heller, E. Loretz, D. Moser, S. Parapatics, B. Saletu, A. Schmidt and G. Dorffner, "Interrater reliability for sleep scoring according to the Rechtschaffen & Kales and the new AASM standard," *Journal of Sleep Research,* vol. 18, p. 74–84, 3 2009.

[231] G. S. Chung, J. S. Lee, S. H. Hwang, Y. K. Lim, D.-U. Jeong and K. S. Park, "Wakefulness estimation only using ballistocardiogram: Nonintrusive method for sleep monitoring," in *2010 Annual International Conference of the IEEE Engineering in Medicine and Biology*, 2010.

[232] C. Brüser, J. M. Kortelainen, S. Winter, M. Tenhunen, J. Pärkkä and S. Leonhardt, "Improvement of force-sensor-based heart rate estimation using multichannel data fusion," *IEEE journal of biomedical and health informatics,* vol. 19, p. 227–235, 2015.

[233] S. Brummelte, R. E. Grunau, V. Chau, K. J. Poskitt, R. Brant, J. Vinall, A. Gover, A. R. Synnes and S. P. Miller, "Procedural pain and brain development in premature newborns," *Annals of Neurology,* vol. 71, p. 385–396, 2 2012.

[234] P. J. Bradshaw, P. Stobie, M. W. Knuiman, T. G. Briffa and M. S. T. Hobbs, "Trends in the incidence and prevalence of cardiac pacemaker insertions in an ageing population," *Open Heart,* vol. 1, p. e000177, 12 2014.

[235] N. Bilous, M. Bondarenko, G. Kobzar, A. Krasov and A. Rogozyanov, "Normal ECG and Recognition for Express-Diganostics Based on Scale-Space Representation and Dynamic Matching," in *Information Science and Computing*, 2008.

[236] R. Barbieri, E. C. Matten, A. A. Alabi and E. N. Brown, "A point-process model of human heartbeat intervals: new definitions of heart rate and heart rate variability," *American Journal of Physiology-Heart and Circulatory Physiology,* vol. 288, pp. 424-435, 2005.

[237] A. Akhbardeh, S. Junnila, M. Koivuluoma, T. Koivistoinen and A. Värri, "The Heart and Disease Diagnosing and System based on Force and Sensitive and Chair's Measurement and Biorthogonal Wavelets and Neural Networks," in *Proceedings of the 2005 IEEE/ASME TA5-03 International Conference on Advanced Intelligent Mechatronics Monterey, California, USA, 24-28 July*, 2005.

[238] S. Aghabozorgi, A. S. Shirkhorshidi and T. Y. Wah, "Time-series clustering – A decade review," *Information Systems,* vol. 53, p. 16–38, 10 2015.

[239] M. Walter, B. Eilebrecht, T. Wartzek and S. Leonhardt, "The smart car seat: personalized monitoring of vital signs in automotive applications," *Personal and Ubiquitous Computing,* vol. 15, p. 707–715, January 2011.

[240] R. Krishnan, B. Natarajan and S. Warren, "Two-Stage Approach for Detection and Reduction of Motion Artifacts in Photoplethysmographic Data," *IEEE Transactions on Biomedical Engineering,* vol. 57, p. 1867–1876, August 2010.

Consolidated list of figures

Figure 1: Hospitalization rate of short-term care units in France, 2017. The dashed green curve represents women excluding pregnancy, childbirth, and puerperium. 17

Figure 2: Multi-parameter patient monitor screen 19

Figure 3 : Ballistocardiogram waveform construction..... 27

Figure 4 : Fluid mechanics model of ballistocardiography..... 28

Figure 5: Starr ballistocardiographic instrumentation..... 30

Figure 6: Publication rate of BCG-related research during the 1955-2015 period 31

Figure 9: BCG-derived respiration..... 33

Figure 10: A Starr bed ballistocardiograph 38

Figure 11: A Nickerson ballistocardiograph..... 39

Figure 12: A Dock ballistocardiograph 40

Figure 13: Starr (A) BCG with pneumogram (RESP.) and electrocardiogram (EKG); Nickerson (B) BCG during apnea; Dock (C) ballistocardiograms with electromagnetic (EM) and photoelectric method (PE) methods, and electrocardiogram (EKG) reference. Time divisions are 0.1s-long..... 41

Figure 14: Force sensors connected to the AC-coupled instrumentation amplifier 44

Figure 15: SCA11H sensor (A), SCA11H block diagram (B), SCA10H block diagram (C) .. 47

Figure 16: EMFIT raw data download interface..... 48

Figure 17: Setup of EMFIT QS..... 48

Figure 18: Example of SCG with simultaneous bipolar ECG lead reference from averaged data [108]..... 50

Figure 19: Illustration of a vibrocardiography setup in [111] 50

Figure 20 : Fealing BCG Wireless module (A), Biopac module (B) and ST module (C) 51

Figure 21: Internal composition and symbolic of the LTC6910 programmable gain amplifier 56
Figure 22: AC coupling with AD8691 and 40dB amplification with LTC6910 56
Figure 23: Bode diagram of the transfer function 57
Figure 24: AC filtering and 40 dB amplification on the same stage 57
Figure 25: AC filtering and 40 dB amplification on two different stages 57
Figure 26: Charging curve of the capacitor after a voltage step from 1.65 V (0 g) to 2.31 V (1 g), using the generator convention. 58
Figure 27: Voltage outputs after a voltage from 1.65 V (0 g) to 2.31 V (1 g) 58
Figure 28: Fast-settling time AC amplifier 59
Figure 29: Test of 1N4148 diode. 59
Figure 30: Resistance curve of 1N4148 diode depending on reverse voltage. 60
Figure 31: Zoom of the resistance curve of 1N4148 diode depending on reverse voltage. 60
Figure 32: Bode diagram of the fast-settling time AC amplifier compared with the single-stage circuit. 60
Figure 33: Charging curves of the capacitor after a voltage step, in the single-stage circuit (C11) and in the fast settling time circuit (C31). 61
Figure 34: Comparison of the settling times in the single-stage circuit (vout1) and in the fast settling time circuit (vout3). 61
Figure 35: MP36 Biopac and its DB9 connector pinout 62
Figure 36: Picoscope 4444 oscilloscope 62
Figure 37: Fealing Biopac BCG module, with Nihon-Kohden ECG synchronization. 63
Figure 38: Illustration of the sensor position in the bed. The head of the patient is on the side of the axes origin. 64
Figure 7: Body lying on a bed (A) and reduced model (B) 66

Figure 8: A typical BCG compared to the simulated cardiac force. Signals' amplitudes have been normalized by zero-mean and one-maximal amplitude..... 68
Figure 39: Number of different Android smartphone models released each year and referenced in the Phyphox database. 70
Figure 40: Accelerometer resolution of the different Android smartphone models released each year and referenced in the Phyphox database. 71
Figure 41: Setup of the bedding waveguide experimentation. 72
Figure 42: Flowchart of the bedding waveguide methods. 72
Figure 43: Amplitude modulation of J peaks during respiration. 73
Figure 44: Absolute performance indices of different waveguide configurations. 74
Figure 45: Setup of smartphone-based BCG experimentation, with waveguide bedding in orange. 76
Figure 46: Flowchart of the smartphone-based BCG methods 78
Figure 47: Pseudo-electronic circuit of the front-end 82
Figure 48: Example of a 4th order IIR filter, a cascade of two biquadratic filters, as implemented by the CMSIS DSP library..... 83
Figure 49: 6 bits poles distribution (A) ; 64 bits to 32 bits quantization of a pole (B). 84
Figure 50: Effect of quantization and passband rectification. 85
Figure 51: Frequency responses of the lowpass equivalent of the designed filters and the typical analog RC filter. 87
Figure 52: Illustration of baseline wander removal with 21 dB amplification. 88
Figure 53: Comparison of frequency responses for a 21 dB gain, quantized IIR versus experimental points 89
Figure 54: Effect of offset initialization on settling time. 89
Figure 55: Settling times for different offset initialization with a 21 dB amplification. 90

Figure 56: Noise frequency identification and filtering pseudo-algorithm. 90
Figure 57: Example of a simulated BCG pulse and its single-sided frequency spectrum computed by the microcontroller. 91
Figure 58: Typical ballistocardiogram (A) with absence (B), movement (C), and presence (phases). 93
Figure 59: Workflow of BCG digital signal processing algorithms. 94
Figure 60: MMO 3000 medical bed (A), Aerospacer mattress (B) and SCA11H sensor on overlay (C) 96
Figure 61: Setup for the LSI database acquisition 97
Figure 62: Recording page on SleepLogger (A) and Ollie (B) mobile applications 98
Figure 63: Setup of R2P2 database acquisition 99
Figure 64: Synchronization of the Biopac ECG with the Murata SCA11H BCG 102
Figure 65: SJ delays distribution in a 1-minute long recording. 102
Figure 66: Illustration of the most common actigraphy metrics : TAT or time above threshold (A), ZCM or zero crossing mode (B), PIM or proportional integral mode (C) 105
Figure 67: Amplitude distribution of motion-free (A) and motion-polluted (B) ballistocardiograms of an individual [148] 107
Figure 68: Variance distribution of motion-free (A) and motion-polluted (B) of 1-second long ballistocardiograms of an individual [Alivar2017] 109
Figure 69: Adaptive noise cancellation using a noise sensor, with n1 the noise measured by the noise sensor, s the ballistocardiogram and n0 the noise measured by the ballistocardiograph 110
Figure 70: Typical ballistocardiogram with absence (red), movement (blue), and presence (green) phases. 111
Figure 71: Motion segmentation process. 112

Figure 72: Cardiac and respiratory envelopes detection in the example BCG. 113
Figure 73: Cardiac and respiratory envelopes detection during presence, absence and movement phases of the BCG example. 114
Figure 74: Respiratory standard deviation and mean features of the segmented ballistocardiogram. 115
Figure 75: A Tukey window with a 50% shape parameter in the time (A) and frequency (B) domains. 116
Figure 76: Power spectral density of BCG segments during the presence and absence phases. The average PSDs of each phase are darkened. 117
Figure 77: Dendrogram of hierarchical clustering of presence and absence on motion-free segments. 120
Figure 78 : Hierarchical clustering with Euclidean distance and single linkage, for three (A) and four (B) clusters. 122
Figure 79: Iterative Mahalanobis linkage clustering. 123
Figure 80: HMM motion clustering 124
Figure 81: Hierarchical clustering of occupancy with Mahalanobis distance. 125
Figure 82: HMM motion clustering of occupancy with HMM method. 126
Figure 83: A superposition of averaged heartbeats from different patients (A) and heartbeats from one patient (B) that show inter- and intra-variabilities. 127
Figure 84: Spectrograms of a synchronous ballistocardiogram (A) and electrocardiogram (B) [66] 128
Figure 85: Two consequent heartbeat interval periods and corresponding spectra and cepstra [65]. 129
Figure 86: Dual threshold as implemented in [159] of the Moving Window Integrated BCG. 130

Figure 87: Iterations of the distance adaptive threshold clustering: 0.2 s (A), 0.4 s (B), 0.65 s (C)..... 132
Figure 88: Times features of local maxima (A) and clustering after PCA (B) in [40]..... 133
Figure 89: Clustering of local extrema of the BCG in the (prominence, distance to beat reference) space..... 134
Figure 90: Peak clusters used to detect fiducial points. 134
Figure 91: Trajectory of the clustered fiducial points. 135
Figure 92: Sym4 wavelet and scaling approximated functions at the first decomposition level. 136
Figure 93: BCG scalogram example with the Sym4 wavelet 136
Figure 94: Envelope extraction on a wavelet coefficient. 137
Figure 96: Brute (A) vs normalized (B) correlation coefficient and heartbeat detection..... 138
Figure 97: Flowchart of the DTW template matching algorithm..... 140
Figure 98: BCG envelope detection and segmentation. 141
Figure 99: Initialization of the template. 141
Figure 100: Pairwise Euclidean distance matrix of a heartbeat candidate and the template (A), and warping of the two waveforms (B)..... 143
Figure 101: DTW distance of local minima with the template and heartbeat detection (A), and heart rate measurement (B). 143
Figure 102: Refinement of the template..... 144
Figure 103: SNR of BCG segments and their corresponding sensitivities and positive predictivities. Bullet size is proportional to segments' durations..... 145
Figure 104: Pseudo algorithm of the patient dependent HMM..... 148
Figure 105: HMM architecture and initial parameters. 150

Figure 106: Training of HMM parameters on the ten first seconds, through iterations of the Baum-Welch algorithm. 152
Figure 107: Viterbi path of a 10-s long observation sequence in the testing set. 153
Figure 108: Identification of the longest consecutive states interval to be reduced. 155
Figure 109: Reduction of the longest consecutive states' interval using the Fast HMM reduction algorithm. 156
Figure 110: Training of a generic heartbeat model for supervised learning. 157
Figure 111: Patient-specific HMM computed from a patient independent HMM and reduced using the Robust HMM reduction algorithm. 158
Figure 112: Result of heartbeat detection using a patient-dependent HMM before (A) and after (B) refinement. 159
Figure 113: HMM heartbeat detection (A) and beat-to-beat series after refinement (B)..... 160
Figure 114: Computation time of the training and testing of a patient-dependent HMM with Robust HMM reduction depending on the HMM number of states. 160
Figure 115: Neural network architecture, inspired by an electrocardiogram delineation U-Net [168]. 162
Figure 116: Binary entropy losses after epochs of training for IJK segmentation (A) and precision-recall curve for IJK segmentation by trained the U-Net (B) 163
Figure 117: Example of heartbeat detection on a BCG signal with the U-Net output IJK prediction probability 164

Résumé substantiel

1. Introduction générale

1.1. Contexte clinique

Cette thèse s'inscrit dans un contexte clinique où le nombre et le coût des admissions à l'hôpital sont élevés. Lors de ces hospitalisations, un suivi physiologique est nécessaire mais parfois insuffisant.

1.1.1. Épidémiologie mondiale

En 2017, 12 millions de patients ont été admis à une hospitalisation complète et 16,8 millions de patients ont été admis à une hospitalisation partielle en France selon la Direction de la Recherche, des Etudes, des Evaluations et des Statistiques [1]. Les journées d'hospitalisation complète diminuent légèrement de -0,8% tandis que les journées d'hospitalisation partielle augmentent de +2%. Cette tendance est principalement due au vieillissement de la population et à l'augmentation des maladies chroniques multiples.

Les maladies chroniques sont définies par l'Organisation mondiale de la santé (OMS) comme des maladies à long terme qui évoluent généralement lentement [2]. Elles comprennent principalement les maladies cardiovasculaires, les cancers, le diabète et les maladies pulmonaires chroniques. Les maladies chroniques sont responsables de 36 millions de décès dans le monde en 2008, ce qui représente 63 % du nombre total de décès chaque année. Les pays à faible et moyen revenu sont responsables de 80 % de ces décès, et les trois quarts des décès ont plus de 60 ans.

Pour les systèmes de santé des pays développés, les patients chroniques font généralement des allers-retours entre leur domicile et l'hôpital car leurs maladies peuvent durer plusieurs années et entraîner des comorbidités. En France, 35 % de la population générale souffre de maladies chroniques et leurs soins coûtent 84 milliards d'euros à la

CNAM (Caisse Nationale d'Assurance Maladie), qui est l'assurance maladie publique française [3].

1.1.2. Suivi physiologique

L'état physiologique et la stabilité d'un patient sont reflétés par ses signes vitaux. Ils doivent être surveillés, en particulier dans les phases aiguës de l'hospitalisation qui nécessitent une attention et une surveillance étroites des soignants, mais aussi pendant les soins à domicile ou pour la prévention secondaire. Les signes vitaux des patients sont surveillés en permanence pendant l'hospitalisation par un moniteur multiparamétrique : il fait en effet partie de toute unité de soins médicaux moderne, par exemple dans l'unité de chirurgie ou l'unité de soins intensifs. Dans de nombreux cas, les équipements de surveillance physiologique utilisés pour les soins médicaux sont intrusifs, c'est-à-dire qu'ils touchent le patient et nécessitent l'implication soit du patient, soit du soignant, soit des deux.

Il est difficile de surveiller les enfants en raison de leur grande mobilité qui entraîne des artefacts répétitifs et des fausses alertes. De plus, les électrodes peuvent se décoller de l'épiderme, et les sondes d'oxymétrie de pouls peuvent se détacher régulièrement du doigt ou de l'orteil. Plusieurs facteurs sont en cause : l'enfant bouge et tire sur les sondes, l'adhésif des électrodes est usé ou le personnel infirmier n'a pas pu installer correctement les électrodes. L'application prolongée de l'oxymètre de pouls est susceptible de provoquer des escarres, comme cela a été observé dans les unités de soins intensifs pédiatriques (USIP) [4]. La surveillance d'un enfant peut donc entraîner un stress et éventuellement des douleurs. Cependant, la douleur des enfants affecte le développement neuromoteur et cognitif, en particulier chez les prématurés. Dans une unité de soins néonatals, les chercheurs ont en effet observé sur des nourrissons très prématurés que l'exposition à la douleur a un effet primaire et précoce sur les structures sous-corticales avec des modifications de la substance blanche [5].

La surveillance des personnes âgées est également un défi pour d'autres raisons. Selon l'OMS, 15 % des patients âgés de 60 ans sont atteints d'une maladie mentale dans le monde. Ces pathologies provoquent des comportements agressifs et l'oubli : les patients refusent ou oublient leurs traitements. Ce manque d'observance les empêche d'être suivis efficacement. Aucun cas d'ulcère de pression avec oxymètre de pouls n'a été trouvé dans la littérature gériatrique ; cependant, les patients gériatriques sont, comme les enfants, susceptibles d'être concernés en raison de la fragilité de leur épiderme.

1.1.3. Télésanté

La télésanté est définie par l'OMS comme *"l'utilisation des télécommunications et des technologies virtuelles pour fournir des soins de santé en dehors des établissements de santé traditionnels"*. La télésanté, ou télémédecine, peut être classée en plusieurs catégories : surveillance des patients à distance, télé-expertise, téléconsultation et téléassistance. La surveillance à distance des patients (RPM), ou télémonitoring, consiste explicitement à surveiller le patient à distance. Les outils de RPM sont généralement des questionnaires numériques sur des tablettes ou des smartphones et des appareils connectés pour les signes vitaux, par exemple des glucomètres pour le diabète ou des moniteurs de fréquence cardiaque et de pression artérielle pour l'insuffisance cardiaque.

Les deux principales promesses des stratégies de télésanté sont la qualité de la prestation des soins et la réduction des coûts des soins de santé. De nombreuses études cliniques ont été menées depuis plusieurs décennies et ont montré un intérêt croissant pour la télésanté, à une époque où les télécommunications numériques permettent d'enregistrer et de partager de plus en plus facilement des données comportementales et physiologiques. En raison de la diversité des pathologies que les systèmes RPM non standardisés peuvent surveiller, les résultats des études cliniques RPM ne sont jamais les mêmes et sont difficiles à comparer. Cependant, les

conclusions de ces études indiquent généralement que les expérimentations de RPM produisent des taux de morbidité et de mortalité au moins aussi bons que les soins habituels.

Le coût des programmes pour les patients de RPM ne doit pas être sous-estimé. Il a été évalué en 2016 dans une fourchette de 275 à 7 963 dollars par patient et par an, ce qui inclut l'achat d'équipement, l'entretien et la surveillance [10]. La limite supérieure de cette fourchette est assez impressionnante et n'inclut pas le coût des réadmissions à l'hôpital qui se produisent encore. Des technologies moins coûteuses pourraient rendre les programmes de RPM plus efficaces en termes de coûts et de soins. Au vu de ces conséquences prometteuses, de nombreux gouvernements des pays développés ont encouragé la télésanté, en particulier la surveillance des patients à distance. En France, par exemple, 199 200 hospitalisations ont été transférées à domicile grâce à la RPM en 2017, soit 5 % de plus qu'en 2016 [1].

1.2. Ballistocardiographie

La technologie de surveillance ballistocardiographique a le potentiel d'accroître l'engagement des patients dans les programmes de télésanté et d'améliorer la sécurité et le bien-être des patients dans les hôpitaux. Toutefois, cette technologie n'est pas encore arrivée à maturité sur le plan clinique. La ballistocardiographie est une méthode de surveillance sans contact de l'activité cardiaque. Elle repose sur la mesure des forces balistiques : lors d'une systole ventriculaire, le sang est éjecté du ventricule gauche par l'arc aortique, générant une force balistique cardiaque pulsée.

La force ballistocardiographique a été modélisée [13] par des équations mathématiques comme la perte de pression hydraulique se produisant à travers l'arc aortique. La force ballistocardiographique se répercute de l'arc aortique à l'ensemble du corps à travers les tissus organiques, puis du corps au support du patient, par exemple un lit. Par conséquent, l'ensemble du lit est soumis à une courte et minuscule contrainte mécanique qui peut être mesurée comme un déplacement sur des surfaces libres, par exemple sur la surface du matelas

à l'aide d'un accéléromètre, ou comme une contrainte sur des surfaces contraintes, par exemple sous le matelas à l'aide de jauges de contrainte.

1.2.1. Formes d'ondes physiologiques

La forme d'onde du ballistocardiogramme a été définie par Starr [19] et récemment modélisé par simulation [13]. Un ballistocardiogramme est une succession de battements cardiaques, segmentés en systole marquée par des points de repère IJK, et en diastole marquée par des points de repère LMN. Le pic J a généralement la plus grande amplitude, tandis que les points de repère LMN ne sont pas toujours discernables selon l'instrumentation. Cette convention est respectée tout au long de ce travail, sauf dans les sections 3.2.2et 33.2.3.

On peut trouver une composante respiratoire en ballistocardiographie de deux façons : soit une composante linéairement superposée, qui peut être facilement filtrée ; soit un signal modulant l'amplitude du ballistocardiogramme, comme dans la respiration dérivée de l'ECG. Dans ce dernier cas, la respiration peut être extraite par interpolation spline des pics J du ballistocardiographe.

La variabilité de la fréquence cardiaque est corrélée à l'activité du système nerveux autonome. Elle est utile pour la surveillance de la douleur [42] ou des études sur le sommeil.

1.2.2. Potentiel de surveillance sans contact et de télésanté

Les développements récents ont rendu la ballistocardiographie plus portable, moins chère et plus fiable. En tant que méthode de surveillance cardiaque passive et sans contact pouvant être intégrée dans des matelas, des chaises ou des balances, la ballistocardiographie pourrait devenir l'un des meilleurs dispositifs de télésanté.

Au début de 1953 [43]Le Dr Mandelbaum a établi, pour plus de cent infarctus aigus du myocarde, que le BCG pouvait être utilisé pour déterminer le rétablissement du myocarde dans les 18 mois suivant une crise cardiaque. Pinheiro a énuméré [44] une série d'études cliniques publiées au XXe siècle montrant les troubles physiologiques qui influencent les formes

d'onde du BCG, en particulier : les maladies coronariennes où le BCG est un bon prédicteur de l'apparition et de la récurrence de l'ischémie myocardique ; la sténose mitrale augmente l'amplitude du BCG tandis que la sténose aortique l'augmente ; la coarctation de l'aorte ; l'infarctus du myocarde ; l'insuffisance cardiaque congestive. À cette époque, les ballistocardiographes n'étaient pas automatiques et difficiles à mettre en œuvre en routine clinique.

Plus récemment, des études cliniques ont montré des résultats prometteurs en utilisant la ballistocardiographie. Inan a observé en 2009 [45] sur un sujet présentant une contraction auriculaire prématurée que l'amplitude du BCG était corrélée au temps de remplissage diastolique. Bruser a réalisé en 2013 [46] La preuve de concept de la fibrillation auriculaire a automatisé la détection sur 10 patients avec une sensibilité moyenne de 94% et une spécificité moyenne de 98%. Wang utilisé en 2017 [47] BCG pour évaluer la gravité des syndromes d'apnée du sommeil de 136 patients : il a obtenu une précision de 94% par rapport à l'étalon-or du PSG. Aydemir a montré en 2018 [48] plus de 36 patients HF que la variabilité de la forme d'onde du BCG était un prédicteur significatif de décompensation. Enfin, M. Yousefian a étudié l'utilisation de ballistocardiographes portables pour la surveillance de la pression artérielle [49].

1.2.3. Limitations

Cependant, la plupart de ces études cliniques sont des preuves de faisabilité concernant quelques dizaines de patients au maximum. Les limites des systèmes de BCG actuels sont détaillées dans les paragraphes suivants. Les systèmes BCG manquent encore de fiabilité et de couverture, car ils sont très sensibles aux artefacts de mouvement à la maison ou dans l'environnement hospitalier. La plupart des instruments du BCG ne sont pas normalisés. Il existe quelques exceptions, mais elles ne sont pas pratiques pour la télésanté. Les ballistocardiographes de type Starr et Nickerson, qui sont inconfortables, ne sont pas

compatibles avec les lits médicaux ou à domicile standard actuels. Les pèse-bébés modernes sont plus pratiques et peuvent également être normalisés, mais ils ne sont pas passifs et nécessitent l'intervention de l'infirmière ou du patient, ce qui risque de compromettre l'engagement du patient. Enfin, le débit cardiaque des nourrissons et des personnes âgées est plus faible que celui des adultes. Cependant, les études cliniques ne recrutent souvent que des adultes entre 19 et 60 ans. Par exemple, par rapport aux études cliniques récentes présentées dans la section précédente, seules deux études se situaient en dehors de cette fourchette, avec respectivement des patients de 58±13 ans et de 63±18 ans [48] [45]. En outre, peu d'études [50] [51] se concentrent sur la ballistocardiographie pédiatrique, où les signaux du BCG, en raison du faible poids et de la faible force contractile cardiaque, sont plus bruyants que ceux des adultes. Par exemple, l'amplitude du BCG d'un nourrisson de 3 kg est environ 30 fois plus faible que celle d'un adulte [51].

1.3. Question de recherche et méthodologie

La principale question de recherche abordée dans cette thèse est la suivante : la *ballistocardiographie peut-elle surveiller les conditions cardiaques des enfants et des personnes âgées dans un contexte clinique ?* L'auteur se concentrera sur la ballistocardiographie passive au lit.

Des questions secondaires sont également abordées : *comment améliorer la détection des battements cardiaques en ballistocardiographie ? La ballistocardiographie peut-elle être normalisée au lit de chacun ? Quelles sont les applications possibles de la ballistocardiographie autres que la surveillance des signes vitaux ?*

Au cours de cette thèse, ni une base de données des signaux du BCG ni un ballistocardiographe commercial n'étaient disponibles. L'auteur a donc dû passer du temps à développer son instrumentation BCG et à mener ses expériences cliniques à partir de zéro.

Même si cela a été difficile, cela a apporté une connaissance complète très utile des systèmes ballistocardiographiques.

2. L'instrumentation en balistique

Dans ce chapitre, les instruments de la ballistocardiographie sont étudiés. Comme ils mesurent un phénomène mécanique, l'ensemble du système mécanique, y compris le capteur et le lit, est défini comme une instrumentation BCG. L'influence de la masse du patient est également prise en compte dans le système mécanique.

2.1. Benchmark des instruments BCG existants

2.1.1. Instruments historiques du BCG

En 1952, Scarborough [52] a classé les ballistocardiographes de lit en trois catégories :

- Starr BCG [19] avec une fréquence de résonance élevée (10-15 Hz) et un système mécanique non amorti
- Nickerson BCG [53] avec une fréquence de résonance basse (1,5 Hz) et un système mécanique amorti de façon critique
- Dock BCG [25] qui est en contact direct avec le corps.

Ces lits permettent un seul degré de mobilité, par exemple, la translation dans une direction (tête-pied, latéralement et d'avant en arrière) [14] [18] [54] [55] ou la rotation autour d'un axe unique [56]. Le principe consiste à concentrer l'énergie de la force ballistocardiographique sur le capteur de mesure, en tenant compte de la fréquence de résonance du système mécanique. En effet, le corps humain, et sa force ballistocardiographique par extension, ont une fréquence naturelle comprise typiquement entre 3 et 7 Hz, selon la masse et la graisse corporelle. Ce degré de mobilité du lit BCG est limité par des ressorts, dont les raideurs sont réglées de telle sorte que le lit BCG pondéré avec une masse morte en acier de 75 kg a une fréquence de résonance différente de la force ballistocardiographique. Par exemple, le BCG à lit Starr a des ressorts plus rigides que le

BCG Nickerson. La rigidité des ressorts est adaptée à chaque patient, dont la masse peut varier. Le capteur analogique était à l'époque soit un traceur direct sur une bande mobile, comme pour les premiers sismomètres, soit un galvanomètre, tous deux enregistrant un déplacement du corps. Le BCG du lit Nickerson, comparé au BCG du lit Starr, était conçu pour amplifier les événements systoliques précoces (ondes G et H) et pour atténuer les événements diastoliques (ondes L, M et N). Dans ces deux systèmes de ballistocardiographie, la force ballistocardiographique est modifiée par le corps et le matelas jusqu'au capteur. Ainsi, elle est amplifiée avant la détection analogique, par exemple, 7000 fois par un système optique dans le BCG original du lit Starr [19].

Les ballistocardiographes de Dock ont été conçus pour élargir l'utilisation du ballistocardiographe dans la salle d'opération, dans le service ou à la maison. Au lieu d'inclure un lit coûteux et encombrant, ce sont des systèmes plus simples et portables qui peuvent être déplacés d'un lit à l'autre pour de courts examens, comme les électrocardiographes à l'époque. Ils sont en contact direct avec le patient et n'ont pas particulièrement besoin d'un gain d'amplification élevé. Dock a constaté que la méthode électromagnétique était la plus simple pour enregistrer des ballistocardiogrammes. Cela a été confirmé plus tard avec l'invention et l'utilisation des MEMS (systèmes micro-électro-mécaniques), et des films capacitifs, piézoélectriques et résistifs dans la plupart des ballistocardiographes récents, même si des méthodes optiques et à ultrasons ont également été développées. Même si le ballistocardiographe Dock a été conçu pour être portable et adaptable à différents lits, son utilisation clinique a été limitée aux tables rigides sans roulettes, sinon, la fréquence de résonance du lit peut se mélanger à la gamme force-fréquence du ballistocardiographe. Même s'ils sont plus simples et plus portables, les ballistocardiographes Dock sont moins conviviaux pour les patients que ceux de Starr et Nickerson, car les lits utilisés sont aussi rigides, mais la mesure est directement en contact avec le patient.

Les ballistocardiographes des lits Starr, Nickerson et Dock permettent des examens de ballistocardiographie standardisés et répétables de plusieurs minutes. Cependant, même si la numérisation et le traitement des signaux numériques pourraient automatiser le processus, ils utilisent des tables rigides et inconfortables et ne conviennent pas à la surveillance à long terme.

2.1.2. Progrès récents dans les instruments du BCG

En ballistocardiographie, les capteurs de pression utilisent différentes technologies : les capteurs pneumatiques [71] [67] [70]capteurs hydrauliques [32]jauges de contrainte [40] [63]Capteurs de force de type film [62]Capteur BCG à fibre optique à microcourbures [66] [64] [34]capteurs de films électromagnétiques [65]capteurs à film piézoélectrique [68] ou des capteurs en fluorure de polyvinylidène (PVDF) [69].

Les signaux d'accélération sont mesurés par des MEMS portables [87] [88] [102] [103] [104]. Il se trouve que les unités de mesure inertielle (IMU) intégrées au smartphone sont suffisamment sensibles pour mesurer la ballistocardiographie lorsque le smartphone est sur le thorax [95]. Il convient de noter que pour les vêtements, l'amplitude du signal est suffisamment élevée pour utiliser des accéléromètres numériques sans filtrage analogique de base.

2.1.3. Modules BCG commerciaux avec accès aux données brutes

Le capteur BCG SCA11H est alimenté par un adaptateur mural CA et communique par Wifi. Il peut fonctionner dans deux modes différents : soit un mode BCG où il transmet la fréquence cardiaque, la fréquence respiratoire et les battements du cœur, soit un mode enregistreur de données où il ne transmet que les données brutes de l'accéléromètre. Nous utiliserons ce dernier mode dans le cadre de cette thèse pour construire la base de données ballistocardiographiques CHArt. De plus, les algorithmes de traitement des signaux numériques utilisés dans le mode BCG sont propriétaires et non validés cliniquement. Le

capteur SCA11H est basé sur l'accéléromètre analogique SCA61T avec une faible densité de bruit de 15 μg/s2/√Hz [105]. La sortie analogique est couplée en courant alternatif, filtrée contre le repliement et amplifiée avant la numérisation à 1 kHz.

Le capteur EMFIT QS est un capteur de pression basé sur un film électromagnétique [65] qui, placé sous un matelas, mesure le ballistocardiogramme. Il fournit aux cliniciens et aux chercheurs des composantes respiratoires et cardiaques, respectivement dans les gammes de fréquences de 0,1-3 Hz et de 6-16 Hz. Il ne peut exporter que les données des nuits ou des siestes de plus de 20 minutes.

2.2. Lignes directrices pour la conception d'un accéléromètre BCG

Comme nous n'avons pas trouvé de module d'accéléromètre commercial pour nos expérimentations sur le BCG, nous avons décidé de concevoir notre accéléromètre BCG. Dans cette section, nous expliquons comment concevoir correctement un accéléromètre BCG. Les trois grandes lignes directrices concernent le capteur lui-même, le circuit de conditionnement et l'intégration mécanique. L'accéléromètre BCG conçu est appelé le module BCG de conditionnement. Il est disponible en trois versions différentes :

- Module sans fil BCG Fealing, qui communique via Bluetooth 5 et est alimenté par une batterie au lithium
- Module BCG Biopac de Fealing, qui communique et est alimenté via une connexion DB9 sur une unité d'acquisition Biopac MP36R
- Le module ST du BCG de Fealing, qui communique et est alimenté par une carte de prototypage ST Nucleo L476RG.

2.2.1. Capteur

Le capteur doit répondre à plusieurs exigences : la densité de bruit de sortie doit être faible ; il doit être suffisamment petit ; il doit être bon marché pour être utilisé dans les routines de télémédecine.

La densité de bruit est la racine carrée de la densité spectrale de puissance du bruit de sortie. Elle peut être exprimée en $g/\sqrt{Hz}$ ou en $V/\sqrt{Hz}$ en fonction de la nature de la production. La largeur de bande est de 25 Hz et le bruit doit être inférieur à 0,1 mg, car habituellement, le BCG mesuré par les accéléromètres de lit a une amplitude de 0,1 à 10 mg. Par conséquent, la densité de bruit de sortie doit être idéalement inférieure à 16 $\mu g/\sqrt{Hz}$. Il y a une marge dans cette valeur, qui dépend de l'amplitude du BCG. La sensibilité est également une exigence, en particulier pour les accéléromètres numériques qui contiennent déjà un circuit de conditionnement. Cependant, à l'exception de l'ADXL355 qui atteint 3,9 µg/LSB mais qui est très cher, la plupart des accéléromètres numériques ont une sensibilité trop faible. Par conséquent, nous préférons les accéléromètres analogiques à faible bruit dont la sortie peut être amplifiée, à moins qu'une amplification mécanique puisse être effectuée - voir section 2.3.

Toutes les références indiquées sont des MEMS à haute compacité, qui peuvent donc être facilement soudés sur de petits circuits imprimés. Même si la force ballistocardiographique se propage souvent dans une seule direction, les accéléromètres à trois axes peuvent être préférés, par exemple lorsque le patient change de position dans son lit. Le coût est une préoccupation majeure pour les applications de télémédecine, où les maisons de soins infirmiers peuvent avoir un budget limité. En outre, il est également important de tenir compte du coût lors de la réalisation d'expériences à grande échelle. Les MEMS doivent coûter moins de 10 $ pour être compétitifs et permettre un prix commercial du module BCG inférieur à 100 $.

En rassemblant toutes ces exigences, nous avons constaté que le LIS344ALH était un très bon candidat pour la ballistocardiographie [115]Il sera utilisé dans les modules Fealing Wireless et ST BCG. Le SCA61T, ou sa version à deux axes SCA100T, est le plus silencieux et sera utilisé dans le module BCG Fealing Biopac pour des enregistrements de haute qualité.

2.2.2. Circuit de conditionnement

En ce qui concerne les accéléromètres analogiques, le signal doit être amplifié avant la numérisation. En effet, les convertisseurs analogique-numérique (ADC) les plus courants ont une résolution de 12 bits. Avec un CAN 12 bits numérisant la sortie d'un accéléromètre avec une seule alimentation de 3,3 V, la résolution est égale à 806 µV. En appliquant une sensibilité de 0,66 V/g dans le cas du LIS344ALH sélectionné, la résolution est équivalente à 1,22 mg, ce qui est insuffisant pour mesurer les ballistocardiogrammes des accéléromètres de lit. En règle générale, le facteur d'amplification doit être au moins supérieur à 100, soit 40 décibels (dB), pour atteindre la résolution souhaitée. Cependant, une dérive de base est présente dans la sortie de l'accéléromètre. Ainsi, ce déplacement de base peut varier dans le temps, par exemple lorsque le patient change de position. Avant l'amplification, il est important de filtrer la sortie de l'accéléromètre pour ne pas saturer la sortie de l'amplificateur. Dans cette application, la limite entre la gamme de fréquences CA et CC est de 0,05 Hz, ce qui correspond à la limite inférieure de fréquence de l'activité respiratoire. Par conséquent, le premier étage du circuit de conditionnement est un filtre passe-haut actif avec un gain unitaire et une fréquence de coupure de 0,044 Hz. Le deuxième étage du circuit de conditionnement est l'amplificateur de 40 dB, par exemple un amplificateur de gain programmable (PGA) dont le gain peut être réglé par des broches numériques de 0 à 40 dB. Un tel PGA a une structure d'amplificateur opérationnel inversé, comme pour le LTC6910-1 [118]. Il est suivi d'un filtre passe-bas de premier ordre avec une résistance de 66,5 kΩ et un condensateur de 47 nF pour l'anticrénelage et la coupure de la partie du spectre non nécessaire dont les fréquences sont supérieures à 50 Hz. Son diagramme de Bode confirme le gain de 40 dB et la fréquence de coupure de 0,044 Hz. De plus, la phase est approximativement égale à zéro dans la gamme de fréquences du BCG, c'est-à-dire au-dessus de 1,5 Hz.

L'amplificateur d'instrumentation AD8691 qui est utilisé pour le couplage CA pourrait également être utilisé pour une amplification de 40 dB en plaçant une résistance 11 MΩ dans la boucle de rétroaction du circuit inverseur plutôt que de séparer le filtrage et l'amplification en deux étapes consécutives [119]. Une topologie inspirée par [120] permet à la fois de réduire le conditionnement du circuit à un seul étage avec un gain élevé et un temps de stabilisation acceptable. Il consiste à commuter automatiquement le gain de l'amplificateur, lorsqu'il est proche de la saturation, sur un gain plus faible. Le condensateur peut ainsi se charger à grande vitesse, et lorsqu'il est presque chargé, le gain est automatiquement ramené à sa valeur initiale. La commutation automatique est effectuée par des diodes à commutation rapide au lieu de la résistance de rétroaction. En effet, ces diodes peuvent être modélisées comme une résistance variable avec un seuil de tension directe, au-dessus duquel la résistance est très faible et en dessous duquel la résistance est très élevée. Par exemple, la diode à commutation rapide 1N4148 [121] a un seuil de tension directe à 0 V, où sa résistance est de 18 MΩ. Ces valeurs ont été obtenues avec un balayage de la tension continue, de -1,0 V à 1,0 V, et de -100 mV à 100 mV. Plus loin dans cette thèse, le circuit à temps de décantation rapide n'est pas utilisé car il a été inventé récemment ; le circuit à deux étages avec PGA est utilisé à la place.

Concernant le module Fealing Biopac BCG, la sortie de l'accéléromètre est connectée à une unité d'acquisition Biopac MP36. Cet équipement apporte une très faible 9 $nV/\sqrt{Hz}$ densité de bruit d'entrée, dispose de filtres AC matériels avec des fréquences de coupure allant jusqu'à 0,05 Hz, des gains très élevés allant jusqu'à 94 dB, une très haute résolution de 24 bits avec une plage de 8 V en pleine échelle, et une impédance d'entrée très élevée 11 MΩ [122]. Il est adapté aux signaux de très faible amplitude tels que les EEG et mesurera très précisément la sortie du capteur BCG. De plus, ses connecteurs DB9 ont une broche d'alimentation de +5V et il ne nécessite pas d'alimentation externe. Un filtre anti-repliement au-dessus de 50 Hz est

ajouté à la sortie du capteur pour minimiser le bruit lors de l'échantillonnage au-dessus de 100 Hz. Comme l'unité d'acquisition a de grandes dimensions et ne peut pas être encastrée dans le lit du patient, un câble coaxial blindé de 2 à 5 mètres de long relie le capteur, qui se trouve dans le lit, à l'unité d'acquisition. C'est l'inconvénient majeur du module BCG de Fealing Biopac, car ce câble peut apporter des bruits électromagnétiques et des bruits mécaniques.

2.2.3. Intégration mécanique

Pour les modules Fealing Biopac et ST BCG, une connexion câblée à une unité d'acquisition est nécessaire pour numériser la sortie du capteur et pour l'alimentation. Ce fil, qui transmet des informations analogiques, doit être blindé contre la pollution électromagnétique. Cependant, de nombreux câbles coaxiaux sont épais et non flexibles, ce qui empêche le mouvement du module pendant les cycles cardiaques ou respiratoires. Nous avons évalué plusieurs fils coaxiaux fabriqués par AlphaWire [123]. Nous avons choisi l'EcoCable Mini 78103 en raison de son diamètre très fin ; cependant, le câble EcoFlex Pur 80102 sera également testé à l'avenir. Le câble est fixé sur le module BCG par un presse-étoupe ou un connecteur Jack.

Le boîtier doit être suffisamment petit pour être intégré au lit. Plusieurs boîtiers de fabrication Hammond [124] [125] ont été sélectionnés :

- 1551 FGY pour le module BCG de Fealing Biopac
- 1551 NGY pour le module BCG sans fil de Fealing
- 1591XXTGY pour le module Fealing ST BCG.

De plus, il doit être étanche pour pouvoir être nettoyé dans l'environnement hospitalier.

2.3. Amplification du signal pour le BCG des smartphones

2.3.1. Introduction

L'amplification analogique est nécessaire pour obtenir de bonnes performances de détection et concerne généralement l'électronique et les capteurs. Cependant, nous avons observé que la nature de la literie et du cadre de lit modifie la propagation de la force d'éjection vers le capteur, en particulier dans le cas de mousse visqueuse ou de lits médicaux amortissants : les comportements mécaniques de la literie et du cadre de lit peuvent avoir un rôle sur l'amplification analogique. L'utilisation de l'accéléromètre intégré pour la ballistocardiographie au lit est renforcée par deux facteurs : l'amplification mécanique de la force ballistocardiographique, expliquée dans cette section ; et des UMI de plus en plus sensibles qui sont examinées dans le paragraphe suivant.

Un examen des résolutions de l'accéléromètre du smartphone est effectué avec trois bases de données différentes. Tout d'abord, la base de données des capteurs Phyphox [127] est constitué de 760 modèles de smartphones différents soumis par un total de 2325 utilisateurs, au moment de la rédaction de cette thèse. Elle présente les spécifications des accéléromètres utilisés dans ces smartphones, telles que le taux d'échantillonnage, la résolution, le nom et le fabricant. Lors du traitement de la base de données, certains smartphones ont été rejetés parce qu'il manquait des spécifications, par exemple les smartphones Apple. Elle fournit également une estimation de la répartition des différents modèles de smartphones à des moments précis. Deuxièmement, la base de données GSMArena (www.gsmarena.com) donne la date de sortie de nombreux modèles de smartphones. Enfin, la base de données Mouser (www.mouser.com) donne des spécifications plus fines que la base de données des capteurs Phyphox de tous les accéléromètres numériques du marché des smartphones, comme la densité de bruit de sortie. Même si la représentativité de la base de données Phyphox est discutable, elle fournit de bonnes indications pour la période 2014-2019, c'est-à-dire les cinq dernières années. En effet,

plus de 30 appareils figurant dans la base de données ont été mis sur le marché chaque année au cours de cette période. Pour chaque année de la période 2014-2019, les modèles de smartphones publiés sont regroupés en fonction de leur résolution. De plus en plus de modèles sont publiés chaque année avec une résolution d'au moins 2^{12} LSB/g. En cinq ans, la répartition des plus grandes et égales 2^{12} Les modèles LSB/g sont passés de 30% à 80% ; la distribution des modèles strictement inférieurs à 2^{10} Les modèles LSB/g sont passés de 40 % à 10 %.

Dans ce contexte d'augmentation de la sensibilité des accéléromètres des smartphones, nous présentons des modèles de literie qui amplifient le signal du BCG.

2.3.2. Guide d'ondes pour la literie

Le lit utilisé pour cette expérimentation est constitué d'un lit à lattes en bois de pin massif Utaker home et d'un matelas Malvik en latex de polyuréthane ferme de 200x80 cm de dimensions, tous deux produits de la marque Ikea. Le lit est équipé d'un capteur, détaillé dans la section 2.2, placé sur le dessus et à 5 cm du côté du matelas. Ce capteur est basé sur un accéléromètre analogique bidimensionnel Murata SCA100T-D02 avec une densité de bruit de sortie aussi faible que 14 $\mu g/\sqrt{Hz}$. Le capteur est intégré dans un boîtier en plastique ABS et relié par un câble blindé à une unité d'acquisition Biopac MP36R pour le couplage, l'amplification et l'alimentation en courant alternatif. La sortie analogique est couplée en courant alternatif, filtrée anti-aliasing et amplifiée 100 fois avant la numérisation à 1 kHz. Dans cette configuration, la résolution est aussi faible que 2^{21} LSB/g (bit le moins significatif). Un volontaire en bonne santé, pesant 75 kg, âgé de 25 ans et mesurant 1,90 m, a été invité à s'allonger, immobile et calme en position couchée pendant 2 minutes. Ce processus est répété pour plusieurs configurations de matelas (avec ou sans housse) et les literies à guide d'ondes suivantes : pas de guide d'ondes, ruban adhésif en polypropylène (PP), ruban de coton, tissus d'espacement. Un échantillon témoin, sans personne sur le lit, est ajouté

pour mesurer la ligne de base du bruit. Chaque configuration est répétée trois fois pour éliminer la variabilité de la position du lit.

Le but ultime de ces méthodes est d'évaluer la performance relative des couches de guides d'ondes sélectionnées. La première minute est éliminée de chaque enregistrement pour s'assurer que le volontaire est détendu et respire lentement et régulièrement pendant les enregistrements d'une minute qui en résultent. Les signaux numériques du BCG sont filtrés avec des filtres de Butterworth de troisième ordre, en particulier un filtre passe-bas de 25 Hz et un filtre passe-haut de 2 Hz. Ils sont appliqués en avant et en arrière pour éviter toute distorsion de phase. Enfin, le signal est décimé à une fréquence d'échantillonnage de 200 Hz. Les battements de cœur sont détectés à l'aide d'un algorithme de correspondance de gabarit de distorsion temporelle dynamique (DTW) [128]dont les étapes sont rappelées au point 3.2.2. Les pics J du BCG sont fixés comme étiquettes de référence pour les battements du cœur. L'indice de performance absolu est la valeur médiane de ces premiers déciles sur les trois enregistrements de cette configuration.

La configuration du matelas a un impact direct sur l'indice de performance ; de plus, les indices de performance sont dépendants de l'axe. Premièrement, l'axe Y transmet mieux le signal du BCG que l'axe X. Cela a été vérifié ($p<0,05$) pour chaque configuration, sauf pour {couverture+espaceur} où $p = 0,053$, et {couverture+bande de coton} où $p = 0,171$. Deuxièmement, l'ajout d'une housse à la configuration du matelas modifie la transmission du signal BCG le long de l'axe Y ($p<0,05$), sauf lorsqu'aucun guide d'onde n'est utilisé ($p=0,177$). Troisièmement, le guide d'ondes en ruban de coton améliore, indépendamment de la configuration du matelas, l'indice de performance le long de l'axe Y, ce qui n'est pas le cas des autres guides d'ondes. Cela a été vérifié pour l'axe Y avec un matelas sans couverture ($p=0,001$) mais pas avec un matelas couvert ($p=0,230$).

2.3.3. BCG basé sur le téléphone intelligent

Dans cette deuxième expérimentation, également appelée expérimentation BCG basée sur le smartphone, les positions du lit et du capteur sont les mêmes que dans l'expérimentation précédente. Cette fois, le capteur est basé sur un smartphone : il s'agit d'un accéléromètre numérique 3D LSM6DSM de STMicroelectronics, intégré dans un téléphone Motorola One. Dans cette configuration de smartphone, le taux d'échantillonnage est de 200 Hz, la résolution est $2^{12}\ LSB/g$ et la densité de bruit de sortie est de 90 $\mu g/\sqrt{Hz}$. Il convient de noter que ces spécifications sont bien pires que celles du capteur fait maison dans l'expérimentation 1. L'application non divulguée Fealing SleepLogger a été utilisée pour enregistrer les échantillons de l'accéléromètre et les exporter sur un ordinateur. Le même adulte s'allonge sur le lit, immobile et calme en position couchée pour une sieste de 30 minutes, dans deux configurations différentes : avec le smartphone fixé par un velcro sur une literie à guide d'ondes ou directement sur le couvre-matelas. Le guide d'ondes est confortable et n'est pas remarqué par le sujet, même après une nuit de sommeil. Un autre capteur est utilisé comme référence : l'EMFIT QS [129] capteur de pression normale, qui fournit un service d'exportation de signaux bruts pour les siestes de plus de 20 minutes, dans les bandes de fréquence de la respiration (0,07-3 Hz) et du cœur (1,5-35 Hz).

Les signaux BCG sans mouvement sont segmentés et leur moyenne est ramenée à zéro. La valeur moyenne quadratique des signaux des capteurs est calculée à l'aide de la méthode $RMS()$ fonction. Une fonction de transfert est calculée comme le rapport de la valeur efficace des capteurs de téléphones intelligents sur la valeur efficace du capteur de pression de référence. L'unité de cette fonction de transfert est mg/Navec A l'accélération mesurée par le smartphone le long d'un axe et P la mesure de la pression normale par le capteur Emfit QS. Idéalement, les capteurs 1 et 2 du smartphone enregistrent le BCG simultanément ; cependant, la configuration est compliquée car la literie à guide d'ondes couvre toute la largeur du

matelas. Par conséquent, deux siestes de 30 minutes sont enregistrées : une avec (capteur 1 du smartphone) et une sans (capteur 2 du smartphone) literie à guide d'ondes. Pour chacune de ces siestes, les ballistocardiogrammes sont segmentés en segments sans mouvement, avec ou sans présence et avec deux largeurs de bande de fréquences différentes. Les trois axes des capteurs de l'accéléromètre sont étudiés.

Le facteur de gain est supérieur à 3,4 dans la bande de fréquence cardiaque sur chaque axe. Pour conclure, nous avons testé plusieurs lits de guides d'ondes pour amplifier un signal BCG et avons constaté que le ruban de coton permet en général une meilleure transmission que les tissus d'écartement ou le ruban adhésif en PP. Les auteurs sont prudents quant à la signification de ce résultat car seuls trois enregistrements ont été réalisés par configuration. D'autres enregistrements sont nécessaires pour confirmer les résultats, et d'autres cadres de lit et matelas devront être étudiés. Pour une configuration de matelas donnée, certains guides d'ondes améliorent la transmission le long de l'axe Y mais la modifient le long de l'axe X, par exemple le ruban PP adhésif sur le matelas sans couverture. Deux explications sont plausibles : soit le guide d'ondes a transféré la contrainte de l'axe X à l'axe Y, soit la friction en position couchée sur le lit a fait tourner le capteur autour de l'axe Z. Des caméras pendant l'expérimentation ou la simulation permettront d'élucider ce phénomène. Le confort du guide d'onde sera quantifié dans des expériences ultérieures et par simulation.

Les lits de guides d'ondes permettent la ballistocardiographie sur smartphone, grâce à un facteur d'amplification de 3,4 à 4 du signal de l'accéléromètre du smartphone. Enfin, l'étude sur les smartphones montre que les résolutions des accéléromètres des nouveaux modèles de smartphones sont de plus en plus fines. Les résolutions des 2^{14} Le LSB/g a subsisté sur le marché jusqu'en 2017, mais après un examen détaillé des bases de données, c'est parce que les portées des smartphones-accéléromètres sont également plus élevées. La plus haute résolution 2^{14} Les modèles LSB/g, jusqu'en 2017, où 16 bits avec un ± 2 g, alors

qu'aujourd'hui les fabricants exigent au moins ± 4 g et jusqu'à ± 16 g, ce qui réduit inévitablement la résolution de l'accéléromètre. Malgré tout cela, nous pouvons nous attendre à ce que les nouvelles technologies apportent des résolutions plus élevées. La densité du bruit est également une caractéristique importante, et son évolution sera détaillée plus tard.

2.4. Multiplexage du signal pour l'imagerie BCG

2.4.1. Introduction

Une amplification analogique est nécessaire pour obtenir de bonnes performances de détection. Par conséquent, elle est très sensible à l'errance de la ligne de base qui se produit lors d'un changement de position, par exemple de la position couchée à la position allongée, et doit être filtrée. Cependant, pour mesurer l'activité respiratoire dont les composantes de basse fréquence sont d'environ 0,1 Hz [130]Les filtres passe-haut habituels sont lents à s'installer et le signal du BCG peut saturer pendant plusieurs décennies de secondes, comme le montrera cette thèse. L'ajout de composants non linéaires, par exemple des diodes de commutation dans la boucle de rétroaction de l'amplificateur [116], peut aider à réduire le temps de stabilisation de l'amplificateur, c'est-à-dire le temps avant la fin de la saturation, pour quelques secondes seulement. De plus, l'individu et son lit peuvent être considérés comme un système d'amortissement qui génère du bruit à sa fréquence de résonance.

Des bruits environnementaux, par exemple la marche des infirmières, les appareils de ventilation, ou pendant le transport dans une unité de soins intensifs pédiatriques, peuvent également se produire. Pour les mêmes raisons de saturation, ces bruits répétitifs doivent être filtrés, sinon la couverture de surveillance risque d'être réduite.

Dans ce contexte, nous introduisons un nouveau frontal BCG intelligent qui identifie la fréquence de résonance du système, filtre le vagabondage de la ligne de base et le bruit d'amortissement, et amplifie fortement le signal BCG sans saturation après le mouvement.

2.4.2. Matériel

Le simulateur de battements de coeur de bébé a été utilisé pour l'expérience. Une architecture à signaux mixtes est une topologie dans laquelle un signal analogique est numérisé par un ADC, filtré sur un DSP puis synthétisé par un DAC [131]. Ces circuits présentent les mêmes avantages que les filtres numériques, par exemple une bande de fréquence de transition nette ou un temps de stabilisation rapide, et peuvent être associés à un amplificateur analogique. Dans le cas du BCG, les composantes indésirables du signal d'accélération analogique doivent être filtrées avant l'amplification et la numérisation. L'architecture conçue élimine ces composantes indésirables et amplifie le signal résultant à l'aide d'un amplificateur d'instrumentation. Des architectures similaires ont été utilisées dans le traitement des signaux biologiques. En 2003, Analog Devices a proposé un frontal d'électrocardiographie utilisant le microcontrôleur ADuC842 avec une simple rétroaction par étapes sur la broche de décalage de référence de l'amplificateur d'instrumentation AD620 [132]. En 2004 et plus récemment, le frontal d'électroencéphalographie a intégré des filtres passe-haut pour l'élimination des vagabondages de base [133] [134]. Cependant, ces documents ne se sont concentrés que sur l'élimination de l'errance de base, avec une fréquence de coupure beaucoup moins contraignante que dans le cas du BCG (5 et 0,05 Hz pour l'EEG et le BCG respectivement).

Pour éliminer les composantes indésirables du signal, deux types de filtres linéaires numériques ont été étudiés : les filtres à réponse impulsionnelle finie (FIR) et une cascade de filtres à réponse impulsionnelle infinie (IIR) du second ordre, communément appelée cascade de filtres biquadratiques. Par convention, a_0 est fixé à 1. Les coefficients de filtrage sont calculés à l'aide de la bibliothèque Python *scipy.signal* sur un ordinateur 64 bits. Ils doivent être quantifiés à des coefficients de 32 bits avant d'être implémentés sur le DSP, ce qui peut générer des erreurs, en particulier pour les filtres IIR avec des filtres à fortes contraintes et une

fréquence de coupure très basse. Le temps de stabilisation des filtres dépend de l'initialisation. L'état du filtre est généralement initialisé à zéro : le signal est donc causal. Cependant, le capteur a une position de repos qui est connue ou peut être estimée. On peut supposer que l'accéléromètre est posé à plat sur le matelas qui est lui-même horizontal : l'axe Z devrait voir une valeur de décalage d'environ +1 g, soit 2,31 V dans ce réglage. Le filtre est initialisé en considérant que le signal est de 2,31 V avant de commencer l'enregistrement.

2.4.3. Suppression de l'errance de base

Une composante souvent indésirable du signal physiologique est l'errance de la ligne de base. Il s'agit d'une composante à basse fréquence qui empêche une amplification à haut gain. En ballistocardiographie, l'excursion de base est un décalage de tension qui dépend de la position du corps et du poids dans le lit. Par exemple, lors d'un changement de position du patient, l'orientation de l'accéléromètre et la projection de la gravité sur les axes de l'accéléromètre changent. Nous avons observé que cette valeur de décalage varie généralement de 0,1 à 0,5 g, pour laquelle l'amplificateur saturerait avec $G > 3\ dB$. La respiration, dont la fréquence varie de 0,5 à 1,0 Hz en néonatologie [135] et jusqu'à 0,1 Hz en gériatrie [130]peut être considéré soit comme un élément de la ligne de base, soit comme un élément utile du signal. Dans ce travail, la respiration n'est pas filtrée, par conséquent, la fréquence de coupure du filtre de l'errance de base est fixée à 0,05 Hz. Dans le cas de la FIR, la méthode de la fenêtre est appliquée avec une fenêtre de Kaiser de 40 dB d'atténuation minimale dans la bande passante et une largeur de bande de transition de 0,1 Hz. Le filtre FIR résultant a 5716 coefficients. Dans le cas du FIR, un filtre de Butterworth de second ordre, choisi en raison de sa réponse maximale plate dans la bande passante, est conçu et répété deux fois pour accentuer la transition. Dans ce travail, le filtre choisi est ce filtre IIR du quatrième ordre, car le filtre FIR est trop coûteux en calcul pour le microcontrôleur.

Le filtre IIR réussit à filtrer l'errance de la ligne de base, et celle-ci est éliminée par l'amplificateur. À l'état d'équilibre, l'amplitude maximale crête à crête des impulsions est dix fois plus élevée à la sortie qu'à l'entrée. En utilisant ce filtre, des vibrations à différentes fréquences constantes sont générées et les accélérations mesurées sont comparées avant et après le filtrage et l'amplification par leurs valeurs moyennes quadratiques.

2.4.4. Identification et filtrage des fréquences de bruit

La fréquence du bruit est identifiée et filtrée à l'aide de l'algorithme intégré. L'étape de détection des vibrations est paramétrée par un seuil de tension, ci-après appelé seuil, au-delà duquel la vibration est détectée. La vibration commence à cet endroit et a une durée fixe. La densité spectrale de puissance de la vibration segmentée est calculée par le microcontrôleur. Son maximum est situé à la fréquence du bruit, de sorte qu'elle se situe en dehors de la plage de fréquence du BCG, sinon, les battements du cœur dans le signal du BCG seraient déformés ou filtrés. Plusieurs filtres coupe-bande, avec des facteurs de qualité Q=0,707, ont été précédemment calculés à l'aide de la bibliothèque *scipy.signal en* dehors du microcontrôleur. Le filtre coupe-bande dont la fréquence est la plus proche de la fréquence du bruit est sélectionné et ajouté au filtre d'errance de la ligne de base de l'IIF.

Le seuil et la durée ont été fixés respectivement à 1,5% de l'errance de base et à 0,25 seconde. Le bruit était généré par des vibrations pulsées, c'est-à-dire le BCG simulé. La fréquence du bruit déterminée par le microcontrôleur est d'environ 68 Hz. Il s'agit de la fréquence de résonance du système d'amortissement. Un filtre coupe-bande a ensuite été sélectionné par l'algorithme pour filtrer la fréquence de bruit identifiée.

2.4.5. Conclusion

Ces travaux ont permis d'introduire un nouveau frontal BCG intelligent qui identifie la fréquence de résonance du système, filtre le vagabondage de la ligne de base et le bruit

d'amortissement, et amplifie le signal du BCG sans saturation après les mouvements du patient.

Au cours des expérimentations, un gain limité de 21 dB a été utilisé pour illustrer le principe de l'entrée du BCG intelligent. Des gains plus élevés ont entraîné des signaux bruyants et une saturation, en raison de l'utilisation de cartes de prototypage plutôt que d'un circuit électronique spécifique avec un plan de masse approprié. À l'avenir, un amplificateur avec un gain plus élevé sera conçu et testé sur des patients réels.

Par rapport aux instruments BCG habituels, ce circuit de conditionnement a un temps de stabilisation plus court et une transition de fréquence plus nette. Le principe d'un frontal BCG intelligent a été démontré ; il ouvre des possibilités d'applications médicales, en temps réel et à faible coût.

3. Traitement numérique des signaux en balistique

Les ballistocardiogrammes contiennent de nombreuses informations physiologiques : les activités motrices, respiratoires et cardiaques, ainsi que les cycles du sommeil. Comme les patients sont susceptibles de sortir du lit la nuit, il peut être important de détecter également l'occupation. Un ballistocardiogramme typique contient différentes périodes : mouvement, absence et présence. Dans les segments de présence, le ballistocardiogramme contient des signes vitaux tels que les fréquences respiratoires et cardiaques, ou les points de repère des activités respiratoires et cardiaques, qui doivent être détectés par des algorithmes spécifiques.

Dans ce chapitre, nous présentons les bases de données ballistocardiographiques qui ont été acquises au cours de cette thèse, car aucune base de données publique n'était disponible. Dans chacune de ces sections, nous passerons en revue les algorithmes de traitement numérique du signal existants et détaillerons les nouveaux algorithmes que nous avons mis au point pour détecter les informations physiologiques contenues dans les ballistocardiogrammes.

3.1. Enregistrement et prétraitement des bases de données ballistocardiographiques

Avant de développer des algorithmes de traitement numérique des signaux pour segmenter les ballistocardiogrammes et détecter les signes vitaux, des bases de données étaient enregistrées. Les bases de données présentées dans cette section contiennent des ballistocardiogrammes bruts et des signes vitaux de référence. Les signes vitaux de référence ont été obtenus soit avec des instruments de référence (par exemple, l'ECG), soit avec des étiquettes qui ont été vérifiées manuellement par deux experts. Par exemple, les points de référence I, J et K des ballistocardiogrammes bruts ont été calculés en utilisant [128] et annoté dans les bases de données. Les séries de fréquences cardiaques de référence sont reconstruites à l'aide de ces annotations.

Ces bases de données sont stockées dans un serveur privé au format normalisé du FED [136]qui a été développé en 1992 et amélioré en 2002 pour stocker efficacement les bases de données polygraphiques. Tous les processus d'acquisition de ces données ont été validés par une commission éthique conformément à la législation européenne sur les données. Dans les sections suivantes, ces bases de données sont décrites.

3.1.1. CHArt

La base de données ballistocardiographiques CHArt a été acquise dans un des bureaux de l'Ecole Pratique des Hautes Etudes. Des adultes en bonne santé, employés bénévoles du laboratoire, ont été invités à se reposer pendant 20 à 50 minutes à la pause déjeuner, en position couchée. Nous avons utilisé un MM0 3000 [137] un lit médicalisé et un recouvrement MMO Aerospacer [138]. Un capteur BCG Murata SCA11H a été placé sur le recouvrement, dans le sens tête-pied. 27 volontaires n'ont accidentellement pas été invités à rester immobiles et silencieux. Par conséquent, de nombreux enregistrements ont été pollués par des artefacts de mouvement et ont été rejetés de la base de données. En fin de compte, la

base de données CHArt comprend 10 adultes en bonne santé pour des enregistrements de 20 à 50 minutes.

3.1.2. LSI

Cet acronyme signifie "La Science Infuse", un événement d'une semaine de la Cité des Sciences et de l'Industrie à Paris, en France, qui vise à vulgariser la science auprès du public. Des volontaires, recrutés parmi le public, ont été invités à s'allonger et à se tenir tranquillement en position couchée pendant 35 secondes. Le module Fealing Biopac BCG est utilisé pour les enregistrements de ballistocardiogrammes dans le sens gauche-droite - voir section 2.2. À des fins pédagogiques, les ballistocardiogrammes étaient affichés en temps réel sur un écran et un autre visiteur, généralement un ami ou un parent du volontaire, était invité à taper des mains devant un microphone dès qu'une forme d'onde "W", c'est-à-dire un battement de cœur, apparaissait sur le ballistocardiogramme. Le ballistocardiographe et le microphone ont été acquis de manière synchrone sur un appareil BIOPAC MP36. Le lit utilisé pour cette expérimentation est constitué d'un lit à lattes en bois de pin massif Ikea® Sniglar pour bébé et d'un matelas Tediber® Tedi en latex de polyuréthane ferme de 70x140 cm. Le capteur est placé sur le dessus et à 5 cm du côté du matelas.

Seuls les enfants étaient initialement visés par cette étude, avec le consentement des parents ; toutefois, les accompagnateurs et les visiteurs adultes étaient également disposés à participer à l'étude. Les auteurs ont trouvé intéressant de les recruter et de comparer les adultes au BCG des enfants dans le cadre d'études physiologiques complémentaires. Pour les sujets mesurant plus de 140 cm, la taille du lit n'était pas appropriée et les jambes étaient inconfortables hors du lit. Cela ne semblait pas altérer la qualité de l'enregistrement, tant que les sujets étaient immobiles. Au total, 336 sujets ont été enregistrés ; cependant, de nombreux enregistrements ont été rejetés parce que les signaux étaient pollués par des artefacts de

mouvement, les enfants ayant des difficultés à se concentrer pour ne pas bouger ou parler. Au final, 40 sujets sont inclus, avec des âges allant de 8 à 74 ans.

3.1.3. Ollie

La base de données Ollie est liée au nom d'un produit Fealing, consistant en un amplificateur de guide d'ondes de literie à placer autour du matelas. Chaque nuit, le volontaire fixe son téléphone sur l'aimant du guide d'ondes et effectue un enregistrement avec l'application Ollie. La première version de l'application mobile Ollie s'appelle SleepLogger. Elle est uniquement disponible sur iOS et en français via TestFlight pour les tests bêta.

Lorsque c'est possible, un capteur BCG EMFIT QS est utilisé pour enregistrer des ballistocardiogrammes et des signes vitaux bruts et les comparer avec le système Ollie. Une étude du sommeil sur 30 athlètes est également sur le point d'être menée avec ce système et des mesures polysomnographiques de référence avec des bandeaux Dreem et des polysomnographes portables plus traditionnels à l'Institut National du Sport, de l'Expertise et de la Performance (INSEP).

Jusqu'à présent, cinq personnes ont été enregistrées leurs nuits pendant une semaine avec ce dispositif. Outre la partie INSEP de la base de données Ollie, Fealing lance un programme de recherche pour enregistrer les ballistocardiogrammes de 100 volontaires pendant 6 mois dans des conditions écologiques.

3.1.4. R2P2

La base de données R2P2 est liée à la "Réanimation Pédiatrique de l'hôpital Raymond Poincaré", l'unité de soins intensifs pédiatriques (USIP) qui héberge cette acquisition de base de données à Garches, en France. L'objectif de l'étude initiale est de confronter les mesures de BCG des nouveau-nés sains et malades aux mesures cliniques de l'ECG et de la SPO2, afin de voir si le BCG est pertinent pour la surveillance physiologique néonatale en milieu hospitalier.

40 nouveau-nés seront recrutés parmi les patients hospitalisés pour au moins une nuit à l'USIP.

3.2. Mesure de la fréquence cardiaque et respiratoire

Les ballistocardiogrammes de présence sans mouvement sont segmentés et vérifiés visuellement par deux experts. Sur ces segments de BCG, les signes vitaux tels que les fréquences cardiaque et respiratoire peuvent être mesurés. Dans cette section, nous nous concentrons principalement sur la détection de la fréquence cardiaque ; cependant, les méthodes développées peuvent également être appliquées à la détection de la fréquence respiratoire.

La principale préoccupation du traitement numérique du BCG pour la détection des signes vitaux est le bruit et la variabilité du signal, qui sont beaucoup plus importants que dans l'ECG.

Dans cette section, l'état de l'art et les algorithmes nouvellement développés sont présentés.

3.2.1. État de l'art

Des algorithmes spécifiques de traitement numérique des signaux ont été mis au point pour détecter les battements cardiaques, la fréquence cardiaque battement par battement et la variabilité de la fréquence cardiaque (VFC) dans les signaux BCG en utilisant des méthodes du domaine temporel ou du domaine temps-fréquence. Sprager a comparé plusieurs algorithmes pour la détection des battements cardiaques mais a trouvé de meilleurs résultats dans le PCG que dans le BCG [64].

Pour de nombreuses applications qui ne nécessitent pas d'informations sur la variabilité de la fréquence cardiaque, la fréquence cardiaque moyenne sur une période donnée est suffisamment utile. Zhu a observé que contrairement à l'électrocardiogramme, le ballistocardiogramme a une fréquence fondamentale qui est différente de la fréquence

cardiaque. Il associe cette fréquence fondamentale du ballistocardiogramme à la troisième harmonique du rythme cardiaque. Dans cette méthode, la fréquence cardiaque moyenne est donc estimée en divisant par 3 la fréquence fondamentale du ballistocardiogramme. La transformée de Fourier à court terme peut également être appliquée à une enveloppe de signal, c'est-à-dire un signal de modulation cardiaque, pour estimer régulièrement la fréquence cardiaque moyenne [158]. Une méthode de cepstre à fenêtre adaptative est expliquée dans [65]une transformation cepstrale réelle à court terme peut être appliquée sur le ballistocardiogramme avec une fenêtre adaptative qui couvre deux battements de coeur. Les cesptra de deux fenêtres avec un intervalle entre les battements différent montrent le potentiel de cette méthode pour estimer un rythme cardiaque moyen.

Pour les applications relatives aux arythmies ou à la variabilité de la fréquence cardiaque, par exemple les études sur le sommeil, la fréquence cardiaque instantanée est nécessaire : les battements cardiaques doivent être détectés un par un. Les séries HR et BB sont interpolées linéairement entre deux battements de cœur, par exemple pour uniformiser leurs fréquences d'échantillonnage.

L'algorithme de référence de Pan-Tompkins pour la détection des pics R [159] dans les performances de l'ECG est difficile à appliquer à la détection du pic J dans le BCG. L'algorithme donne les meilleurs résultats sur le signal filtré ; cependant, ce signal est déformé, ce qui tend à faire la moyenne de la fréquence cardiaque. La méthode Pan-Tompkins fait partie de plusieurs méthodes de segmentation utilisées pour détecter les complexes QRS dans les électrocardiogrammes [160] [161] [162] [163] [164]. Ces méthodes seront comparées à nos bases de données dans des travaux ultérieurs.

Les battements de cœur peuvent être détectés parmi un ensemble de maxima locaux et de règles de décision basées sur les délais entre ces maxima [63]. L'utilisation d'un algorithme de recherche de pics avec une contrainte de distance permet d'afficher des groupes de

battements de cœur sur un diagramme de Poincaré, en fonction du paramétrage de la distance. Sur des séries de battements, ils forment un amas gaussien avec une matrice de covariance diagonale. Par conséquent, ils sont utiles pour la détection des arythmies, où deux intervalles consécutifs de battement à battement peuvent être très différents et apparaître comme un point aberrant sur le diagramme de Poincaré.

Les points de repère d'une forme d'onde de ballistocardiogramme ont des formes spécifiques qui peuvent être identifiées par plusieurs paramètres. Après l'analyse en composantes principales, les points de référence peuvent être regroupés par l'algorithme de la moyenne k. Nous avons détecté ces points de synchronisation et tracé des vecteurs caractéristiques représentant les extrêmes locaux du signal BCG dans l'espace (proéminence, distance), où la distance est comprise comme le retard entre un extrême local et le point de synchronisation. Après une transformation logarithmique, ces extrema peuvent être regroupés en utilisant des moyennes k. Le nombre approprié de grappes est sélectionné en optimisant la silhouette moyenne. Les grappes de points repères sont identifiées par leur proéminence et leur retard respectifs ; par exemple, le centroïde de la grappe de proéminence la plus élevée indique la grappe de pic J. La trajectoire des points de repère dans un espace bidimensionnel comme dans [40] est utile si les groupes ne sont pas parfaitement séparés. Lorsque les extrema sont loin de leur centre de gravité, les points précédents et suivants sont négligés : s'ils appartiennent respectivement à l'amas précédent et suivant, l'extremum est confirmé dans son amas, sinon, son appartenance est réévaluée. Un algorithme de segmentation aveugle, BSeg++, trouve les points de synchronisation, c'est-à-dire les maxima locaux d'un BCG filtré passe-bande étroite dans la gamme de fréquences de 1-2 Hz [165]. Les minima locaux du BCG brut, dans le voisinage de ces points de synchronisation, sont identifiés comme des pics I. Les maxima locaux dans un voisinage spécifique avant et après ces pics I sont identifiés par des pics H et J, respectivement.

L'analyse par ondelettes a été un peu utilisée dans le traitement des signaux du BCG. En 1996, la multirésolution par ondelettes combinée à un seul réseau neuronal de feedforward pouvait classer les ballistocardiogrammes normaux, l'hypertension et les crises cardiaques [39]. Cependant, il n'a pas été utilisé comme détecteur de battements de cœur. Akhbardeh a amélioré les performances de classification avec un support compact Daubechies wavelet et deux couches cachées [166]. Jin a utilisé en 2009 des ondelettes pour débruiter le ballistocardiogramme et applique un seuil adaptatif pour détecter les battements cardiaques [167]. L'ondelette Sym4 a été utilisée pour générer un scalogramme BCG, c'est-à-dire une représentation temps-fréquence à différentes échelles d'ondelettes. Les modèles de battements de cœur sont facilement reconnaissables dans cette image. Les avantages des ondelettes symétriques sont leurs symétries. Comme équivalent d'un filtre passe-bande étroit, le coefficient de détail qui a la variance la plus élevée est sélectionné. Ainsi, une seule échelle avec une gamme de fréquences étroite est sélectionnée et son enveloppe peut être extraite par la méthode de Hilbert. Un seuil peut être utilisé pour détecter les battements de cœur sur cette forme d'onde simplifiée.

Dans les méthodes d'appariement des modèles, une forme de battement de cœur est modélisée et corrélée au signal. La forme du battement de cœur peut être estimée manuellement [37] [153] ou automatiquement [40][41]. Cependant, la fonction de corrélation croisée peut être difficile à définir en raison de l'amplitude du complexe IJK. Comme le ballistocardiogramme est modulé en amplitude par la respiration, la corrélation croisée oscille et peut être malaisée au seuil.

3.2.2. Déformation dynamique du temps

Nous présentons une nouvelle méthode de détection des battements de coeur basée sur un algorithme de correspondance de gabarit amélioré par la DTW et la normalisation des battements de coeur [128]. La détection qui en résulte est robuste aux variations de bruit et de

battements de cœur. La méthode a été testée par rapport à la base de données CHArt. L'objectif ultime des méthodes est de détecter avec précision les battements de cœur dans le BCG, pour les analyses de fréquence cardiaque et de VRC. Avant l'algorithme de détection, les signaux du BCG sans mouvement étaient isolés manuellement. Dans ce travail, nous nous concentrons sur ces signaux.

L'algorithme de correspondance du modèle DTW présenté dans ce travail a été testé sur la base de données BCG CHArt décrite à la section 3.1.1. Un expert médical a vérifié manuellement chaque battement de cœur à l'aide d'un logiciel de visualisation des données dédié. Un battement de coeur détecté est classé comme vrai positif uniquement si son pic J se trouve au même endroit que le pic J d'un vrai battement de coeur. La spécificité n'a pas été calculée car les vrais négatifs sont mal définis. La sensibilité globale et la prédictivité positive sont respectivement de 95,6 % et 96,8 %, avec un SNR des enregistrements allant de 2,0 à 14,6. Si nous séparons les enregistrements dont le SNR est inférieur à 3 (quatre enregistrements) de ceux qui sont supérieurs à 3 (six enregistrements), la sensibilité et la prédictivité positive seront de 85,3 % et 88,5 % dans le cas le plus bruyant ; 98,7 % et 99,2 % dans le second cas.

Nous avons présenté une méthode d'appariement de modèles pour détecter et déterminer automatiquement la forme des battements de cœur dans les signaux BCG, qui résout les problèmes d'amplitude et de variabilité temporelle par déformation et normalisation dynamiques du temps. Cet algorithme a été testé avec succès sur une base de données dans des conditions de bruit variables. Les mesures physiologiques synchronisées de l'étalon-or telles que l'ECG étant manquantes, les battements cardiaques détectés ont été vérifiés manuellement. Ce processus est fastidieux, surtout dans des conditions de bruit où il est difficile de marquer manuellement les battements de cœur. De plus, l'étape de détection des battements cardiaques de l'algorithme impose un délai minimum entre deux battements

cardiaques consécutifs sur la base d'une estimation du rythme cardiaque moyen. Cette hypothèse forte pourrait être affinée localement en utilisant la transformée de Fourier à court terme en fonction de la longueur du signal. En outre, comme les battements de cœur sont sélectionnés par leur distance DTW ascendante avec le modèle, un battement de cœur mal étiqueté entraîne souvent de multiples faux positifs dans son voisinage ; ce problème pourrait être résolu en ajoutant des caractéristiques pour l'étape de détection des battements de cœur.

3.2.3. Modèles de Markov cachés

Une autre façon de modéliser le signal de manière non linéaire est d'utiliser des modèles de Markov cachés. De nombreux signaux physiologiques, en raison de leur pseudo-périodicité, ont tendance à être bien modélisés par les modèles de Markov cachés gaussiens (HMM). Par exemple, les signaux ECG peuvent être modélisés comme une séquence récurrente d'états P, Q, R, S, T crête, qui génèrent des amplitudes de tension qui suivent différentes lois gaussiennes et ont des durées différentes [170] [171] [172] [173]. Les séismocardiogrammes, c'est-à-dire les signaux cardiaques mesurés par l'accélération thoracique, ont également été modélisés en utilisant une architecture différente avec plus d'états [174] pour mesurer les intervalles entre les battements. En raison des similitudes entre les signaux SCG et BCG, cette dernière méthode pourrait être appliquée au BCG. Cependant, elle présente plusieurs inconvénients. Tout d'abord, elle ne détecte pas les battements cardiaques mais seulement les retards entre les battements cardiaques car aucun état n'est associé à un point de référence. Deuxièmement, elle est spécifique au patient et nécessite des annotations manuelles pour chaque nouveau sujet afin de former le HMM. Troisièmement, il est coûteux en termes de calcul en raison du nombre élevé d'états, généralement des centaines.

Dans ce contexte, nous présentons une nouvelle méthode, inspirée par [174]pour détecter les battements de cœur du BCG sur la base d'un HMM indépendant du patient et d'un algorithme de réduction du modèle. La détection qui en résulte est robuste au bruit et à la

variabilité des battements de cœur. La base de données CHArt a été utilisée pour tester les performances de détection.

Les algorithmes HMM dépendant et indépendant du patient, avec ou sans les algorithmes optionnels de réduction HMM robuste ou rapide présentés dans ce travail, ont été testés sur la base de données CHArt. Les performances sont en cours de traitement et de comparaison avec d'autres algorithmes. L'étape optionnelle de réduction diminue le temps de calcul de l'entraînement (itérations de Baum-Welch) et des tests, soit l'algorithme de Viterbi, soit le marquage des battements de cœur. Le temps de calcul a été mesuré sur un ordinateur portable Thinkpad T400 et des bibliothèques Cython. Cette figure montre les avantages de la diminution du nombre d'états dans le modèle de Markov caché en termes de temps de calcul.

3.2.4. Réseau neuronal U-Net

Une autre façon de modéliser non linéairement un ballistocardiogramme consiste à utiliser des réseaux de neurones. Les réseaux de neurones ont été utilisés pour détecter et classer les battements de cœur et les points de référence des signaux ECG [176]. Les réseaux neuronaux convolutionnels ont été appliqués pour détecter les segments IJK dans le BCG, avec une précision assez faible de 88%. [177]. U-Net, une architecture de réseau neuronal récente, a obtenu des résultats impressionnants pour la délimitation des ECG [178]avec un score F1 allant jusqu'à 99,9 % pour la segmentation du QRS et un petit ensemble de données. Cette méthode est appliquée à la détection des battements de cœur du BCG dans ce travail. Dans ce contexte, nous introduisons une nouvelle méthode de segmentation des complexes IJK et de détection des battements cardiaques dans le BCG, basée sur un modèle U-Net. Cette méthode est testée sur la base de données LSI.

Cet algorithme a introduit une nouvelle façon de détecter les battements de cœur en ballistocardiographie qui apprend la périodicité physiologique du rythme cardiaque et les variabilités des battements de cœur avec de bonnes performances. U-Net est pertinent pour

cette tâche, car il permet une étape de segmentation intermédiaire qui aide à détecter les battements cardiaques dans les étapes suivantes. Cette étude comporte plusieurs questions qui devront être abordées dans des études ultérieures. Premièrement, le processus de recrutement a changé au cours de l'expérience, de sorte que tous les matériaux n'ont pas été adaptés pour les adultes, par exemple le lit d'enfant. L'expérience sera répétée et répartie entre les adultes et les enfants, qui utiliseront une taille de lit adaptée. Deuxièmement, de nombreux disques ont été jetés à cause d'artefacts de mouvement, par conséquent, le protocole de mesure sera révisé, par exemple, la durée des disques sera augmentée. Si cette révision n'est pas suffisante pour obtenir des segments sans mouvement du BCG dans chaque enregistrement, le matériel sera également révisé. Troisièmement, les paramètres des hyperparamètres ont été inspirés par un tracé d'électrocardiogramme existant U-Net [178]L'optimisation des hyperparamètres pourrait être intéressante pour améliorer la précision de détection des battements de cœur du BCG. D'autres améliorations, telles que l'augmentation des données et la segmentation multi-classes, basées sur les autres points de référence présents dans le BCG, doivent également être étudiées.

4. Discussion générale et perspectives d'avenir

Des instruments de ballistocardiographie ont été développés pour amplifier les ballistocardiogrammes et enregistrer plusieurs bases de données. En raison du nombre limité d'enregistrements utilisés pour la section 2.3et la section 2.4. Les performances obtenues avec les nouveaux amplificateurs devront être confortées par d'autres expériences.

Plusieurs algorithmes de segmentation des mouvements et de l'occupation, ainsi que de détection des battements de cœur, ont été détaillés dans ce document. Dans la suite des travaux, ces algorithmes seront systématiquement comparés aux algorithmes de référence de la littérature, sur toutes les bases de données enregistrées. Ainsi, les meilleurs algorithmes seront sélectionnés quantitativement.

Ces algorithmes seront testés sur les bases de données acquises afin de déterminer si un appareil de RPM de qualité médicale peut être conçu en utilisant la ballistocardiographie.

Ce travail sera poursuivi avec des applications sur l'imagerie, la télésanté, les soins néonatals et l'étude du sommeil.

RÉSUMÉ

À l'échelle mondiale, les systèmes de santé ont des coûts croissants et le nombre d'hospitalisations augmente. La télémédecine permet de ramener l'hôpital à la maison et offre aux structures de santé de nouvelles possibilités d'améliorer le parcours de soins des patients.
Les dispositifs médicaux connectés qui surveillent les signes vitaux ne sont pas entièrement automatisés, ce qui entraîne un désengagement du patient ou nécessite du personnel soignant supplémentaire. Les moniteurs passifs et sans contact des signes vitaux tels que les ballistocardiographes, qui mesurent les microdéformations du matelas dues aux activités cardiaques, respiratoires et motrices, sont plus confortables et plus sûrs pour les patients mais moins précis que les moniteurs traditionnels.
Dans cette thèse, de nouvelles méthodes d'amplification analogique et de filtrage numérique sont étudiées pour améliorer la précision de la ballistocardiographie, qui seront prochainement évaluées cliniquement.

MOTS CLÉS

Ballistocardiographie, télésurveillance, traitement du signal, électronique

ABSTRACT

Globally, health systems are facing rising costs and the number of hospitalizations is increasing. Telemedicine brings hospital at home and offers new opportunities for healthcare facilities to improve the patient care pathway.
Connected medical devices that monitor vital signs are not fully automated, resulting in patient disengagement or requiring additional nursing staff. Passive and contactless vital signs monitors such as ballistocardiographs, which measure mattress micro-deformations due to cardiac, respiratory and motor activities, are more comfortable and safer for patients but less accurate than traditional monitors.
In this thesis, new analog amplification and digital filtering methods are studied to improve the accuracy of ballistocardiography, which will soon be clinically evaluated.

KEYWORDS

Ballistocardiography, remote patient monitoring, signal processing, electronics